Philipp M. Leufke

Magnetoelectric coupling in layered LSMO/PZT nanostructures

Magnetoelektrische Kopplung in LSMO/PZT Nano-Schichtstrukturen

– Dissertation –

TECHNISCHE UNIVERSITÄT DARMSTADT

Fachbereich
Material- und Geowissenschaften
Technische Universität Darmstadt

Institut für Nanotechnologie (INT)
Karlsruher Institut für Technologie (KIT)

Magnetoelectric coupling in layered LSMO/PZT nanostructures

Magnetoelektrische Kopplung in LSMO/PZT Nano-Schichtstrukturen

Vom Fachbereich Material- und Geowissenschaften
der Technischen Universität Darmstadt

zur Erlangung des Grades
eines Doktors der Naturwissenschaften
(Dr. rer. nat.)

genehmigte Dissertation
von
Dipl. Phys. Philipp Moritz Leufke
aus Titisee-Neustadt

1. Gutachter:	Prof. Dr.-Ing. Horst Hahn
2. Gutachter:	Apl. Prof. Dr. Andreas Klein
Tag der Einreichung:	06.12.2013
Tag der Prüfung:	29.01.2014

Februar 2014 Darmstadt – D17

Erklärung zur Dissertation

Hiermit versichere ich, die vorliegende Dissertation ohne Hilfe Dritter nur mit den angegebenen Quellen und Hilfsmitteln angefertigt zu haben. Alle Stellen, die aus Quellen entnommen wurden, sind als solche kenntlich gemacht. Diese Arbeit hat in gleicher oder ähnlicher Form noch keiner Prüfungsbehörde vorgelegen.

Darmstadt, den 02.12.2013

(Philipp M. Leufke)

Abstract / Zusammenfassung

Abstract

Multiferroic thin film composites with electric field-effect driven magnetoelectric (ME) coupling offer the possibility to reversibly tune magnetic properties in materials intended for device applications. The structural and functional versatility of such artificial heterostructures makes them attractive not only for various data processing, storage and sensor applications but also for studying the fundamental ME coupling mechanisms.

$La_{1-x}Sr_xMnO_3$ (LSMO)/$PbZr_yTi_{1-y}O_3$ (PZT) is an ideal choice for such a composite, combining the unrivaled ferroelectric (FE) properties of PZT with the multiple electronic and magnetic phenomena exhibited by the mixed valency manganite LSMO. The main physical feature used in realization of the LSMO/PZT ME composites is a striking sensitivity of LSMO magnetism to the charge carrier density. Here, the low-doping region is of particular interest, where the competition between the fundamental magnetic coupling mechanisms, Double-Exchange (DE) *versus* Superexchange (SE), is most distinctive.

In the present work an unconventional sputtering technique – the Large-Distance Magnetron Sputtering (LDMS) method – has been established, which allowed for epitaxial deposition of these heterostructures with highest crystallinity and markedly smooth interfaces, necessary for effective field-effect control of magnetism. The large target-substrate distance effectively suppressed the destructive oxygen ion bombardment, inherently connected with oxide sputtering, and yielded an outstanding lateral uniformity of the film stack. The latter was vital for the fabrication of large capacitor structures of several square millimeter area that were required for detecting the ME coupling in a Superconductive Quantum Interference Device (SQUID) magnetometer.

The growth of LSMO on various single crystalline substrates was mastered by exploring a vast deposition parameter space, encompassing Radio Frequency (RF) and Direct Current (DC) sputtering. Commensurately grown on $SrTiO_3$ (STO) substrates, the $x = 13\,\%$-doped LSMO thin films were found to be stabilized in a metallic low-temperature phase, exhibiting an elevated Curie temperature (T_C), as compared to their bulk counterparts.

Regarding the PZT deposition, the LDMS technique naturally compensated for high volatility of the PbO vapor yielding a stoichiometric and phase pure film. Thus, with an optimal choice of deposition conditions, LSMO/PZT/Au thin film capacitors with excellent FE properties, i.e., high polarizability and long retention time, were obtained.

The high yield of 75 % of 1 mm^2 large capacitor structures was an excellent starting point for the ME tuning studies which were then carried out in a SQUID magnetometer in order to enable a quantitative analysis of the ME coupling. For this purpose, the measurement device needed to be modified, to allow for *in situ* application of electric fields. Furthermore, a SQUID measurement cell was designed to be used at low-temperatures and to keep the spurious magnetic signals as low as possible. All key *in situ* measurements were performed in FE remanence mode in order to

avoid artifacts of leakage current and to protect the samples from Time-Dependent Dielectric Breakdown (TDDB).

The ME tuning measurements revealed a direct correlation of the FE remanent hysteresis and the magnetic response of the LSMO layer, evidencing a purely field-effect driven coupling and a virtual absence of any magnetostrictive coupling to possible piezo-strain of the PZT layer.

In temperature-dependent measurements, a reversal of the sign of the ME effect was observed, with a positive extremum for the electron hole (h^+) accumulation mode around the Curie temperature of the magnetic transition. The effect gradually decreased with the lowered temperature to become negative eventually. On the basis of the phase diagram and the dependence of the Mn magnetic moment on the Sr doping level, the shape of the curve was phenomenologically modeled by a transformation of the original Field Cooling (FC) curve. The resultant transformation was a superposition of a FC curve shift along the temperature axis and a rescaling of the magnetic moment.

The dependence of the magnetic response to the modulation of the surface charge showed a mostly linear behavior with a coupling coefficient of $\alpha_{\mathrm{MQ}} \approx -3.6\,\mu_{\mathrm{B}}/h^+$ for low charge concentration. As this value stunningly matches the magnetic moment of a Mn atom per one formula unit, this result suggests an appearance of antiferromagnetic (AF) coupling upon surface charging. At higher charge modulation, the absolute value of the tuning coefficient decreased, indicating the onset of another magnetic exchange mechanism.

Eventually, the quantitative analysis of the ME coupling at the LSMO/PZT interface has allowed for developing a physical picture based on the electronic phase separation of competing AF and ferromagnetic (FM) phases immanent to LSMO.

Zusammenfassung

Multiferroische Dünnschicht-Kompositsysteme mit Feldeffekt-basierter magnetoelektrischer (ME) Kopplung ermöglichen das reversible Durchstimmen magnetischer Eigenschaften. Dies ist nicht nur aus technischer Sicht attraktiv für potentielle Anwendungen im Bereich der Sensorik, sowie der Datenverarbeitung und -speicherung. Vielmehr eröffnet die Vielfalt solcher künstlicher Heterostrukturen die Möglichkeit die unterschiedlichen grundlegenden ME Kopplungsmechanismen dieser Systeme zu analysieren und zu verstehen.

$La_{1-x}Sr_xMnO_3$ (LSMO)/$PbZr_yTi_{1-y}O_3$ (PZT) stellt eine ideale Materialkombination für ein solches Komposit dar, welches die herausragenden ferroelektrischen (FE) Eigenschaften von PZT mit den komplexen elektronischen und magnetischen Phänomenen des gemischtvalenten LSMO vereint. Hierbei beruht das physikalische Konzept der ME Wechselwirkung auf der Sensibilität der magnetischen Kopplung im LSMO bezüglich der vorherrschenden Ladunsträgerdichte. Diese ist besonders ausgeprägt im Bereich niedriger Sr-Dotierungsgrade, da hier die beiden konkurrierenden Kopplungsmechanismen – Doppelaustausch und Superaustausch – in besonderem Wettbewerb stehen.

Im Rahmen der vorliegenden Arbeit wurde eine unkonventionelle Dünnschicht-Abscheidungsmethode etabliert: Mithilfe der sogenannten Large-Distance Magnetron Sputtering (LDMS)-Technik – also der Magnetron-Kathodenzerstäubung mit großen Quelle-Substrat-Abständen – lässt sich das Bombardement des Substrates durch hochenergetische Sauerstoffionen, das ein zentrales Problem des Oxidsputterns darstellt, effektiv unterdrücken. Auf diese Weise wurden epitaktische LSMO/PZT Heterostrukturen mit herausragender Kristallinität abgeschieden, die besonders glatte Grenzflächen aufweisen, welche eine Grundvoraussetzung für die Anwendung des Feldeffektes

darstellen. Infolge des durch die Geometrie der Sputteranlage bedingten diffusen Teilchenflusses wurde eine sehr hohe laterale Homogenität der Schichten erreicht. Diese ist essenziell für die Herstellung großflächiger FE-Kondensatorstrukturen von einigen Quadratmillimetern, wie sie notwendig sind für die Detektion des ME-Effekts mittels eines SQUID-Magnetometers (Superconductive Quantum Interference Device).

Für das Aufwachsen von LSMO auf diversen Einkristallsubstraten wurde ein großer Depositionsparameterraum erkundet, welcher sowohl Gleichstrom- (Direct Current, DC), als auch Hochfrequenz-Sputtern (Radio Frequency, RF) umfasste. Kommensurat auf $SrTiO_3$ (STO)-Substraten abgeschieden, wies 13 %-dotiertes LSMO eine stabilisierte metallische Tieftemperaturphase sowie eine im Vergleich zum Volumenmaterial deutlich erhöhte Curie-Temperatur (T_C) auf.

Bei der Abscheidung von PZT wurde die hohe Flüchtigkeit von PbO durch die LDMS-Methode automatisch kompensiert, sodass stöchiometrische und phasenreine Schichten erzielt wurden. Damit ließen sich bei optimaler Wahl der Wachstumsbedingungen LSMO/PZT/Au Kondensatoren herstellen, die exzellente FE Eigenschaften, wie eine hohe Polarisierbarkeit und lange Aufrechterhaltung (Retention), aufweisen.

Eine Ausbeute von 75 % an voll funktionsfähigen, 1 mm^2 großen Kondensatorstrukturen bildete einen hervorragenden Ausgangspunkt für die Untersuchungen zur ME Kopplung, welche im SQUID-Magnetometer durchgeführt wurden, um eine quantitative Analyse des ME Effekts zu ermöglichen. Hierzu musste zunächst das Messgerät modifiziert werden, um das Anlegen eines elektrischen Feldes *in situ* zu ermöglichen. Des Weiteren wurde eine SQUID-Messzelle konstruiert, die tiefen Temperaturen standhält und gleichwohl parasitäre magnetische Signale so gut wie möglich vermeidet. Alle wesentlichen *in situ* Messungen wurden in ferroelectric (FE) Remanenz durchgeführt, wodurch sich Artefakte durch etwaige Leckströme verhindern und zugleich die Proben vor dielektrischem Durchschlag schützen lassen.

Die ME Druchstimmexperimente offenbarten eine direkte Korrelation zwischen der remanenten FE Hysterese auf der einen, und der magnetischen Systemantwort auf der anderen Seite. Dies lässt darauf schließen, dass die ME Kopplung vollständig Feldeffekt-gesteuert abläuft und somit eine grundsätzlich mögliche magnetostriktive Kopplung an den inversen Piezoeffekt ausgeschlossen werden kann.

In temperaturabhängigen Messungen wurde ein Vorzeichenwechsel des ME Effekts beobachtet, mit einem positiven Extremum im Bereich der Curie Temperatur, für den Zustand der Akkumulation an Defektelektronen (h^+). Mit sinkender Temperatur war eine Abnahme des Effekts zu verzeichnen, die bei tiefen Temperaturen schließlich zu einer negativen magnetischen Antwort führte.

Auf Grundlage des Phasendiagramms und der Abhängigkeit des magnetischen Moments der Manganatome vom Sr-Dotierungsgrad, wurde der Verlauf der Temperaturkurve des Effekts phänomenologisch anhand der ursprünglichen Field Cooling (FC)-Kurve modelliert. Der resultierende Verlauf spiegelt dabei eine Verschiebung der FC-Kurve entlang der Temperaturachse bei gleichzeitiger Reskalierung des magnetischen Moments wider.

Die Abhängigkeit der magnetischen Modulation von der Variation der Oberflächenladungsdichte zeigte ein nahezu lineares Verhalten für niedrige Ladungskonzentrationen und ergab einen Kopplungskoeffizienten von $\alpha_{MQ} \approx -3.6\,\mu_B/h^+$. Da dieser Wert auffällig mit dem magnetischen Moment eines Manganatoms pro Formeleinheit übereinstimmt, legt dies das Hervorrufen antiferromagnetischer (AF) Kopplung als Resultat der h^+-Akkumulation nahe. Bei stärkerer

Ladungsmodulation war eine leichte Abnahme des Kopplungskoeffizienten zu verzeichnen, die auf das Einsetzen weiterer Kopplungsmechanismen schließen lässt.

Schlussendlich wurde anhand der quantitativen Analyse der ME Kopplung an der LSMO/PZT Grenzschicht eine physikalische Anschauung entworfen, die die Kopplungsphänomene auf die räumliche Separation konkurrierender antiferromagnetischer und ferromagnetischer elektronischer Phasen zurückführt, welche für LSMO immanent ist.

Acknowledgments

I would like to thank Horst Hahn for giving me the opportunity to study in his group, granting me freedom to choose a scientific topic of interest and providing an excellent lab infrastructure and for all the confidence in me and my work.

Robert Kruk gave me a lot of support in many aspects. I appreciate his commitment to solving scientific challenges: I will never forget our active discussions at the time we entered the field of ferroelectrics.

With Richard Brand I had another senior scientist at my side who always gave me valuable and scientifically sound input and who was always helpful with respect to native language proof-reading of publications and the present dissertation.

I am particularly grateful to Ajay Kumar Mishra for being a dedicated companion. He always kept the Magnetic Properties Measurement System in a functional state, helped modifying the system to allow for *in situ* electric field cycling and performed many Field Cooling measurements – to name only a few of his contributions.

It is virtually impossible to name all the small but essential contributions to my work which I owe to our technician Martin Limbach. He managed to speed-up the repair of broken components and was eager and helpful designing new mechanical parts like sample holders or sputtering masks. His assistance in setting up the Ultra-High Vacuum lab from scratch was truly invaluable.

Having access to a working X-ray diffractometer was vital for my thesis. Therefore, I am much obliged to Anna Castrup and Ralf Witte for doing a good job at maintaining this machine.

I want to thank the entire Hahn research-group and especially the group on tunable materials for a commendable working atmosphere where everybody takes care of their co-workers. Furthermore, I am happy to have found two promising successors, namely Christian Reitz and Alan Molinari, who will keep the multiferroics project alive and who I wish good success.

The Rutherford Backscattering Spectroscopy measurements performed by André Beck (Institut für Festkörperphysik, IFP) were of great importance for optimization of the deposition processes. Likewise, the Transmission Electron Microscopy studies, which involved services from Di Wang, Christian Kübel, Torsten Scherer, Emma Tröster and Robby Prang (Karlsruhe NanoMicro Facility, KNMF), were essential for a detailed picture of the microstructure of the present heterostructures.

I also want to acknowledge the help from various colleagues from the Institute of Nanotechnology (INT). Frank Schramm and Holger Hain often helped me out in questions related to chemistry. Moreover, Holger was very valuable in setting up and maintaining the institute-wide resource booking and knowledge management web applications. Cornelius Thiele was patiently doing the wire-bonding jobs for me. Our secretaries Erika Schütze and Birgit Limmer were always very responsive taking care of our needs.

On the financial side, the support by Deutsche Forschungsgemeinschaft (DFG), Contract No. HA1344/28-1, as well as the State of Hessen (for an equipment grant) is gratefully acknowledged.

I also want to use this opportunity to express my thanks to the often unmentioned honorary developers of open-source software projects, such as Foswiki, Debian, Linux, LaTeX, Gnuplot or ImageJ, which facilitated my work substantially. Special thanks go to David Nečas from the

Gwyddion team, who did not hesitate to implement support for our scanning and transmission electron microscopy data files.

Last but for sure not least, I want to thank my whole family for their support, especially my parents, Clemens and Maria Leufke, who enabled me to study physics. Moreover, I want to thank my wife Christine for all her love and consideration during my writing of this dissertation, while taking care of our lovely daughter Amelie.

Index

Contents

List of Figures

List of Tables

Definition of acronyms and symbols

Quite a substantial amount of acronyms is being used in this work. Partly for the sake of shortening, but in many cases also due to the fact that some acronyms are simply more common than the corresponding spelled-out forms. The lists below give an overview of the acronyms and symbols. Furthermore, to facilitate comprehensiveness of the single chapters and their summarizing sections, all acronyms will be re-introduced there as well.

Acronyms

AC Alternating Current

AFM Atomic Force Microscopy

AF antiferromagnetic

ALD Atomic Layer Deposition

BE Bottom Electrode

BFO $BiFeO_3$

BTO $BaTiO_3$

CMR Colossal Magnetoresistance

CV Cyclic Voltammogram

DC Direct Current

DE Double-Exchange

DOS Density of States

EB Exchange Bias

EDX Energy-Dispersive X-ray Spectroscopy

EOT Equivalent Oxide Thickness

EELS Electron Energy Loss Spectroscopy

FC Field Cooling

FET Field-Effect Transistor

FE ferroelectric

FIB Focused Ion Beam

FM ferromagnetic

FWHM Full Width at Half Maximum

GIXRD Grazing-Incidence X-ray Diffraction

GMR Giant Magnetoresistance

HRXRD High-Resolution X-ray Diffraction

ITO In_2O_3:Sn

JT Jahn-Teller

LAO $LaAlO_3$

LBMO $La_{1-x}Ba_xMnO_3$

LCMO $La_{1-x}Ca_xMnO_3$

LDMS Large-Distance Magnetron Sputtering

LNO $LaNiO_3$

LSAT $(La_{0.3}Sr_{0.7})(Al_{0.65}Ta_{0.35})O_3$

LSCO $La_{1-x}Sr_xCoO_3$

LSMO $La_{1-x}Sr_xMnO_3$

LSSO $La_{1-x}Sr_xSnO_3$

MBE Molecular Beam Epitaxy

ME magnetoelectric

MF multiferroic

MFP Mean Free Path

MFT Mean Field Theory

ML Multilayer

MOKE Magneto-Optical Kerr Effect

MPMS Magnetic Properties Measurement System

MPB Morphotropic Phase Boundary

MR Magnetoresistance

PEEK Polyether Ether Ketone

PIPS Precision Ion Polishing System

PLD Pulsed Laser Deposition

PM paramagnetic

PMMA Poly(Methyl MethAcrylate)

PMN-PT $Pb[(Mg,Nb)Ti]O_3$

PPMS Physical Properties Measurement System

PUND Positive-Up Negative-Down

PVD Physical Vapor Deposition

PTO $PbTiO_3$

PZO $PbZrO_3$

PZT $PbZr_yTi_{1-y}O_3$

QCM Quartz Crystal Microbalance

QMS Quadrupole Mass Spectrometry

RAM Random-Access Memory

RBS Rutherford Backscattering Spectroscopy

RC Rocking Curve

RF Radio Frequency

RKKY Ruderman-Kittel-Kasuya-Yosida

RSM Reciprocal Space Map

RSO Reciprocating Sample Option

r.s.u. reciprocal space units

RT Room Temperature

RTA Rapid Thermal Annealing

SAED Selected-Area Electron Diffraction

SE Superexchange

SEM Scanning Electron Microscopy

SMU Source Meter Unit

s/n signal-to-noise

SQUID Superconductive Quantum Interference Device

SRO $SrRuO_3$

SSTO $SrTi_{1-x}Sb_xO_3$

STEM Scanning Transmission Electron Microscopy

STM Scanning Tunneling Microscopy

STO:Nb $SrTiO_3$:Nb

STO $SrTiO_3$

TDDB Time-Dependent Dielectric Breakdown

TEM Transmission Electron Microscopy

TE Top Electrode

TMP Turbo Molecular Pump

TMR Tunnel Magnetoresistance

u.c.^{2} unit cell area

u.c. unit cell

UHV Ultra-High Vacuum

VSM Vibrating Sample Magnetometer

XAS X-ray Absorption Spectroscopy

XPS X-ray Photoelectron Spectroscopy

XRD X-ray Diffraction

XRR X-ray Reflectometry

YBCO $YBa_2Cu_3O_{7-x}$

ZFC Zero-Field Cooling

Symbols

A area

a, b, c crystal lattice constants

a_{pc} pseudocubic lattice constant

α_{ME} ME coupling coefficient

α_{MQ} charge-dependent magnetic tuning coefficient

β, γ critical exponents

C capacitance

d film thickness

$d_{h,\,k,\,l}$ lattice plane spacing

d_{LSMO} LSMO thickness

d_{sep} target-substrate separation

d_{PZT}	PZT thickness
E	electric field
E_b	binding energy
E_c	coercive electric field
ε_0	vacuum permittivity
ε	strain
Γ	tolerance factor
$h,\ k,\ l$	Miller indices
h^+	electron hole
H	magnetic field
H_c	coercive magnetic field
κ	relative permittivity
m	magnetic dipole moment
$m_\square$	magnetic moment per u.c.[2]
m_{tot}	total magnetic moment
M	magnetization
M_r	remanent magnetization
μ_0	vacuum permeability
μ_B	Bohr magneton
n_0	charge carrier density
p_{O2}	O_2 partial pressure
p_{work}	working pressure
P	FE polarization
P_r	remanent FE polarization
φ	azimuth angle
Q	charge
R	resistance
ρ	resistivity
R_q	root mean squared roughness

S	spin angular momentum
σ	stress
σ_{m}	mass magnetic moment
σ_{XRR}	XRR-determined roughness
t	time
T	temperature
T_{C}	Curie temperature
T_{i}	FC inflection point temperature
T_{MI}	metal-insulator transition temperature
T_{x}	crossover temperature of magnetic modulation
θ	Bragg angle
τ	time constant
U	electric potential (voltage)
U_{pol}	poling voltage
V	volume
ω	angle of incidence
x	doping level
y	doping level (alternative symbol)
χ^2	coefficient of determination
Z	atomic number

1 Introduction

1.1 Motivation

About eight decades after its invention [1, 2], there is still no end in sight for the success story of the Field-Effect Transistor (FET). The wide range of current and future applications – such as data processing and storage, signal amplification and power electronics – illustrates the immense potential of the physical concept of an electric-field driven modulation of the charge carrier density of a functional material.

In the field of material science the electric-field effect complements the portfolio of available methods for the manipulation of material properties. The desired characteristics of a material are determined by various factors – including stoichiometry (e.g., doping levels), structure and microstructure (e.g., grain size distribution, grain boundaries, dislocations) – which can be tailored by the choice of suitable fabrication and post-treatment parameters. In contrast to the tailored, irreversible, modifications, the intrinsic reversibility of electric-field tuning opens up new pathways for both fundamental research and potential applications.

The direct comparison between chemical doping and the non-intrusive modulation of the charge carrier density by an applied electric field may provide valuable insight into the role of charge distribution and elemental charge states on micro- and macroscopic physical properties. In view of applications, among the most promising approaches and considered as a serious contender in the quest for a non-volatile replacement for conventional Random-Access Memory (RAM), is the electric-field induced modulation of magnetism.

The combination of mutually interacting ferromagnetic (FM) and ferroelectric (FE) materials is often considered a *holy grail* for new data storage applications [3], as these so-called magnetoelectric (ME) multiferroics are expected to lead to new reading and writing mechanisms, even allowing for simultaneous data encoding in both FM and FE switching states. As intrinsic ME materials are extremely scarce, composite materials represent a natural alternative with an enormous number of possible combinations of FM and FE materials.

Such systems are naturally of great interest for fundamental research, as the principles of interaction between magnetism and ferroelectricity are diverse and intricate. Considering only strain-mediated or electric-field driven coupling one can observe a broad spectrum of effects, especially if strongly correlated systems, like e.g., the class of manganites, are chosen as the magnetic material. The perovskite manganites exhibit remarkable sensitivity to changes in structure and charge carrier density (n_0), which renders these materials ideal candidates for the use in ME composite structures.

As a prototypical system $La_{1-x}Sr_xMnO_3$ (LSMO) has been selected, where the Sr doping level is used to control the electron hole (h^+) density and thus its magnetic and electronic properties. The ability to reversibly modulate the charge carrier density by means of the electric field effect, without introducing any extra chemical impurities, may help understand the complex mechanisms of the interplay between Double-Exchange (DE) and Superexchange (SE) interactions.

1.2 Scope and outline of this thesis

In this thesis the effect of electrostatic tuning of the charge carrier density in low-doped LSMO will be presented. Inspired by the promising results obtained from electrolyte-gated LSMO nanoparticles [4], the field-effect tuning concept was applied to a geometrically well-defined system, which allows for a quantitative analysis and a deeper insight into underlying phenomena. The final objective was to study the ME coupling mechanisms of LSMO/FE thin film heterostructures in a series of *in situ* charging experiments in a Superconductive Quantum Interference Device (SQUID)-based Magnetic Properties Measurement System (MPMS).

For the growth of the oxide thin films, a brand-new, unconventional custom-made Large-Distance Magnetron Sputtering (LDMS) system was thoroughly tested, which proved to be exceptionally well-suited for the deposition of highly uniform oxide thin films.

The first milestone was to grow low-doped epitaxial LSMO thin films, of a few nanometers in thickness, that exhibit pronounced magnetic properties with a sharp para- to ferromagnetic transition and high Curie temperature (T_C).

Then $PbZr_yTi_{1-y}O_3$ (PZT) was chosen as FE component to be optimized in the second step, in order to reach a high polarizability with significant remanence, good retention and most notably sufficiently low leakage, especially when large-area capacitor structures were required for further experiments.

The final step before the actual measurements consisted of the construction of a SQUID-compatible contacting and wiring setup which would withstand low temperatures and repeated temperature cycling while keeping spurious magnetic signals at a minimum.

For the *in situ* tuning experiments in the MPMS, a measurement strategy needed to be developed and put into action, in order to get reproducible and quantitatively significant data of the ME coupling in LSMO/PZT heterostructures.

The present dissertation is organized in logical sections as follows:

Chapter 1 gives an introduction into the field of tunable materials and different gating strategies. First, the past and present research encompassing field-effect devices is elaborated. Then the focus is moved on the field of intrinsic and composite multiferroic (MF) materials and the subset of ME systems. At last, an introduction to the strongly correlated manganites in general and to $La_{1-x}Sr_xMnO_3$ (LSMO) in particular is presented.

Chapter 2 summarizes the findings gathered from preliminary electrolyte-based tuning experiments on LSMO nanoparticles. These qualitative results form the starting point for the thin film experiments presented in the following chapters.

Chapter 3 explains the key features of the employed materials, the Large-Distance Magnetron Sputtering (LDMS) system and the various analysis methods used for production and characterization of the LSMO/PZT thin film heterostructures. Furthermore, it contains background information about selected materials and methods that is considered as reaching beyond textbook standards.

Chapter 4 starts with a literature review on LSMO thin film deposition and is followed by the comprehensive investigation of the substrate dependence and the influence of deposition parameters on Direct Current (DC)- and Radio Frequency (RF)-sputtered LSMO thin films.

Special attention is paid to the implications of the unusual sputtering geometry of the LDMS system.

Chapter 5 describes the role of LSMO as an electrode for PZT-based FE devices and informs about common deposition methods of PZT thin films, before reporting on the growth, structural and FE characterization and optimization of PZT on LSMO Bottom Electrodes (BEs). Moreover, the influence of the chosen deposition method on the conservation of the PZT stoichiometry is discussed.

Chapter 6 gives an overview of recent studies in the field of FE gating of perovskite manganites. Then the final implementation and assembly of the ME devices is elucidated, followed by the presentation and comprehensive discussion of the ME measurement results.

Chapter 7 contains some concluding remarks and an outlook regarding possible future work on ME heterostructures and FE gating and on prospects of the LDMS technique in general.

1.3 Tunable materials

The success of the FET illustrates the potential that is inherent in the family of the so-called tunable materials. The fundamental concept of tunable materials is based on the *reversible* modulation of a physical property by an external field. In the case of the FET, an external voltage – the gate potential – is used to modulate the conductivity of the channel material by tuning its charge carrier density. However, while the electric field effect may be the most prominent mechanism to control material properties, many other effects have been implemented in a broad range of applications.

Tunable materials seem to be predestined for use in sensor devices: The positive or negative temperature coefficient materials used in resistive temperature sensors (thermistors) [5] may be classified as comparatively simple tunable materials; other sensor applications are based on more sophisticated mechanisms. In the field of gas sensing, resistive or capacitive sensors have been established, based on functional materials that exhibit a pronounced change in conductivity or dielectric constant when exposed to varying humidity/moisture or specific gases like e.g., oxygen [6]. FET-based hydrogen sensors rely on the shift in threshold voltage that is tuned by the hydrogen concentration [5]. Magnetic sensors based on magnetoresistance, magnetostriction or the magneto-optical Faraday and Kerr effects employ tunable materials which feature distinct response to external field modulations [5].

Also in optical applications tunable materials play a significant role. Acousto- and electro-optic modulators are of great importance for high-end laser applications as well as signal modulation in telecommunications. On the low-cost side, phototropic glass – used e.g., for sunglasses and glass façades – the light absorption is modulated as a function of the irradiated intensity of ultraviolet light [7, 8]. While this process is subject to some unwanted latency, hysteretic effects with bistable states are essential for optical data storage applications based on phase change materials [9]. The information stored on optical data disks is encoded in digital bits whose two switching states differ in reflectivity. In the case of re-writable media, this is commonly achieved by the reversible light-induced phase change of the reflective alloy layer. A related, but nowadays exotic, hybrid solution is based on the Magneto-Optical Kerr Effect (MOKE), where the intensity modulation of the reflected read-out laser is caused by the interplay of Kerr rotation

and a polarizer [10]. In this case the stored information is encoded in the magnetic domains of the reflective layer, which can be reversibly altered with an external magnetic field.

From the above examples it becomes apparent that the family of tunable materials is large but actually not quite well-defined. The two different concepts of re-writable optical data storage may help identify where the line may be drawn: While the purely optical solution actually modulates a physical property, changing the phase between polycrystalline and amorphous, the magneto-optical method only alters the magnetization state.

In order to clarify the term, the tunable materials should also be differentiated from tailored materials. While the optimization for best tunability usually requires careful tailoring of its properties – e.g., by adjusting doping level, purity, crystallinity, strain state and dimensions, or via combination with other materials –, the tailoring process itself is *irreversible*. Tab. 1.1 summarizes the comparison between *tuning* and *tailoring* on the example of the h^+ density in LSMO.

Table 1.1.: Disambiguation of the term of *tuning* in comparison with *tailoring* on the example of the h^+ density in LSMO.

tailoring	tuning
h^+ density adjustment: (chemical) Sr doping	h^+ density modulation: field effect
volume effect (homogeneous bulk)	surface effect (limited by screening depth)
permanent result	ideally fully reversible

1.4 Field-effect devices

The technical application of the electric field effect is still dominated by semiconductor devices. This is mostly due to the fact that the electric field penetration depth, i.e., the screening length, is strongly dependent on the charge carrier density (n_0) of the tunable material. The comparatively low carrier density of semiconductors allows for the carriers in a relatively large FET channel volume to become either fully depleted or accumulated – even when only SiO_2 with its relative permittivity of $\kappa = 3.9$ is used as a gate dielectric – thus resulting in enormous changes in the conductivity.

But even materials with significantly higher charge carrier densities can be attractive for electrostatic tuning – despite their smaller screening length – as long as they feature distinct electronic phases within the field-effect accessible n_0 range. Fig. 1.1 depicts the electronic phases as a function of the interface carrier density for selected classes of materials which are in the focus of current field effect studies. Unlike the semiconductors (shown at the bottom), these materials exhibit phases that depend on the carrier density (as indicated by different colors). Thus, with a sensibly tailored staring point, phase transitions may be induced by tuning the screening charge. This is both interesting for potential applications exploiting the switching between individual physical properties of phases, as well as for fundamental research aiming to study the nature of the electronic phases and their transitions. In order to achieve the surface charge density modulations that are high enough to influence phase transitions in correlated

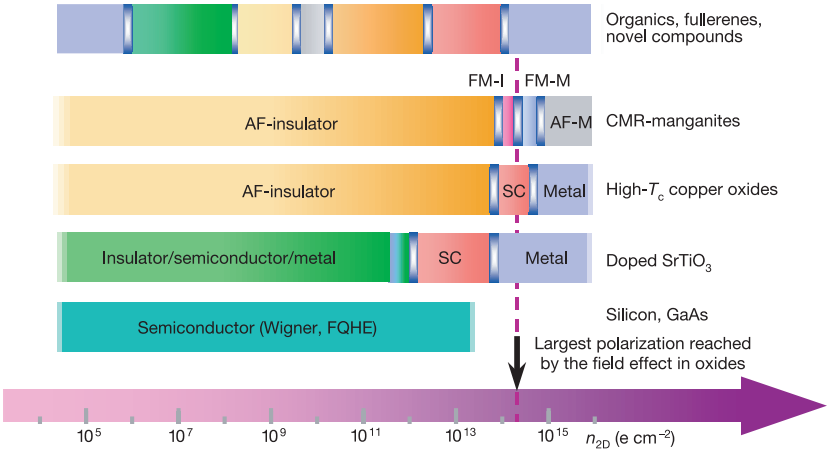

Figure 1.1.: Sheet charge carrier density n_{2D} dependence of the zero-temperature behavior of various correlated materials, with silicon shown as a reference. The examples for the high-T_C cuprates and the CMR manganites reflect YBCO and LSMO, respectively. The top bar summarizes the variety of other materials available for field-effect tuning, with the color code representing the spectrum of their electronic phases. I, SC, M, FQHE and Wigner stand for insulating, superconductive, metallic and fractional quantum Hall effect and Wigner crystal, respectively. (*Reprinted with permission from* [11]. ©2003, MACMILLAN PUBLISHERS LTD)

materials like the high-T_C superconductors or the Colossal Magnetoresistance (CMR) manganites, a very large induced polarization in the order of $\approx 10^{14}$ e/cm^2 (or $\approx 10\,\mu$C/cm^2) is required [11] (marked by the black arrow). Furthermore, the high carrier density limits the screening length to a single, or at best, a few unit cells, rendering the field effect in such materials a surface effect.

The required high surface-to-volume ratio is typically achieved by depositing ultra-thin films of a few unit cells in thickness onto a substrate or by producing nanoporous materials or nanopowders. While thin films provide well-defined geometries with highest homogeneity and possibly even single-crystalline epitaxial growth, allowing for quantitative analysis and modeling, nanoparticulate systems are not subject to any substrate-induced strain and usually feature a much higher total surface area, resulting in increased relative and absolute tuning effects. However, in both cases the low amount of bulk volume, in comparison to the interfacial volume, has significant influence on the intrinsic material properties, which can differ significantly from the bulk behavior. This situation often requires extra tailoring and process optimization steps, in order to yield the desired starting properties.

1.4.1 Electrolyte gating

Before considering the classic thin-film based solid-state devices, the more exotic electrolyte-based ones shall be discussed first, especially since they seem to be underrated and sometimes ignored, even in closely related literature [12]. Recently, Dasgupta *et al.* have demonstrated for

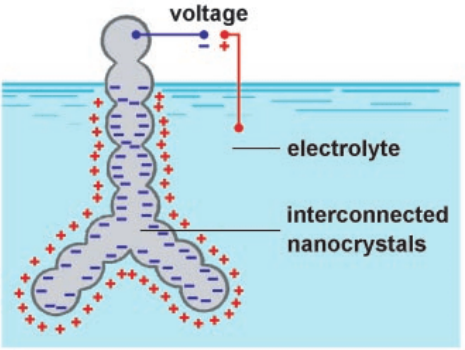

Figure 1.2: Schematic representation of electrolyte gating of an array of interconnected conductive nanoparticles. (*Reprinted with permission from* [15]. ©2005, AAAS)

a printable In_2O_3:Sn (ITO)-based long-channel transistor, that the switching speed is not limited by the ionic conductivity of the electrolyte, thus ruling out one of the major criticisms against usability of this technique in printed electronics [13].

In an electrolyte-gated device, a capacitive double layer, the so-called Helmholtz double layer, is formed by the electrolyte at the interface of the tunable material, and acts as a working electrode. The applicable voltage range is limited by the so-called capacitive window, where no redox reactions at the electrodes are taking place[1]. This prerequisite is also the major constraint for the application of electrolyte gating: the range of tunable materials is limited by the electrochemical reactivity and depends on the availability of compatible electrolytes which at the same time have to exhibit sufficient ionic conductivity in the temperature range of interest. As a consequence, the first nanoporous materials to be tuned by this technique were noble metals.

As nanoporous materials can – for geometrical reasons – hardly be gated by means of dielectric materials, the electrolyte gating has been suggested by Gleiter *et al.* as a well-suited alternative which procures enough surface charge to even tune the highly conductive noble metals [14]. The concept is illustrated in Fig. 1.2. A short time later, this was demonstrated for nanoporous Pt [15] and Au [16] which exhibited a pronounced reversible strain modulation upon charge cycling, large enough to be comparable with the one of piezoelectric actuators. This was particularly interesting, since other gating methods which enable for high carrier densities would always induce misfit strain from the substrate and/or the gate dielectric interface, tampering or even concealing the electrostatic tuning effect on the strain.

In addition, the conductivity of noble metals and alloys, namely Pt, Au and AuFe, were found to be tunable this way; this time not merely in a nanoporous morphology [17–19], but also for the first time for a sputtered thin film [20].

Concerning the magnetic properties of nanoporous metals, the magnetization was found to be tunable by electrolyte gating in Ni-Pd alloys [21] and in Au-Fe alloys by Mishra *et al.* [22], where the modulation was correlated with the charge-induced strain. The coupling was also suggested earlier by Ghosh *et al.* who reported on the magnetization modulation in nanoporous Co-Pd. Other reports on metals encompass the electrolyte tuning of the paramagnetic (PM) susceptibility

[1] Extending the scanned voltage interval to regions where reactions and intercalation into the electrodes are taking place may, however, provide powerful possibilities for reversible tuning of various properties, beyond the field effect.

of nanoporous Pd [23] and the modification of the magnetocrystalline anisotropy in FePt and FePd thin films by Weisheit *et al.* [24].

Recently, Shimamura *et al.* reported on pure Co ultra-thin films that were electrolyte gated by means of a polymer film containing an ionic liquid [25], yielding an impressive shift in T_C of $\approx$100 K and large changes in magnetization, which were explained by the shift in T_C. Technically, the chemical integrity of the only 0.4 nm thin Co layer was ensured by protecting it with a 2 nm thin MgO capping layer. Similar experiments carried out with *dielectric* gating were reported by the related groups of Chiba and Ohno *et al.*; the respective results will be discussed later on. The remarkable difference to those experiments is that the charging measurements were carried out *in situ* in a SQUID magnetometer. This was possible due to the large device area of $\approx$4 mm^2, which is much easier achievable in an electrolyte-gated device than it is in the case of dielectric gating.

Besides pure metals and alloys, various oxides were shown to be compatible with this gating method as well. Ueno *et al.* demonstrated that superconductivity can be induced at the surface of an insulating bulk $SrTiO_3$ (STO) substrate at low temperature (T) by means of the electric-double-layer capacitor [26]. Regarding more common superconductors, Dhoot *et al.* recently have been able to induce a significant increase of the critical temperature in a $YBa_2Cu_3O_{7-x}$ (YBCO) thin film by applying a negative potential [27]. One year later a similar effect was found for another cuprate superconductor: $La_{2-x}Sr_xCuO_4$ [28].

With respect to magnetic oxide semiconductors, Yamada *et al.* have successfully demonstrated that a field-induced PM to FM transition can be achieved in $(Ti,Co)O_2$ [29].

The first report on electrolyte tuning of magnetism in a nanoporous CMR manganite represents the preliminary work to the present thesis and will thus be presented separately in Chapter 2.

In summary, the electrolyte double layer is a serious alternative to classic dielectric gating, which has gained considerable interest in the field of fundamental research of field-effect tuning within the last decade.

1.4.2 Dielectric gating

The application of dielectric (thin film) gating in recent fundamental research studies has benefitted from the developments in the field of high-relative permittivity (κ) dielectrics, that were driven by the need for ever smaller structure sizes in chip industries. The DC capacitance $C = Q/U$ – i.e., the capability of accumulating a charge Q at an applied voltage U – of a plate capacitor with an area A and its plates separated by a dielectric of the relative permittivity κ and a film thickness d is defined by

$$C = \varepsilon_0 \kappa \cdot \frac{A}{d}. \tag{1.1}$$

Thus, the surface charge density induced by the electric field ($E = U/d$) is

$$\frac{Q}{A} = \varepsilon_0 \kappa \cdot \frac{U}{d} = \varepsilon_0 \kappa E \tag{1.2}$$

From this relationship it is obvious that a high value of κ improves the attainable charge density. On the other hand, decreasing film thickness (d) or increasing electric potential (voltage) (U) will help, but only as long as electric field (E) does not exceed the breakdown threshold. For this reason, κ is not the only relevant parameter, but also e.g., the band gap, the conduction

band offset and chemical compatibility with respect to the channel material. For silicon the interplay of these parameters is often characterized by a single parameter, the Equivalent Oxide Thickness (EOT) [30]. The choice of the best dielectric for a specific application is furthermore dependent on the gate electrode material, since the influence of work functions and electronegativities must be taken into account as well [31].

In terms of breakdown, i.e., a sudden voltage drop, one has to distinguish between immediate breakdown and the so-called Time-Dependent Dielectric Breakdown (TDDB). While the first appears instantaneously when applying a very strong electric field, the latter effect happens at lower fields, in the working range of the capacitor: When electrons get injected into the dielectric by Fowler-Nordheim tunneling into the conduction band of the dielectric [32], they can break bonds and create traps on their way through the layer. Simultaneously, electron holes (h^+) can be injected from the anode. Both processes generate defects at a certain rate, thus the whole breakdown mechanism is charge- or in other words time-dependent [33]. Generally, it can be said that breakdown voltages and breakdown times are lower for dielectrics of lower thickness and insufficient stoichiometry (i.e., higher intrinsic defect density). Larger device areas impair the breakdown characteristics in the same way [34, 35]. These phenomena have considerable impact on the applicability of dielectric gating, when large areas may be required.

All of the above constraints emphasize why there exists no all-round solution for a perfect gate dielectric. Instead, the portfolio of high-κ dielectrics is large; among the most popular are Al_2O_3, ZrO_2, TiO_2, HfO_2 and STO [36]. For FET applications, amorphous gate oxides are often preferred over polycrystalline ones, as the absence of grain boundaries decreases leakage and diffusion of dopants and because the isotropic dielectric constant of the amorphous gate oxide does not cause fluctuations in polarization from differently oriented oxide grains, which otherwise induce scattering of the carriers in the channel. However, most high-κ dielectrics are not good glass formers [30].

The most common approach for building dielectric-gated solid-state devices is the planar thin film geometry, due to the availability of low-roughness substrates and sophisticated coating and structuring methods. But recent developments in coating technology, such as the Atomic Layer Deposition (ALD) [37], allow for the deposition of extremely thin high-κ dielectrics on irregular 3D surfaces (e.g., FinFET structures [38]) and even porous materials with high step coverage and low defect density [30].

Like for the electrolyte-gated field-effect devices, the range of dielectric-gated systems that are in the focus of current research comprises high-T_C superconductors, magnetic semiconductors, metals, alloys and CMR manganites[2].

The dielectric gating of superconductors has – compared to other tunable materials – a rather long history. Using STO as high-κ gate material for YBCO-based FET devices was already suggested in 1992 by Walkenhorst *et al.* [39]. An early review on dielectric (and FE) gating of high-T_C superconductors can be found in [40].

Some of probably the most remarkable investigations in the field of dielectric-gated magnetic semiconductors were reported by Ohno and Chiba *et al.*. In these studies Mn-doped semiconductors, such as InAs [41, 42] or GaAs [43, 44], were gated with polyimide [41], SiO_2 [42], ZrO_2 [43] or HfO_2 [44], yielding tunable T_C or coercive magnetic field (H_c) or modulating domain wall motion [45] and employing the spin-torque effect [43] for switching the magnetization.

[2] Although the CMR manganites will be introduced later in Section 1.6, some important field-effect tuning results shall already be presented here.

Recently, Chiba *et al.* also made some considerable contribution to the dielectric field-effect tuning of FM metals. In a Pt/Co bilayer structure with perpendicular magnetic anisotropy, where the Co layer thickness was as low as 0.4 nm, a 12 K shift in T_C was achieved with a field modulation of ± 2 MV/cm [46]. The HfO_2 gate insulator with a dielectric constant of ≈20 was grown by ALD on top of an MgO capping layer[3]. Furthermore, a modulation of the domain wall velocity in the creep regime by more than one order of magnitude was observed [47], which was ascribed to the modulation of the energy barrier for domain wall motion. In these studies, the magnetization was indirectly monitored by Hall-resistance measurements, presumably since in this way the device area and thus the risk of leakage and breakdown could be kept small.

In a similar experiment by Schellekens *et al.* [48], perpendicular anisotropic Pt/Co and Pt/CoB heterostructures, with 0.8 nm thin Co and CoB layers, were gated by plasma-oxidized aluminium and tantalum[4]. The magnetic properties were investigated by means of polar MOKE microscopy. The results confirmed the tunability of the domain wall motion.

Another way to stabilize the easy axis perpendicular to the film plane – even for ultra thin films – can be found in the $L1_0$ phase in FePt alloys. Such a film of around 1.5 nm in thickness was investigated by Seki *et al.* [49]. An ALD-grown aluminum oxide layer on top of *in situ* MBE-deposited MgO was used as gate dielectric. The MgO layer was found to help maintain squareness of the MOKE-measured magnetic hysteresis loops. With the MgO capping layer present, a shift of ≈40 Oe in H_c was achieved upon an electric field modulation of around ± 5 MV/cm, which was ascribed to a modulation of the anisotropy energy of the $L1_0$-ordered FePt system.

Another experiment dealing with the field-effect tuning of the magnetic anisotropy, that is worth to be mentioned, is one of the first based on dielectric gating, which was reported by Maruyama *et al.* [50]: A 2 to 4 monolayers thin iron film, capped by an MgO layer was gated by polyimide as a dielectric. The magnetic measurements were conducted by MOKE magnetometry, where the Kerr ellipticity, as a measure for the magnetic anisotropy, was modulated by the electric field.

The need for employing an MgO capping layer emphasizes the difficulty in using oxide dielectrics for tuning metallic thin films, as the oxidation state of the metal layer may be altered at the interface, leading to adverse side-effects. If the tunable layer already is an oxide, this issue does not exist. One of the first studies on dielectric gating of a CMR manganite was performed by Ogale *et al.* [51], where STO was employed as high-κ gate dielectric for tuning $Nd_{0.7}Sr_{0.3}MnO_3$ in a top-gate geometry. It yielded some remarkable findings: The electric field (E) gating resulted in a decrease of the resistance above the metal-insulator transition temperature (T_{MI}), independent of the field direction. A proportionality of the modulation to E^2 was observed, with a reversal of the sign of the resistance modulation below T_{MI}. As a conclusion, the modulation of the spin and charge transport could be explained by polarization-induced lattice distortion. Thus, the tuning in this system is – similar to the mechanisms for electrolyte-gated noble metals – caused by (symmetric) strain that is induced by the modulation of the charge carrier density[5].

The *prototypical* [52] CMR oxide LSMO was also field-effect tuned with STO as gate dielectric. In a side-gate geometry a resistivity modulation of up to 250 % was achieved by Pallecchi *et al.* [53]. A dead layer at the LSMO bottom interface of about 6 u.c. (unit cells) thickness was

[3] It should, however, be mentioned that the actual oxidation state of the thin Co layer was not specified.

[4] Again, the oxidation state of the Co and CoB layers may be questionable, though.

[5] It is important to distinguish the internal strain formed by the charge carrier density from the external strain as imposed by coupling to piezoelectric materials. The latter will be addressed in Section 1.5.

reported, which was later on confirmed by Brivio *et al.* [54], who found that the magnetic T_C modulation of around 5 K in the LSMO/STO heterostructure was only achievable in a top-gate geometry, whereas the bottom gating showed no modulation. The dead layer issue of epitaxial LSMO will be discussed later on in more detail (see Section 3.2.1).

Using STO as a gate dielectric opens up unrivaled possibilities – as long as it is compatible with the channel and gate electrode materials – due to its extremely high relative permittivity κ. With values of around 300 at Room Temperature (RT) and increasing up to $\approx$ 2000 at 10 K [31, 53], it is sometimes denoted a *nearly FE material* [12]. The dielectric constant can, to a certain extent, be tailored by mixing STO with the very similar tetragonal FE $BaTiO_3$ (BTO). Of course, at some point this solid solution exhibits a FE hysteresis, which may be undesirable for many applications, where linearity, high switching speed and low energy consumption are targeted.

However, for memory applications the hysteresis can even be beneficial (e.g., FE-FETs for FE-RAM) and for fundamental research, the polarizability of FE materials of up to 50 μC/cm^2 and above allows for a charge density modulation that is unrivaled by electrolyte and dielectric gating. The equivalent DC permittivity for good FEs like BTO or PZT can be as high as $\kappa \approx 5000$ [55], even at RT. One should keep in mind, though, that this value strongly depends on the coercivity of the FE layer – which is not well defined, being a function of the voltage ramp time [56] – and that this permittivity is of course non-linear. A more meaningful measure for the strength of a FE is therefore the attainable (remanent) charge on the given device area, i.e., FE polarization (P) and remanent FE polarization (P_r), respectively.

As an early example for FE gating, the superconductive cuprate $GdBa_2Cu_3O_{7-x}$ was gated with PZT in a transistor geometry by Ahn *et al.* [57]. In slightly underdoped films, a shift in superconductive T_C was observed upon polarization modulation. In more underdoped films even a transition to an insulating state could be induced. The reported effects were found to be purely field-effect driven with no apparent crystalline modification of the material. This does not necessarily have to be the case, though. While the FE gating opens up uncharted areas of field effect tuning, the piezoelectric behavior that is inherently present in any FE material, can cause strain-mediated effects on the tuned material, which have to be distinguished from the field effect.

In FM/FE heterostructures this (possible) entanglement of ferroelectricity, ferromagnetism, piezoelectricity, field effect and magnetostriction can lead to a variety of multiferroic (MF) and magnetoelectric (ME) coupling phenomena, which will be discussed separately in the following section.

1.5 Multiferroics and magnetoelectrics

In recent years, there has been tremendous interest in MF and ME materials. The number of articles published on these topics has continuously increased by a factor of more than 13 within the last decade (see Fig. 1.3). The popularity of those materials is also reflected in the ample number of topical reviews on this subject in general [12, 58–73] or a branch of it [3, 74–78].

The revival of a class of materials, that had been given relatively little attention over about three decades, was based on outstanding findings from studies on Cr_2O_3 and $BiFeO_3$ (BFO), and was accompanied by some of the most-cited review articles in this field by Spaldin (née Hill) and

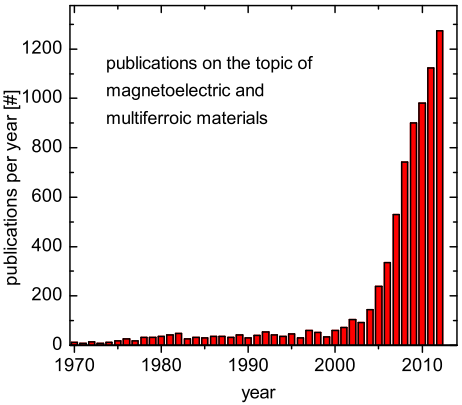

Figure 1.3: Chronological development of publications per year on the topic of MF and ME materials and phenomena. Based on statistical data according to THOMSON REUTERS *Web of Knowledge*, as returned for the search criterion `Topic=(multiferroic OR magnetoelectric)`.

Fiebig [58–60] and Eerenstein *et al.* [61]. But before delving into the history[6] and the various effects and mechanisms reported in the literature, first a brief introduction to the subject shall be given.

Multiferroic (MF) materials combine at least two *ferroic* order parameters – like e.g., P, M, or ε, in the case of ferromagnetism, ferroelectricity, or ferroelasticity, respectively – that are spontaneously nonzero below their respective critical temperatures (T_C). Fig. 1.4 depicts the control of those ferroic properties by their driving forces as well as possible interactions among them. While for a material to be classified as MF only the coexistence of two or more ferroic forms is necessary, a uni- or bi-directional coupling of M and P as a function of their mutual driving forces is mandatory (green arrows in Fig. 1.4), to be classified as a magnetoelectric (ME) material, in analogy to the piezoelectric materials, where the coupling acts between ε and P. As some examples presented below will demonstrate, the ME coupling can, of course, also include the ε component as a mediator between M and P.

[6] Considering the large number of publications on ME phenomena, it is virtually impossible to even cover a single branch of the field comprehensively. For this reason, the following survey will focus on materials and effects which played a key role in the evolution of MEs or which compare to the above presented studies based on electrolyte or dielectric gating. A comprehensive historical overview can be found in e.g., [67].

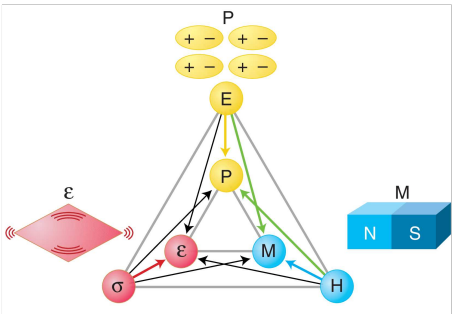

Figure 1.4: Phase control and coupling in (multi-)ferroics. Polarization (P), magnetization (M), and strain (ε) are (externally) controlled by electric field (E), magnetic field (H), and stress (σ), respectively. (*Reprinted with permission from* [59]. ©2005, AAAS)

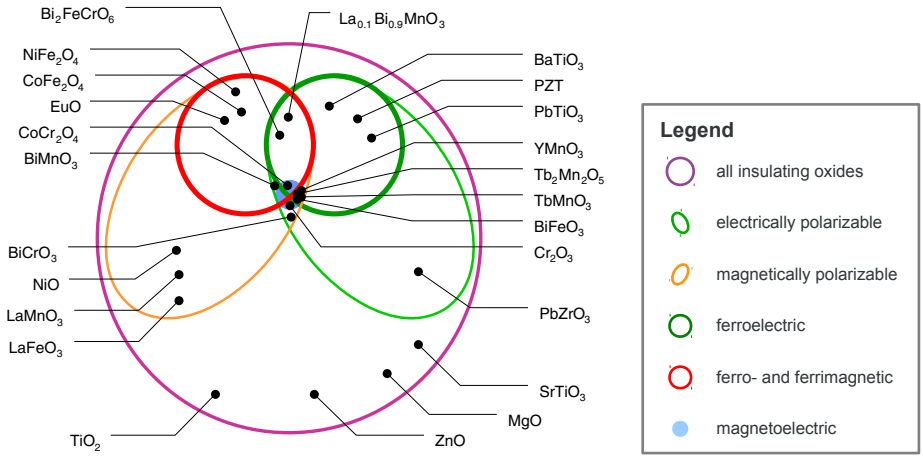

Figure 1.5.: Classification of the family of insulating oxides with its partially overlapping subsets of electrically or magnetically polarizable, where the FE and FM materials are proper subsets thereof, respectively. The intersecting set of FE and FM is commonly regarded MF. The small set of ME materials partially overlaps the MF materials, but also covers materials which are not ferroic in any parameter. (*Reprinted with permission from* [65]. ©2008, IOP PUBLISHING)

Considering the disambiguation of MF and ME materials, it should be noted that neither of them is a proper subset of the other one[7]. While there exist MF materials which do not show any coupling between their ferroic properties, like e.g., $La_{0.1}Bi_{0.9}MnO_3$ or composite materials with decoupled interfaces, there also exist magnetoelectrically coupled materials, that are not *ferroic* in *both* polarizabilities. For the latter, Cr_2O_3 is a prototypical example, which possesses spontaneous antiferromagnetic (AF) polarization, but only features dielectric polarizability [79]. This circumstance can be understood by means of Fig. 1.5, which illustrates a schematic classification of insulating oxides and the subsets of polarizable, ferroic and ME materials.

The strict definition of MF materials is often softened by including AF materials into the set of the FM materials, due to their spontaneous magnetic ordering [3]. For this reason FE AF materials like BFO, $YMnO_3$ and $TbMnO_3$ are commonly included to the small group of MF MEs. As mentioned, the AF Cr_2O_3 is not classified as MF material because ferroelectricity is absent. However, accidental allocation sometimes happens [80, 81]. Furthermore, strictly speaking, the ME effect denotes the modification of the electrical polarization by an external magnetic field. Consequently, the influence of an external electric field on the magnetization constitutes the *converse* ME effect [72]. Nevertheless, it seems a common practice to omit this discrimination for linguistical simplicity [82].

The strong interest in ME materials and especially MF MEs originates from the diverse fundamental mechanisms on the one hand and from the promising prospect of future applications in spintronics in general and data storage in particular. So far, the writing process of magnetic bits is typically based on comparatively high currents which generate the necessary magnetic

[7] A valuable glossary of the established terminology in this field can be found in [61].

field. This method, however, comes with the disadvantages of energetic inefficiency and Ohmic heating, which both render this technology inapplicable for nano-sized electronics for mobile applications. Another approach can be found in spin-torque driven switching, but as this is still a current-based process, the *holy grail* is often seen in MF MEs, which may allow for virtually current-less E-field writing.

1.5.1 Single-phase multiferroic magnetoelectrics

Single-phase MF MEs are extremely scarce. The reason for this is generally seen in the fundamental contradictoriness of ferromagnetism and ferroelectricity. The incompatibility was elaborated by Spaldin, Fiebig [58, 59] and Eerenstein [61] on the basis of inversion symmetry considerations: While the electric polarization – represented by a point charge that is asymmetrically located in a unit cell – is invariant with respect to time inversion, the dipole moment reverses with spatial inversion. In contrast, the magnetic moment – represented by the dynamic orbit of a charge – is flipped by a time reversal operation, while staying invariant with respect to spacial inversion. This reasoning was later on criticized by Catalan and Scott [78] for being too narrowly focusing on oxide perovskites, while not considering the family of the fluorides. Nevertheless, the oxides still play the major role in this research area.

The few genuine single-phase MF MEs, like e.g., $CoCr_2O_4$ and A-site doped $DyFeO_3$ have low or very low T_C and their net magnetic moment is a result of cycloid and conical spin canting [83, 84]. Other intrinsically AF materials, like $TbMnO_3$ and BFO were reported to develop magnetostatically induced lattice modulations, which lead to weak FM moments [70, 82]. Apart from some examples, however, the AF behavior is still predominant.

A very recent example for successful ME tuning in a single-component MF was reported by Tokunaga *et al.* [84]. A bulk single crystal of the orthoferrite $DyFeO_3$, A-site doped with Gd or Tb, was electrically cycled in a SQUID magnetometer, resulting in a reversal of M, which was found to depend on T and the sweeping speed of the E-field. On the downside, the reported effect was only observed at very low $T \leq 2.5\,\mathrm{K}$.

A lot of research on MEs has been focused on Cr_2O_3 and BFO, due to their uniqueness of exhibiting the ME coupling even at RT. But although being single-phase ME materials, the actual applicability of the coupling is only attained in composite structures.

1.5.2 Magnetoelectric and multiferroic composite systems

The idea of composite ME materials is not new. Already in 1976 van den Boomgard *et al.* demonstrated that ME coupling effects much larger than in single-phase Cr_2O_3 in a eutectic of cobalt ferrite and BTO [85] or in bulk sintered composites of these oxides [86] can be achieved. However, the advances in thin film deposition, structuring and analysis methods, together with the new perspectives for ME devices in data storage and spintronics, have led to a revival of the research on ME composites, but now in thin film geometry, where the most established layout consists of stacked planar layers of different components, sometimes denoted (nano-) laminates. However, depending on the coupling mechanisms, also vertically aligned ME thin film heterostructures have been found to be interesting.

A straightforward approach to exploit the coupling of antiferromagnetism to an external E-field – like present in Cr_2O_3 or BFO – is to employ the exchange coupling which arises when the AF

material gets in contact with a thin FM layer. An Exchange Bias (EB) is typically induced between an antiferromagnet and a ferromagnet, when the FM Curie temperature exceeds the AF Néel Temperature [77].

Considerable progress in this area has been achieved by Kleemann *et al.* with their EB heterostructures on ME Cr_2O_3 [79–81, 87–89]. This material is often considered the simplest system for exploring such EB coupling effects [77], as it is so far the best-understood ME material [79, 80]. Successfully demonstrated devices, where the coercivity – or more precisely the EB field – could be modulated by an applied E-field, consisted of a Cr_2O_3 substrate with electrodes at the bottom and the top surface, where the top electrode was formed by an EB-coupled Co/Pt Multilayer (ML). Different effects regarding the interplay of magnetic and electric freezing fields have been studied. For this purpose, a SQUID magnetometer had to be modified in order to allow for *in situ* measurements of the linear ME susceptibility of such devices [81]. It should be noted, that reversible tuning with considerable effects required Field Cooling (FC) procedures, which drastically limit the practical employability of the investigated effects. Regarding future applications, various spintronics devices, like e.g., Giant Magnetoresistance (GMR), Tunnel Magnetoresistance (TMR) and ME-RAM, have been proposed [79, 87, 89]. However, apart from the GMR layout, where the ME pinning layer can be implemented as a thick substrate, the other devices depend on Cr_2O_3 thin films, which tend to be very leaky, effectively reducing the applied E-field.

Regarding the leakage issue, Cr_2O_3 is in good company with other ME materials. BFO is nowadays certainly the most popular MF ME, as it is the only known single-phase MF with a magnetic T_C above RT [77], while simultaneously being an exceptional FE material with extremely high polarizability of up to $\approx 150\,\mu C/cm^2$ [90]. However, the outstanding FE properties are almost inevitably undermined by the substantial leakage observed in BFO thin films [77], which makes the BFO films being generally prone to various artifacts in FE and ME measurements [76][8].

EB composites have also been implemented with BFO as a magnetoelectrically tuned AF pinning layer. With 7.5 nm thin CoFeB as FM layer, a tunable EB coupling as a function of the FE/AF domain size has been realized [91]. Switching of the FM and FE domain patterns was demonstrated for microstructured BFO/$Co_{0.9}Fe_{0.1}$ bilayers [92]. The domain patterns were found to be in registry when applying an in-plane E-field, but this switching effect might not be too closely related to the MF nature of BFO, since a similar correspondence of FM and FE domains has also been reported for strain-coupled CoFe thin films on purely FE BTO substrates [93].

Apart from BFO, $YMnO_3$ was employed as well for the same purpose, even before many of the BFO-related studies were reported [94, 95]. Using permalloy ($Ni_{81}Fe_{19}$) thin films as FM layer, it was possible to ferroelectrically alter an EB field which was set by a FC procedure [95]. However, the fact that the EB effect for the preferential FE polarization orientation in $YMnO_3$ was minimal, led to the conclusion that an effective utilization of a ferroelectrically driven EB effect in such a heterostructure is unlikely to be successful [94].

As an alternative to composites that are based on a single-phase ME material, artificial heterostructures consisting of exclusively electrically or magnetically polarizable materials can be constructed, that interact via field effect or lattice strain. This way, by combining FE and FM materials into a composite structure where an effective coupling between ferroelectricity and

[8] Although the leakage is often not explicitly specified in many publications, conclusions can be drawn from the short sweeping time employed in FE hysteresis measurements. Cycling frequencies above ≈ 1 kHz may be a reasonable indication.

ferromagnetism is attained in at least one direction, those heterostructures can be regarded as MF ME materials.

For single-phase MEs, the ME coupling coefficient $\alpha_{\mathrm{ME}} = \mu_0 \cdot \Delta M / \Delta E$ has been established for benchmarking the performance of a material. While this coefficient sometimes is also employed for planar composite systems, its application is at least questionable when FEs are involved, since due to the nonlinear nature of the FE response to an external E-field, the FM response of such ME heterostructures is also rather abrupt. The sense in evaluating ME coupling coefficient (α_{ME}) can be seen in analogy to providing an equivalent DC permittivity of a FE. In both cases, such a coefficient may be helpful for comparison with conventional materials – i.e., single-phase MEs and dielectrics, respectively – but one should be aware that the calculated coefficients are not representative over the full range of the applied E-fields, but usually represent the magnetic response around the FE switching field. The pronounced dependence of the coercive electric field (E_{c}) on FE film thickness and the cycling frequency of the applied voltage weaken the informative value of α_{ME} in those composite systems even further. Eventually, the relative change in M cannot account for the local interface nature of the tuning effect, which in field-effect mediated devices is a result of the finite screening depth. As a consequence of the normalization to the sample volume, the calculated value of α_{ME} is strongly reduced by an increased thickness of the FM layer, which is physically not meaningful, as the strength of the coupling at the interface, where the interaction actually takes place, remains unchanged[9]. For these reasons, an alternative benchmarking approach for field-effect mediated systems will be introduced and employed in the present work, the charge-dependent magnetic tuning coefficient $\alpha_{\mathrm{MQ}} = \Delta m_{\mathrm{tot}} / \Delta Q$, which correlates the total magnetic modulation with the total screening charge at the interface (see Chapter 6). For the reasons stated above, a discussion of the various reported magnitudes of α_{ME} will be omitted in the following literature review.

Due to the fact that all FE materials necessarily are piezoelectrics, the ME coupling mechanisms in FE/FM composites can be based on an interplay of piezoelectricity and magnetostriction on the one hand, or on a charge carrier density modulation in the FM part due to the ferroelectrically induced field effect on the other hand. As the two mechanisms do not exclude each other, a superposition of both of them may also be expected and is observed.

When strain-mediated tuning is to be attained, a pronounced inverse piezoelectric effect is desirable, which – in the case of thin-film FEs – may be hampered by substrate clamping effects. Accordingly, pronounced ME coupling has been reported for vertically aligned heterostructures, where the out-of-plane components of the piezoelectric tensor are decisive [96]: a composite thin film comprising of self-assembled, Pulsed Laser Deposition (PLD)-grown $CoFe_2O_4$ nanopillars, embedded in a BTO matrix, was observed to possess strong interaction between the two phases, which manifested itself by a drop in M at the FE Curie temperature at around 380 K. However, as no external E-field was applied, this has to be regarded just as a proof of concept.

Instead of avoiding substrate clamping effects, they can also be intentionally used by employing FE substrates and depositing a FM layer atop. For a 10 nm Fe thin film grown on a (100)-oriented BTO single crystal substrate, abrupt steps in M were observed by Sahoo *et al.* [97] at the crystallographic phase transitions of BTO from tetragonal to orthorhombic and from orthorhombic to rhombohedral, during FC measurements in a SQUID magnetometer. Furthermore, *in situ* MOKE measurements revealed a tunable value of H_{c} which differed by ≈20 % for the opposite remanent states after perpendicularly polarizing the BTO in fields of ± 10 kV/cm.

[9] When magnetically dead layers come into play (see Section 3.2.1), this normalization becomes even more dubious.

Very similar experiments were reported by Brivio *et al.* [98]. While the results were generally consistent with the aforementioned, some interesting aspects were brought up: in contrast to the strain-mediated tuning of H_c, a field-effect mediated modulation of the magnetic anisotropy was observed, although an iron oxide layer at the BTO/Fe interface was found to be present. Moreover – and this should be kept in mind when evaluating reports on MOKE-based *in situ* tuning studies – a pronounced spurious contribution to the Kerr signal caused by electrooptic effects from the FE substrate was reported.

Strain-mediated tuning was also observed for composite systems with FE thin films. For a 10 nm $Ni_{80}Fe_{20}$ film on a 100 nm thick BTO layer, H_c and M were reported by Zhang *et al.* [99] to be controllable by an applied DC E-field, which was attributed to coupling of piezo-polarization and magnetostrictive deformation, due to the observed symmetry of the effect. However, these results are at least questionable, since similar effects – lowering of H_c and M – could as well be caused by leakage currents and the thereby induced Ohmic heating. Unfortunately, this possibility was not addressed and no leakage current data was provided, but the chosen 2 kHz cycling frequency for the FE hysteresis and the fact that no tuning in remanent polarization was observed, corroborate the conjecture that the sample may not have been suitable for DC measurements.

In a follow-up study on the same system, Li *et al.* [100] performed Alternating Current (AC) tuning measurements in a MOKE setup. While the above reported modulation of H_c was not addressed, a reversible modulation of the remanent magnetization (M_r) was investigated as a function of the applied E-field. At fields below 0.3 kV/cm a field-effect dominated mechanism could be identified by a hysteretic shape of the magnetic response to the cycled E-field. In contrast, at higher fields this effect was increasingly outshined by the stronger symmetric, butterfly-shaped response, indicating a transition to a piezoelectric-strain dominated regime.

When a FE thin film is mainly employed as stronger replacement for a high-κ dielectric or electrolyte gating, then any piezoelectric-magnetostrictive coupling component is usually an unwanted side-effect. As the latter is a long-range effect, it can be diminished in favor of the short-ranged field effect by reducing the thickness of the tunable FM layer towards a value that comes close to the screening length. However, a minimum thickness is often imposed by adverse size effects that may compromise the magnetic properties.

Another effective method to minimize strain effects was found by Mardana *et al.* [101]: by employing a FE copolymer which was mechanically significantly softer than the underlying Co wedge, so the latter could effectively be field-effect tuned. An anisotropy modulation of up to 50 % led to a considerable change in H_c and – at the thinnest point of the Co wedge – even to a flip of the magnetic easy axis from out-of-plane to an in-plane orientation.

The choice of film thicknesses, of the FE material and various geometrical aspects – like e.g., top gating *versus* bottom gating – plays a major role for the predominance of either strain or field-effect mediated tuning mechanisms, as soon as CMR manganites are employed as tunable FM material. This class of strongly correlated systems is extremely sensitive to changes in chemical composition, charge carrier density and lattice strain. It is this complexity which has driven extensive research activity in this field during recent years. But in order to be able to comprehensively elaborate and evaluate the reported results and effects, some background knowledge regarding the CMR manganites in general and LSMO in particular is essential. For this reason, the literature survey on MF ME composites based on CMR manganites as FM component will be postponed to Chapter 6 (Section 6.1), in favor of a more specific introduction into the CMR manganites which will be presented in the following section.

1.6 LSMO and related CMR manganites

$La_{1-x}Sr_xMnO_3$ (LSMO) is one of the most prominent members of the material class of strongly correlated oxides, which are often denoted rare-earth, perovskite, mixed-valence or Colossal Magnetoresistance (CMR) manganites or simply just manganites[10]. The class encompasses perovskite compounds of the form $R_{1-x}A_xMnO_3$, where R is a rare-earth cation and A is an alkali, alkaline-earth or Pb cation. Typically, the R component is one of the lanthanides, like e.g., La, Pr, Nd or Sm, while the A dopant is one of the following alkaline earth elements: Ca, Sr or Ba.

Historically, the mixed-valence manganites were the first oxides to exhibit FM exchange interaction accompanied by a striking correlation between magnetism and transport properties, as reported in the seminal publications by Jonker and Van Santen in the 1950's [102, 105, 106]. Only one year after the first report, Zener came up with his theory of Double-Exchange (DE) interaction [107, 108], which could explain the ferromagnetic (FM) metallic behavior in optimal doping regions, and which holds true till date. In the same decade, Volger discovered considerable

[10] Strictly speaking, the term *manganite* should only be employed for the 100 % Mn^{4+} compound [102].

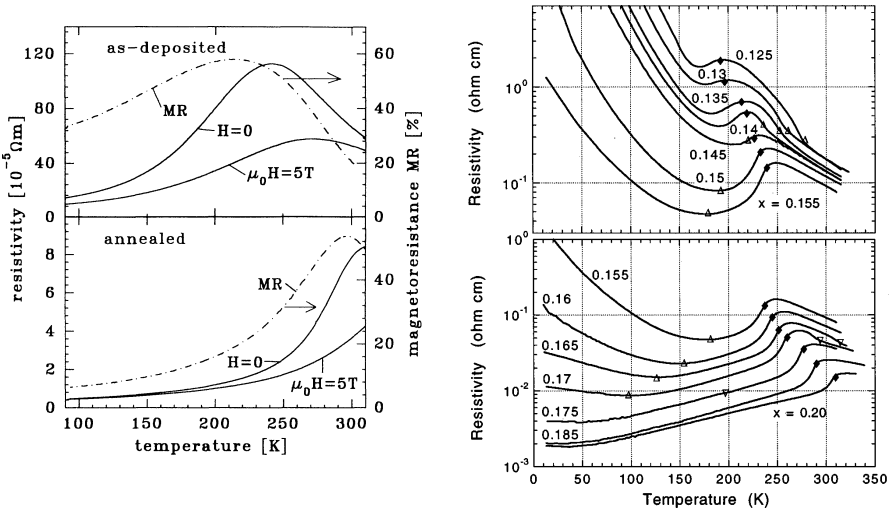

(a) CMR of LBMO **(b)** transport properties of bulk LSMO

Figure 1.6.: CMR effect and transport properties of manganites. (a): Temperature dependence of the resistivity at 0 T and 5 T of as-deposited and annealed in $x = 1/3$-doped LBMO. MR is the relative change in resistance, i.e., the *colossal* magnetoresistance. (b): Temperature dependence of the resistivities of *bulk* $La_{1-x}Sr_xMnO_3$ in the low Sr doping region of $x = 0.10$ to $x = 0.20$. The triangle and diamond symbols denote structural and ferromagnetic transitions, respectively. (*Reprinted with permission from* [103, 104]. ©1993, 1999, AMERICAN PHYSICAL SOCIETY)

negative magnetoresistance (MR) in 20 %-doped LSMO, featuring a remarkable peak near the FM Curie temperature [109].

After four mostly silent decades, interest in the topic was revived through the new possibilities provided by modern thin film deposition techniques, which led to a drastic increase in MR. The studies by Von Helmolt *et al.* in 1993 [103], who reached an MR value of 60 % for PLD-grown $La_{1-x}Ba_xMnO_3$ (LBMO) thin films [see Fig. 1.6(a)], laid the foundation for still ongoing research in the field of CMR materials. The term *colossal* was coined one year later by Jin *et al.* [110], in order to clearly differentiate the phenomenon from the Ruderman-Kittel-Kasuya-Yosida (RKKY) interaction based GMR effect observed in ML structures.

Even without an applied magnetic field, the temperature behavior of transport properties in manganites was found to be quite remarkable, featuring a metal-insulator transition intimately correlated with the FM-PM phase transition. The temperature dependence of resistivity as a function of Sr doping level in LSMO was investigated by Urushibara *et al.* [111] and Dabrowski *et al.* [104], yielding valuable data for the compilation of a phase diagram (discussed later, Fig. 1.12, or [104, 111–113]). In the low-doping region, a transition from insulating to metallic state – in terms of $d\rho/dT > 0$ – could be observed, as depicted in Fig. 1.6(b), which renders this region most interesting for CMR applications as well as for the investigation of the underlying physical mechanisms.

Another milestone on the road to applications and fundamental understanding can be found in the studies by Park *et al.* [114] in 1998, who experimentally proved that full intrinsic spin polarization is reached in 30 %-doped, i.e., metallic, LSMO; a property which was theoretically predicted by the DE formalism and which is of great interest for potential spintronics applications.

In the buzz of activity on the field of CMR manganites, a significant amount of theoretical work has been accompanying the experimental progress, attempting to draw a consistent picture that would account for all the complexity of the rich phase diagrams. As a result, a number of excellent and in many aspects very comprehensive reviews [112, 115–119] and books [120–122] have been written, which the reader is referred to for delving deeper into the topic. In the following, the mechanisms that are essential for the present work will be summarized, namely the structural and geometric factors, electronic states, exchange mechanisms and the complex interplay among them. The latter aspect, however, is of intricate self-consistent nature and thus requires some recursions in the line of argument, in order to embrace the rich versatility of effects.

The CMR manganites can be considered as a solid solution between two endmembers with distinct valence states. In the example of LSMO, the endmembers $La^{3+}Mn^{3+}O_3^{2-}$ and $Sr^{2+}Mn^{4+}O_3^{2-}$ form the mixed-valence serial dilution $(La^{3+}_{1-x}Sr^{2+}_x)(Mn^{3+}_{1-x}Mn^{4+}_x)O_3^{2-}$. While each of the endmembers is antiferromagnetic (AF) and insulating, the mixed valency of their solid solution brings about FM metallic behavior in a Sr doping range of $x \approx [0.2, 0.4]$.

The effect of A-site doping with a bivalent alkaline earth element is twofold. On the one hand, obviously, the charge carrier density (n_0) gets increased by a number of x electron holes (h^+) per formula unit, resulting in typical values of n_0 in the order of $10^{21}\,h^+/cm^3$. But albeit being close to metallic carrier densities, the considerable carrier *density* alone does not suffice to yield metallic behavior of the manganite, as long as the carrier *mobility* is too low. So there are other factors that have great influence on the charge carrier mobility which in turn determines peculiar properties of manganites. Notable among these factors are the modifications of interatomic distances and bond angles, induced by the different ionic radius of the dopant.

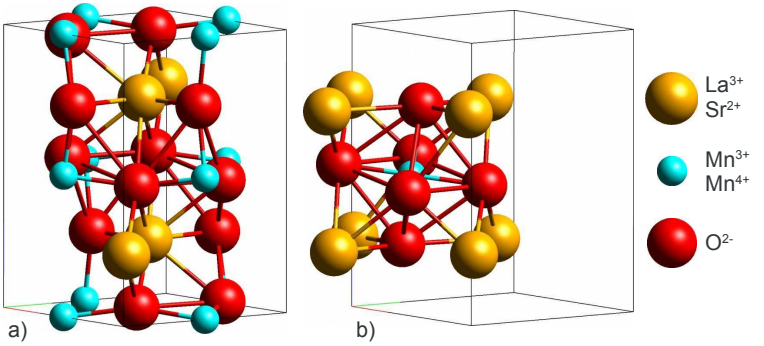

Figure 1.7.: Crystal structure of LSMO: orthorhombic unit cell (a) and pseudocubic perovskite representation relative to the wireframe of the unit cell (b). The illustrations were modeled with *CrystalExplorer* [123], using crystallographic data for $La_{0.875}Sr_{0.125}MnO_3$ from [124]. For clarity, the ionic radii are scaled by a factor of $1/2$.

In an ideal perovskite with the generic chemical formula ABO_3, the A-site cations are placed on the vertices of a cube, the B-site cation is located in the body center and the six oxygen anions surround the B-site cation in an octahedral geometry, located on the face centers of the cube. However, beyond ideal sterical conditions, this unit cell is subject to distortion reducing its potential energy. Fig. 1.7(a) illustrates the orthorhombically distorted unit cell of low-doped LSMO, which crystallizes in the *Pbnm* space group[11]. The pseudocubic representation shown for comparison [Fig. 1.7(b)] highlights the significant distortion of the oxygen octahedron.

The main reason for this distortion is the mismatch of A- and B-site cation ionic radii. A figure of merit which accounts for this mismatch is the so-called tolerance factor (Γ), defined as

$$\Gamma = \frac{d_{A-O}}{\sqrt{2} \cdot d_{Mn-O}}, \tag{1.3}$$

where d_{A-O} is the distance between the A-site cation and the nearest oxygen and analogously d_{Mn-O} is the distance from the manganese to the closest oxygen [117]. To visualize this factor, it is useful to consider a different view of the pseudocubic perovskite cell, where the B-site Mn is located in the eight vertices, the A-site cation sits in the body center and, accordingly, the oxygen anions are placed on the edges in-between the Mn cations. From this perspective, it is obvious, that a value of $\Gamma = 1$ is equivalent to a Mn–O–Mn bond angle of 180° with the atoms placed at their ideal position. If the A-site cation is too small, the O^{2-} moves inward, reducing d_{A-O} and simultaneously increasing d_{Mn-O}, which leads to a reduction of Γ. Obviously the Mn–O–Mn bond angle then also deviates from the ideal 180°. Regarding a complete crystal instead of a single unit cell, this shift leads to a *cooperative* tilting of the oxygen octahedra, one of the driving forces for orthorhombic and rhombohedral distortion. The fact that an Mn–O–Mn angle of 180° is optimal for the high carrier mobility, is imposed by the linear geometry of the bonding oxygen 2p orbitals. Consequently, the hopping probability for carriers moving along this bond gets reduced

[11] The *Pbnm* space group is equivalent to *Pnma*, only differing in the assignment of axes [116], accounting for the Jahn-Teller (JT) distortion (see below).

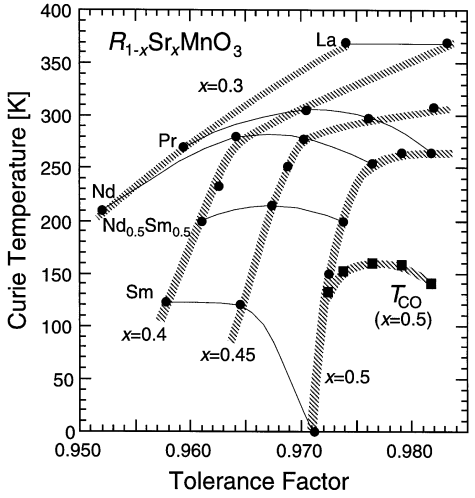

Figure 1.8: The dependence of T_C of various Sr-doped rare-earth manganites on the tolerance factor. The latter is influenced by the A-site lanthanide and the doping level (x). The hatched thick lines and the solid thin ones are the guides to the eye, connecting identical x and A-site lanthanides, respectively. (*Reprinted with permission from* [112]. ©1999, ELSEVIER)

as this angle decreases. As a result, the carrier mobility – and thus the conductivity – as well as the FM Curie temperature will be reduced[12].

In the case of a solid solution, Γ is the density-weighted average of the individual tolerance factors of the endmembers [117]. The impact of different rare-earth A-site cations on magnetic properties for various Sr doping level is shown in Fig. 1.8. The highest value of Γ is achieved for lanthanum, which is the largest of the rare-earth ions covered in the chart. Regarding the impact on the transition temperature, it is evident that a larger deviation from $\Gamma = 1$ generally results in decreased T_C.

Another important fact that becomes apparent from Fig. 1.8, is that a higher doping level for the same A-site lanthanide does not necessarily increase T_C (thin solid lines), although naïvely this might be expected, since both the carrier density n_0 and the tolerance factor Γ are elevated and the latter has a great influence on the carrier mobility. These extra complexities are a direct result of strong coupling between charge, spin (magnetic), lattice and orbital degrees of freedom.

While the major reason for crystallographic distortion is the cation size mismatch, another cause for either local or collective distortions arises from the orbital configuration of the Mn^{3+} ions, as illustrated in Fig. 1.9 [112]: When exposed to the electrostatic field of octahedrally coordinated oxygen ions – the crystal field – the five-fold degeneracy of the atomic Mn 3d levels is partially lifted into triply degenerate t_{2g} and doubly degenerate e_g electronic states. A further lifting of the degeneracy, and further energy lowering, occurs due to the so-called Jahn-Teller (JT) effect, i.e., a reduction of symmetry caused by the uniaxial distortion of the MnO_6 octahedra [125]. In this way, the oxidation state of the Mn^{3+} is stabilized, which otherwise would tend to disproportionate into Mn^{2+} and Mn^{4+}, as both are energetically disinclined toward such a distortion [116].

In the undoped or slightly doped $LaMnO_3$ endmember the strong Coulomb electron–electron repulsion and the collective JT splitting blocks the e_g electrons and prevent them from hopping

[12] The complexity of this mechanism will get clarified, when the DE interaction is discussed below.

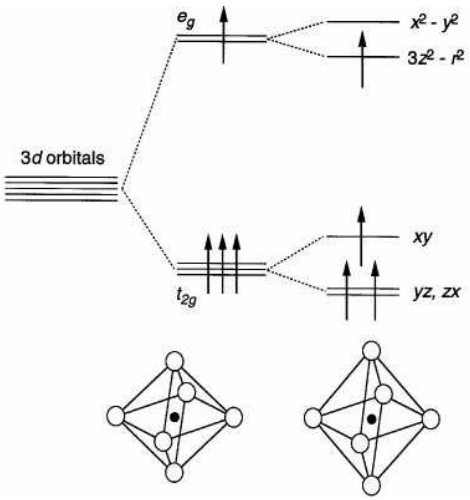

Figure 1.9: Lifting of the Mn^{3+} $3d^4$ degeneracy due to crystal field splitting in an octahedral site (middle) and uniaxial JT distortion of the MnO_6 octahedron (right). (*Reprinted with permission from* [112]. ©1999, ELSEVIER)

between neighboring Mn sites. Thus, the Mn valence electrons get localized, which results in an insulating state of $LaMnO_3$: a good example of a so-called Mott insulator.

The zero-temperature AF state of $LaMnO_3$ is a result of the Superexchange (SE) interaction [126] [see Fig. 1.10(a)]: Along an Mn–O–Mn bond, the antiparallel spin configuration of the intervening oxygen 2p orbital determines the antiparallel state of the Mn valence electrons. Due to the strong intra-atomic Hund-rule exchange, the Mn^{3+} $3d^4$ core electrons couple parallel to these valence electrons, resulting in antiparallel alignment of total spins of adjacent Mn^{3+} cations, i.e., an AF configuration in the ground state.

Mixed valency in Sr doped LSMO promotes electron hopping and creates the possibility for a new kind of indirect exchange, i.e., the Double-Exchange (DE) interaction. When sufficient h^+-doping comes into play, the SE coupling gets gradually replaced by the DE coupling, which till date is regarded as the main mechanism behind metallic conductivity and ferromagnetism in the CMR manganites. The two fundamental considerations of the theory developed by Zener [107, 108] are the strong Hund-rule coupling of the electrons in the Mn ions on the one hand, and, on the other hand, a transfer of a spin orientation between Mn ions via the hopping of the charge carriers. Due to the former, Mn ions generally have a high-spin configuration, causing the spin magnetic moments of Mn^{3+} and Mn^{4+} to be $4\,\mu_B$ ($S = 2$) and $3\,\mu_B$ ($S = 3/2$), respectively. The

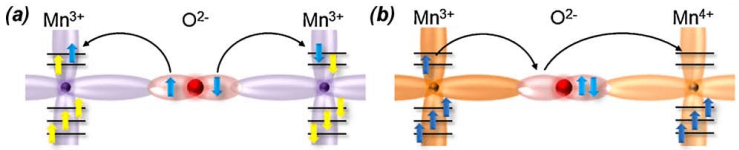

Figure 1.10.: Magnetic coupling in manganites: Superexchange (a) *versus* Double-Exchange (b). See text for detailed explanations. (*Reprinted with permission from* [70]. ©2010, ELSEVIER)

latter effect means that carrier hopping is enhanced and preferred between ions with parallel spin alignment.

As illustrated in Fig. 1.10(b), the DE mechanism between a Mn^{3+} d^4 and a Mn^{4+} d^3 via an O^{2-} p^6 consists of a simultaneous transfer of the e_g electron – the *Zener electron* – from the Mn^{3+} to the oxygen and from the oxygen to the neighboring Mn^{4+}. In combination with the strong Hund-rule coupling, the spin memory of the mobile Zener electrons results in a FM metallic ground state, as they simultaneously act as conduction electrons and as mediators of the FM exchange. There thus arises a strong correlation between the transport properties and the magnetism.

Some general properties of such systems can be deduced from this coupling mechanism, like e.g., the optimum doping level, the temperature behavior, the CMR effect and the spin polarization.

The magnetism in mixed-valence manganites is determined by the competition between SE and DE coupling. The more the DE dominates, the higher T_C is and with it T_{MI} and the conductivity. The optimum doping level is reached when the largest number of Mn^{3+} ions has exactly one Mn^{4+} nearest neighbor to couple with it via DE mechanism. This is not the case at the naïvely expected $x = 0.5$, but at $x = 0.25$, assuming a well ordered lattice. In a random distribution of the Mn^{3+} and Mn^{4+} ions, the maximum is reached at $x = 0.31$ [127]. As a result, the stable high-T_C region for LSMO is in the interval of $x \approx [0.2, 0.4]$. In optimally doped LSMO, the experimentally attainable magnetic moment per Mn ion reaches the theoretical value [114], which is an average of the high-spin magnetic moments of the ferromagnetically coupled Mn ions [104, 113, 128]:

$$m_{Mn} = (1 - x) \cdot 4\,\mu_B + x \cdot 3\,\mu_B = (4 - x)\mu_B. \tag{1.4}$$

The $3.7\,\mu_B$/Mn in 30 %-doped LSMO is in perfect agreement with the full spin polarization of the electronic Density of States (DOS), as was first experimentally evidenced by Park *et al.* [114] by means of spin-resolved photoemission measurements. Fig. 1.11 schematically illustrates this half-metallic behavior, i.e., a metallic DOS for one spin orientation and an insulating band gap for the opposite. This perfect intrinsic spin polarization is the reason for the increased low-field magnetoresistance, which is caused by FM domain boundaries, as a reversal of carrier spin orientation is required to pass a domain boundary.

The temperature behavior of magnetism and transport properties can qualitatively be explained in the frame of the DE mechanism as well. If the Mn spins are not parallel, the carrier mobility decreases due to spin dependent carrier scattering, which in turn weakens the parallel coupling of magnetic moments. Upon cooling, the spin fluctuations decrease and the system lowers its total energy by FM alignment of the spins via DE interaction, resulting in a gradually enhanced mobility, and thus a decreased resistivity [compare $x = 0.2$ curve in Fig. 1.6(b)]. For this reason the metal-insulator transition temperature (T_{MI}) typically coincides with the FM Curie temperature (T_C) in these materials.

Furthermore, the application of an external magnetic field facilitates the alignment of the Mn spins and, as a consequence, increases the mobility and thus the conductivity as well as the FM coupling. The result is an increased metal-insulator transition temperature and a significant drop in resistivity in this region [compare Fig. 1.6(a)]. This is the essence of the CMR effect. The effect is typically more pronounced for low- or intermediate-bandwidth manganites, i.e., for systems with lower Γ; the high-bandwidth LSMO requires a low doping level around the

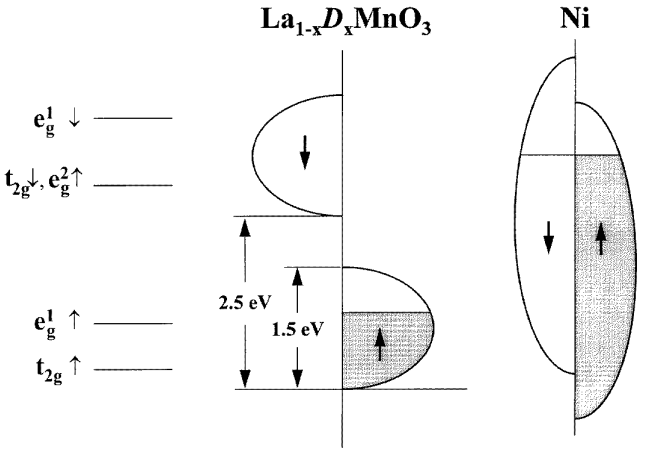

Figure 1.11.: Schematic zero-temperature DOS in mixed-valence manganites in comparison with the level diagram of undoped $LaMnO_3$ [129] (left) and the DOS in nickel, which features a much lower amount of spin polarization (right). *D* is a divalent doping cation. The energy scale represents levels from $x = 1/3$-doped LSMO [130]. The figure was adapted from [131]. (*Reprinted with permission from* [115]. ©1997, IOP PUBLISHING)

metallic-insulating boundary in order to yield a large CMR effect. In other words, the highest values are achievable for systems with very low T_C.

While the DE interaction can qualitatively explain the CMR phenomenon, the reason for the high magnitude of the effect at low T_C is still under debate. Partially this may be caused by the fact that electron-phonon interactions – the so-called JT polarons – are influencing the conduction electrons. As mentioned above, the JT distortion lowers the energy for Mn^{3+} only, while Mn^{4+} is not subject to this distortion. Hence, carrier mobility would be reduced for polarons because the electron (or hole) has to carry the lattice distortion with it, across an $Mn^{3\pm}$ O^{2-} Mn^{4+} bond, which requires a higher energy [112].

However, according to Dagotto *et al.* [117, 122], to fully explain the magnitude of the low-T_C CMR effect, only electronic phase separation and disorder-induced phase separation are of importance: Since in the low-doping region, the ground states are competing and intrinsically inhomogeneous[13], electronic percolation paths can be opened or closed by comparatively small changes in the distribution of electronic phases, effecting considerable modulations in the conductivity. The fact that the highest CMR effects were observed in thin films rather than in bulk systems, where the probability for percolation paths is evidently higher due to the additional third dimension, corroborates this concept.

At this point it becomes evident how apt the term *CMR manganites* is for this class of materials. The CMR effect combines virtually all the exceptional mechanisms of the mixed-valence manganites, like DE interaction and its competition with SE, the spin polarization and the electronic

[13] It should be stressed, that the electronic phase separation and the disorder-induced phase separation are intrinsic and even present in single crystals [122].

phase separation. However, there are some other mechanisms that are less prominently reflected by the CMR effect, but which still play significant role in determining physical properties of these materials.

Now that the magnetic coupling concepts have been clarified, it is worth revisiting the geometric conditions, namely the tolerance factor (Γ) and the Mn–O–Mn bond angle, since they have significant influence on the magnetic exchange coupling. The hybridization with the oxygen 2p orbitals requires a 180° bond angle for best overlap, which results in best exchange coupling. The more the bond is bent, the more the DE interaction gets hampered and the more the mobility decreases. Therefore, the value of Γ directly influences the effectiveness of DE coupling. This can be readily followed in Fig. 1.8, where the highest value of T_C is reached for optimal $x = 0.3$ doping in the case of LSMO, while some of the manganites with generally lower Γ have their highest Curie temperature for elevated doping levels, as caused by the trade-off between enhancing Γ and degrading Mn^{3+}/Mn^{4+} ratio. The experimentally obtainable Curie temperature for optimally doped LSMO of ≈360 K is a result of cation disorder, i.e., the segregation of dopants, and cation size effects. As an experimental estimate Rodriguez-Martinez *et al.* determined a value of T_C as high as ≈530 K for an ideal, disorder-free perovskite [132].

With regard to the complex phase diagram (see Fig. 1.12, or [104, 111–113]), even more refined correlations, including magnetic, charge and orbital ordering become significant[14]. Charge ordering is possible at low T and in doping regions, where x is a rational fraction, e.g., $1/8$, $1/2$ or $3/4$, and leads to small oxygen displacements in the ordered lattice [116]. The Mn–O distance in combination with the orbital arrangement has great influence on the electronic nature of the bonding.

[14] For declaration of the AF phases, see e.g., [134].

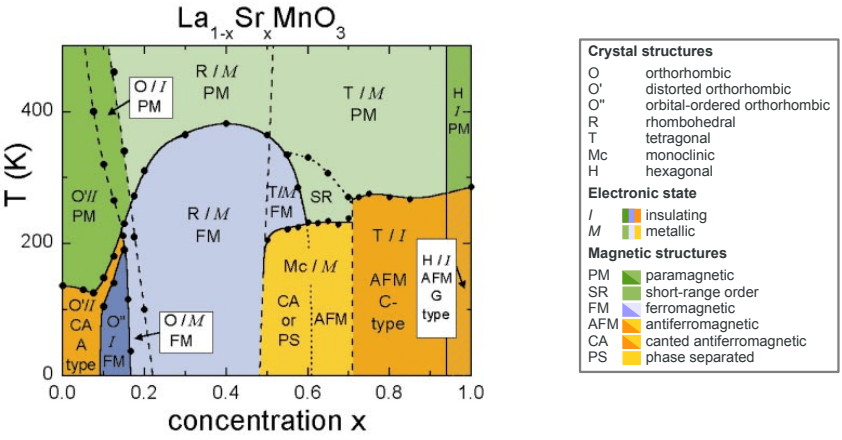

Figure 1.12.: Complex phase diagram of bulk $La_{1-x}Sr_xMnO_3$. The ordering types of the AF phases are as denoted, or A-type if not specified in the graph. (*Reprinted with permission from* [133]. ©2002, American Physical Society)

To elucidate the rich phase diagram, a theoretical framework was established by Goodenough [127] and Kanamori [125] on the basis of geometric considerations on the distorted crystal lattice and its implications on orbital order and overlap[15]:

The magnetic coupling configurations of the $x = 0$ and the $x = 1$ endmembers – namely A-type AF (in-plane FM and out-of-plane AF) and G-type near-neighbor AF coupling, respectively – is a consequence of hybridization of the manganese and oxygen orbitals, since the dsp^2 hybridization between Mn^{3+} d and O^{2-} p orbitals forms square and coplanar bonds, while Mn^{4+} and O^{2-} hybridize in octahedral d^2sp^3 orbitals to six nearest neighbors. In the mixed-valence manganite, the manganese and oxygen ions can interact in four different ways:

Covalent bonds are formed between O^{2-} and Mn e_g orbitals. Being in the same 2p orbital, two bonding electrons in these short and strong bonds have to be antiparallel. Due to the strong Hund-rule coupling in the Mn ions, these bonding electrons couple parallel to the other Mn electrons. The result is AF SE coupling along an Mn–O–Mn bond.

Ionic bonds of long distance are formed, when there is no orbital overlap between the Mn ions and the considered O^{2-}, due to dsp^2 hybridization. In this case, which only encompasses Mn^{3+} cations, no indirect exchange is happening.

Semicovalence is a hybrid form of the above cases, where one bond is covalent and the other one is of ionic nature due to missing orbital overlap. Due to the imbalanced forces, the oxygen is shifted towards the covalently bound Mn. Again, the 2p electrons are antiparallel, while the bonding electron is coupling parallel to the Mn electrons. On the side of the ionic bond, there is a direct, AF exchange between the Mn magnetic moment and the anion. The result is an overall FM coupling between both Mn cations. This arrangement becomes more obvious, when longer Mn-O—Mn-O chains are considered.

Double-Exchange (DE) requires the presence of a Mn^{3+} and a Mn^{4+} ion inline with the O^{2+} anion in between, facilitating the simultaneous transfer of an electron from the Mn^{3+} to the oxygen and from the oxygen to the Mn^{4+}, as stated above. This hopping is most pronounced when the spin-only moments of the Mn ions are aligned, i.e., for FM coupling.

The above four cases can be compiled to a simple set of rules for the coupling along an Mn–O–Mn bond [116]:

- Mn^{3+} and a Mn^{4+} couple ferromagnetically due to DE interaction.
- Two Mn^{4+} ions always couple antiferromagnetically due to SE interaction along the covalent bonds.
- Two Mn^{3+} ions couple antiferromagnetically via SE interaction, in case of covalent bonding, or ferromagnetically in the case of semicovalence.

For varying Mn^{3+}/Mn^{4+} ratios, i.e., for different doping level, the balance of these competing ground states gets gradually shifted, not only due to the obvious change in h^+ density, but also as a result of altered bond lengths and angles. As a result, the transitions in the phase diagram tend to be gradual as well.

[15] The summary below is also inspired by Coey's interpretations [116] of Goodenough's and Kanamori's theory.

In terms of practical use, the doping regions of interest for LSMO are typically determined by the possible application areas. On the one hand, the optimal doping level, with its high value of T_C, conductivity and spin polarization, is particularly suitable for various sorts of spintronics devices that are functional in ambient conditions[16]. On the other hand, the low-doping region at around the metal-insulator transition is of interest especially for CMR applications. However, these are pretty limited due to the low value of T_C. Furthermore, the CMR effect requires rather high fields of typically 5 T or more[17]. Thus, for magnetic sensor devices, solutions based on the GMR effect are much more qualified, as they sense fields of around 0.01 T [117].

Besides applications, especially the low-doping region is of great scientific interest, as it allows for observing the intrinsic competition of the fundamental coupling mechanisms, where small fluctuations in the carrier density result in drastic effects: As can be seen from the phase diagram (Fig. 1.12), within the doping level (x) interval of 10 to 20 %, T_C grows linearly with a coefficient of about 1670 K/x. However, this high sensitivity is of course the result of two distinct mechanisms, which both tend to elevate the DE coupling in this doping region and which are tightly entangled in any chemical doping series, namely the variation of the Mn^{3+}/Mn^{4+} ratio on the one hand and an enhancement of the tolerance factor on the other hand. In order to experimentally quantify the magnitude of both effects, it is necessary to find such experimental conditions where only one of them is varied. In contrast to chemical tailoring, electrostatic tuning allows exactly this. By employing the electric field effect, the h^+ density can be reversibly modulated without introducing any lattice distortions due to differences of the substituting A-site cation radius.

[16] For a review of (spintronics) applications, the reader is referred to [135].

[17] It is worth mentioning, that the requirement for high magnetic fields in case of CMR should not be confused with the general sensitivity to magnetic fields; typically, H_c of LSMO is orders of magnitude lower. Fig. 4.9(b) on p. 73 may serve as an example.

2 Preliminary work: Tuning of electrolyte-gated LSMO nanoparticles

The starting point[1] for this thesis is given by the preliminary work of Mishra, Leufke et al. on the electrolyte-based electrostatic modulation of magnetism in $La_{1-x}Sr_xMnO_3$ (LSMO) nanopowder [4]. A brief summary shall be presented here.

As pointed out in Section 1.6, the Colossal Magnetoresistance (CMR) manganites possess rich complex phase diagrams, unquestionably very sensitive to the A-site electron hole (h^+) doping. With their strong correlation between magnetism and transport properties, in combination with their fully spin-polarized Density of States (DOS), they are ideal candidates for electric field-effect tuning devices with a wide range of thinkable applications. At the same time, from the scientific point of view a purely electrostatic modulation provides the possibility to investigate their magnetic and electric properties as a function of charge carrier density (n_0), without introducing any chemical impurities from doping elements.

For a proof-of-concept survey, electrolyte tuning was considered to be well suited, as it is naturally capable of creating a surface space charge on exceptionally large sample areas, unlike dielectric or ferroelectric (FE) gating which, for large areas, is very prone to electrical breakdown. Of course, the limited applicability of electrolytes at low temperature (T) imposes some boundary conditions for the practical implementation of an electrolyte gated CMR devices, though, as summarized in the following two points.

In order to be able to investigate the magnetic properties, the Curie temperature (T_C) had to be well within the operating temperature range of the electrolyte. For this reason, LSMO was considered the most suitable system (compare Fig. 1.8 on p. 20).

Furthermore, the initial doping level had to be chosen in a sensible way. As stated earlier, the highest sensitivity of magnetism with respect to the doping level (x) is within the interval of $x \approx [0.1, 0.2]$, where T_C is mostly below Room Temperature (RT). On the other hand, when the doping level is chosen too close to the optimum for Double-Exchange (DE) coupling, i.e., $x \approx 0.3$, in order to push T_C up to temperatures where liquid electrolytes are sufficiently conductive, the plateau of T_C (compare Fig. 1.12 on p. 24) suggests a stable regime which is not very sensitive to modulations of the carrier density[2]. As a compromise, a doping level of 25 % was selected for the present electrolyte tuning studies. A nanoparticulate sample morphology was chosen in order to maximize the surface-to-volume ratio and thus yield the highest field effect efficiency.

[1] Albeit being published late in 2013, the preliminary studies summarized in this chapter had been finished well before the thin-film based experiments reported in the following chapters were initiated.

[2] It should of course be stressed that the phase diagram always reflects the *chemical* doping effects and thus not only contains the impact of a variation of the Mn^{3+}/Mn^{4+} ratio, but also the significant influence of changes in the tolerance factor (Γ). Nevertheless, for lack of more specific data, the phase diagram has to suffice for this approximation.

2.1 Nanopowder sample preparation

Nanocrystalline LSMO powder with a nominal doping level of $x = 0.25$ was prepared by spray pyrolysis [136] at 1000 °C from an aqueous precursor solution consisting of molar ratios of lanthanum nitrate hexa-hydrate $\left[La(NO_3)_3 \cdot 6H_2O\right]$, strontium nitrate $\left[Sr(NO_3)_2\right]$ and manganese nitrate tetra-hydrate $\left[Mn(NO_3)_2 \cdot 4H_2O\right]$ [137].

In order to tailor particle size and crystallinity, annealing in flowing O_2 gas was performed at temperatures of 800 °C and 1000 °C for 1 h or at 1100 °C for 3 h, respectively. The chosen three different powder samples will be denoted A800, A1000 and A1100 in the following. The annealing step is also necessary in this synthesis route in order to fix oxygen deficiency, which is otherwise directly counteracting the chemical h^+ doping, leading to reduced T_C [115].

The samples were gently compacted to pellets of 3 mm in diameter, employing a pressure of 0.03 GPa, which allowed for preserving the porosity of the nanopowder.

2.2 Microstructural properties

X-ray Diffraction (XRD) analysis of the as-synthesized powder revealed a nanocrystalline, phase-pure perovskite structure [see Fig. 2.1(a)] with an average crystallite size of ≈7 nm, as estimated by means of the Scherrer equation and using the strongest single peak at (024) after compensating for the instrumental broadening [138, 139]. After annealing, the Full Width at Half Maximum (FWHM) as expected was smaller [see inset in Fig. 2.1(a)], yielding increased crystallite sizes of 18 nm, 25 nm and 48 nm for the samples A800, A1000 and A1100, respectively. The annealing temperature and time dependence of the crystallite size is depicted in the graphs in Fig. 2.1(b).

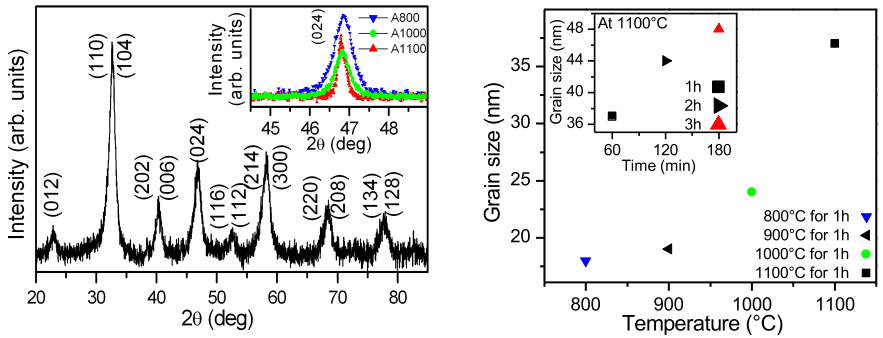

(a) powder XRD pattern

(b) crystallite size evolution

Figure 2.1.: XRD analysis of LSMO nanopowder. (a): X-ray diffractogram of as-synthesized powder. The inset allows for comparing the width of the (024) reflection of the annealed samples. (b): Evolution of the average crystallite size as a function of T for 1 h of annealing. The inset shows the grain growth at constant $T = 1100$ °C as a function of annealing time. (*Published in* [4], ©2013, American Institute of Physics)

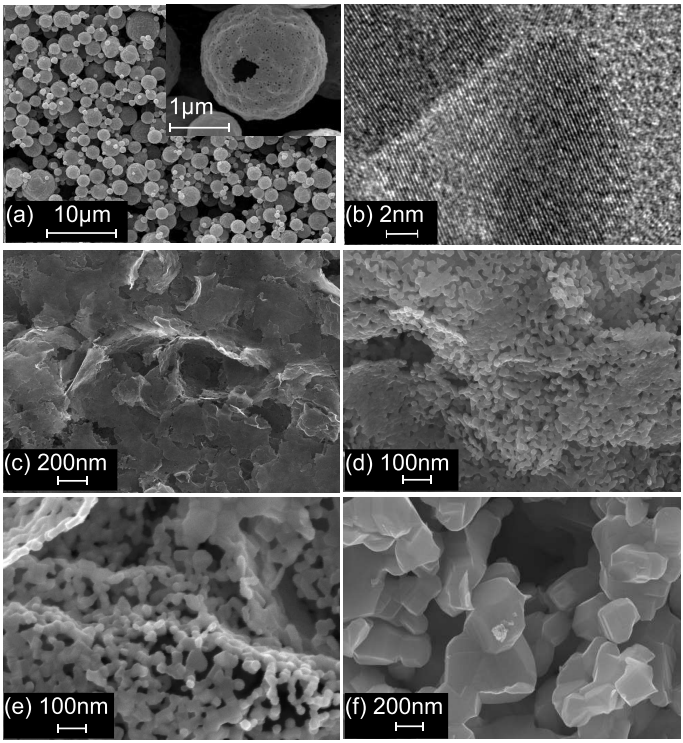

Figure 2.2.: Electron microscopy analysis of LSMO nanopowder. (a)&(c)-(f) SEM micrographs of as-synthesized powder (a), sample A800, featuring a flattening of hollow spheres (c&d), a sample annealed at 1100 °C for 1 h (e), and sample A1100 (f). (b): TEM micrograph of as-synthesized LSMO. (*Published in* [4], ©2013, American Institute of Physics)

Scanning Electron Microscopy (SEM) revealed that the actual grain size of the as-synthesized LSMO particles was in fact significantly larger than the crystallographic one, due to a hollow-spherical shell morphology with a wall thickness of ≈20 nm, as a result of the spray pyrolysis process [Fig. 2.2(a)]. The nanocrystallinity as determined by XRD could qualitatively be confirmed by Transmission Electron Microscopy (TEM) [Fig. 2.2(b)]. In the 1 h annealed samples, the spherical morphology transformed into flattened flakes with clearly visible interconnected ligaments [Fig. 2.2(c-e)]. Further annealing at 1100 °C for two more hours (sample A1100) resulted in sintered crystals with an increased grain size of 150 to 200 nm [Fig. 2.2(f)], which on the one hand effected an enhanced sharpness of the magnetic transition (as discussed below, see Fig. 2.3), but which was on the other hand undesirable because of the diminished surface-to-volume ratio.

2.3 Electrostatic tuning of magnetic properties

Combined Field Cooling (FC)/Zero-Field Cooling (ZFC) measurements were performed in a Superconductive Quantum Interference Device (SQUID) magnetometer, with the FC external field set to 5 mT, in order to determine the magnetic state of the nanoparticles. A pronounced improvement of magnetic properties due to the annealing steps was observed (Fig. 2.3). The very broad low-T transition of the original as-synthesized powder, characteristic of superparamagnetism, which featured a blocking temperature of ≈85 K, could be significantly increased towards Curie temperatures of 330 to 345 K in all annealed samples. This temperature is virtually identical to the literature bulk value (compare LSMO phase diagram, Fig. 1.12 on p. 24) and therefore suggests a balanced oxygen stoichiometry only reached after annealing. As a consequence, only

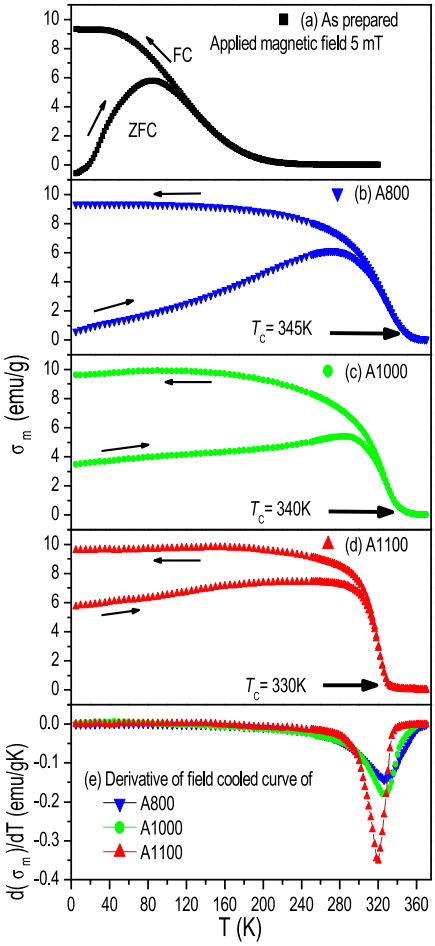

Figure 2.3: FC/ZFC magnetic moment measurements at an external magnetic field of 5 mT of the as-synthesized LSMO nanopowder (a) and annealed samples A800 (b), A1000 (c) and A1100 (d). The derivatives of the FC curves of the annealed samples are shown to compare the sharpness of magnetic transition (e). (*Published in* [4], ©2013, American Institute of Physics)

the annealed samples qualified for electrolyte gating, due to their electrolyte-compatible values of T_C, well above RT. The sharpness of the paramagnetic (PM)-ferromagnetic (FM) transition, as determined by the derivative of the FC curve, increased for higher annealing temperatures, presumably as a result of increased stoichiometric homogeneity and/or narrower particle size distributions (Fig. 2.3(e); compare SEM pictures in Fig. 2.2 and [140]).

Thus, in analogy to the CMR effect, the field-effect tuning would be expected to be most effective for the sharpest PM-FM transitions, where a small shift in T_C yields the largest difference in magnetic moment. On the other hand, with the field effect being a surface phenomenon, an effective modulation of n_0 also requires a large surface-to-volume ratio. As a consequence, the optimal annealing settings proved to be a trade-off between sharpness of magnetic transition and specific surface area.

From hysteresis measurements at 5 K, a saturation magnetic moment per Mn ion of $\approx 3.2\,\mu_B$ was obtained for all annealed samples. The difference from the theoretical spin-only moment in bulk of $3.75\,\mu_B$ (compare Eqn. 1.4 on p. 22, using $x = 0.25$) may be attributed to the irregular nature of the nanoporous morphology including interface effects and/or nonstoichiometric element distribution.

The *in situ* electrostatic cycling, with simultaneous measurement of the total magnetic moment, was carried out in a Physical Properties Measurement System (PPMS), equipped with a custom-made electrochemical cell, which featured a gold-wired three-electrode configuration with the sample as working electrode and high surface area carbon fiber cloth and Ag/AgCl as counter and reference electrodes, respectively. The liquid electrolyte consisted of 0.5 mol/dm^3 of 99.99 % pure lithium perchlorate $(LiClO_4)$ dissolved in anhydrous propylene carbonate $(C_4H_6O_3)$.

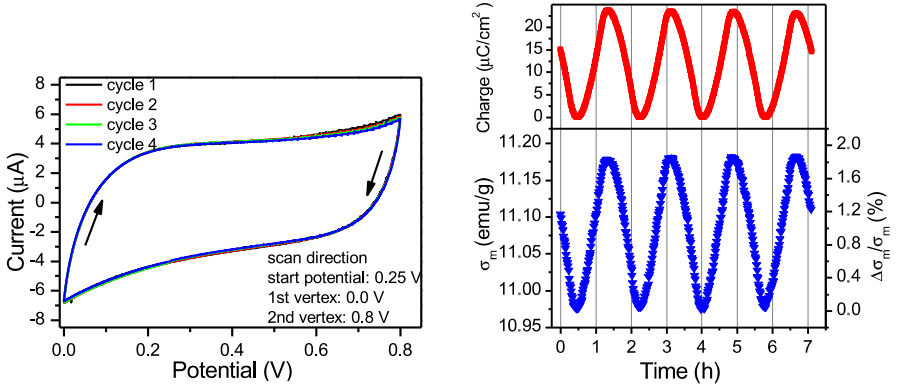

(a) CV in the capacitive voltage window

(b) modulation of charge and magnetic moment

Figure 2.4.: Cyclic charging on the example of sample A800. (a): Four consecutive CV scans, i.e., the charging current as a function of applied potential. (b): Induced surface charge (upper panel) and the magnetic response (lower panel) as a function of time. Measured at 325 K and 50 mT. (*Published in* [4], ©2013, American Institute of Physics)

The magnetic moment was monitored in Direct Current (DC) extraction mode during repeated Cyclic Voltammogram (CV) scans, which were limited to the determined Helmholtz double layer voltage window of 0.0 to 0.8 V – in order to avoid any redox reaction at the electrode-electrolyte interfaces – and performed at a rate of 0.25 mV/s, where the vital reversibility was attained [Fig. 2.4(a)].

The resulting induced charge on the LSMO surface was calculated by integration of the charging current, with the constant of integration setting the minimum charge to zero. The charge modulation of $\approx 22\,\mu C/cm^2$ was equivalent to a surface charge doping per unit cell area of $\approx 0.2\,h^+/\text{u.c.}^2$. Plotted as a function of time, the simultaneously monitored mass magnetic moment (σ_m) confirmed a direct correlation between surface charge modulation and a fully reversible magnetic response [Fig. 2.4(b)].

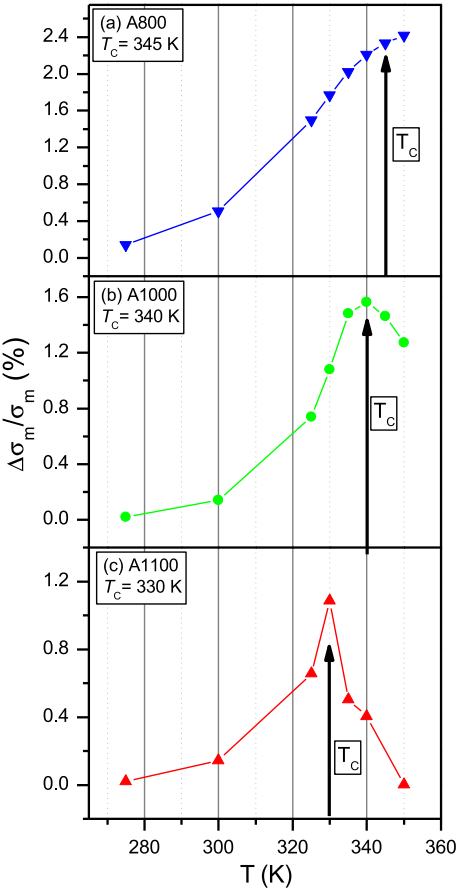

Figure 2.5: Temperature dependence of the relative variation of the mass magnetic moment upon charging of the annealed LSMO nanopowder samples at an applied field of 0.1 T. (*Published in* [4], ©2013, American Institute of Physics)

To systematically study the magnetoelectric (ME) tuning at the PM-FM phase transition, the *in situ* cycling measurements were conducted as a function of temperature (T), while keeping the magnetic field (H) constant, or vice versa, as a function of H at constant T. The former case was performed as a part of a FC procedure, i.e., the external field was set above T_C prior to cooling to the desired working temperature.

For the T-dependent measurements, a pronounced increase in the relative change in σ_m around the respective Curie temperatures of the three samples was observed, while towards lower T the ME modulation was significantly reduced (Fig. 2.5). For sample A800, the one with highest T_C and the broadest transition, not the entire relevant temperature range was accessible due to the instrumental limit at 350 K. However, for A1000 and A1100, the elevated modulation around T_C could clearly be identified as a local maximum, as a drop in the tuning response was also observed at higher T.

In a direct comparison of the three samples regarding the magnitude of the ME modulation, a decrease of the effect with rising annealing temperature was observed, despite the sharper transition of these samples. The maximum modulation of $\Delta\sigma_m/\sigma_m \approx 2.5\,\%$ was obtained for the A800 sample (compare Fig. 2.5). The particular temperature dependence was attributed to the reduced surface-to-volume ratio which resulted from sintering of the nanoparticles.

As mentioned above, the interpretation of the temperature dependence is based on the well-established complex LSMO phase diagram (see Fig. 1.12 on p. 24, or [104, 111–113]). An accumulation of positive space charge during a CV scan increases the h^+ density within the affected screening length in the LSMO nanoparticles. In other words, the Mn^{3+}/Mn^{4+} ratio is expected to be shifted towards higher Mn^{4+} concentrations. Assuming a screening length of $\approx$2 u.c., the average carrier density modulation per formula unit is $0.1\,h^+$. According to the phase diagram in the low Sr doping region, such a modulation should yield an increase in T_C in h^+ accumulation state, due to enhanced DE coupling. Furthermore, according to Eqn. 1.4, the total spin-only moment of the affected Mn ions should experience a corresponding drop in view of the lowered electron concentration. The superposition of both these phenomena is illustrated

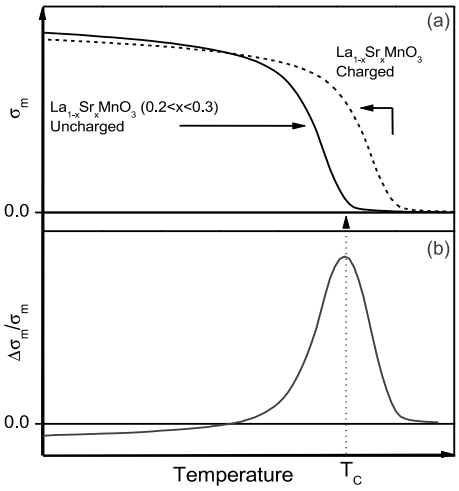

Figure 2.6: Schematic model of the ME modulation mechanism: (a): The PM-FM transition in uncharged and h^+ accumulation (charged) state. (b): The difference of the two curves of the upper panel, normalized on the uncharged curve, resulting in a maximum around T_C and a reversal of the sign of the tuning effect for low temperatures. (*Published in* [4], ©2013, American Institute of Physics)

in Fig. 2.6(a), which shows a comparison of two representative FC curves: one in an uncharged state and the other one in h^+ accumulation state (charged). The competition between the shift in T_C and the modulation of σ_m leads to the relative modulation which, at decreasing T, features a pronounced maximum around T_C, a crossover in sign and a negative effect at low T [Fig. 2.6(b)].

Evidently, this phenomenological model was able to reproduce all the main features that were experimentally observed. Beyond that, it even predicted the existence of a negative ME coupling which would only be observable at $T \ll T_C$, where the positive tuning effect that originates from the shift in T_C would not dominate the weaker reduction of σ_m.

As the limited operating temperature range of the electrolyte prohibited the direct experimental verification of the crossover at low T, the challenge was tackled by shifting the transition temperature with application of a strong external field [3]. Indeed, the isothermal magnetoelectric modulation of samples A1000 and A1100 exhibited a significant drop [Fig. 2.7(a)] upon increasing the applied field.

With sample A800, which combines highest T_C and largest porosity, the actual crossover of the tuning effect was realized at 325 K, eventually. In comparison with the low-field modulation at

[3] See also Section 1.6.

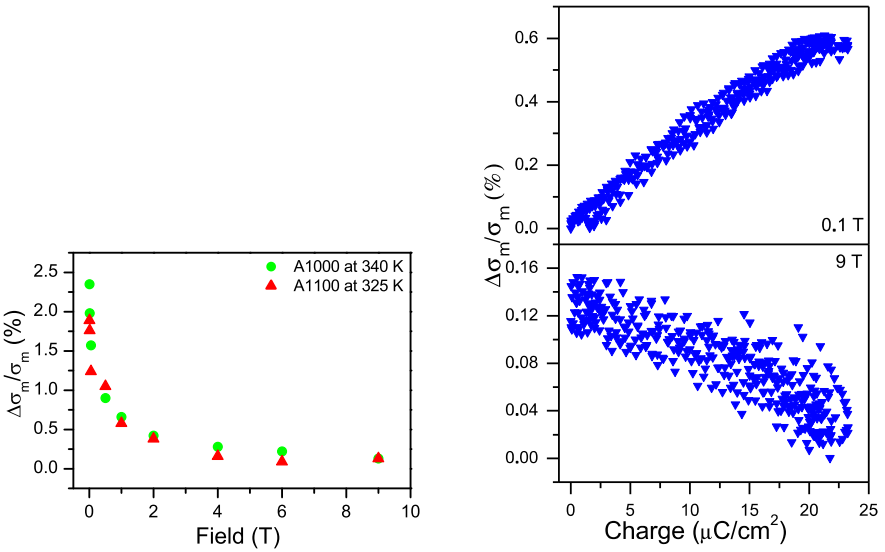

(a) magnetic field dependence **(b)** low- and high-field charge dependence

Figure 2.7.: Magnetic field dependence of the magnetic modulation. (a): Relative change in mass magnetic moment as a function of the external field, measured near the Curie temperatures of samples A1000 and A1100. (b): Reversal of the ME tuning effect on sample A800, from low external field (0.1 T, upper panel) to high field (9 T, lower panel), measured at 325 K for four consecutive charging cycles. (*Published in* [4], ©2013, American Institute of Physics)

0.1 T, the high-field response at 9 T exhibited an inverted slope of the charge-induced modulation [Fig. 2.7(b)].

2.4 Conclusions

The two phenomena deduced from the studies on reversible electrolyte tuning of LSMO, namely the shift of T_C accompanied by a simultaneous reduction of the magnetic moment, were taken as a clear experimental proof of the electrostatic h^+ doping concept. In this experiment the extraordinary big surface-to-volume ratio favored the nanopowder morphology, as it allowed for a drastic reduction of the untuned volume. However, a serious handicap diminishes their applicability: The irregular morphology presupposes the use of a (liquid) electrolyte in order to ensure full coverage of the whole sample surface, which brings about a limitation to a rather narrow temperature range, where the electrolyte is sufficiently conductive. This hampers measurements at temperatures $T \ll T_C$, that would be required to separately determine the magnetic moment reduction by suppressing the contribution of T_C shift[4] and thus allow for a quantitative analysis of this contribution to the ME coupling mechanism. Furthermore, the whole low-doping region below $x \approx 0.2$, where the competition between Superexchange (SE) and DE is most fierce, unfortunately is not reachable by this method.

To overcome the limitations of the electrolyte gating a FE thin-film based approach suggests itself. The thin film geometry is much more uniform and homogeneous and thus facilitates any theoretical modeling. Furthermore, with a suitable FE material, much higher polarizations are achievable and the low-T compatibility is provided for.

Of course, this concept, which forms the basis for the present work, entails other challenges. Epitaxial CMR manganite layers are sensitive to substrate-induced strain and therefore require a sensible choice of substrate. Moreover, due to the plane geometry, the surface-to-volume ratio is drastically reduced as compared to a nanoporous system. Consequently, the manganite layer thickness has to be as thin as possible. Finally, the reduced surface area limits the total achievable modulation of the magnetic moment. Therefore, to yield an experimentally appreciable modulation signal, a challengingly large FE device area is required.

[4] A clear separation of both effects requires a broad plateau of the FC curve at low T, so that the shift in T_C has no effect on the magnetic moment in this temperature region.

3 Materials & Methods

Apart from informing about experimental details, the scope of this chapter covers background information on the employed materials and methods that is considered as reaching beyond textbook standards.

An overview of the crystallographic properties of the thin film and substrate materials used in this work is given in Tab. 3.1. Except for MgO, all of them crystallize in the perovskite structure and have quite similar lattice parameters. The table also lists the in-plane lattice misfit with respect to $x = 13\,\%$-doped $La_{1-x}Sr_xMnO_3$ (LSMO), which is a crucial criterion for the epitaxial growth mode.

Before introducing the functional thin film materials – i.e., LSMO and $PbZr_yTi_{1-y}O_3$ (PZT) – and elaborating on the deposition method, we will focus on the substrate materials used in this study.

3.1 Substrates

Five different single crystalline substrates – $SrTiO_3$ (STO), $SrTiO_3$:Nb (STO:Nb), $(La_{0.3}Sr_{0.7})(Al_{0.65}Ta_{0.35})O_3$ (LSAT), $LaAlO_3$ (LAO) and MgO – were chosen on the basis of their crystal structure, diamagnetic behavior [146], availability[1] and cost. Their in-plane lattice mismatches with respect to the LSMO pseudocubic lattice constant $a_{pc,LSMO}$ are listed in Tab. 3.1[2].

All employed substrates were epi-polished and – in (pseudo-)cubic coordinates – (100)-oriented. Details about suppliers and crystal batches are given in Tab. A.2 on p. 140. In most cases substrates of 5 mm in width were preferred as they fit into the Superconductive Quantum Interference Device (SQUID) magnetometer without further cutting.

3.1.1 $SrTiO_3$ and $SrTiO_3$:Nb

STO is certainly one of the most common perovskite substrates, used for epitaxial growth of various oxides and superconductors. It is often considered a model perovskite system; the cubic unit cell is illustrated in Fig. 3.1(a). STO substrates are reasonably priced and available in very high crystalline quality. With respect to the low-doped LSMO the in-plane lattice mismatch is almost negligible (see Tab. 3.1).

A common procedure to reach highest epitaxial growth quality on STO substrates is to etch the surface in a buffered HF solution in order to generate a TiO_2-terminated surface [148, 149]. However, due to the considerable hazard posed by hydrofluoric acid, this step was omitted. In Chapter 4 it will be demonstrated that even on as-purchased, epi-polished STO a remarkable epitaxial quality is obtainable, when the substrates are annealed in Ultra-High Vacuum (UHV) prior to deposition.

[1] A helpful diagram of common oxide substrates and their lattice constants can be found in [147].

[2] STO:Nb is not listed separately as its lattice parameters are virtually identical to those of pure STO.

Table 3.1.: Crystallographic properties (at RT) of the employed functional thin film materials (LSMO and PZT) in comparison with the substrates (STO, LSAT, LAO and MgO). The specified LSMO and PZT compositions are the ones which shall turn out to be the most relevant for the present studies. a_{pc} denotes the pseudocubic lattice constant.

material	$La_{0.87}Sr_{0.13}MnO_3$ (LSMO)	$PbZr_{0.52}Ti_{0.48}O_3$ (PZT)	$SrTiO_3$ (STO)	$(La_{0.3}Sr_{0.7})(Al_{0.65}Ta_{0.35})O_3$ (LSAT)	$LaAlO_3$ (LAO)	MgO
structure	mixed perovskite ($GdFeO_3$)	mixed perovskite ($PbTiO_3$)	perovskite ($CaTiO_3$)	mixed perovskite	perovskite ($NdAlO_3$)	halite (NaCl)
lattice system	orthorhombic	tetragonal	cubic	tetragonal ($\approx$ cubic)	rhombohedral	cubic
space group	*Pbnm* (#62)	*P4mm* (#99)	$Pm\bar{3}m$ (#221)	$I\bar{4}$ (#82)	$R\bar{3}cH$ (#167)	$Fm\bar{3}m$ (#225)
lattice constants	$a = 5.545$ Å $b = 5.526$ Å $c/\sqrt{2} = 5.510$ Å $a_{pc} = 3.906$ Å	$a = 4.043$ Å $b = a$ $c = 4.132$ Å —	$a = 3.901$ Å $b = a$ $c = a$ —	$a = 5.468$ Å $b = a$ $c/\sqrt{2} = 5.465$ Å $a_{pc} = 3.866$ Å	$a = b = 5.366$ Å $\gamma = 120°$ $a = 13.111$ Å $a_{pc} = 3.791$ Å	$a = 4.214$ Å $b = a$ $c = a$ —
misfit in (100)-plane (w.r.t. $a_{pc,LSMO}$)	—	3.5 %	−0.13 %	−1.0 %	−2.9 %	7.9 %
crystallogr. density	6.55 g/cm^3	8.00 g/cm^3	5.13 g/cm^3	6.63 g/cm^3	6.52 g/cm^3	3.58 g/cm^3
references	[104, 124]	[141]	[142]	[143]	[144]	[145]

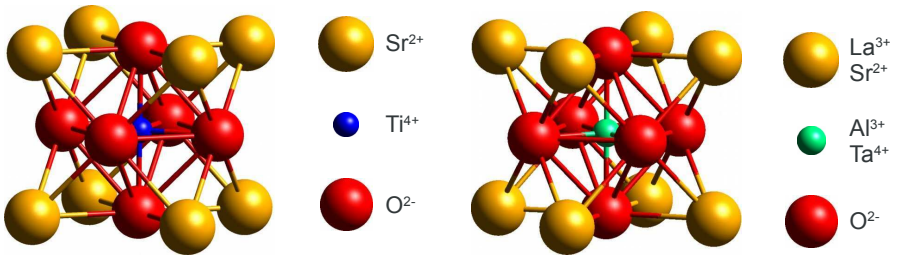

Figure 3.1.: Crystal structures of STO (a) and LSAT (b), modeled with *CrystalExplorer* [123], using crystallographic data from [142] and [143], respectively. For clarity the ionic radii are scaled by a factor of $1/2$.

STO:Nb, the only conductive material among the employed substrates, is virtually identical to pure STO with respect to crystallographic properties. The low doping level of $x = 0.5$ wt.% generates sufficient conductivity in this n-type conductor for use as a back electrode in ferroelectric (FE) capacitors, as will be shown in Chapter 5. According to the supplier (SurfaceNet), higher doping was not practicable as it would result in Nb segregation upon annealing.

3.1.2 $(La_{0.3}Sr_{0.7})(Al_{0.65}Ta_{0.35})O_3$

LSAT, a perovskite with the rather synthetic composition $(La_{0.3}Sr_{0.7})(Al_{0.65}Ta_{0.35})O_3$, has a tetragonal unit cell [143]. However, the tetragonality is so low, that it is often considered cubic [150, 151]. Fig. 3.1(b) shows the LSAT structure[3] at Room Temperature (RT). Historically, LSAT was designed as an improved replacement for LAO [152], forming a suitable substrate for materials that required very low lattice mismatch, such as cuprate superconductors [150] or GaN [151]. The absence of structural phase transitions in the whole temperature range up to the high growth temperatures required for many oxides [150] and a low density of dislocations [151], renders LSAT a well suited substrate for high quality epitaxial growth. With respect to the low-doped LSMO there is a small compressive lattice mismatch of about -1 %.

3.1.3 $LaAlO_3$

LAO was chosen as a substrate for the present studies, as its small unit cell is suitable to generate pronounced compressive strain to an LSMO layer grown on top. Fig. 3.2 illustrates the rhombohedral unit cell (a) and the pseudocubic interpretation (b) of LAO. The pseudocubic lattice constant of LAO imposes a compressive in-plane misfit of about -2.9 % onto the low-doped LSMO. There exist, however, two properties that compromise the quality of epitaxial films grown on LAO, that should be kept in mind; first because of its rhombohedral structure, LAO is susceptible to twinning [153], and second because of the structural phase transition from rhombohedral to cubic above $\approx$800 K [150, 153].

[3] The A- and B-site ion radii shown belong to the respective larger species (Sr and Ta).

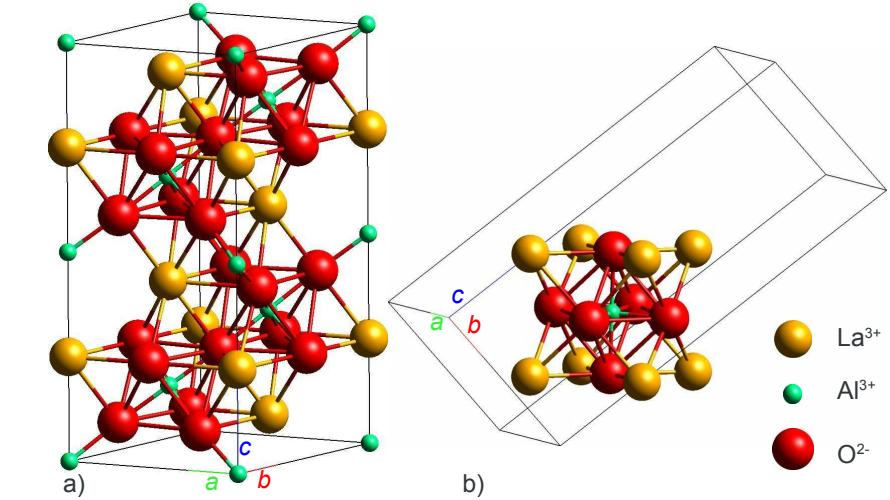

Figure 3.2.: Crystal structure of LAO: rhombohedral unit cell (a) and pseudocubic perovskite representation relative to the wireframe of the unit cell (b). The illustrations were modeled with *CrystalExplorer* [123], using crystallographic data from [144]. For clarity the ionic radii are scaled by a factor of $1/2$.

3.1.4 MgO

The cubic halite crystal structure of MgO with its lattice constant of $a = 4.214\,\text{Å}$ [145] provides the largest tensile in-plane lattice mismatch of all five employed substrates, with respect to LSMO (compare Tab. 3.1). MgO as a substrate material is very common, because of the simple chemistry and structure of the typical ionic crystal [154]. Furthermore, it is the cheapest among the chosen substrates. A drawback, however, is its hygroscopic nature [154] that it shares with the isostructural NaCl (rock salt). As a practical precaution, MgO substrates were always stored in small batches in a dry, continuously pumped desiccator.

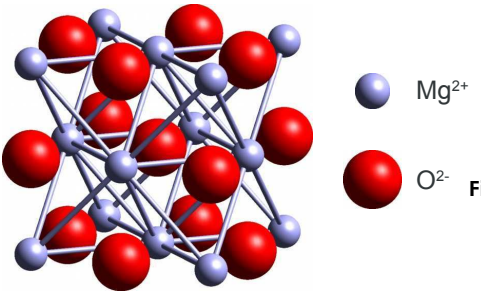

Figure 3.3: Crystal structure of cubic MgO, modeled with *CrystalExplorer* [123], using crystallographic data from [145]. For clarity the ionic radii are scaled by a factor of $1/2$.

3.2 Functional thin film materials

The functional thin film materials used in this work comprise LSMO as the Colossal Magnetoresistance (CMR) manganite and PZT as the gate FE. Details about the suppliers, geometries and compositions of the respective sputter targets can be found in Tab. A.1 on p. 139.

As the correct choice of film deposition parameters is of utmost importance for the sample's characteristics, and because this choice is a result of careful literature studies on the one hand and conclusions from previous findings on the other hand, these experimental conditions will be discussed in detail in Chapters 4 and 5 for LSMO and PZT, respectively.

3.2.1 LSMO

When changing over from bulk to thin films, virtually all the fundamental mechanisms of the CMR manganites introduced in Section 1.6 still hold true. However, regarding the practical implementation of the thin film systems, the chosen deposition method can substantially influence the film characteristics, for example, due to varying interface smoothness, uniformity, crystallinity and (oxygen) stoichiometry. But apart from these experimental aspects, there are also intrinsic alterations of characteristic properties that arise from the thin film geometry and which are typically caused by interface effects like the reduced symmetry or elemental interdiffusion or by substrate-induced biaxial strain. These effects encompass e.g., the variation of transition temperatures, coercive magnetic field (H_c), magnetic anisotropy and transport properties[4].

The effect of substrate-induced in-plane strain is most pronounced when the lattice misfit of substrate and film is small enough to allow for fully commensurate growth of the manganite. Even if there is nominally no misfit with respect to the pseudocubic lattice parameter of the manganite, there still can be a significant impact on the film structure when it grows e.g., on a cubic substrate, since the distorted manganite structure can be forced into a tetragonal or maybe cubic geometry[5]. The imposed changes in crystal symmetry – i.e., the lattice parameters and the space group – are directly altering the tolerance factor (Γ). Or in other words, the reconstruction of the substrate's lattice directly affects Mn–O–Mn bond angles and bond lengths and thus creates orbital overlaps for given Mn^{3+}/Mn^{4+} ratios that are not accessible in bulk solid solutions.

The misfit strain not only depends on the substrate, but also on the lattice parameters for the respective doping level (x) of the manganite. Fig. 3.4(a) illustrates the evolution of lattice parameters in bulk LSMO. The increasing unit cell volume for decreasing x can be explained by the added distortion of the unit cell and the reduced number of covalent bonds.

For the specific doping level of $x = 1/3$, a strain-dependent phase diagram [see Fig. 3.4(b)] has been constructed by Tsui *et al.* [155] on the basis of 25 to 50 nm thin films[6]. For this composition the highest Curie temperatures (T_C) were attained at zero or low tensile strain. Nevertheless, the bulk value of T_C was not reached.

A suppressed Curie temperature was also reported by Sirena *et al.* [157] for strongly textured LSMO on STO and MgO, with an even higher Sr content of 40 %. The suppression was most pronounced for films of thicknesses below 100 nm. At the same time those films exhibited elevated coercivities [158]. Also for optimally doped films of $La_{1-x}Ba_xMnO_3$ (LBMO) on STO

[4] For a thin-film specific topical review on CMR manganites, the reader is referred to [118].

[5] Compare bulk lattice structures of LSMO (Fig. 1.7) and STO or LSAT (Fig. 3.1).

[6] For the definition of bulk strain (ε_b) and Jahn–Teller strain (ε_{JT}), see [155, 156].

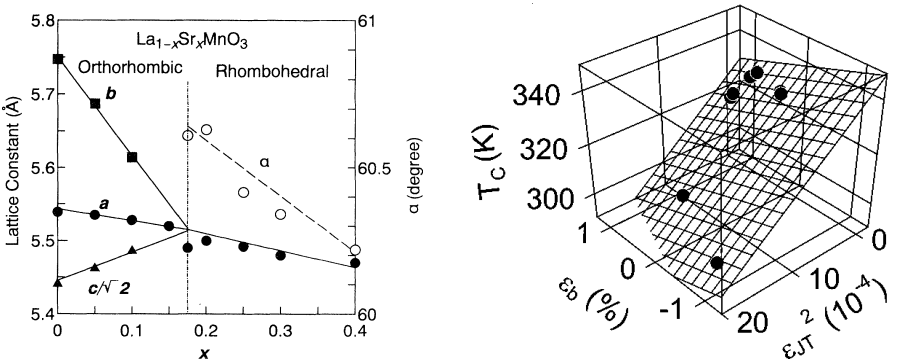

(a) lattice parameters of LSMO **(b)** LSMO strain dependence of T_C

Figure 3.4.: (a): The RT lattice parameters of LSMO as a function of the doping level (x). (*Reprinted with permission from* [111]. ©1995, AMERICAN PHYSICAL SOCIETY). (b): Curie temperatures of 25 nm and 50 nm thick LSMO ($x = 1/3$) epitaxial films as a function of bulk strain (ε_b) and square of Jahn–Teller strain (ε_{JT}). (*Reprinted with permission from* [155]. ©2000, AMERICAN INSTITUTE OF PHYSICS).

(100) this reduction in T_C was observed [159]. However, in the low-doping region opposite effects on T_C were reported by the same group of Kanki *et al.* [159, 160]: For $x \leq 0.2$ a significant increase in the transition temperature and Magnetoresistance (MR) was found for decreasing film thicknesses below ≈100 nm. At 10 % Sr doping, the bulk T_C value was exceeded by the 20 nm thin film on STO by 100 K. In analogy, Razavi and Vigliante *et al.* [161, 162] found an elevated Curie temperature with a metallic low-temperature phase in 10 %-doped LSMO grown on STO (100), for thicknesses below 50 nm. In bulk, this low Sr content creates an insulating phase. In both cases, the interpretation of the enhancement of magnetic and transport properties was based on the fully commensurate growth on the cubic substrate, which provided a low mismatch strain and presumably rectified the Double-Exchange (DE) interaction by reducing the static Jahn-Teller (JT) distortion [159, 161, 162].

The magnetic anisotropy was observed to be affected by the biaxial strain induced by the substrate. For 30 %-doped LSMO, the misfit strain is tensile for STO and compressive for LAO substrates. For the former the easy axis is oriented in-plane [163] and possesses a fourfold symmetry [164]. On LAO the formation of C-type antiferromagnetism was reported [165, 166].

The lattice distortion caused by in-plane strain is not fully elastic, i.e., the unit cell volume of the manganite is not conserved [118]. Instead, the higher the tensile (compressive) strain is, the larger (smaller) is the volume, as observed for LSMO [167] and $La_{1-x}Ca_xMnO_3$ (LCMO) [168].

Also the layer thickness has significant influence on the physical properties of a manganite layer. Obviously, the percolation paths through electronically phase separated films change drastically when changing over from a three-dimensional bulk system to a two-dimensional plane. Thus, especially in the low-doping region, the transport properties are very sensitive to the film thickness (see also Section 1.6).

Another substrate-driven property modification can be traced to the strain relief with increasing layer thickness. The aforementioned effects of the biaxial strain on magnetic and transport properties are caused by initial commensurate growth and generally most pronounced for film thicknesses below 20 to 50 nm, depending on the lattice misfit [169, 170]. Beyond that, strain relaxation causes the lattice to gradually approach bulk properties, which are typically reached at about 100 nm [171]. Of course these numbers are only rough estimates; the relaxation threshold is lower for higher mismatched substrates. If the mismatch is too high, as in the case of MgO (compare Tab. 3.1), the strain relief happens right at the interface and commensurate growth is unavailable [118].

The layer thickness cannot be scaled down arbitrarily. This is due to the fact that interface effects lead to the creation of so-called *dead layers* which are magnetically and/or electrically inactive[7]. The dead layer thicknesses are strongly dependent on the employed substrates and typically range from about 1 to 5 nm [172, 173], but do not necessarily have to be identical for magnetic and electric properties [173, 174]. For LSMO films grown on STO, the dead layer seems to form at the substrate-film interface but not at the surface of the LSMO layer [54]. The origin of the dead layer has not yet been resolved completely. Possible explanations for the apparently suppressed DE coupling include Mn e_g orbital rearrangements driven by the broken translational symmetry [53], charge localization [175] or Sr segregation [176]. In a very recent paper Lepetit *et al.* have discussed theoretical aspects of interface effects in STO/LSMO heterostructures.

For the objective of the present work, i.e., the construction of magnetoelectric (ME) multiferroic (MF) thin film composites based on a CMR manganite, LSMO was chosen due to its outstanding properties. Even for low Sr concentrations, it has a reasonably high tolerance factor and thus comparatively high T_C. The possibility to increase the transition temperature by means of epitaxial strain renders LSMO particularly attractive for studying the low electron hole (h^+) density region, where the coexistence of Superexchange (SE) and DE interactions is most delicate. In this region, the strongest magnetic response to surface charge density modulation is naturally to be expected. Moreover, LSMO has the highest conductivity among the mixed-valence manganites [116] – an important prerequisite for building FE capacitor structures where one electrode consists of the manganite. The lattice expansion of the orthorhombic LSMO in the low-doping region [compare Fig. 3.4(a)] renders the in-plane misfit with respect to STO virtually negligible, which is an ideal starting condition for growing fully commensurate epitaxial thin films.

3.2.2 PZT

Despite the ongoing quest for lead-free electronics [177], $PbZr_yTi_{1-y}O_3$ (PZT) thin films still play a major role in scientific research on memory applications and field-effect devices[8]. It is – besides $BaTiO_3$ (BTO) – one of the most extensively studied FE and piezoelectric materials [178]. With its high switchable polarization and dielectric constant, long retention time with relatively low leakage and extensive tailorability of the ferro- and piezoelectric properties, it is still an unrivaled material of choice for many advanced applications. One of the most promising competitors in terms of polarizability is probably $BiFeO_3$ (BFO). However, not only the existing challenges

[7] A readable summary of the dead layer problem can be found in the introduction of [53].

[8] Unlike in bulk applications, the Pb content in a thin film chip is very low. Assuming a 100 nm thin PZT film, the Pb of a 1 cm^2 chip dissolved in ≈5 l of water would already result in a Pb concentration below the allowed limit of the German Drinking Water Ordinance.

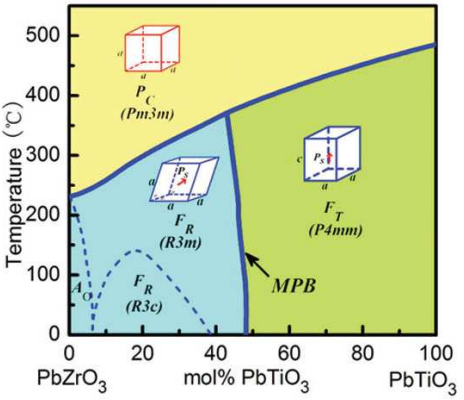

Figure 3.5: Structural phase diagram of PZT. The MPB is located around a Zr/Ti ratio of 52/48. (*Reprinted with permission from* [181]. ©2010, American Physical Society)

regarding leakage, retention and fatigue characteristics [179], but also the co-existence of an antiferromagnetic (AF) ordering in this material render BFO rather unsuitable in this work, as BFO may bring about other magnetic coupling effects (e.g., exchange bias and cross-interface coupling) with the magnetic LSMO layer [70]. Although these are certainly interesting aspects, the focus of the presented studies is the investigation of a purely field-effect driven magnetic modulation.

PZT is a perovskite solid solution of the endmembers $PbZrO_3$ (PZO) and $PbTiO_3$ (PTO) (see phase diagram, Fig. 3.5), which assumes a rhombohedral crystal structure in the Zr-rich and a tetragonal structure in the Ti-rich region. Above the FE Curie temperature the material is in a cubic, thus paraelectric, phase for any composition. At a mixing ratio of PZO/PTO $\approx$ 52/48, the so-called Morphotropic Phase Boundary (MPB), there is a co-existence of the rhombohedral and the tetragonal phases at RT. This region is of particular technological interest for many applications, as it features pronounced piezoelectric coefficients, dielectric permittivity and remanent polarization for (sintered) polycrystalline ceramics [178, 180]. The latter fact is attributed to the large number of easy axes which are available for FE reorientation with six possible domain states for the tetragonal and eight possible states for the rhombohedral phase [180].

Although this high polarizability at the MPB is not expectable for PZT single crystals [180], this composition was chosen as the nominal composition for the sputter targets used in this study (compare Tab. A.1 on p. 139 for details). On the one hand it also enables to grow *polycrystalline* PZT films with high polarizability. On the other hand it may ease *epitaxial* growth on various different substrates, as the rhombohedral and the tetragonal structure are both available for strain relaxation.

Fig. 3.6(a) illustrates the tetragonal crystal structure[9] of PZT at the MPB at RT, which will turn out to be the relevant phase for the present studies (see Chapter 5). The corresponding lattice parameters for the tetragonal phase of the 52/48 composition are listed in Tab. 3.1. The polarization is effected by the relative displacement of the B-site cation against the surrounding oxygen octrahedron along the *c* axis of the unit cell, as shown in Figs. 3.6(b)&(c).

[9] The B-site ion radius represents the one of the larger species (Zr).

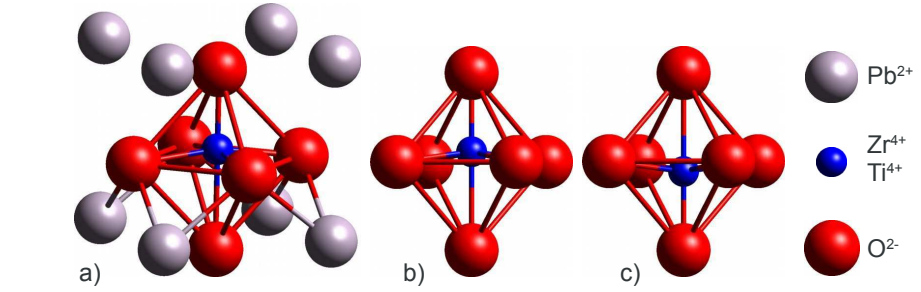

Figure 3.6.: Crystal structure of the perovskite phase of PZT: tetragonal unit cell (a) and the relative displacement of the B-site cation against the oxygen octahedron upon upward (b) and downward (c) polarization along the *c*-axis. The illustrations were modeled with *CrystalExplorer* [123], using crystallographic data for $PbZr_{0.52}Ti_{0.48}O_3$ from [141]. For clarity, the ionic radii are scaled by a factor of $1/2$.

Regardless of the actual deposition method, the challenge in growing high quality PZT thin films lies in the difficulty of reaching good crystallinity while maintaining the desired stoichiometry and crystallographic phase. As in many complex oxides, the oxygen stoichiometry has tremendous influence on the physical properties of PZT. Oxygen deficiency is known to deteriorate all relevant FE properties such as polarizability, leakage [and thus Time-Dependent Dielectric Breakdown (TDDB)], fatigue, imprint and retention. Oxygen vacancies locally alter the potential profile due to dangling bonds in the oxygen octahedra and thus create defect dipoles (see Fig. 3.7). A theoretical discussion of the effects of oxygen deficiency can be found in [182].

Another problem regarding stoichiometry arises from the fact that PZT – like other oxides – requires elevated temperatures in order to promote surface diffusion which is needed for crystal-

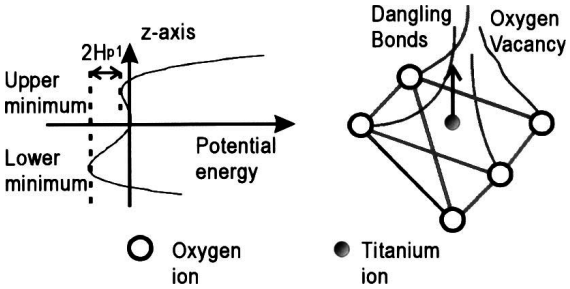

Figure 3.7.: Asymmetry of the potential profile of the B-site ion (left) in the presence of an oxygen vacancy at the top of an oxygen octahedron cage (right). $2\Delta H_{\mathrm{p1}}$ denotes the additional energy required for the B-site ion to be displaced to the upper potential minimum, due to the dangling bonds. (*Reprinted with permission from* [182]. ©2002, American Institute of Physics)

lization. However, the high volatility of PbO conflicts with the PZT crystallization temperature[10]. A common workaround is to deposit PZT thin films at lower temperature (T) and subsequently apply Rapid Thermal Annealing (RTA) in order to crystallize the PZT while suppressing long range diffusion and thus PbO evaporation. However, if epitaxial growth without any annealing step is desired, the substrate needs to be heated during deposition and at the same time excess PbO vapor has to be provided in order to compensate re-evaporation from the surface.

The correct balance of substrate temperature and excess PbO vapor is delicate, since the temperature alters the PbO vapor pressure. At too low T, fluorite $Pb_{2+x}Ti_{2-x}O_{7-y}$ and pyrochlore $Pb_2(Ti,Zr)_2O_7$ and $Pb_2(Ti,Zr)_2O_6$ phases are favored [184, 185]. Additionally, when the PbO vapor pressure cannot be adjusted separately [unlike e.g., in Molecular Beam Epitaxy (MBE)], the excess PbO causes formation of PbO, Pb_3O_4 and PbO_2 phases [184]. At too high deposition temperatures the heavy Pb loss can lead to the formation of a pyrochlore $PbTi_3O_7$ structure [178, 184]. The pyrochlore phases are paraelectric and detrimental to the electrical characteristics of the PZT thin films [185]. Above a critical temperature a self-stabilization of the Pb stoichiometry in PZT can usually be observed, even for large quantities of excess PbO [184]. However, the optimal substrate temperature range depends on the deposition method and the amount of excess PbO vapor; for the sputtering deposition method these ranges will be discussed in Chapter 5.

[10] At 600 °C PbO possesses a vapor pressure of ≈1.1 Pa [183].

3.3 Large-distance magnetron sputtering

3.3.1 Background

There exist many different chemical and physical routes for thin film deposition of complex oxides and most of them have their justification in the trade-off between purity and simplicity, quality and costs, stoichiometric accuracy and processing speed. The best choice depends on the requirements for the thin film – like e.g., area, thickness, crystallinity and various other physical properties – and not least on the material itself. The material-specific discussion for LSMO and PZT will be given in the following chapters, in Section 4.1 and Section 5.1, respectively. In the current section, the Large-Distance Magnetron Sputtering (LDMS) technique shall be discussed.

A general problem in the sputtering deposition [186, 187] of oxide thin films is the bombardment of the substrate and the growing thin film by negatively charged oxygen ions being accelerated in the Direct Current (DC)-bias field between the target and the chamber [154, 188]. This bombardment can drastically decrease crystallinity and often raises the need for a subsequent annealing step [189, 190], which can in turn bring about adverse side-effects like partial film regrowth and increased surface roughness [166], strain relaxation [191, 192], segregation [193] and interdiffusion at the interfaces [194].

As a viable workaround, off-axis sputtering – where the substrate is literally moved out of the fireline – is employed, preferably with facing targets geometry for recycling of target material [155, 195]. This setup, of course, significantly reduces film homogeneity and deposition rate on large wafers and does not allow for rapid sequential deposition of different films or Multilayers (MLs) [154].

Another way to avoid oxygen ion bombardment can be found in the application of a negative DC bias potential to the sample holder, which decelerates the ions [196]. However, when sputtering conductive coatings, short circuiting of the sample holder and the chamber may happen.

In the framework of this thesis the LDMS technique was developed as an alternative to off-axis sputtering. Like the latter, it aims at significantly reducing the oxygen ion bombardment, but in contrast to an off-axis geometry, it allows for sequential and simultaneous sputtering from many different targets and a high growth rate deposition of metals in the same setup. While technical details of the employed LDMS system will be addressed in the next section (Section 3.3.2), its physical principles will be discussed below.

The fundamental concept of LDMS is the unusually large target-substrate separation (d_{sep})[11] of nearly 300 mm in combination with an elevated working pressure (p_{work}). This way, the Mean Free Path (MFP) of the fast oxygen ions can be reduced to well below d_{sep} and thus the damaging of the crystal structure is effectively prevented. Additionally, the large distance ensures uniform vapor diffusion and thus enables a more homogeneous film deposition even on larger substrates.

As the MFP of oxygen is higher than that of the metal species, good thermalization of all species is achieved when arriving at the substrate surface, which is generally desirable for good control over film composition [178]. The thermalization process is comprehensively discussed in [197–200] and in a very recent theoretical study by Depla *et al.* [201].

[11] Typical d_{sep} values normally range in between 30 to 100 mm.

Apart from the MFP effect, another positive side-effect of the large target-substrate separation is that the electric field in which the oxygen ions are accelerated is altered significantly. In a classic setup with the grounded sample holder facing the DC-biased target (cathode) in a short distance, the electric field between the target and the substrate is more homogeneous and stronger than in a setup where the sample holder occupies a much smaller solid angle of the approximately radially distributed electric field between the target and the chamber.

The minimal working pressure that is required for sufficient thermalization of the high energetic oxygen is of course a function of the acceleration voltage, i.e., the DC bias that builds up on the target and this in turn depends on the sputtering power, the O_2 content in the sputtering gas and p_{work} itself: typically, in a power-regulated mode, the DC-bias decreases when p_{work} or the O_2 partial pressure (p_{O2}) are increased, as the conductivity of the plasma rises.

There are, however, also a few drawbacks of the LDMS technique which should be mentioned. The large distance in combination with the elevated pressure reduce the deposition rate significantly, in a similar way to off-axis sputtering. Furthermore, the challenge of stoichiometric accuracy due to the elemental dependence of the sputtering yield at the target [70, 154] is augmented with a secondary aspect: Also the flux towards the substrate is subject to elemental dependence, as cross-sections and scattering angles differ for the various sputtered species [201]. The Monte-Carlo simulation shown in Fig. 3.8 gives a clear idea of this effect for two different working pressures, albeit the simulation conditions differ from the present setup, where d_{sep} is nearly three times larger and the sputtering gas does not contain pure Ar but is an Ar/O_2 mixture.

Finally, a small practical disadvantage of the LDMS setup arises from the rarity of such systems. Hence, sputtering recipes found in the literature cannot be followed directly, but only serve as a very rough starting point for parameter optimization.

To the best of the author's knowledge the combination of a large sputtering distance d_{sep} and an increased pressure for thermalization of fast oxygen ions has not been reported so far. Yet, at pressures as low as necessary to prevent almost all scattering, the large distance was found to be suitable for large-area sputtering of metallic thin films with enhanced step coverage [202, 203]. The benefit of this so-called long-throw sputtering technique is the mostly collimated atom flux and a nearly unchanged deposition rate, when compared to standard distances.

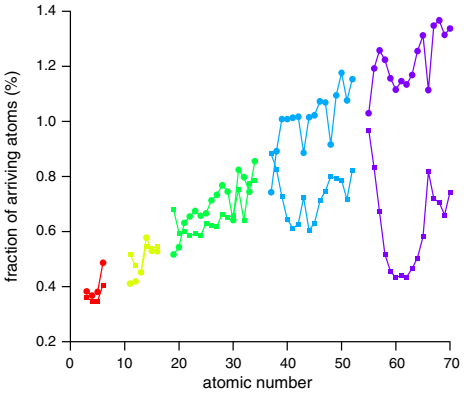

Figure 3.8: Monte-Carlo modeled elemental dependence of the fraction of sputtered atoms arriving at the substrate, for a 100 mm × 100 mm substrate, a target diameter of 50.8 mm and $d_{\mathrm{sep}} = 100$ mm. Square markers and round markers represent an Ar pressure of 0.4 Pa and 1.0 Pa, respectively. (*Reprinted with permission from* [201]. ©2012, ELSEVIER)

Thus, the LDMS system, which will be described in detail in the following section, can be beneficial for both oxide deposition at elevated pressures and metal thin film coating at very low p_{work}, while the large value of d_{sep} guarantees excellent uniform thickness distribution even across large wafers [204].

3.3.2 Details of the sputtering system

The LDMS system was custom-made by CREATEC FISCHER & CO. GMBH, delivered and installed at the end of 2008. For this reason several testing experiments were performed prior to using it as a production system; these results will also be presented here and in the Appendix (Section A.1.1).

The fairly large sputtering chamber is equipped with eight 76.2 mm (3") magnetrons[12] which are arranged in an octagonal geometry, where the substrate is located in the center in an on-axis geometry with an angle of incidence (with respect to the surface normal of the substrate) of 37.5° and a target-substrate separation of $d_{sep} = 285$ mm.

Fig. 3.9(a) depicts the cross-section view of the technical drawing of the chamber. The top view photo (b), taken through the port of the heated manipulator, shows the target shutters covering target, the liquid-N_2 coolable manipulator which can optionally be moved to the center and the

[12] Initially, the system had comprised of five 76.2 mm (3") and three 104.6 mm (4") magnetrons, as the top view image in Fig. 3.9 shows. However, this was changed some time later for higher flexibility in target-magnetron assignment.

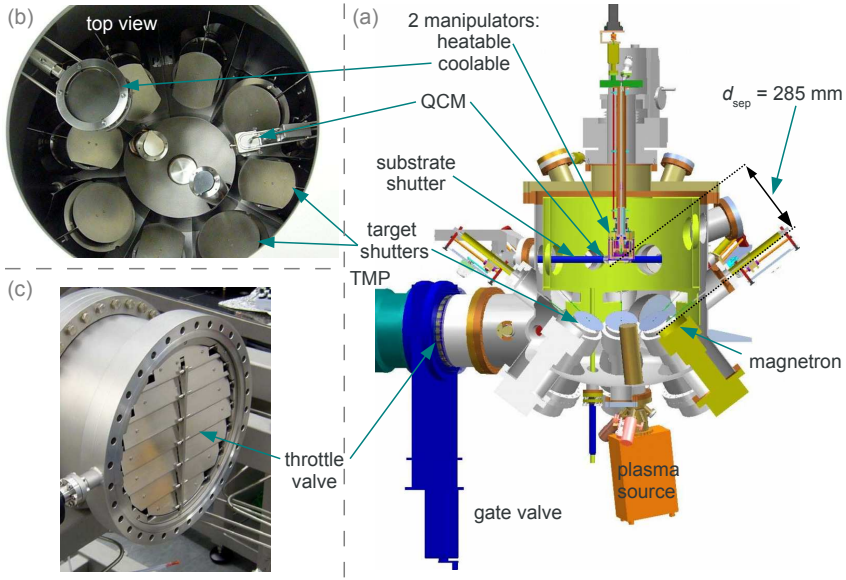

Figure 3.9.: Schematic cross-section view of the sputtering chamber and photographs of the top view through the manipulator port and of the throttle valve. (*Reprinted with permission.* ©2008, CREATEC FISCHER & CO. GMBH)

Quartz Crystal Microbalance (QCM) thickness monitor which is mounted on the same height as the sample. Image (c) provides a view onto the throttle valve which is mounted directly in front of the Turbo Molecular Pump (TMP) and which is used in feedback with a capacitive MKS INSTRUMENTS *Baratron* vacuum gauge for regulation of p_{work} during sputtering.

The chamber also features a cooling shroud which may be used for further reduction of the background pressure. However, this was never considered necessary, as the base pressure could be sufficiently reduced within a couple of days after a maintenance vent by baking the system using the heatable manipulator[13] and occasionally sputtering of some getter material like e.g., titanium[14]. The cleanliness of the chamber was tested with a Quadrupole Mass Spectrometry (QMS) which was temporarily installed during characterization of the system.

The heatable manipulator is equipped with four 24 V, 250 W halogen lamps[15], switched in series, which allow for heating of the samples of up to 850 °C. A type-K thermocouple mounted next to the lamps can be used for automatically controlled temperature ramping[16]. To ensure a uniform distribution of heat and deposited material, the manipulator was rotated at a speed of ≈7 rpm.

Depending on the type of sample holder, a single 50.8 mm wafer or alternatively up to four 10 mm × 10 mm (or smaller) substrates can be mounted and coated simultaneously. Stainless steel (V2A, mat. no. 1.4301) proved to be a well suitable sample holder material for all investigated materials and managed to resist even high temperatures and high p_{O2} without any problems. Care was taken to expose the same sample holders only to a single material or material combination in order to prevent any intermixing with evaporating material. The same applied to the steel masks which were employed for tightly clamping the substrates at the corners, ensuring good thermal contact to the 500 μm thin steel backing plate which acted as an absorber for the heat from the halogen bulbs.

The eight planar magnetrons (THIN FILM CONSULTING *ION'X-3"UHV*) are all equipped with a balanced magnet assembly which is also strong enough to be suitable for ferromagnetic (FM) targets. The use of balanced magnetrons is beneficial in the current setup since the ion flux is smaller as the plasma is more confined and the material flow is more directed [205]. Three DC and two Radio Frequency (RF) power supplies are available to be attached at any of the eight magnetrons, allowing for the growth of sequentially or co-sputtered thin film systems.

Prior to each deposition, the targets were sputter-cleaned for more than 30 min (depending on the last used sources) with target and/or substrate shutter closed, in order to remove adsorbates and thus effectively reduce cross-deposition effects from neighboring magnetrons.

The film thickness was monitored live by means of the QCM. As the tooling factor in a sputtering system depends on p_{work} [204], tooling samples of ideally ≈10 to 30 nm in thickness were produced and evaluated using X-ray Reflectometry (XRR) for each set of p_{work} and p_{O2} of interest.

The pressure regulation is an interplay of the Ar and O_2 flows, the throttle valve [see Fig. 3.9(c)] and the TMP. The latter can be throttled in rotation speed in order to reach higher p_{work} with reduced gas flows and thus reduced pump load. A diagram depicting the accessible pressure ranges can be found in the Appendix (Fig. A.2 on p. 138). For metals a very low working pressure

[13] A heating current of 6.5 A (at 45 to 50 V) was found to be a reasonable value for a soft chamber bakeout.

[14] Also other materials like Ta, Al or Mg helped improve the base pressure.

[15] The original OSRAM *64655* lamps were later on replaced by model *64657* which feature an increased nominal lifetime by a factor of five.

[16] The substrate temperature calibration and a photo of the heating head can be found in Fig. A.1 on p. 137.

of 0.05 Pa was found to usually deliver highest deposition rates and remarkably smooth films[17]. For oxides this optimal pressure was typically higher (≈3 Pa) and the resultant growth rate much lower because of the necessity to add O_2 to the sputtering gas. However, a maximized deposition rate for a given oxide does not automatically guarantee best physical properties, as will be shown for LSMO in Chapter 4, where the best films were grown at much higher pressures.

3.4 Structural analysis

As the structure determines the physical properties of both the magnetic LSMO and the FE PZT thin films, great care was taken to comprehensively investigate the influence of various deposition parameters on the structural quality of the films. X-ray Diffraction (XRD) delivers information of the whole sample exposed to the X-ray beam, while cross-section Transmission Electron Microscopy (TEM) provides an insight into the local microstructure. Both techniques were applied complementarily.

3.4.1 X-ray diffraction

XRD [206–208] studies were carried out on every produced sample, using a BRUKER *D8 Discover* diffractometer, equipped with a four-circle goniometer (Euler cradle) and employing copper K_α radiation.

For High-Resolution X-ray Diffraction (HRXRD), XRR and Reciprocal Space Map (RSM) measurements in θ-2θ geometry, the setup of the primary beam consisted of a Göbel mirror for beam parallelization, a four-step automatic absorber and a four-bounce germanium monochromator. The secondary beam was shaped by an anti-scattering slit (0.5°) and the *Pathfinder* optics before hitting the NaI:Tl scintillation counter detector. For Grazing-Incidence X-ray Diffraction (GIXRD)[18] the primary beam was shaped by the Göbel mirror, the secondary beam was collimated by a Soller slit arrangement, allowing a divergence of 0.23°.

As the original metallic vacuum chuck caused significant spurious reflections in Bragg-Brentano geometry for small samples, it was replaced by a custom chuck made of Poly(Methyl MethAcrylate) (PMMA), which only contributed a broad amorphous background.

Virtually all thin film samples were studied by XRR, as the determined properties – thickness, density and interface roughness – provide valuable information of the sample quality and the reproducibility of a deposition recipe at a glance. The gathered thickness data was also used for tooling of the QCM of the sputtering machine.

In order to investigate the structural quality along the growth direction, HRXRD scans in θ-2θ geometry were performed on all thin films grown on single-crystalline substrates. A typical 2θ scan range of 19 to 110°, a step width of $\Delta(2\theta) = 0.05°$[19] and an acquisition time of ≈30 s per step were found to be appropriate for most measurements. For select samples, RSM

[17] E.g., Cu deposition at moderate 200 W (≈4.4 W/cm^2) DC power resulted in a growth rate of 1.5 Å/s and a roughness of 2 Å for a 26 nm thick film grown on Si/SiO_2.

[18] GIXRD was only employed for a few polycrystalline thin films grown on Si substrates with an amorphous oxide layer.

[19] In order to save measurement time, some LSMO samples were only scanned in the angular regions around their (00l) reflections up to the 4th order. However, PZT-containing samples needed to be studied along the full range to be able to detect spurious phases in between the main reflections.

measurements were carried out to examine the structural quality, layer tilt, lattice relaxation and the in-plane lattice components.

Sample alignment was generally performed on the substrates' (001) or (002) peaks. In case of RSMs the fine adjustment was made on the substrates' reflections of the respective orientations.

Being a multi-user tool, the employed device was subject to frequent changes of the diffraction setup. For this reason it was decided not to determine the instrumental broadening. Thus, the measured Full Width at Half Maximum (FWHM) of the crystallographic reflections represents the upper limit; the real FWHM will always be lower.

3.4.2 Transmission electron microscopy

Additionally to the XRD measurements, representative samples were further investigated using TEM. Cross-sections of the samples were prepared by either standard dimpling and Precision Ion Polishing System (PIPS) techniques or cutting of thin lamellae using Focused Ion Beam (FIB): both preparation techniques delivered samples of comparable quality.

The TEM, Scanning Transmission Electron Microscopy (STEM) and Selected-Area Electron Diffraction (SAED) studies were carried out in a FEI *Titan 80-300* electron microscope operated at 300 kV, which also allowed for Energy-Dispersive X-ray Spectroscopy (EDX) and Electron Energy Loss Spectroscopy (EELS).

3.5 Elemental analysis

Another very important aspect for the optimization of the thin film deposition parameters is the elemental analysis [209]. This was mainly performed during TEM investigation by means of the abovementioned EDX and EELS, as this way also the elemental distribution across the film interfaces could be resolved. The both methods are complementary techniques, as the former is more sensitive to heavier elements, while the latter is more suitable for lower atomic numbers.

Complementarily, Rutherford Backscattering Spectroscopy (RBS) [210] was performed, employing 2 MeV $^4He^+$ ions, to determine the cation ratios of the oxide thin films.

In the present RBS setup, the parallel beam of α particles, accelerated by a van de Graaff accelerator, has a cross-section of 1 mm^2 and hits the sample surface perpendicularly. The backscattered helium ions travel partially through the sample and subsequently through UHV at a base pressure of $\approx 10^{-4}$ Pa and are analyzed under a backscattering angle of 152°, where the detector is located. The divergence of the ion beam is less than 0.02° and the ion current typically amounts to ≈15 nA. The solid angle of the detector is in the order of a few 10^{-3} sr, and the energy resolution of the system is ≈25 keV.

Compared to the TEM studies, RBS is a macroscopic technique, as it integrates the elemental distribution over the irradiated area of ≈1 mm^2 and over the full film thickness. For the better accuracy, only samples of more than ≈30 nm in thickness were investigated.

The RBS spectra were fitted with the *SIMNRA* analysis software [211] and quantitatively evaluated for samples on MgO substrates, since the Mg edge does not overlap with the signal of any species of the thin film.

3.6 Surface analysis

On select samples, Atomic Force Microscopy (AFM) or Scanning Tunneling Microscopy (STM) was performed, in order to verify the information on surface roughness derived from XRR data. The STM studies were carried out *in situ* at RT in an OMICRON *VT STM* system which is attached to the same UHV-cluster as the the sputter deposition device. AFM was measured *ex situ* at RT, using a VEECO / DIGITAL INSTRUMENTS *MultiMode AFM* in tapping mode, using non-contact Si cantilevers.

3.7 Ferroelectric properties measurement

3.7.1 Background

The quality of a FE thin film – i.e., its suitability for the respective intended use – can be assessed by a series of frequency and voltage dependent tests like FE hysteresis loops, Positive-Up Negative-Down (PUND) tests, fatigue and imprint cycling and retention measurements. The proper interpretation of the acquired data, however, requires profound understanding of the FE material itself and correct identification of artifacts. Fortunately, perhaps for this reason, appropriate literature about FE materials, measurement methods, data interpretation and sources and consequences of artifacts is abundant [180, 184, 186, 212–214].

Artifacts are often caused by the simple fact that the FE polarization (P) state – unlike e.g., the magnetic moment of a FM material – cannot be read out non-destructively, but requires a read pulse which in turn determines the state after read-out[20]. In other words, the charge (Q) on a FE capacitor cannot be measured directly but requires integration of its time derivative, the switching current. However, this brings about two major implications for FE measurements: First, the constant of integration is undefined and so is the net value of polarization: as only relative changes can be measured, FE hystereses are usually centered with respect to the P axis by convention. Second, the measured switching current contains, among other (dynamic) components, the parasitic signals of the dielectric constant (linear signal), non-persistent paraelectric polarization and the leakage current (lens-shaped signal). While the former contributes to the real charge on the sample, the latter leads to an overestimation of P, as these charges are not accumulated but lost. In cases where the real FE polarization is small, the combination of the linear signal of the dielectric constant and the lens-shaped signal of the leakage can result in loops of hysteretic appearance [213].

Timing is of significant importance for dynamic hysteresis measurements. The longer the cycle time (the lower the frequency), the more pronounced is the contribution of the leakage current[21]. On the other hand, if the cycle time is too short, the FE switching may become incomplete. This can be caused by a high serial resistance (R) in the RC-circuit and/or a high capacitance (C) of the FE capacitor. Furthermore, intrinsic effects in the FE, like e.g., domain pinning [216, 217], can limit the switching speed. Not only P is affected by the choice of the cycle time, but also the coercive electric field (E_c) is, which is thus generally not well-defined [56]. A detailed study of

[20] It is worth mentioning that this is one of the biggest challenges for FE-Random-Access Memory (RAM), since, as a consequence, each read-out causes unwanted fatigue cycling.

[21] The reader is also referred to Scott's snappy comment on leakage-dominated artifacts, titled *Ferroelectrics go bananas* [215].

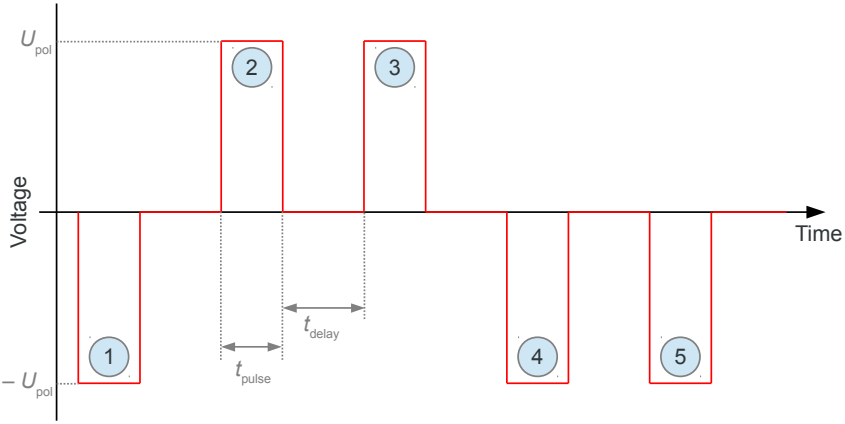

Figure 3.10.: Schematic pulse train for PUND tests, used for determination of switched polarization and parasitic effects. The current towards and from the FE capacitor is measured for all pulses but the 1st (preset) pulse and for the delays thereafter.

the FE switching time and its dependence on the capacitor area and the instrumental limitations can be found in [218].

An established method for distinguishing the remanent FE polarization (P_r) from parasitic contributions is the so-called PUND test [219, 220]. In the most common case, a PUND test consists of a pulse train of five square or trapezoid voltage pulses of same amplitude and duration (t_{pulse}), the same delay time (t_{delay}) between the pulses and a polarity sequence of 1. negative, 2. positive, 3. positive, 4. negative, 5. negative (see Fig. 3.10).

The series can be understood as logically divided into two parts, which overlap in the 3rd pulse (with the second part denoted in parentheses): The 1st (3rd) pulse is a write or preset pulse, which sets a downward (upward) remanent state. The 2nd (4th) pulse, the *switching* pulse, switches the FE into the upward (downward) state and thus contains the real switching current but also all parasitic components. As the FE is now already in upward (downward) remanence, the 3rd (5th) pulse, the *non-switching* pulse, only contains the parasitic currents and no switching current. By subtracting the parasitic currents of the 3rd and the 5th pulse from their preceding pulses, the modulation of the remanent charge, and thus P_r, can be calculated. Furthermore, the measurement of the discharging current in the delay intervals allows for estimation of non-persistent polarization. By varying poling voltage (U_{pol}) and pulse duration, the FE switching speed and E_c can be determined as functions of the former parameters; adjusting the delay time after the write pulse(s) yields information about the retention time.

In cases where the switching dynamics is of interest, e.g., in systems which contain two FE components with distinct coercivities, a so-called remanent hysteresis can be measured [221]. The remanent hysteresis test is a special case of a PUND test, where all voltage pulses are triangular[22]. In other words, the 2nd and 3rd pulse are two consecutive positive half FE hysteresis loops, with the former starting from negative remanence and the latter starting from positive

[22] The 1st write pulse is not necessarily triangular.

remanence; for the 4th and 5th pulse this applies analogously with opposite sign. Subtraction of the consecutive switching (2nd & 4th) and non-switching (3rd & 5th) half loops and combination of the vertically centered positive and negative half loops allows for constructing a dynamic hysteresis loop which contains the remanent FE components only. By jointly plotting a remanent hysteresis with the respective standard bipolar hysteresis loop measured with the same cycle time[23], the contribution of spurious effects to the standard FE hysteresis can be determined and visualized.

However, for all PUND tests, including remanent hysteresis measurements, one should be aware of the limits of validity of the conclusions and sources of possible artifacts. The fundamental assumption of a PUND test is that the parasitic currents are reproducible and not affected by the polarization or the switching process. This may not always be the case, especially when the switching is slow, since the effective electric fields inside the FE can differ for the switching and non-switching pulses. Furthermore, the subtraction of switching and non-switching pulses is only meaningful as long as the non-switching pulse only contains parasitic signals. If the pulse times are too small, saturation is not reached in the switching pulse[24] and the switching process continues in the non-switching pulse, leading to an overestimation of the parasitic currents. Time-resolved current measurements on a long voltage pulse help determine the time where the charging currents die down and the constant leakage is dominating. However, too long pulse or cycle times bear the inherent risk of inducing fatal TDDB [222, 223].

The device area plays an important role for the characteristics of a FE capacitor. First of all, the exact determination of the Top Electrode (TE) area is obviously of great importance for the correct normalization of the FE polarization (P). Especially when the TEs are deposited through shadow masks by sputtering or Pulsed Laser Deposition (PLD), depending on the deposition parameters – such as p_{work}, d_{sep} and the lateral dimensions of the masks – the actual resulting electrode size can be quite different from the nominal one, where the error is typically larger for smaller structure sizes. Secondly, the TE area has a huge impact on the leakage properties of a FE device. For a rough estimation of the relationship between device area and device yield, we assume that a FE device with an electrode area A_1 has a probability for a fatal defect of p_1, or in other words a device yield of $q_1 = 1 - p_1$. If we furthermore assume a binomial distribution of defects, the probability for incorporating $i = 0$ fatal defects into an n times larger device $A_n = n \cdot A_1$ is

$$q_n(i) = \frac{n!}{i! \cdot (n-i)!} \cdot p^i \cdot (1-p)^{n-i} \overset{i=0}{=} (1-p_1)^n = q_1^n. \tag{3.1}$$

This exponential relationship of the device yield is one of the main reasons why smaller FE device areas are usually favored. However, for the investigation of the ME coupling, comparatively large device areas will be needed. The practical implications of this prerequisite will be discussed in Chapter 5, Section 5.3.2.

[23] This can also be constructed from the 2nd and 4th pulses.

[24] Saturation may even not be reached in the first write pulse, depending on the previous polarization state.

3.7.2 Experimental details

In the present study, the FE properties of the PZT thin films were characterized with a RADIANT TECHNOLOGIES *RT66B* FE tester[25]. Although the same measurements could in principle be performed with a standard Source Meter Unit (SMU), using a dedicated FE tester has the huge advantage that virtually all typical testing procedures – comprising voltage pulse train, current or charge readout, analysis, data extraction and plotting – are readily defined. The possibility to compile comprehensive sequences along with iterative adjustment of test variables allows for quick and reproducible characterization of supposedly similar FE capacitors.

For *ex situ* measurements, the samples were contacted using a SÜSS MICROTEC probe station equipped with tungsten probes. The shared Bottom Electrode (BE) was connected to the drive output of the tester – as recommended by RADIAN – in order to reduce noise pickup.

The TE arrays were deposited in a DC sputter coater through custom-made laser-cut shadow masks. Gold and platinum were tested as TE materials, but no significant difference in FE properties was found, although the apparent differences are extensively and critically discussed in literature [178, 213, 224]. For *in situ* ME measurements, the diamagnetic Au was preferred over the paramagnetic Pt as TE material: details on the device preparation will be presented in Chapter 6 (Section 6.2). Initially, arrays of many small circular electrodes of four different sizes (160 to 480 μm in diameter) were employed, in order to reduce susceptibility to possible pinholes and to investigate the size-dependent leakage behavior. Later, for the ME measurements, 1 mm^2 large square contact pads were used. To assure reliable polarization values, accurate determination of the TE area was done with special care. To determine the actual TE areas, the samples were investigated with an optical microscope and the areas were calculated employing the *ImageJ* [225] and *Gwyddion* [226] image processing software.

3.8 Magnetic characterization

3.8.1 Background

SQUID magnetometry – based on the 50 years old, Nobel price awarded invention of the Josephson junction [227] – is nowadays certainly the most established technique to study magnetic material properties at variable T with highest accuracy [228, 229]. Due to the ability to detect very low magnetic moments, it is particularly useful for the investigation of ultra-thin magnetic films.

Over the years, different SQUID variants have been developed, such as the sensitive DC-SQUID and the less complex Alternating Current (AC)- and RF-SQUIDs [228]. A significant leap in performance and sensitivity is accomplished by the Reciprocating Sample Option (RSO) [229, 230], which is illustrated in Fig. 3.11. In this technique, a small sinusoidal displacement of the sample inside the Magnetic Properties Measurement System (MPMS) second order gradiometer, performed either at the position of maximum slope of the SQUID response or over a larger amplitude, results in an oscillating AC signal detected by the SQUID sensor. By using smoothly operating sample transport mechanics, low frequency noise can effectively be suppressed by repetitive cycling and subsequent averaging of the raw data.

[25] The accuracy of the FE tester was confirmed by testing a few samples using a competitive product (AIXACCT *TF 1000*).

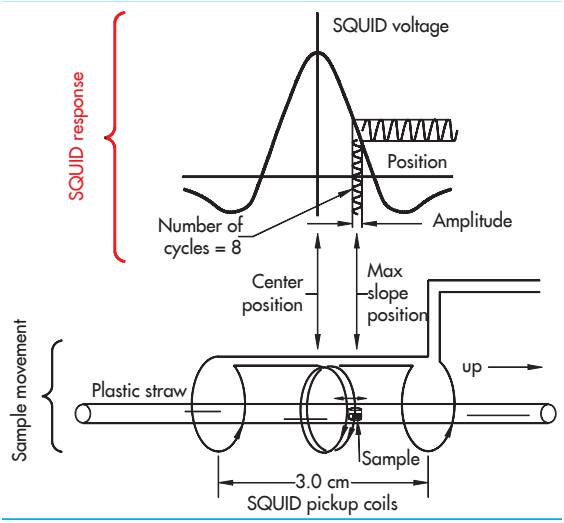

Figure 3.11: Illustration of the SQUID RSO measurement principle. (*Reprinted with permission from* [230]. ©2005, QUANTUM DESIGN INC.)

The magnetic moment determined by SQUID measurements is a superposition of the magnetic moments of all components of a sample, including the substrate and sample fixture, as long as they do not homogeneously extend along the whole longitudinal scan range. While dia- and paramagnetic moments can be subtracted from hysteresis measurements comparatively easily, provided the magnetic field range is chosen sufficiently large, care has to be taken not to introduce some other spurious FM moments.

Due to the high sensitivity and especially when very small magnetic moments are to be measured, the SQUID magnetometry is prone to a number of artifacts and pitfalls, that one should be aware of. A comprehensive discussion, including size, geometry and orientation effects of the sample, but also intrinsic effects of the MPMS itself, as well as sample handling and mounting advice, can be found in [231, 232].

Another source of artifacts, which is not covered in the literature, appears in electrical measurements, e.g., ME measurements, performed inside the MPMS. Thus, the effect of sensing the magnetic field of a small (leakage) current will be roughly estimated here:

For simplicity, we assume that the sample wiring features a single loop with an enclosed area of 1 mm, in projection along the magnetic field direction. With the magnetic moment being the product of the area of the loop and the current flowing through it, and a SQUID sensitivity of $1 \cdot 10^{-8}$ emu $= 1 \cdot 10^{-11}\,\mathrm{A\,m^2}$, a current of only $10\,\mu$A is sufficient to be distinctly visible in a SQUID measurement. The best way to avoid this severe pitfall is, of course, to ensure that no current is flowing during data acquisition, whenever possible (see Chapter 6).

3.8.2 Measurement setup

All magnetic characterization was carried out using a QUANTUM DESIGN *MPMS XL5* SQUID magnetometer, equipped with a *M130* RSO measurement head for highest sensitivity. The system

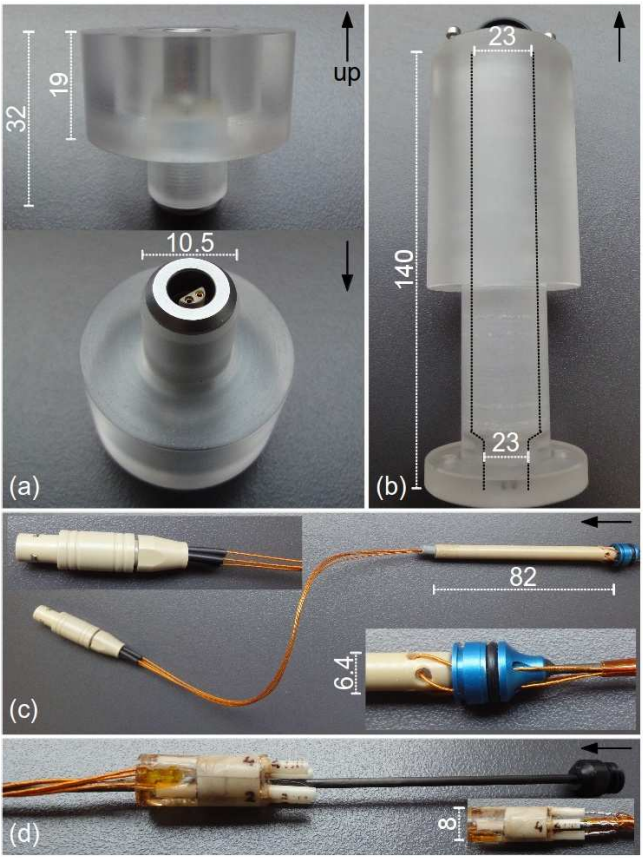

Figure 3.12.: Modifications of the SQUID system for electrical connections to the sample, consisting of an PMMA vacuum plug with high vacuum compatible 4-pin LEMO connector/feedthrough (a), PMMA vertical extension of the sample space cylinder with the inner diameters as depicted by the dotted black lines (b), wiring arrangement at the sample rod, including PEEK-made LEMO plug and rod extension (c) and an epoxy-cast cable coupler at the lower end of the sample rod where the sample straw is to be installed (d). The black arrows in the images denote the upward orientation with respect to the installation position. The insets in (c) show close-up images of the important parts; the inset in (d) illustrates the cable connection from the sample to the cable coupler. All measures in mm.

provides 16 measurement ranges from $1 \cdot 10^{-5}$ to 5 emu with a sensitivity of $1 \cdot 10^{-8}$ emu in the field range of 0 to 2500 Oe [230].

Apart from standard magnetic hysteresis measurements and Field Cooling–Zero-Field Cooling (ZFC) (FC-ZFC) scans, also the ME characterization was done in the same MPMS. However, as the MPMS normally does not provide any standard solution for contacting the sample, the system needed to be modified to that effect.

Fig. 3.12 summarizes the main parts of the modification. The standard vacuum plug was replaced by a custom PMMA plug housing a vacuum-tight 4-pin LEMO *0S-series* fixed coupler[26] as electrical feed-through (a). The sample space is vertically extended by a PMMA tube, which is mounted between the original socket of the vacuum plug and the RSO head (b). This extension and the rod extension shown in (c) are needed to ensure that the four flexible *Kapton*-coated Cu wires[27] are freely movable and do not hamper the RSO stroke. The inner LEMO plug is made of Polyether Ether Ketone (PEEK)[28] (c), in order to reduce weight load, and thus the risk of breaking the carbon sample rod during handling. The holes in the sample rod plug [inset in (c)] and in the radial centering discs distributed along the rod allow for an easy placement of the wires along the rod. At the lower end of the sample rod, the wires terminate in a PEEK- and ceramic-insulated cable coupler, cast in epoxy, which provides sockets for silver wires of 1 mm in diameter. *Teflon* tape and *Kapton* tape were employed to attach any protruding cables to the sample rod.

All employed materials, such as PEEK, *Kapton*, *Teflon*, and various epoxies were tested for compatibility with low-T and vacuum conditions.

The design of the contacting setup for the ME devices requires some deeper considerations and will thus be comprehensively described later, in Chapter 6 (Section 6.2).

3.9 Transport properties measurements

The T-dependent transport properties measurements were performed in the same MPMS like the magnetic measurements, as the cryostat of this system provides a better liquid helium efficiency than the one of the also available Physical Properties Measurement System (PPMS). The temperature dependence was investigated in order to compare the magnetic Curie temperature (T_C) with the metal-insulator transition temperature (T_{MI}). No magnetic field was applied during these measurements, as the custom-made measurement cell (see Fig. 3.13) did not allow for in-plane orientation. Furthermore, magnetoresistance studies of LSMO and other manganites are abundant, e.g., [111, 112, 172, 176, 233–235], to name only a few.

The measurement cell consists of a threaded brass bolt screwed into the center of a PEEK cylinder, which also houses four smaller threaded brass pins arranged in a square layout. On the back side, *Kapton*-coated Cu wires are soldered to the four pins; on the front side the four pins are coated with Pt to facilitate Al wire bonding.

The samples were cut into rectangular or square pieces with a wire saw, and directly contacted with the Al bonding wires which turned out to stick firmly on the LSMO. The temperature-dependent sheet resistance was measured with a KEITHLEY SMU using the van-der-Pauw method [236] with a constant current set to 1 μA.

[26] LEMO product number SWH.0S.304.CLLSV.

[27] A wire length of 190 mm, from extension rod to LEMO plug, was found to be sufficient to allow for full sample motion.

[28] LEMO product number FFA.0S.304.GLAC27.

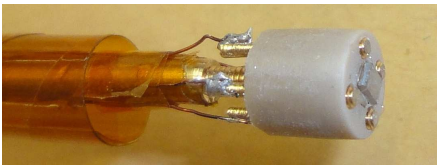

(a) side view

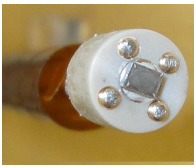

(b) front view

Figure 3.13.: Side and front view of the custom-made 4-point transport measurement setup to be mounted in the cryostat of the MPMS. The outer diameter of the PEEK cylinder is 8 mm. The sample attached in the center is contacted by Al wire bonding.

4 Large-distance magnetron sputtering of epitaxial LSMO thin films

Selected parts of this chapter are also published in [237] within the framework of this thesis. The respective paragraphs – with minor conformations included – are indicated by a vertical gray bar at the inner page margin[1].

The first prerequisite to compose a magnetoelectric (ME) multiferroic (MF) thin film composite with $La_{1-x}Sr_xMnO_3$ (LSMO) as ferromagnetic (FM) material is the ability to deposit thin layers of this manganite with good FM properties. As the latter are intimately connected to the crystal structure, the best results are to be expected for films grown epitaxially on suitable substrates. This chapter focuses on the influence of deposition parameters on the growth of LSMO (ultra-) thin films, aiming for optimization of their properties with respect to high crystallinity, smooth interfaces and a sharp magnetic transition accompanied by a high Curie temperature (T_C). Furthermore, the results of these studies are employed to explore the opportunities awaiting in the uncharted field of oxide Large-Distance Magnetron Sputtering (LDMS).

4.1 Background

In the last five years, there has been a growing interest in thin and ultra-thin [54, 174, 238] epitaxial films of LSMO with great emphasis on bilayer heterostructures [54, 55, 239–241] and Multilayers (MLs) [242–244]. Owing to its unique properties [193] – being a strongly correlated half-metal ferromagnet with a Curie temperature around Room Temperature (RT) – LSMO was demonstrated to be a good candidate for multiferroic heterostructures when combined with ferroelectric (FE) substrates [245] or FE thin films [54, 243, 246–250].

An essential prerequisite for the reliability of such ML systems is the attainment of high quality interfaces since the investigated effects, be it charge injection or strain effects, are interfacial phenomena [54, 245]. Therefore, the capability of the chosen deposition technique to grow the thin films consecutively in a way that achieves the cleanest film interfaces is of great importance. A survey of the available Physical Vapor Deposition (PVD) methods shows that Pulsed Laser Deposition (PLD) has earned increasing popularity for oxide deposition as it generally offers good stability of the target stoichiometry[2] and high deposition rates. However, it requires costly laser equipment, can result in inhomogeneous films due to ejection of large particles from the target [70, 116] and is not yet suitable for large-scale production [70, 154]. Reactive Molecular Beam Epitaxy (MBE) allows for the growth of extremely pure and defect free films with an excellent control of stoichiometry and crystallinity, but is limited with respect to large-scale applications and high growth rates [70]. On the other hand, magnetron sputtering is easily scalable [70, 154] and generally allows for high deposition rates, but the elemental dependence of the sputtering yields can be challenging [70, 154].

[1] *Reprinted with permission from* [237]. ©2012, Elsevier.

[2] Nevertheless, also off-stoichiometric manganite compositions have been reported for PLD [251].

The most negative effect in sputtering deposition of oxides certainly is the oxygen ion bombardment, which causes severe crystal damage in the growing thin film. As introduced in detail in Section 3.3, in the present studies this issue – commonly tackled by a subsequent annealing step or by off-axis sputtering – will be avoided by applying a new method, the LDMS technique.

In the following it will be shown that LDMS is a competitive alternative to other well-established PVD methods by a judicious choice of the deposition parameters. The critical parameters for LSMO with respect to crystalline quality and magnetic properties, i.e., high T_C with a sharp transition, are substrate temperature [252], O_2 partial pressure (p_{O2}) [253], the Sr content [104, 111] and the in-plane strain induced by the substrate lattice mismatch [155, 167, 195].

After the presentation of the experimental procedures, the high quality of the LSMO thin films prepared by the LDMS method regarding surface smoothness, stoichiometry, crystallinity and magnetic and electronic properties will be demonstrated. Subsequently, the influence of p_{O2} will be discussed with a focus on structural and magnetic properties.

4.2 Sample preparation

The LSMO thin films were deposited in the custom-made sputtering chamber described in Section 3.3.2, employing a stoichiometric $La_{0.75}Sr_{0.25}MnO_3$ target[3]. Up to four epi-polished, (100)-oriented single crystal substrates[4] – $SrTiO_3$ (STO) ($a = 3.901$ Å), MgO ($a = 4.214$ Å), $LaAlO_3$ (LAO) ($a_{pc} = 3.791$ Å) and $(La_{0.3}Sr_{0.7})(Al_{0.65}Ta_{0.35})O_3$ (LSAT) ($a_{pc} = 3.866$ Å) – were mounted next to each other on the rotating sample holder, allowing for simultaneous deposition and thus best comparability.

For the very first LSMO sputtering tests, silicon (100) substrates, covered with a ≈50 nm thick thermally oxidized, amorphous SiO_2 layer, were preferred over the more expensive oxide single crystals. Apart from the financial aspect, this kind of substrate is beneficial for another reason: The amorphous top layer does not impose any preferential orientation on the growing LSMO film, enabling it to grow in a polycrystalline structure. This way the resultant crystallographic phase can be identified more easily by its X-ray Diffraction (XRD) fingerprint than it would be the case for a textured or epitaxially grown thin film.

The optimization of the parameters for the depositions was performed with a focus on STO and MgO substrates, since for both substrates there is an abundance of data available in the literature for comparison. The as-purchased substrates were heated to 850 °C for more than one hour prior to deposition to evaporate the adsorbates. Tab. 4.1 lists the investigated ranges of the deposition parameters as well as the optimized values that were determined in this study. The sputtering power density was kept constant at 4.4 W/cm^2, i.e., 200 W for the circular 76.2 mm (3 ") target, with the power ramping before and after deposition carried out in steps of 50 W/5 min. Deposition rates ranged between 0.007 Å/s for 80 % O_2 content Radio Frequency (RF) sputtering and 0.37 Å/s for pure argon Direct Current (DC) sputtering; under the optimized conditions the rate was around 0.045 Å/s.

4.3 Results and discussion

[3] See Tab. A.1 on p. 139 for details.

[4] For a comparison of substrates and thin film materials, see Tab. 3.1 on p. 38; for the list of substrate batches and supplier information, see Tab. A.2 on p. 140.

Table 4.1.: The investigated and optimized parameters for large-distance magnetron sputtering of LSMO. The *rapid* cool-down followed an exponential decay with time constant $\tau \approx 10\,\text{min}$. (*Published in* [237], ©2012, ELSEVIER)

parameter	investigated	optimized
sputtering mode	RF, DC	RF
substrate temperature	600 to 850 °C	700 to 800 °C
$O_2/(Ar + O_2)$ ratio	0 to 80 %	40 %
working pressure	0.024 to 2.5 Pa	1.8 Pa
cool-down rate	1 K/min to *rapid*	*rapid*

Although literature on sputtering deposition is vast and seems to be exhaustive, the enormous parameter space still remains a challenge when exploring the capabilities of a non-standard sputtering system. Surprisingly, the deposition temperature did not seem to have any notable influence on the sample quality within an interval of 700 to 850 °C, which is a typical range for most of the LSMO deposition reports found in the literature [155, 189, 252, 254]. Various cooling rates from rapid exponential cool-down (time constant $\tau \approx 10\,\text{min}$) to slow 1 K/min were tested, but no noticeable differences in the resulting crystalline and magnetic properties were found. However, it turned out that the other deposition parameters were much more critical for the characteristics of the samples, such as their growth type, microstructure, stoichiometry, interfacial defects and strain.

4.3.1 Structure, microstructure and composition

The preliminary tests employing Si/SiO_2 as substrate resulted in a remarkable dependence of the resultant crystallographic phase on the working pressure (p_{work}) and the O_2 partial pressure (p_{O2}) [see Fig. 4.1(a)]. Both a too low working pressure (blue curve) and a too high O_2 partial pressure (red curve) frustrated the formation of the desired orthorhombic LSMO phase[5], which was obtained at $p_{work} = 0.3\,\text{Pa}$. The effect at low p_{work} can be understood by the large Mean Free Path (MFP) for the high energetic oxygen ions, which as a consequence can reach the substrate and effectively cause severe crystal damage to the growing film. At a closer look, the strongest peaks of the orthorhombic LSMO phase actually can be identified, although shifted to slightly larger values. The expansion of the lattice parameters is likely caused by an oxygen deficiency [253, 255, 256] which can be expected at such a low value of p_{work} with no extra O_2 in the sputtering gas.

In order to investigate the influence of p_{O2}, X-ray Photoelectron Spectroscopy (XPS) was performed on both 0.3 Pa samples; their Mn 2p edge is shown in Fig. 4.1(b). While the oxygen shift of binding energy (E_b) for both samples is comparable, the manganese content in the 10 %

[5] The indices of the Bragg reflexes are denoted in orthorhombic coordinates only in the polycrystalline case (Fig. 4.1); for the epitaxial films shown below all peaks are indexed with respect to the cubic or tetragonal unit cell.

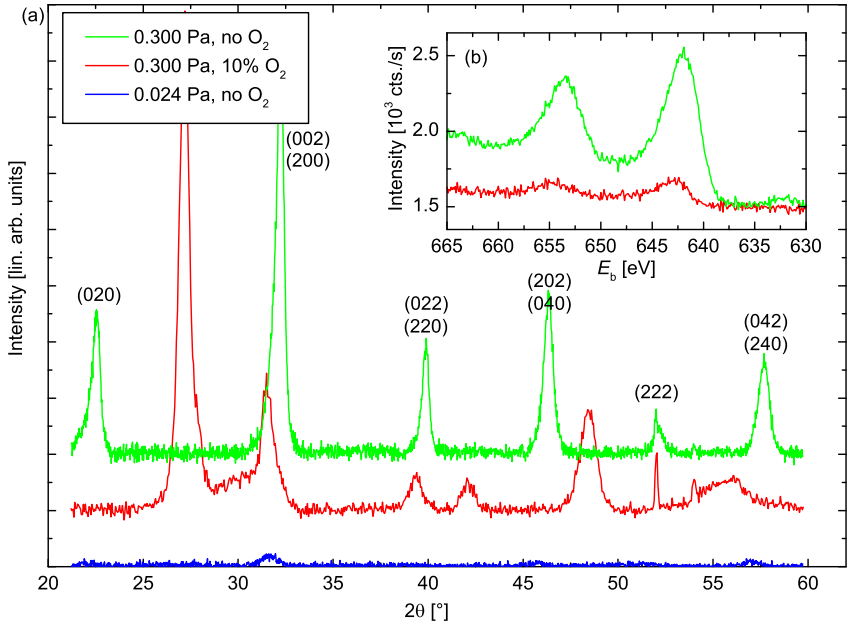

Figure 4.1.: Influence of p_{work} and the O_2 content on the crystal structure and stoichiometry of ≈100 nm LSMO DC-sputtered on Si/SiO_2(50 nm) at a substrate temperature of 700 °C. (a): GIXRD diffractograms; Bragg peak indices are given for the orthorhombic LSMO phase; (b): XPS spectra at the Mn 2p edge.

O_2 sample is drastically reduced. Further tests with quartz substrates and Si/SiO_2 substrates with a 500 nm thick oxide layer, where in both cases the desired LSMO phase was obtained, confirmed that the effect of Mn deficiency in oxygen assisted sputtering only occurred when the oxide layer on the Si substrate was thin enough.

In conclusion, the deposition of polycrystalline LSMO films on amorphous substrates was helpful as a starting point giving a set of reasonable sputtering parameters which yield the right crystallographic phase, albeit some extra chemical effects caused by the Si substrate were encountered when oxygen gas was employed. In contrast, in the main investigations presented below, where solely single crystal oxide substrates were employed, the LSMO was found to grow phase-pure, regardless of the chosen O_2 partial pressure.

For the LSMO films deposited on STO, LSAT, LAO and MgO, thicknesses ranging from 62 nm down to 7 nm were investigated. However, the emphasis was laid on 20 to 30 nm thick samples, as they are thick enough for not being dominated by the interfacial effects and thin enough to enable fully strained growth without any strain relaxation, as long as the in-plane lattice strain is not too high[6]. Moreover, the 20 to 30 nm range turned out to be optimal for X-ray

[6] Compare Section 3.2.1.

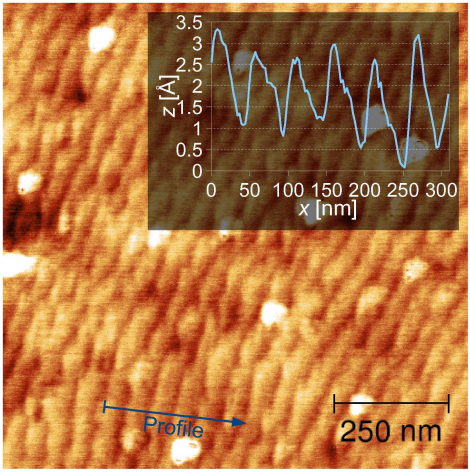

Figure 4.2: AFM micrograph of 7 nm LSMO on STO (100). The inset shows the line profile as marked by the arrow. (*Published in* [237], ©2012, ELSEVIER)

Reflectometry (XRR) measurements, which were performed both for thickness calibration and to verify the AFM-determined surface roughness.

The Atomic Force Microscopy (AFM) analysis revealed a very smooth surface with step-like features as small as half of the pseudocubic unit cell lattice parameter, as shown in Fig. 4.2. The root mean squared roughness (R_q) for the 7 nm thin films was as low as 0.11 nm and increased slightly to 0.25 nm for 40 nm thick films.

The low roughnesses determined by AFM could be confirmed by the XRR measurements of the films grown on MgO and STO substrates; examples for reflectivity curves and the corresponding simulations are shown in Fig. 4.3. The simulation data was created using the BRUKER *Leptos* software, without compensating for the instrumental function[7]. The Kiessig fringes in curve B are more pronounced than in curve C because the densities of substrate and LSMO film are more distinct in case of the MgO substrate. Analogously, XRR analysis was not applicable for the LAO and LSAT substrates, as their crystallographic densities do not differ sufficiently from LSMO (compare Tab. 3.1 on p. 38).

The chemical composition, especially the Sr/La ratio, is of critical importance for the magnetic properties of LSMO. Fig. 4.4 shows an example of a Rutherford Backscattering Spectroscopy (RBS) elemental analysis for a 32 nm RF-sputtered LSMO film on MgO. Quantitative analysis with the Mn stoichiometry normalized to 1 shows that all samples feature a significant shift of the Sr/(La+Sr) ratio towards ≈50 % of the target's composition, but surprisingly the (La+Sr)/Mn ratio remained unchanged within the accuracy of RBS of ≈2 at.%, which suggests a self-accommodation mechanism during the crystal growth. A loss of Sr during sputtering of LSMO has – to the best of the author's knowledge – not been reported so far but the fact is that quantitative elemental analysis for sputtered LSMO is generally scarce.

The loss of ≈50 % Sr was also observed for films deposited from a second sputter target of nominal doping level of $x = 0.35$, where the Sr content in the film, as determined using RBS,

[7] Disregarding the instrumental function leads to an overestimation of the film roughnesses, so the specified roughness represents an upper limit.

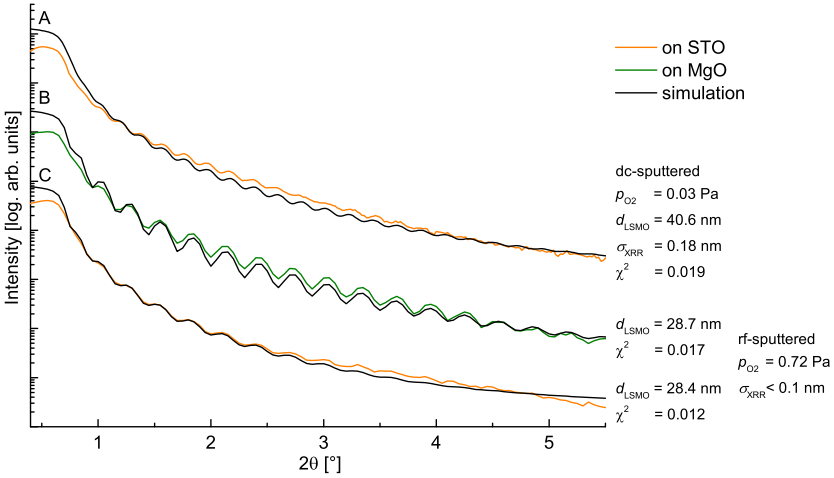

Figure 4.3.: XRR analysis of DC- and RF-sputtered LSMO thin films on STO and MgO substrates, σ_{XRR} and χ^2 are the roughness and the coefficient of determination of the simulation curves, respectively. Curves B and C belong to two simultaneously grown samples.

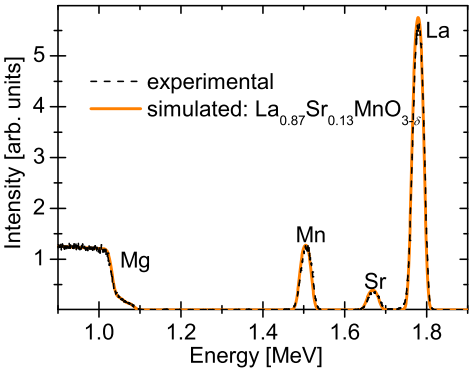

Figure 4.4: Example of a Rutherford backscattering spectrum for 32 nm LSMO on MgO, RF-sputtered at $p_{\mathrm{work}} = 2.5\,\mathrm{Pa}$ with 50 % O_2. The stoichiometry could be confirmed by TEM-EDX for STO/LSMO and Si/SiO_2/LSMO samples. (*Published in* [237], ©2012, ELSEVIER)

was reduced to $x \approx 0.17$. The Sr loss during LDMS may be explained by the larger scattering angles[8] of the lighter (Sr) as compared to the heavier species (La).

The crystal structure – and thus the substrate dependent lattice misfit – is a function of the Sr doping level (x). For the given composition, the native crystal structure of the LSMO is orthorhombic [compare Fig. 3.4(a) and Fig. 4.1]. For the desired epitaxial growth on the (pseudo-)cubic substrates the lattice misfit between the LSMO pseudocubic lattice constant (a_{pc}) and the respective lattice parameters of the substrates are of great importance; a side-by-side comparison can be found in Tab. 3.1 on p. 38.

Representative High-Resolution X-ray Diffraction (HRXRD) plots are shown in Fig. 4.5. As they only display zoomed-in 2θ intervals in order to resolve the fine structure of the reflections, it should be mentioned that, within the scanned range of 19 to 110°, all epitaxial samples reported in this chapter solely featured the $(00l)$ reflections up to the 4th order, with no indication of any spurious phases[9].

[8] Compare Section 3.3.1, Fig. 3.8 and [201, 257].

[9] The reader is also referred to the full-range HRXRD scans shown in the subsequent chapter [Fig. 5.1(a) on p. 84], where the LSMO thin films serve as bottom electrodes.

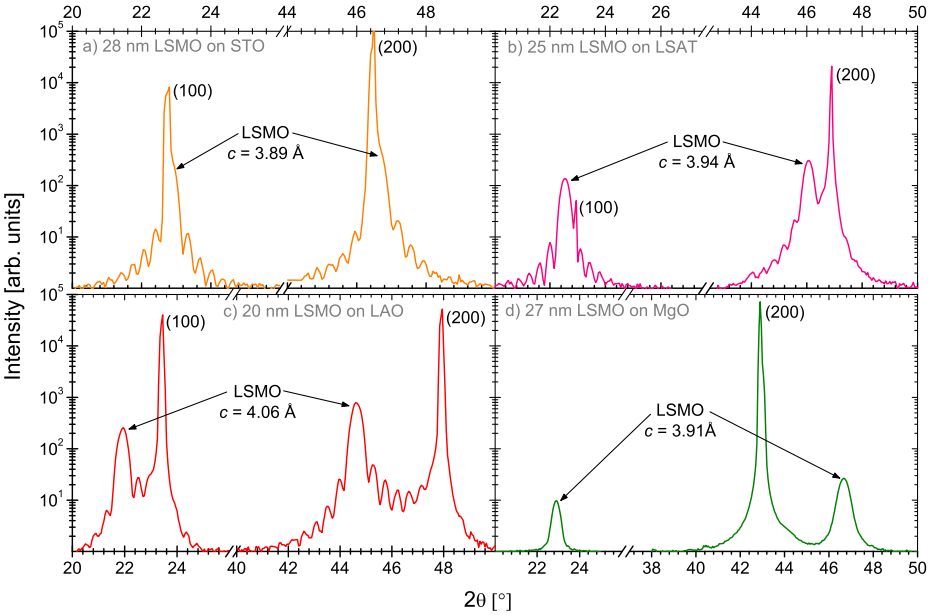

Figure 4.5.: The HRXRD θ-2θ diffractograms of LSMO, RF-sputtered on STO (a), LSAT (b) and MgO (d) and DC-sputtered on LAO (c). The film thickness calculated from the separation of the fringes (a)-(d) confirms the results of the XRR analysis, which is denoted above the graphs. (*Published in* [237], ©2012, ELSEVIER)

For LSMO films grown on the low-misfit substrates STO, LSAT and LAO the expected [00l]-oriented growth can be observed [see examples in Fig. 4.5(a)–(c)] together with the clear occurrence of Laue oscillations [258]. Analogously to the Kiessig fringes observed in XRR, the periodicity of the Laue fringes is not only related to the film thickness, but also provides complementary information: Pronounced Kiessig fringes are merely an evidence for smooth interfaces and a homogeneous crystallographic density of the respective film; they do not even require the films to be crystalline. In contrast, Laue oscillations indicate crystalline coherence and homogeneity of a layer of finite thickness. As demonstrated in Fig. 4.5(b)&(c), the crystallographic density mismatch, while being essential for the Kiessig fringes, is not a necessary criterion for the existence of Laue fringes[10]. Since the thicknesses calculated from the Laue fringes matched the ones determined by XRR[11], it can be concluded that the coherent epitaxial crystal structure extended throughout the whole film thickness, whenever Laue oscillations were observed.

Also on the high-misfit MgO substrate, LSMO grows strongly c-oriented with similar Full Width at Half Maximum (FWHM) of the reflections, as can be seen in Fig. 4.5(d). However, the complete absence of finite thickness fringes indicates that the high crystalline order is absent. The impact of the high tensile mismatch of MgO in contrast to the three low-mismatched substrates is pointed out by a comparison of the Rocking Curves (RCs) at the LSMO(002) peaks (see Fig. 4.6). In contrast to the broadened RC of the MgO sample, for the low-mismatched substrates the FWHM of the RCs at the (002) peak can be less than 0.07°, which is as small as the best values found in the literature, even for PLD-grown films [259], and reaching the quality of the MBE prepared films [260, 261]. The shoulders of the RC of the STO sample and the slightly increased width of the RC of the LAO sample are related to the twinning phenomena in the LSMO film or the substrate, respectively. Both issues will be addressed later in the discussion of the Reciprocal Space Maps (RSMs).

While for the MgO substrate the c lattice constant is very close to the bulk literature value of $a_{pc} \approx 3.906\,\text{Å}$, for the other substrates a nearly elastic behavior was observed, with the additional condition, that the unit cell volume is reduced by the compressive biaxial strain[12] [167].

[10] For the crystallographic densities of the employed materials, see Tab. 3.1 on p. 38.

[11] For the LSMO films grown on LSAT and LAO, the XRR-determined thicknesses of the simultaneously deposited films on MgO and STO were taken as thickness reference.

[12] Also compare the statistical evaluation in Fig. 4.13 below.

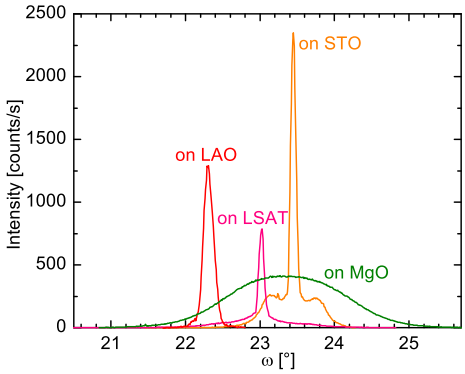

Figure 4.6: Rocking Curves at the (002) peaks for LSMO thin films on STO, LSAT, LAO and MgO, corresponding to the θ-2θ scans in Fig. 4.3.

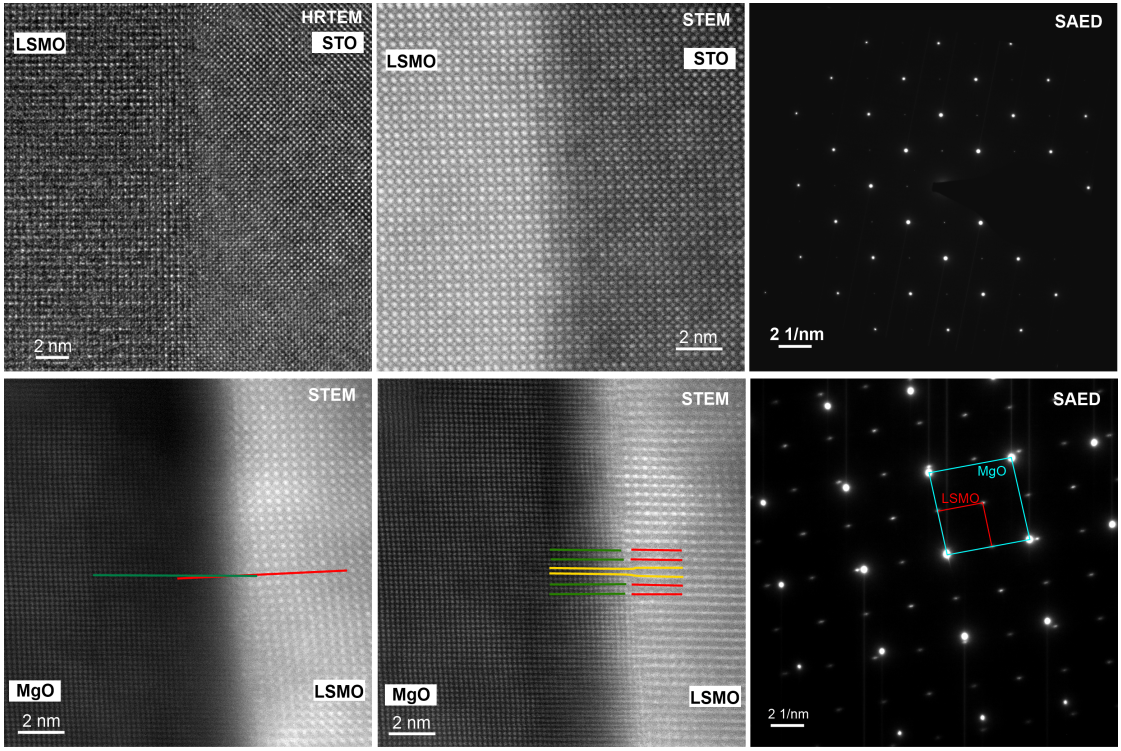

Figure 4.7.: TEM, STEM and SAED images of DC-sputtered LSMO on STO (upper row) and on MgO (lower row). (*Published in* [237], ©2012, Elsevier)

In case of the LAO substrate, fully strained epitaxial growth with pronounced Laue oscillations could only be achieved in the DC sputtering mode; RF sputtering caused strain relaxation at any parameter set, as confirmed in the reciprocal space maps (see Fig. A.5 in the Appendix on p. 144).

The Transmission Electron Microscopy (TEM) investigations confirm the excellent epitaxial growth on STO, as can be seen in the upper row of Fig. 4.7. The DC-sputtered LSMO films grow perfectly cube-on-cube with identical lateral lattice constants[13]. In the Selected-Area Electron Diffraction (SAED) pattern taken from the interface region including equal STO and LSMO areas, no distinguishable discrepancy was observed in diffractions from film and substrate. The lower row of images illustrates that the lattice mismatch of the MgO substrate is too big to allow a fully strained growth. As a result, the LSMO film relaxes by introducing defects such as tilting, bending and dislocations. The SAED pattern confirms the different lattice constants in- and out-of-plane as well as the highly oriented growth mode.

4.3.2 Relationship between microstructure and magnetic properties

The Superconductive Quantum Interference Device (SQUID) Field Cooling (FC) curves were recorded for all samples except for the ones on the LAO substrates, as LAO is known to induce an antiferromagnetic (AF) phase in the LSMO thin films due to the comparatively high compressive in-plane strain [165, 166]. The FC measurements were performed in an external field of 100 Oe. The curves for STO and LSAT substrates were very similar regarding the position and sharpness of the magnetic phase transition, as their in-plane lattice parameters only differ by 0.035 Å $\widehat{=}$ 0.9 %

[13] TEM micrographs of RF-sputtered LSMO on STO will be shown later in Sections 5.3.1 and A.2.2.

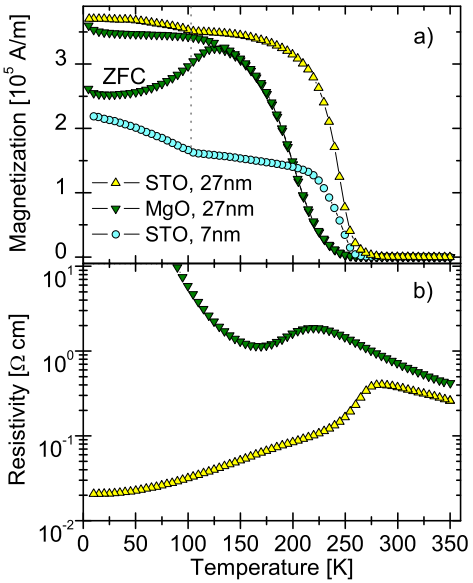

Figure 4.8: In-plane FC (a) and transport properties (b) for 27 nm and 7 nm LSMO, RF-sputtered on STO and MgO at $p_{O2} = 0.72\,\mathrm{Pa}$. The 27 nm films were grown simultaneously. (*Published in* [237], ©2012, Elsevier)

(compare Tab. 3.1 on p. 38). For MgO substrates, T_C was usually lowered and the transition broadened compared to the other substrates. Fig. 4.8(a) shows examples of FC curves of 27 nm LSMO simultaneously deposited on STO and MgO, as well as of a 7 nm film on STO, deposited under identical conditions. On STO and LSAT substrates, where LSMO grows fully strained, T_C is as high as 245 K (determined by the derivative method[14]), which is much higher than the reported bulk value [104] of 177 K.

As described in Section 3.2.1 the increase in T_C, observable for thin, low-strained and commensurately grown films on cubic substrates, is commonly attributed to the cancellation of the orthorhombic lattice distortion and the static Jahn-Teller (JT) distortion, which leads to a straightening of the Mn–O–Mn bond angles and thus to an enhancement of the Double-Exchange (DE) coupling [159–162].

The transition itself is comparable to the sharpest ones found in the literature [see also Fig. 4.12(c)]. Reduction of the film thickness down to 7 nm neither changed the temperature width of the transition nor T_C itself.

All STO/LSMO samples feature a second transition at 105 K (marked by the dotted vertical line in Fig. 4.8), that is not present on LSAT or MgO. It has been reported that the second order phase transition of STO at 105 K, from cubic to tetragonal, can be observed in epitaxial LSMO thin films grown on top [262, 263] and that this coupling is not prominent in resistance measurements [264] [see Fig. 4.8(b)]. However, a direct observation of this coupling in FC curves has not been reported so far. This second transition is even more pronounced for the 7 nm thick film on STO, as the structural transition of the substrate has stronger impact on the LSMO crystal lattice close to the interface.

In comparison to the thicker film, the 7 nm thin film on STO shows a markedly reduced magnetic moment per volume. This apparent discrepancy can be explained by the magnetically dead layer that forms at the interface between substrate and film which has been reported to extend to 2 to 3 nm for pulsed laser deposited LSMO on oxygen-annealed STO [53, 54] (see also Section 3.2.1). To estimate the dead layer thickness of the present STO/LSMO samples, hysteresis loops were measured at 115 K, just above the STO phase transition. From the saturation magnetizations $M_1 = 5.19 \cdot 10^5\,\mathrm{A/m}$ for the $d_1 = 27\,\mathrm{nm}$ film and $M_2 = 3.91 \cdot 10^5\,\mathrm{A/m}$ for the $d_2 = 7\,\mathrm{nm}$ film and under the assumption of identical dead layer thicknesses d_{dl}, the actual saturation magnetization M_{act} and d_{dl} can be linearly approximated by the equations

$$M_{\mathrm{act}} = \frac{M_i \cdot d_i}{d_i - d_{\mathrm{dl}}}, \text{ with } i = \{1, 2\},$$

which result in $M_{\mathrm{act}} \approx 5.60 \cdot 10^5\,\mathrm{A/m}$ and $d_{\mathrm{dl}} \approx 2.1\,\mathrm{nm}$. Considering the unit cell volume $V_{\mathrm{u.c.}} = 59.3\,\text{Å}^3$, the magnetic moment per Mn atom results in $m_{\mathrm{Mn}} = M_{\mathrm{act}} \cdot V_{\mathrm{u.c.}} \approx 3.6\,\mu_B$, which is remarkably close to the theoretical bulk value of $3.87\,\mu_B$ expected for the present level of Sr doping.

Regarding the FC curve for the sample on MgO in Fig. 4.8(a), the lower Curie temperature as well as the broader transition can be explained by the partially relaxed growth mode caused by the large lattice misfit. The relaxation causes the LSMO to approach the bulk value of T_C. But since there is still a substantial amount of residual strain – especially near the interface, as can be seen in the TEM image (Fig. 4.7, bottom row) – the transition is broadened.

[14] In the derivative method the Curie temperature (T_C) is assumed to coincide with the inflection point of the FC curve (T_i).

The abovementioned derivative method employed to assess the value of T_C is frequently used as a quick and convenient solution in order to compare relative differences in the transition temperatures. However, the Arrott plot method [265] is often considered a more accurate (and correct) – albeit fairly time-consuming – way to determine the onset of ferromagnetism. As a representative example, a series of magnetic moment *versus* field isotherms have been recorded for the 27 nm LSMO on STO sample (compare FC curve in Fig. 4.8) and visualized in the Arrott plot in Fig. 4.9(a). With the T_C criterion for the extrapolation of the linear fit crossing the origin, T_C can be determined to be around 255 K for this sample, which is 10 K higher than the value obtained from the derivative method and coincides with the point of the highest curvature of the FC – i.e., the very onset of magnetism – and the inflection point of the resistivity curve, respectively.

Another interesting conclusion from this Arrott plot – with the isotherms not being entirely parallel – is that the chosen set of critical exponents of the Mean Field Theory (MFT), $\beta = 0.5$, $\gamma = 1$ [265], expected for any mean-field interaction model, apparently does not describe the type of magnetic interaction in the LSMO film adequately. This is not surprising, though, considering the strongly correlated nature of magnetism in this system. As alternative trial sets of the critical exponents [266, 267], the ones resulting from the 3D-Heisenberg ($\beta = 0.365$, $\gamma = 1.336$) and the 3D-Ising ($\beta = 0.325$, $\gamma = 1.241$) models were also tested. Only the latter yielded good linearity and comparable slopes of the isotherms. The Curie temperature determined this way is about 250 K. Besides the questionable arbitrariness of the chosen critical exponents, the Arrott plot method suffers from the finite distribution of the transition temperatures of the investigated thin film, brought about by interface, strain and gradual relaxation effects. For these reasons, in the following the derivative method will be favored as a quick and reproducible method for comparing the transition temperatures of the various samples, despite the fact that it results in an underestimation of the actual value of T_C.

To investigate the in-plane FM switching behavior, *M-H* hystereses were recorded for the LSMO on STO samples, resulting in loops with high remanent magnetization and pronounced squareness [see Fig. 4.9(b)]. Depending on the deposition parameters, coercivities of around 25 to 75 Oe were observed.

To delve deeper into the nature of the magnetic phase transitions, the sheet resistance was measured as a function of temperature (T); the corresponding curves are shown in Fig. 4.8(b). For LSMO on STO, the maximum of the resistivity, indicating the metal-insulator transition temperature (T_{MI}), perfectly matches with the onset of magnetism at $T_{MI} = 285$ K. However, the MgO/LSMO sample behaves differently, closely resembling bulk LSMO where the metallic FM phase is followed by a low T magnetic insulating phase at 150 K [268]. The presence of the latter transition is readily visible in Fig. 4.8(a), where the FC and Zero-Field Cooling (ZFC) curves diverge around 150 K. In comparison with the studies of Dabrowski *et al.* [104] on polycrystalline bulk LSMO, the MgO/LSMO sample very well reproduces the magnetic and transport properties of LSMO with a Sr doping level of 13.0 to 13.5 % (see Fig. 1.6(b) on p. 17). This confirms the RBS results within the measurement accuracy.

In contrast, LSMO films grown on STO behave differently, with the temperature dependence of the resistivity resembling the considerably higher doping level of $x \approx 0.17$ in bulk LSMO [compare Fig. 4.8(b) on p. 70 and Fig. 1.6(b) on p. 17]. The suppression of the insulating phase in favor of the FM conductive phase is in perfect accordance with the aforementioned significant increase in T_C.

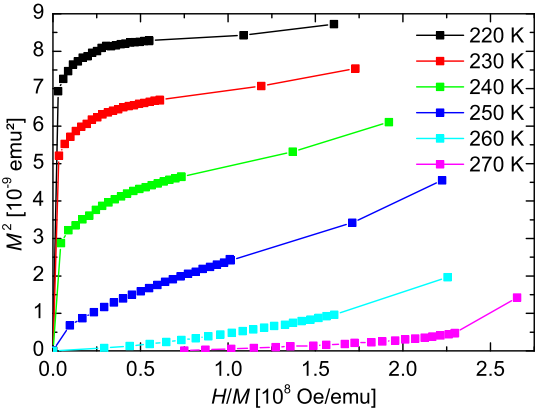

(a) Arrott plot

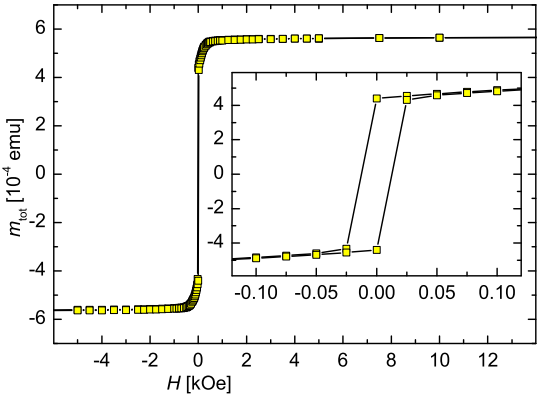

(b) magnetic hysteresis at 65 K

Figure 4.9.: (a): Arrott plot of the 27 nm LSMO on STO sample shown in Fig. 4.8. (b): FM in-plane hysteresis measurement of an LSMO on STO sample deposited with identical parameters; the inset shows a zoomed view of the switching region.

In analogy to the determination of the magnetically dead layer of the LSMO thin film, the same approach can be taken to estimate the thickness of the electrically dead layer, which does not necessarily have to match the former [174]. Fig. 4.10(a) illustrates the mismatch of the temperature dependence of the resistivities of LSMO thin films on STO, which is a consequence of the normalization on the film thicknesses without taking the dead layer into account. Analogously to the above calculations regarding the magnetic dead layer, the electric dead layer can be approximated to be of about 4.9 nm, which is substantially thicker than the

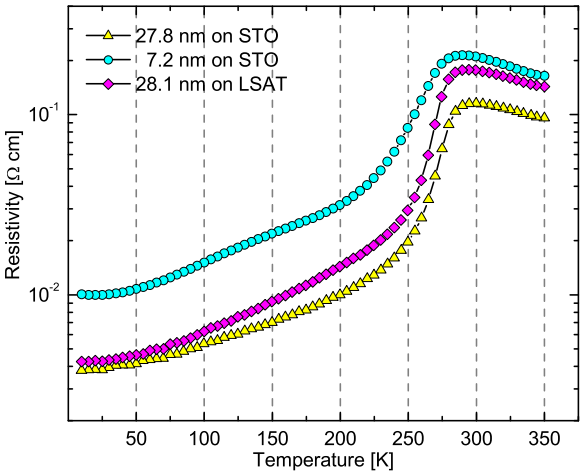

(a) without compensation for dead layer

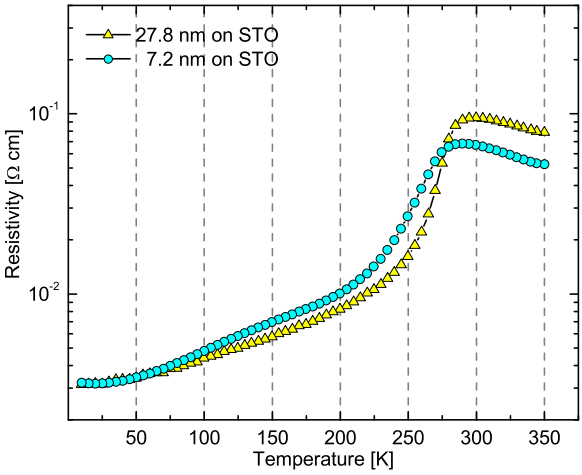

(b) dead-layer compensated

Figure 4.10.: Dead layer influence on the temperature dependence of the resistivity of STO/LSMO, with resistivities as calculated for the full LSMO film thicknesses (a) and for LSMO thicknesses after subtraction of a dead layer of 4.9 nm (b). To illustrate the impact of the small compressive in-plane strain, the simultaneously grown LSAT/LSMO sample is also shown in (a) for comparison.

magnetic one. The result of the dead layer compensation is shown in Fig. 4.10(b). It can be seen that for the transport properties the appropriate subtraction of the electric dead layer is not sufficient to match the whole temperature dependence for both film thicknesses. This can be explained by surface and interface effects, which naturally become more pronounced for thinner films.

As a side note, it should be mentioned that the resistivity curves shown in Fig. 4.10 were recorded for LSMO thin films with an increased Sr doping level of $x = 0.15$, which was obtained by co-sputtering with a Sr-enriched ($x = 0.35$) LSMO target. The higher charge carrier concentration in these films causes the overall resistivity to decrease by about an order of magnitude [compare Fig. 4.8(b)], exhibiting a temperature dependence which again resembles the behavior of higher doped bulk LSMO [compare Fig. 1.6(b)].

For comparison, the simultaneously prepared LSMO on LSAT is also shown in Fig. 4.10(a). While exhibiting a very similar shape as the curve of the ≈28 nm thick STO/LSMO sample, the absolute value of the resistance is a bit higher. This might be caused by a slightly thicker dead layer and/or by the higher compressive lattice mismatch of LSAT (compare Tab. 3.1).

4.3.3 Oxygen stoichiometry

Besides the Sr/La ratio, i.e., electron hole (h^+)-doping, the oxygen stoichiometry is an important factor affecting both the hole doping level and structural properties of LSMO. Although the question of oxygen stoichiometry of LSMO on an oxide substrate cannot be accurately answered by RBS, it can be qualitatively addressed via the magnetic and structural properties of the films. The c-axis lattice constant, as determined by HRXRD, is a direct measure of the unit cell volume, which is known to shrink with higher oxygen content [253, 255, 256]. The other indicator of choice is the Curie temperature, which is reduced by increasing oxygen deficiency.

The following RSM-based discussion of the impact of p_{O2} onto the structural properties is mostly focusing on STO/LSMO samples. Similar effects were observed for the other three substrates; the corresponding results can be found in the Appendix (Section A.2.1, pp. 143).

The impact of the O_2 partial pressure and differences in RF and DC sputtering can be distinctly seen in Fig. 4.11 for the series of RSMs taken on LSMO/STO samples. In DC mode and at lower p_{O2} the growth mode on the STO substrates is fully pseudomorphic and the LSMO film has nearly identical lattice constants as the underlying STO substrate [Fig. 4.11(a)], in agreement with the TEM results (Fig. 4.7). The higher O_2 partial pressure [Fig. 4.11(b)] apparently does not have much effect on the crystal structure, as only a small shoulder at the substrate reflection peak has developed. In contrast, the RF-sputtered films clearly show distinct LSMO reflexes located above the film peaks [Fig. 4.11(c)&(d)]. Furthermore, the lower p_{O2} sample [Fig. 4.11(c)] features four satellites along the rocking curve, which indicate the formation of an in-plane superlattice of shear-strain accommodated domains [269, 270]. The formation of this structural domain pattern gets suppressed at higher p_{O2} [Fig. 4.11(d)], but the larger lateral width of the reflex – i.e., the mosaicity – suggests other forms of strain accommodation.

A statistical overview of relevant parameters illustrating the intimate interplay between p_{O2} and magneto-structural aspects is presented in Fig. 4.12. The plots show the influence of p_{O2} on T_C, the temperature width of the magnetic transition and the c lattice constants. The latter is directly proportional to the unit cell volume, since all LSMO films deposited on STO were growing fully strained cube-on-cube. The plotted values correspond to samples which differ in other parameters like thickness or deposition temperature. In the T_C plot, the dotted horizontal

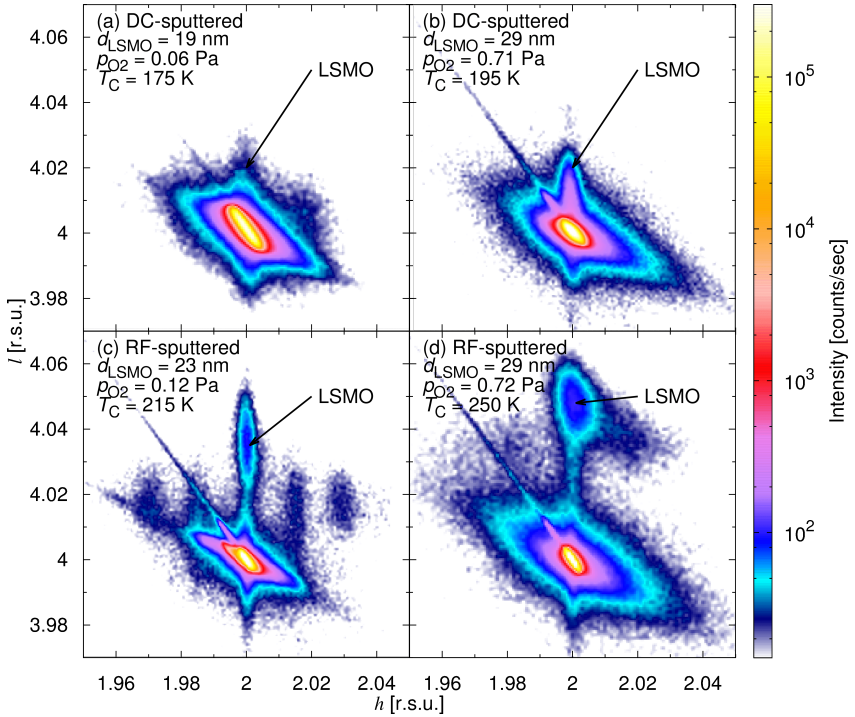

Figure 4.11.: Reciprocal Space Maps on the asymmetric (204)-reflection of LSMO on STO, deposited in DC (a)&(b) or RF mode (c)&(d) and at the O_2 partial pressure (p_{O2}) denoted in the graphs. The annotations describe the sputtering mode, the film thickness, p_{O2} and the resulting development of T_C. (*Published in* [237], ©2012, ELSEVIER)

line marks the bulk literature value [104] of T_C and the accuracy of the RBS measurements (gray area).

The TEM investigations already showed that in case of DC sputtering, the lattice parameters of the LSMO films match those of the bulk values. Although the oxygen stoichiometry is known to affect the unit cell volume [253, 255, 256], an increase of p_{O2} beyond 0.1 Pa turned out to have no significant influence on the c lattice constant – and thus the unit-cell volume – of the DC-sputtered as-grown samples [Fig. 4.12(a)&(b): blue circles].

In contrast to DC, RF sputtering – although generally less favorable for conductive targets because of the reduction of sputtering yield – significantly affects the unit cell volume [Fig. 4.12(a)&(b): red triangles]. At any O_2 concentration, the lattice spacing along the c-direction gets markedly reduced in RF mode. This is most likely caused by the fact, that in RF mode, the plasma plume above the target is much more expanded [271], bringing more reactive oxygen radicals closer to the sample surface. The comparison of Fig. 4.12(a) and (b) shows, that while RF sputtering in any case reduces the c lattice parameter, only for the STO substrate a

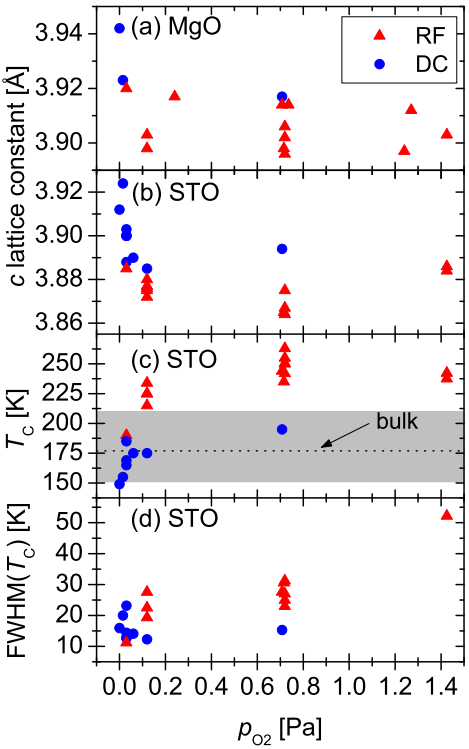

Figure 4.12: Comparison of different samples regarding the influence of p_{O2} for RF and DC sputtering. (a)&(b): c-axis lattice constant of the LSMO thin film on MgO and STO. (c)&(d): value and FWHM of the magnetic transition of LSMO on STO. (*Published in* [237], ©2012, Elsevier)

systematic dependence on p_{O2} with a minimum around 0.7 Pa can be observed. This reflects the different growth modes on MgO (relaxed) and STO (fully strained) substrates, which also causes the absolute values of the c lattice constants to differ.

The above substrate dependence can be visualized when plotting the distribution of the c lattice parameter as a function of the in-plane lattice misfit strain (see Fig. 4.13). Unlike MgO, the amount of strain imposed by LSAT and LAO is small enough not to cause immediate relaxation. Instead, the compressive strain effects an expansion of the c lattice parameter.

As stated before, the oxygen content inherently affects both the LSMO structure and the magnetic properties. Fig. 4.12(c) illustrates the dependence of T_C on p_{O2} for LSMO on STO, itemized for DC and RF sputtering. The comparison with Fig. 4.12(b) shows, that the reduced unit cell volume obtained by RF sputtering results in a considerable increase of T_C. The highest value of T_C of 263 K obtained for $p_{O2} = 0.7$ Pa is much higher than the bulk literature value for the respective Sr doping level of $x = 13\,\%$. For this optimized parameter set a deposition rate of 0.04 Å/s is observed, which is comparable to the rates reported for off-axis sputtering [254, 272] and MBE [250] but eight times smaller than for PLD [55, 273]. The deposition rate for this setup could of course be increased by approaching the power density limits of the sputtering targets or by co-sputtering from several targets at a time.

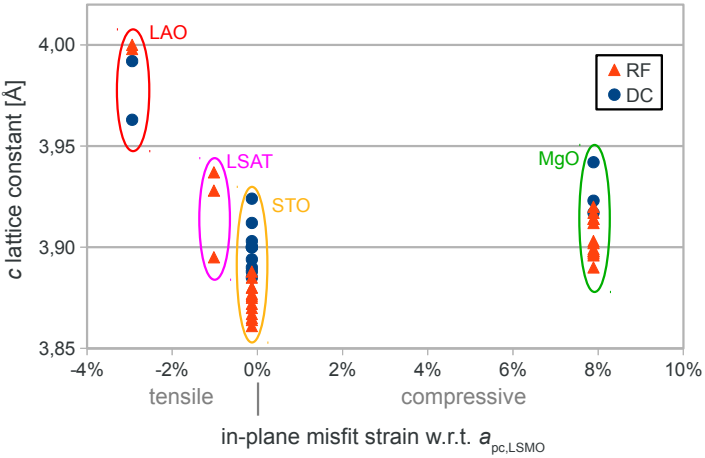

Figure 4.13.: Influence of the substrate dependent in-plane lattice misfit on the *c* lattice parameter of various different epitaxial RF- and DC-sputtered LSMO films. The in-plane lattice misfit are calculated with respect to the pseudocubic LSMO bulk lattice parameter.

While T_C can be increased by applying higher p_{O2} in RF sputtering mode, the sharpness of the magnetic transition gets reduced this way [Fig. 4.12(d)]. A broadening of the transition can generally result from chemical and microstructural inhomogeneities, as the magnetization curve in fact represents a superposition of magnetically different contributions. The crystalline imperfections and strain relaxation mechanisms, like the abovementioned superlattice of shear-strain accommodated domains, broaden the distribution of the Mn–O bonds which in turn smears out the transition temperature. While there is no evidence that RF sputtering causes any local chemical inhomogeneities, the RSM measurements confirm that in RF mode there is a pronounced strain relaxation induced by the reduced unit cell volume leading to an inhomogeneous magnetic state.

Comparing Fig. 4.12(c) and (d), one can conclude that with this deposition technique, LSMO films on STO can be tailored to either match the structural and magnetic properties of bulk LSMO with rather low T_C and a very sharp magnetic transition, or to get much higher T_C in RF mode at the expense of the transition sharpness.

4.4 Summary

On the basis of comprehensive studies on $La_{1-x}Sr_xMnO_3$ (LSMO), it has been shown that Large-Distance Magnetron Sputtering (LDMS) is an effective deposition method, which can compete with other Physical Vapor Deposition (PVD) methods like Molecular Beam Epitaxy (MBE), Pulsed Laser Deposition (PLD), and outclasses the off-axis sputtering technique in many aspects. Unlike sputtering at conventional distances, the presented variant yields smooth and homogeneous LSMO films with highly epitaxial growth and excellent magnetic properties without the need

for any post-annealing or slow cool-down procedures. The suitability for deposition of epitaxial *heterostructures* will be studied and proved in the following chapter.

On the downside, a considerable 50 % reduction of the Sr content in the LSMO films, with respect to the composition of the sputtering target, was observed by Rutherford Backscattering Spectroscopy (RBS) and Energy-Dispersive X-ray Spectroscopy (EDX) – an effect which was attributed to the mass dependence of scattering angles for the different species. Nevertheless, as the (La+Sr)/Mn stoichiometry remained unchanged, remarkably good magnetic properties were obtained.

The LSMO thin films were deposited on different single crystal substrates with varying degree of in-plane lattice misfit. The high tensile misfit of the MgO substrates resulted in a mostly relaxed but highly textured growth mode with the LSMO films' structural, magnetic and transport properties matching the bulk characteristics at the actual Sr doping level of $x = 0.13$.

In contrast, for the fully strained LSMO films grown on low-misfit $SrTiO_3$ (STO) and $(La_{0.3}Sr_{0.7})(Al_{0.65}Ta_{0.35})O_3$ (LSAT), a Curie temperature (T_C) value substantially higher than in the bulk counterpart is attainable. The films deposited on STO provided high tailorability by the choice of O_2 partial pressure (p_{O2}) and Direct Current (DC) or Radio Frequency (RF) sputtering mode. DC-sputtered films matched the reported bulk values in crystal structure and T_C and exhibited an exceptionally sharp magnetic transition, whereas the RF mode with its high sensitivity on p_{O2} allowed for the formation of a ferromagnetic (FM)-metallic phase with a considerable increase in T_C, while decreasing the LSMO unit cell volume. The reduction of the film thickness down to 7 nm neither changed the sharpness of the transition nor T_C itself. Owing to the atomic smoothness yielded by this deposition method, the RF-sputtered LSMO thin films on STO turned out to be perfect candidates for the growth of magnetoelectric (ME) heterostructures.

The promising results of the LDMS deposition of LSMO films suggest the extensibility of this technique towards other materials or processes, including but not limited to conditions where post-annealing is not desirable, e.g., when volatile species such as Pb, Bi or Zn are involved.

5 Ferroelectric PZT thin films on LSMO bottom electrodes

Selected parts of this chapter are also published in [274] within the framework of this thesis. The respective paragraphs – with minor conformations included – are indicated by a vertical gray bar at the inner page margin[1].

The first step in building LSMO/PZT based magnetoelectric (ME) multiferroic (MF) heterostructures was to deposit high-quality epitaxial $La_{1-x}Sr_xMnO_3$ (LSMO) thin films. This was accomplished by means of the in-house developed Large-Distance Magnetron Sputtering (LDMS) technique. The second step was to adapt this deposition method for the subsequent *in situ* growth of functional $PbZr_yTi_{1-y}O_3$ (PZT) thin films. In view of the final objective, that is building of electric field-effect devices, the PZT layers must be combined with LSMO serving as an electrode, assuring a smooth and clean interface. A good quality of the interface is a necessity because the field effect phenomenon in LSMO, due to its high charge carrier concentration, is limited to a few top atomic monolayers. Furthermore, the ferroelectric (FE) properties of the LSMO/PZT heterostructures need to be optimized with respect to the highest attainable polarizability and charge retention. Fortunately, as it turns out, LSMO electrodes match particularly well with PZT – a circumstance which certainly helped in realization of the functioning devices.

5.1 Background

One of the central problems common to all FEs is the gradual degradation of FE characteristics. In PZT thin films this is known to be caused by metal electrodes, so consequently, conductive oxide electrodes were successfully used, lowering leakage and fatigue effects. Along with conductive and superconductive oxides like IrO_2, RuO_2, ZnO and $YBa_2Cu_3O_{7-x}$ (YBCO) [275–278] as electrode materials, conductive perovskites like $LaNiO_3$ (LNO), $SrRuO_3$ (SRO), $La_{1-x}Sr_xCoO_3$ (LSCO), $SrTi_{1-x}Sb_xO_3$ (SSTO), $La_{1-x}Sr_xSnO_3$ (LSSO) and LSMO have been in the focus of research, since they allow for heteroepitaxial growth with the PZT [279–283].

Yet in the course of time it became apparent that the good match of the lattice constants between the electrode and PZT is not the only decisive characteristic determining the usefulness of a particular conducting oxide as an electrode [284]; what also matters is the type of the majority charge carriers in the electrode. Chen *et al.* [282] found that *n*-type perovskites (LSSO, SSTO) cause the FE hysteresis loops to broaden and the fatigue lifetime to reduce dramatically. This behavior was attributed to the very nature of the PZT itself; presently PZT is considered to be a FE with all the characteristics of a wide bandgap *p*-type semiconductor [222]. When *n*-type electrodes are used, during the polarization cycling, accumulation of surface charge at the PZT/oxide interface (*p*-*n* junction) is observed. This brings about carrier injection which leads to accumulation of oxygen vacancies at the interface and in turn speeds up fatigue processes. The

[1] *Reprinted with permission from* [274].

obvious way to overcome these problems, or at least to minimize them, was to choose a *p*-type conducting oxide, such as LSMO, as an electrode [282].

Basically, two classes of deposition techniques of oxide FEs have been established; one class comprises (metal-organic) chemical vapor deposition techniques and wet-chemical routes while the other one encompasses Physical Vapor Deposition (PVD) methods like Pulsed Laser Deposition (PLD), sputtering and oxide- or reactive-Molecular Beam Epitaxy (MBE).

While each of the PVD methods can achieve very high quality PZT films, they differ strongly regarding process requirements and their areas of applications. MBE ensures the highest accuracy of the elemental composition but requires reactive oxygen sources like ozone or plasma and a comprehensive control over a large number of process parameters [178]. For this reason, PLD and sputtering are much more widespread methods. The first is characterized by a generally good stoichiometry preservation[2] and comparatively high deposition rates. On the downside, PLD requires costly and hazardous (excimer) laser equipment and is only suitable for homogeneous coating of comparatively small substrates; in some cases particle ejection from the target can occur [283], destroying the film's crystallinity and raising the need for post-annealing.

Sputtering allows for homogeneous deposition on large substrates, but the elemental dependence of the sputtering yield at the target results in a generally limited control of the film stoichiometry.

While the deposition of PZT films via reactive co-sputtering from metallic targets in Direct Current (DC) mode has also been reported [199, 285], the Radio Frequency (RF) magnetron sputtering from readily sintered compound targets is certainly the more established method. In this case, enriched targets with 10 to 20 mol.% excess PbO [178, 257] are very often employed in order to tackle the PbO loss problem (see Section 3.2.2), albeit an extra PbO may cause unwanted mechanical degradation to the ceramic[3].

When epitaxial PZT thin films with high FE quality are to be deposited, the biggest challenge regarding the optimization of the PZT sputtering process lies in the intimate interplay between excess PbO, substrate temperature, working pressure (p_{work}) and O_2 partial pressure (p_{O2}), target-substrate separation (d_{sep}), sputtering power and DC bias voltage. Of course, like for LSMO sputtering, the spurious oxygen ion bombardment has to be prevented in order to grow crystalline films without any subsequent annealing step. For this reason, the LDMS technique (see Section 3.3.1) is an obvious method of choice, particularly considering the expectable high lateral uniformity enabled by the diffuse vapor flow over the large target-substrate separation. As an added benefit, a right choice of p_{work} may allow for the use of stoichiometric PZT targets, as the Pb/(Zr+Ti) ratio is known to rise with increasing distance [257], which can be explained by the lower scattering angle of heavier species during the thermalization process [201] (compare Fig. 3.8 on 48).

5.2 Sample preparation

LSMO/PZT heterostructures were RF-sputtered using the LDMS setup described in Section 3.3.2. As substrate materials (100)-oriented epi-polished $SrTiO_3$ (STO), $SrTiO_3$:Nb (STO:Nb) and MgO single crystals were used. The 5 to 7 nm thin LSMO Bottom Electrodes (BEs) were deposited from

[2] However, a small mass-separation effect in the laser ablation plumes is known to exist [212].

[3] According to Kurt J. Lesker company, the excess PbO severely compromises the mechanical stability of the sintered target.

a stoichiometric $La_{0.65}Sr_{0.35}MnO_3$ target with the optimized sputtering parameter set determined in Chapter 4 (see Tab. 4.1), which proved to be optimal also for this Sr doping level. The higher nominal Sr concentration – resulting in an actual doping level of $x \approx 0.17$ (see Section 4.3.1) – was chosen in order to get higher conductivity at Room Temperature (RT) on insulating substrates, facilitating the FE characterization.

The subsequent PZT deposition was carried out by RF sputtering from a stoichiometric $PbZr_{0.52}Ti_{0.48}O_3$ target[4]. As optimized deposition parameters, a substrate temperature of 550 °C, a working pressure of 0.3 Pa with 20 % O_2 content and 4.4 W/cm^2 of RF power density were determined, yielding a growth rate of 3 Å/min. The usually ≈90 nm thick films were cooled down in 0.7 Pa of pure oxygen. The ramping of the RF power up and down the 200 W was done in steps of 25 W/5 min, i.e., with half the rate of the LSMO ramping, in order to protect the brittle target from thermal stress.

All temperature ramps were performed at a rate of 6 K/min and the samples were kept in Ultra-High Vacuum (UHV) between all steps. For comparison, samples without the LSMO BE were produced using identical conditions.

In a last step, square-shaped Au contacts with an area of 1.0 mm^2 and a thickness of 25 nm were DC-sputtered through a shadow mask. Gold was chosen as Top Electrode (TE) material, as it is known to cause lower leakage than Pt electrodes at electric fields (E) below 400 kV/cm [224]. Furthermore, diamagnetic Au qualifies better than Pt, which is generally better suited for the sensitive magnetic measurements presented in the next chapter.

5.3 Results and discussion

Additionally to monitoring the deposition rates by a calibrated Quartz Crystal Microbalance (QCM), X-ray Reflectometry (XRR) was performed on selected samples to verify the actual film thickness. With a growth rate of 3 Å/min, the LDMS method is about two times slower than off-axis sputtering of PZT [250] and up to ten times slower than PLD. However, if sputtering rate were of importance, it could still be increased by reaching the RF power density limit of the PZT target, and/or by co-deposition from two or more targets.

In order to evaluate the value of large-distance RF sputtering in comparison with off-axis sputtered or PLD grown PZT thin films, extensive microstructural and functional FE studies were carried out.

5.3.1 Microstructural characterization

The microstructure of all samples was characterized by means of High-Resolution X-ray Diffraction (HRXRD). The θ-2θ scans of LSMO/PZT heterostructures grown on STO and MgO in Fig. 5.1 show phase-pure growth of the perovskite PZT film along the [001] direction on top of the epitaxial LSMO layer of the same orientation (compare LSMO results, Fig. 4.5 on p. 67).

The φ-scan on the (204) reflection of the PZT film confirms that the four-fold symmetry of the substrate and the LSMO BE is retained by the PZT layer.

The satellites of the LSMO (002) reflex, which form a shoulder at the STO (002) in Fig. 5.1(a) are the Laue oscillations of the 6.5 nm thin LSMO layer, confirming that the LSMO crystallinity has not suffered from the subsequent PZT deposition. The same kind of finite thickness fringes

[4] Detailed lists for the targets and substrates can be found in Tab. A.1 and Tab. A.2 on pp. 139.

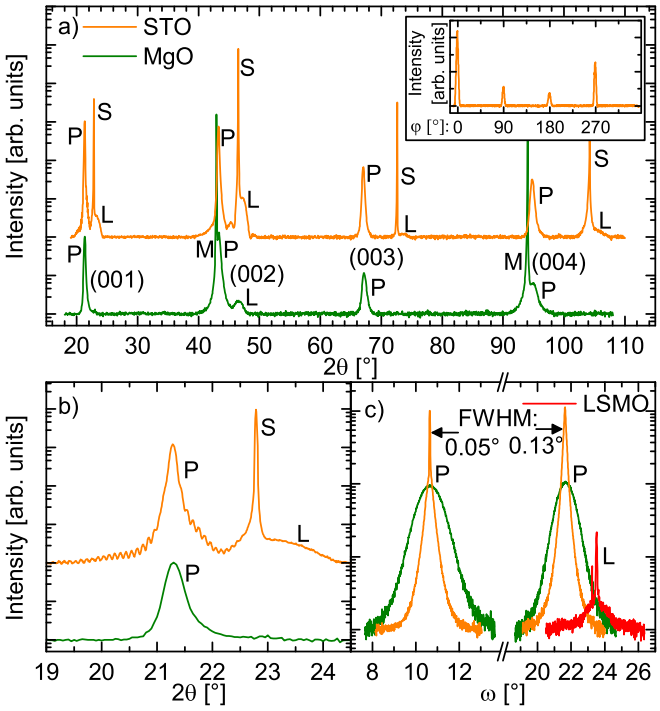

Figure 5.1.: HRXRD analysis of simultaneously deposited STO/LSMO(6.5 nm)/PZT(88 nm) and MgO/LSMO(6.5 nm)/PZT(84 nm) heterostructures; (a): θ-2θ scan, (b): close-up view of the (001) region, illustrating the Laue oscillations of the STO sample, (c): RCs on LSMO and PZT peaks at the first and second diffraction order; the LSMO curve belongs to the sample grown on STO. The inset in (a) shows a φ-scan on the (204) reflection of the PZT layer on STO/LSMO. The annotations P, L, S and M in the plots indicate the affiliation of the reflections for PZT, LSMO, STO and MgO, respectively. (*Published in* [274], ©2012, CC BY 3.0)

are even observable around the PZT (001) reflex for this STO/LSMO/PZT sample, as shown in the high-definition scan in Fig. 5.1(b). The occurrence of Laue fringes for such a ≈90 nm thick film is particularly stunning – especially since the PZT does not grow commensurately (see below) – as it requires perfect crystalline coherence throughout the whole film thickness.

The PZT thickness of ≈89 nm as calculated from the Laue oscillations is in good accordance with the XRR-determined thickness (see Fig. 5.2). The latter also revealed interface roughnesses (σ_{XRR}) of well below a unit cell (u.c.) height. Interestingly the simultaneously grown MgO/LSMO/PZT sample features a thickness deviating by ≈3 nm as compared to the STO sample.

Since both samples were mounted on the sample holder at identical distances from the rotation axis, the origin of this deviation may only be found in the difference of substrate-dependent strain accommodation mechanisms. However, it should also be noted that the XRR curve of

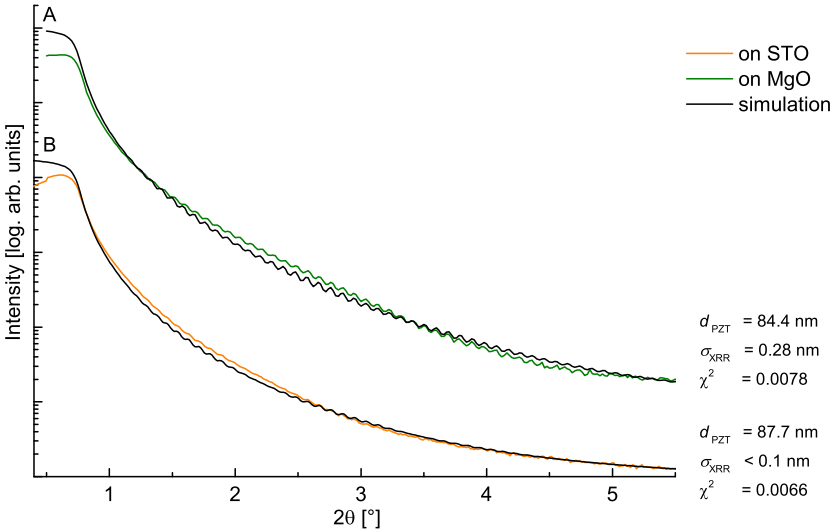

Figure 5.2.: XRR analysis of simultaneously deposited STO/LSMO(6.5 nm)/PZT and MgO/LSMO(6.5 nm)/PZT, the same samples shown in Fig. 5.1. σ_{XRR} and χ^2 are the roughness and the coefficient of determination of the simulation curves, respectively.

the STO sample might not be as trustworthy as the one for the MgO sample, because of the considerably lower contrast in crystallographic densities (compare Tab. 3.1 on p. 38).

Because of the high lattice mismatch, even very thin films of LSMO cannot be grown fully strained on MgO (compare Section 4.3.1). The in-plane relaxation of the LSMO causes the PZT layer on top to develop pronounced mosaicity, which can be seen in the Rocking Curves (RCs) in Fig. 5.1(c). In comparison, the Full Width at Half Maximum (FWHM) values for PZT on STO/LSMO is much smaller and as low as the best values found for PLD grown [282] and off-axis sputtered [250] PZT films, despite the fact that the present films are much thinner than those reported in the literature (90 nm *versus* 250 nm); it is known that the FWHM usually increases with decreasing thickness for highly mismatched layers [207]. It is worth pointing out that Vaz *et al.* found that such high crystallinity could not be achieved with all-sputtered LSMO/PZT films on STO in off-axis geometry [250]; instead, their LSMO layer was deposited by MBE. In their case the sharpness of the RCs was likely an extra benefit of using TiO_2-terminated STO substrates and the lower lattice mismatch of the employed $PbZr_{0.2}Ti_{0.8}O_3$.

PZT layers directly deposited onto the respective substrates, without the LSMO buffer layer, were crystallographically very similar in case of STO and STO:Nb substrates, while on MgO phase pure perovskite PZT growth could not be achieved. Apparently, the relaxed LSMO film, which provides a compressive misfit strain as opposed to the tensile misfit strain from the MgO, acts as a seed layer to the PZT film and helps to stabilize the perovskite phase. On STO there is no

such effect since the LSMO layer anyway grows commensurately, retaining the in-plane lattice constant of the substrate for further PZT layer growth.

In order to investigate the influence of the in-plane lattice misfit of the substrates, Reciprocal Space Maps (RSMs) on the (204) reflexes were recorded for the same samples as shown in Fig. 5.1. On the STO/LSMO substrate, the in-plane lattice of the PZT layer relaxes coherently, reaching similar peak broadening like in perpendicular direction [Fig. 5.3(a)]. With lattice constants of $a = 4.05\,\text{Å}$ and $c = 4.18\,\text{Å}$, the in-plane component is very close to the reported bulk literature value [141] of $a_{\text{bulk}} = 4.043\,\text{Å}$, while the c lattice constant is larger compared to $c_{\text{bulk}} = 4.132\,\text{Å}$ (see also Tab. 3.1 on p. 38). The increased c lattice constant might be ascribed to a slight oxygen deficiency [283] which may be offset by post-deposition cool-down in a higher oxygen partial pressure of up to atmospheric pressure, which is a common practice [250, 282, 283, 286].

In contrast, while featuring the same a and c lattice constants like on STO/LSMO, the horizontal distribution (i.e., along the ω scan direction) of the PZT (204) diffraction of the film on MgO/LSMO is much broader [Fig. 5.3(b)], which is a consequence of the mosaicity observed in the RCs of the symmetric reflections [Fig. 5.1(c)], but may also be caused by a slightly broader distribution of the in-plane lattice constant.

As the LSMO layer is invisible in the RSMs due to its small thickness, Scanning Transmission Electron Microscopy (STEM) images were collected in order to investigate the strain relaxation at the LSMO and PZT interfaces. Despite the small difference in the Sr doping level ($x = 17\,\%$

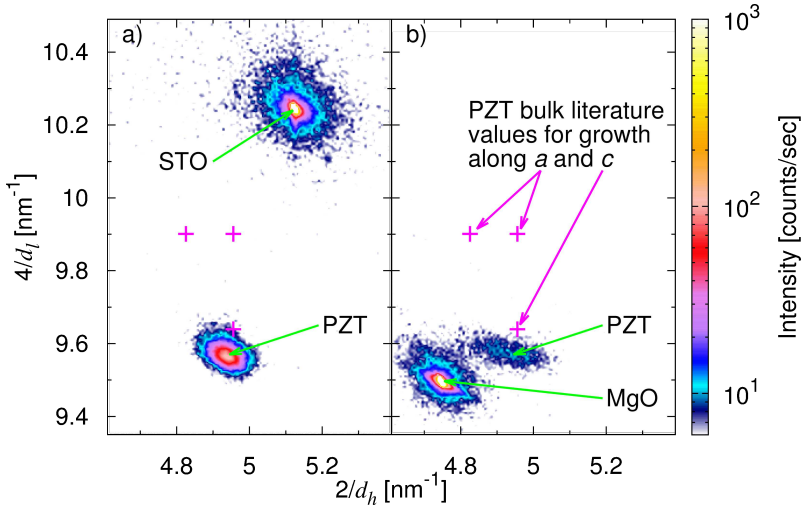

Figure 5.3.: RSMs on the asymmetric (204) reflection of simultaneously deposited LSMO/PZT heterostructures, with the corresponding unstrained locations for a- and c-oriented growth of PZT as indicated. (a): STO/LSMO(6.5 nm)/PZT(88 nm) and (b): MgO/LSMO(6.5 nm)/PZT(84 nm). Pure c-oriented growth with slightly increased lattice constants is apparent. (*Published in* [274], ©2012, CC BY 3.0)

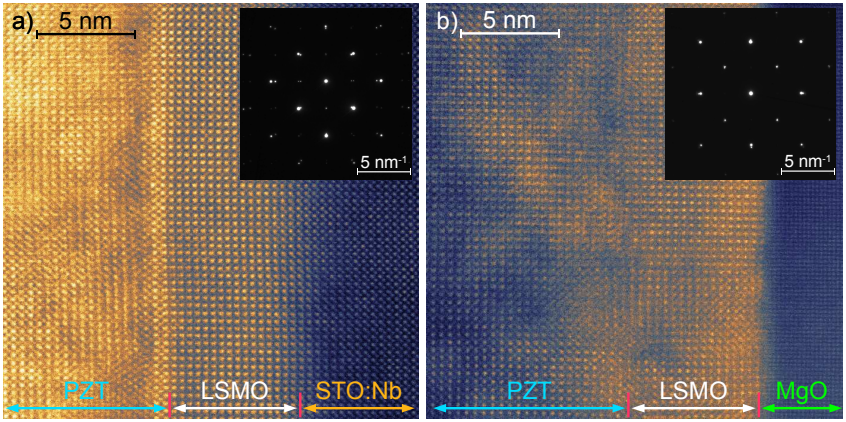

Figure 5.4.: STEM cross-sections of the interfacial region of simultaneously deposited (a): STO:Nb/LSMO(6.5 nm)/PZT(88 nm) and (b) MgO/LSMO(6.5 nm)/PZT(84 nm) heterostructures. The insets show SAED patterns recorded at an equivalent area with similar crystal orientations, covering substrate, LSMO and PZT. (*Published in* [274], ©2012, CC BY 3.0)

instead of 13 %), the LSMO layer still grows cube-on-cube on top of the STO:Nb substrate [Fig. 5.4(a)], confirming the results of the previous chapter (compare Fig. 4.7 on p. 69). The LSMO/PZT bilayer features a very sharp interface. The high compressive misfit strain only allows the first two unit cells of PZT to grow commensurately over the whole investigated range, as evidenced in the atomic number (Z)-contrast STEM image [Fig. 5.4(a)] by the higher intensities on Pb atomic columns compared to La columns. The massive strain relaxation was induced in form of extended dislocations and small highly distorted or even amorphous grains located within a region of ≈5 nm at the interface (for both see Appendix, Fig. A.7 on p. 146).

As evidenced by the Laue fringes in HRXRD [Fig. 5.1(b)], beyond the relaxation region the PZT film shows a coherent crystallinity throughout the entire film thickness (see Fig. 5.5). This fact is also backed by the Selected-Area Electron Diffraction (SAED) measurement [see inset of Fig. 5.4(a)], which exhibits sharp reflections for both layers, LSMO and PZT.

As expected, the LSMO/PZT bilayers deposited on STO and STO:Nb substrates were virtually identical in their microstructural properties.

On the MgO substrate, the tensile misfit strain forces the LSMO layer to immediately accommodate by means of tilting, bending and dislocations (compare Fig. 4.7 on p. 69). The reduced coherence apparently affects the LSMO/PZT interface, blurring it noticeably [Fig. 5.4(b)]. As a consequence, the disturbed interface region extends up to ≈10 nm until the PZT accommodates and forms a single-crystalline layer. Also from the RSM [Fig. 5.3(b)] it can be concluded, that the disorder induced by the strain relaxation of the LSMO layer has significant impact on the PZT crystallinity.

The aforementioned mismatch of the PZT film thicknesses (see Fig. 5.2) of simultaneously grown layers on STO and MgO substrates was also observed in Transmission Electron Microscopy (TEM), where thicknesses of ≈88 nm in contrast to the ≈84 nm were determined, respectively.

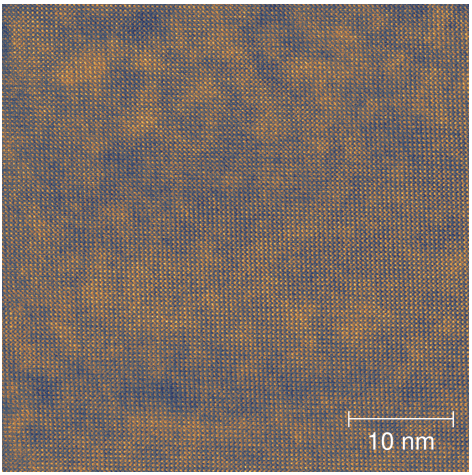

Figure 5.5: STEM micrograph of the single-crystalline PZT microstructure beyond the stress relaxation region at the LSMO interface of the sample shown in Fig. 5.4(a), with the same orientation. Apparent distortions are entailed by sample drift during image capture.

With the PZT *c* lattice constant being identical for both substrates, the cause for this deviation may likely be attributed to the different interface quality.

For elemental analysis, Energy-Dispersive X-ray Spectroscopy (EDX) and Electron Energy Loss Spectroscopy (EELS) were performed in the STEM mode, determining ratios of (56 ± 5) % and (54 ± 5) % for Zr/(Zr+Ti) and Pb/(Pb+Zr+Ti), respectively. As expected, the large target-substrate distance seems to compensate for the PbO loss which normally occurs due to the elevated substrate temperature.

Fig. 5.6 illustrates the elemental distribution across the interfaces in the highlighted mapping region, confirming a generally good sharpness of interfaces with low amount of interdiffusion for all monitored elements except titanium which exhibits a slightly higher diffusivity.

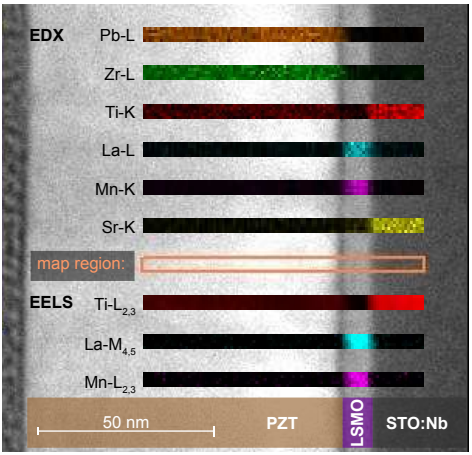

Figure 5.6: Drift-corrected elemental distribution mapping along the surface normal of the STO:Nb/LSMO(6.5 nm)/PZT(88 nm) sample as determined by EDX and EELS.

5.3.2 Ferroelectric properties

For the FE characteristics, the size of the TE is of importance since the likelihood of incorporating crystal defects and pinholes scales exponentially with the area (see Eqn. 3.1 on p. 55). As a consequence, typical lateral dimensions, which are still comfortably accessible in a probe station, are of 50 to 100 μm: an electrode area of 0.05 mm^2 is already considered "large" [250]. Although also FE devices as small as 0.025 mm^2 were investigated, the focus of this report is on devices with a TE area of 1.0 mm^2 – two orders of magnitude larger than common structure sizes – in order to demonstrate the lateral homogeneity of the LSMO/PZT heterostructures and their suitability for future ME tuning.

The disadvantage of such large TEs is that the effective capacity of these FE capacitor devices is so high, that the resistance of the leads – especially of the LSMO BE – significantly increased the circuit's time constant $\tau = RC$. As a consequence, LSMO films thinner than 6.5 nm on MgO substrates did not allow for the saturation of the PZT polarization due to their high resistance. For the same reason conductive STO:Nb was preferred over insulating STO substrates for FE measurements; however, the resistance of the STO:Nb substrates is still in the 10 kΩ range. While

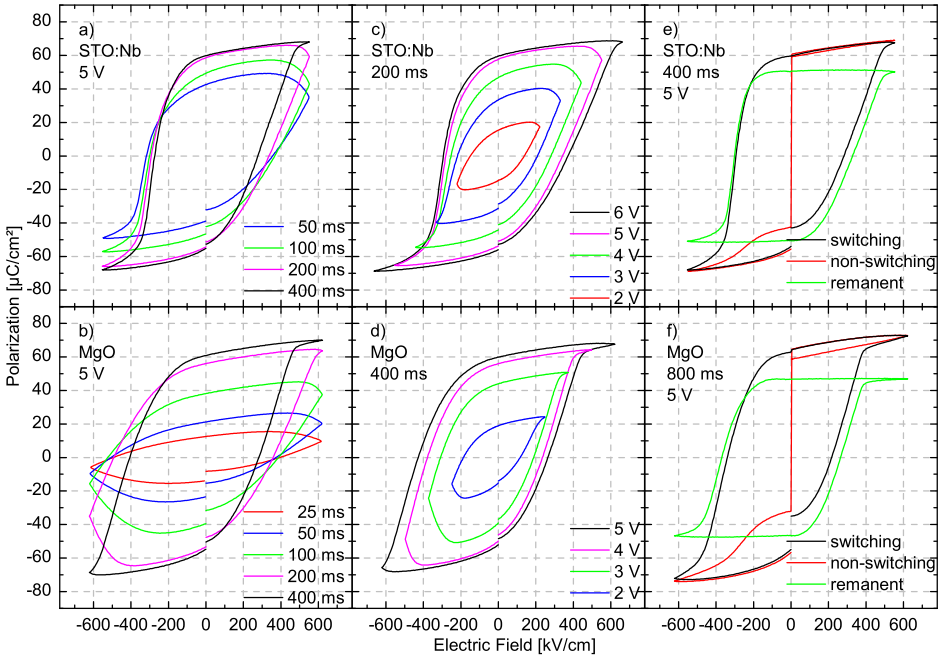

Figure 5.7.: FE properties of 1.0 mm^2 large STO:Nb/LSMO(5.0 nm)/PZT(90 nm)/Au (upper row) and MgO/LSMO(6.5 nm)/PZT(84 nm)/Au (lower row) capacitor structures, with cycle times and voltages as denoted in the graphs; (a)&(b): cycle time dependence; (c)&(d): voltage dependence; (e)&(f): remanent hysteresis. (*Published in* [274], ©2012, CC BY 3.0)

devices as small as 0.025 mm^2 exhibited saturating FE polarization (P) *versus* electric field (E) hysteresis loops at cycle times of 10 ms (100 Hz) and below, the 1.0 mm^2 large devices proved to require much longer cycle times, as shown in Fig. 5.7(a)&(b).

Although the STO:Nb substrate has a lower resistance, enabling faster PZT charging, its combination with LSMO buffer layer brings about an asymmetry in the switching behavior with the right hand side requiring longer time or higher voltage [see Fig. 5.7(c)] to reach FE saturation. This can be explained by the *p-n* junction formed between the LSMO layer and the STO:Nb substrate, which is in reverse bias when applying positive voltages at the STO:Nb, thus causing a voltage drop at the junction and reducing the charging current significantly.

Again, the effect of the electrode charge carrier type on the polarization switching could clearly be seen in PZT films grown directly on STO:Nb without the LSMO buffer layer. They showed very poor performance with low remanence, which is most likely attributed to the fact that STO:Nb as an *n*-type conductor is not a best choice as an electrode for *p*-type PZT thin films [282].

Fig. 5.7(b) illustrates the difficulties in the switching at higher frequencies of PZT layer on MgO/LSMO, due to the high resistance of the LSMO BE. Only at relatively long cycle time of 400 ms, the square-like polarization loops indicate full charging with symmetric charging currents (unlike for the STO:Nb sample with the *p-n* junction). However, another effect, an imprint shift of ≈ -60 kV/cm, becomes apparent. This shift is also present in the STO:Nb samples, albeit disguised by the asymmetric charging currents. The imprint is also the cause for the asymmetry in the MgO samples' hysteresis loops, when the cycle time is too short [Fig. 5.7(b)] or the voltage too low [Fig. 5.7(d)] for full saturation at negative electric fields.

The observed imprint is well known in the literature, especially in cases where the TE and BE materials differ [287], with interpretations and explanations including misfit strain effects and/or oxygen loss at the LSMO/PZT interface [284, 288], electrons and/or Pb vacancies being trapped at the top interface [289, 290], charge compensation for oxygen vacancies generated at the TE interface [290, 291] and defect-dipole complexes due to oxygen vacancies [182, 290, 292] (compare Fig. 3.7 on p. 45).

The dynamic hystereses always contain parasitic contributions, e.g., from linear capacitances and from leakage currents. In order to abstract those from the genuine FE switching, remanent hysteresis loops (see Section 3.7.1) were recorded [Fig. 5.7(e)&(f)].

In the given heterostructures one can see right away that the leakage at positive electric fields is very low in both cases, even at these low cycle frequencies, while there is a significant contribution at negative electric fields. This obvious asymmetry can again be ascribed to the different bottom and top electrode materials. As Scott *et al.* reported [293], there is an *n*-type oxygen deficient region in the PZT located at the metal electrode interface, creating an *n-m* Schottky junction between the PZT and the Au electrode.

Thus, at negative voltages applied to the BE, this Schottky junction is in forward bias, effectively allowing a leakage current, while blocking it when the voltage bias gets reversed.

While the physically meaningful remanent FE polarization (P_r) is determined from the remanent hysteresis loops, resulting in $\approx 50\,\mu$C/cm^2 for the present PZT thin films, it is sometimes difficult to make a straightforward comparison with the values reported in the literature since they are often based on the standard hysteresis loops, where the parasitic contributions are still present (here: $\approx 60\,\mu$C/cm^2). In any case, for the given PZT stoichiometry, the attained value of P_r of the large-distance sputtered PZT films is as high as any of the best, mostly PLD-grown, films reported in literature [282, 283, 294].

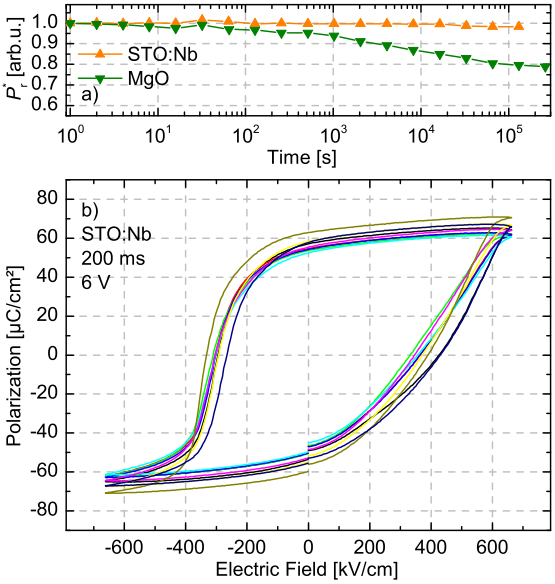

Figure 5.8: (a): Retention of 1.0 mm^2 LSMO/PZT/Au capacitors grown on STO:Nb and MgO. (b): FE hysteresis curves of nine out of twelve 1.0 mm^2 LSMO/PZT/Au devices deposited on a single STO:Nb substrate. (*Published in* [274], ©2012, CC BY 3.0)

Regarding the coercive electric field (E_c), the values reported in the literature are usually 3 to 4 times lower. However, the common thicknesses of epitaxial PZT films are usually around 2.5 to 6 times larger [222, 282, 283, 294] and E_c is known to increase with decreasing thickness [56], especially when metallic TEs are employed [295]. Moreover, epitaxial films are known to have higher E_c compared to textured films [295].

It is worth mentioning that the remarkably good FE properties of the large-distance sputtered PZT thin films are another indication of the correct Pb stoichiometry yielded by this deposition method [178, 216].

Two other figures of merit for FE devices are their retention and fatigue characteristics. The retention measurements are presented in Fig. 5.8(a). There is an apparent difference between the STO:Nb and the MgO samples. While the STO:Nb sample shows virtually no loss of remanent polarization, the MgO sample drops by ≈20 % within three days. The lower retention on MgO can be explained by the defective interface region between the distorted LSMO BE and the PZT, creating a ferroelectrically dead layer which in turn leads to the increased depolarization field inside the PZT layer. As a result in the course of time, the remanent polarization in MgO/LSMO/PZT gets reduced much faster than in STO:Nb/LSMO/PZT.

In this context, the high retention of the STO:Nb sample, which is significantly better than for the RF-sputtered and post-annealed STO/LSMO/PZT systems reported by Ray *et al.* [296], is in good accordance with the superior quality of the interfaces indicated by the XRR measurements and confirmed by the STEM studies.

The fatigue testing was omitted in this study because of the low frequencies required for reliable switching of the device in each cycle. Furthermore, low fatigue is only expected for symmetric perovskite electrodes [282, 283].

Another criterion of the quality of deposition methods of FE thin films is the yield of functioning devices per unit area, which is a measure of thin film uniformity and homogeneity. As stated above, this yield highly depends on the lateral size of the capacitor structure, as the probability for defects scales exponentially with the TE area (see Section 3.7.1). With the LDMS method, the average yields were higher than 50 % on MgO substrates and more than 75 % on STO:Nb; Fig. 5.8(b) illustrates the very similar FE hysteresis curves of nine out of twelve 1.0 mm^2 large devices grown on a single substrate. Assuming a binomial distribution for the defect probability (Eqn. 3.1, on p. 55), the corresponding yields for typical $(100\,\mu\text{m})^2$ devices reach up to $> 99.3\,\%$ and $> 99.7\,\%$ on MgO and STO:Nb, respectively. It should also be noted that this high device yield was achieved without any clean-room equipment and any substrate etching prior to deposition.

5.4 Summary

$PbZr_yTi_{1-y}O_3$ (PZT) thin films with the optimal chemical composition were deposited by means of Large-Distance Magnetron Sputtering (LDMS) from a stoichiometric target without any need for excess PbO adjustment. Using $La_{1-x}Sr_xMnO_3$ (LSMO) as Bottom Electrode (BE) material, the films grew phase-pure and epitaxially on $SrTiO_3$ (STO), $SrTiO_3$:Nb (STO:Nb) and MgO substrates. For the latter, due to the high misfit, the LSMO proved to act as an effective seed layer, stabilizing the perovskite phase of the PZT and leading to a *c*-axis oriented growth.

On STO and STO:Nb, where the LSMO grows commensurately, the presence of this seed layer had no crystallographical implications on the PZT film growth. However, the ferroelectric (FE) properties significantly improved upon introduction of the LSMO BE, as compared to PZT directly grown on STO:Nb. This behavior was attributed to the different types of majority charge carriers in LSMO (*p*-type) and STO:Nb (*n*-type).

With the low-mismatch substrates STO and STO:Nb, the extraordinarily coherent crystallinity of the heterostructures manifested itself through the presence of Laue oscillations in the High-Resolution X-ray Diffraction (HRXRD) patterns of even 90 nm thick PZT layers. Furthermore, superior smoothness of the film interfaces, which is a prerequisite for functional field-effect devices, was directly evidenced by X-ray Reflectometry (XRR) and Transmission Electron Microscopy (TEM). The long polarization retention time observed for the STO:Nb/LSMO/PZT/Au heterostructures indicates that the PZT thin film is ferroelectrically – i.e., also structurally – homogeneous throughout the whole film thickness.

State-of-the-art FE properties were observed for both 1.0 mm^2 large LSMO/PZT/Au capacitor structures grown on STO:Nb and on MgO, featuring high remanent FE polarization (P_r) and pronounced coercive electric field (E_c).

From the technological point of view, with its capability of producing highly crystalline and laterally uniform functional heterostructures with particularly smooth interfaces, the LDMS method once more proved to be a serious competitor for the best-adjusted Pulsed Laser Deposition (PLD) and off-axis sputtering techniques described in the literature. The comparatively low deposition rate is outweighed by its significant flexibility in fabrication procedures, with main advantages encompassing co-and sequential deposition of epitaxial (oxide) Multilayer (ML) systems and a large-area uniformity.

The optimized FE properties of the PZT thin films grown on LSMO as BE material, in combination with the atomically clean interface between these two, provide an excellent starting point for studying the magnetoelectric (ME) coupling phenomena in this multiferroic (MF) heterostructure. This will be the subject of the subsequent chapter.

6 Magnetoelectric coupling in LSMO/PZT heterostructures

Selected parts of this chapter are also published in [297] within the framework of this thesis. The respective paragraphs – with minor conformations included – are indicated by a vertical gray bar at the inner page margin[1].

With the successful deposition of highly epitaxial $La_{1-x}Sr_xMnO_3$ (LSMO)/$PbZr_yTi_{1-y}O_3$ (PZT) multiferroic (MF) heterostructures with distinctive ferromagnetic (FM) and ferroelectric (FE) properties and a particularly smooth interface (Chapters 4 and 5), a good starting point has been reached for the final studies on the magnetoelectric (ME) coupling in such composites. The remaining experimental challenges to be tackled consist of a suitable Superconductive Quantum Interference Device (SQUID) and low-temperature compatible measurement cell design and a sensible data acquisition procedure that allows for a quantitative analysis of the tuning effect. But before delving into these technical details and subsequently presenting the results of this study, the current state of published research in this particular field will be reviewed first.

6.1 Background

The following literature survey can be understood as a logical continuation of the discussion of the MF ME composite systems (see Chapter 1, Section 1.5), where the manganite-based heterostructures were intentionally omitted, in order to first elaborate on their specific electronic and magnetic properties (Section 1.6).

The Colossal Magnetoresistance (CMR) manganites are particularly promising candidates for realization of artificial MF ME composites, due to their sensitivity to changes in the Mn–O–Mn bond angle and the Mn^{3+}/Mn^{4+} ratio, which may be addressed by either strain-mediated or field-effect mediated coupling to an adjacent FE material. As magnetism and conductivity are usually intimately entangled in manganites, the ME coupling effect can be characterized – and maybe exploited – by magnetometry or by transport measurements; the latter is often preferred for its relative experimental simplicity.

One advantage of employing strain coupling to modulate the manganite's crystal lattice, and thus its magnetic and transport properties, originates from the fact that FE bulk substrates with macroscopic thickness – instead of thin films – can be used, whereby leakage issues can be effectively avoided. In an early demonstration of strain-mediated coupling by Lee *et al.* [298] they even refrained from applying external electric fields (E), while solely exploiting the temperature (T)-dependent structural phase transitions of a $BaTiO_3$ (BTO) substrate to reversibly modulate the magnetic moment of an LSMO thin film with a doping level of $x = 0.33$. Later, the same behavior of this system was also observed by Eerenstein *et al.* [245], who additionally performed *in situ* E-field cycling in a Vibrating Sample Magnetometer (VSM).

[1] *Reprinted with permission from* [297]. ©2013, American Physical Society.

A more effective way to provide a tunable biaxial strain is provided by piezoelectric $Pb[(Mg,Nb)Ti]O_3$ (PMN-PT) (001) substrates, in which the crystallographic phase is switchable by an external E-field: initially rhombohedral, the induced transitions encompass two monoclinic phases and a tetragonal phase which is attained at comparatively low fields of ≈10 kV/cm [299]. With LSMO, $La_{1-x}Ca_xMnO_3$ (LCMO) or $La_{1-x}Sr_xCoO_3$ (LSCO) films grown on top of a PMN-PT crystal, the inverse piezoelectric effect can be used to control the in-plane strain of the FM layer by magnetostriction. These kinds of structures were investigated by Zheng *et al.* [300–302], who observed a considerable resistance modulation upon E-field cycling. At the same time, this was confirmed by studies reported by Thiele *et al.* [303] on similar systems. Furthermore, a shift in Curie temperature (T_C) by up to 19 K was observed for 30 %-doped LSMO and LCMO. In all these cases, the strain modulation significantly dominated the FE field effect, which can be easily distinguished by the characteristic shape of the magnetic response to the FE modulation: a strain-dominated modulation results in a butterfly-shaped response, which resembles a typical piezoelectric strain curve and is therefore independent of the sign of the external E-field. In analogy, a field-effect dominated response can be identified by the characteristic hysteretic shape of the FE polarization loop. Zhu and Zheng *et al.* [302] have found that in the case of a PMN-PT/LSCO system the competition between strain and field-effect coupling is a function of T, while the strain coupling strongly dominated at Room Temperature (RT): the balance continuously moved towards field-effect coupling for lower T. Below 170 K a nearly undisturbed hysteretic response was observed.

By employing FE thin films instead of FE bulk substrates, the device design can be changed to structures which are much more likely to be implementable in integrated circuits, not only due to the drastically reduced poling voltages, but also due to the fact that more standard substrates can be used for the production process. Of course, a thin-film based layout poses all the challenges of manufacturing FE thin films with reasonably low leakage. Furthermore, the inverse piezoelectric effect in epitaxially grown FE thin films tends to be hampered by substrate clamping effects [62, 304, 305], which thus impedes the strain-mediated ME coupling.

Electric transport measurements performed by Thiele and Dörr *et al.* [55, 304, 305] on MF bilayers of PZT and a manganite revealed a mostly strain-dominated ME coupling. It was found that the latter was not outshined by the otherwise stronger field-effect coupling for two reasons: On the one hand, the manganite's doping level was chosen to be close to the plateau region of the phase diagram (e.g., $x \approx 0.3$ for LSMO), where changes in the carrier density have less effect. On the other hand, an increased manganite thickness favored the strain effect [305].

In contrast, when a FE thin film is mainly employed as stronger replacement for a high relative permittivity (κ) dielectric or electrolyte gating, then any piezoelectric-magnetostrictive coupling component is unwanted. As the latter is a long-range effect, it can be diminished in favor of the short-ranged field effect by reducing the thickness of the tunable FM layer towards a value that comes close to the electric field screening length. However, a minimum thickness is often imposed by adverse side-effects that may compromise the manganite's magnetic properties.

The majority of published studies cover the modulation of transport properties, mostly electrical resistance [55, 304–310] but also magnetotransport [52, 53, 311] and multiferroic tunnel junctions [311]. The sheet resistance modulation (Mott transition) in a FE field-effect transistor FE-FET structure is comparatively easy to produce as it does not require large defect-free FE layers.

A modulation of the channel resistance by 300 % was reported by Mathews *et al.* [306], employing 30 to 50 nm thick $La_{0.7}Ca_{0.3}MnO_3$ channels. Pallecchi *et al.* [53] achieved an on-

off ratio of 250 % in a side-gated geometry with a 7 u.c. thin $La_{0.7}Sr_{0.3}MnO_3$ channel and $SrTiO_3$ (STO) as gate dielectric. An electrostatically induced shift of 43 K was observed in the metal-insulator transition temperature (T_{MI}), similar to a 50 K shift reported by Hong *et al.* [309]. In $La_{0.85}Ba_{0.15}MnO_3$, a shift of 1.5 K was achieved by Kanki *et al.* [307] – comparatively low, but in contrast to the aforementioned with the magnetic transition taking place around RT. They also demonstrated a mostly linear behavior of both the resistivity modulation and the shift in T_{MI} with respect to the remanent FE polarization. Later the resistance modulation was shown to be accompanied by a modulation of the magnetization [308].

The RT Mott-transition in Field-Effect Transistors (FETs) based on thin films of PZT (200 to 300 nm) and either LSMO, LCMO or LSCO (3.5 to 5 nm) was recently investigated by Hoffman *et al.* [310], in terms of switching speed, data retention and device scalability. As a result, switching speeds down to 80 ns were achievable and only limited by the device-specific time constant $\tau = RC$. This fact and the successful implementation of a cross-point array of four independently switchable devices (measured at 125 K) demonstrated that manganite/PZT based FET devices may be suitable for integrated circuits.

Besides any potential applications, the study of electrostatic tuning of magnetism in electron hole (h^+) doped manganites can lead to new insights into the fundamental physical mechanisms because of the absence of the extrinsic effects of distortion and disorder inherent in chemical doping. However, the investigation of magnetic effects in manganite/FE composite systems is a challenging task as it requires a setup which allows for polarization of the FE and measuring the magnetization, preferably at variable magnetic field (H) and T.

On the one hand Magneto-Optical Kerr Effect (MOKE) is commonly preferred for *in situ* charging experiments over the SQUID magnetometry [54, 247–249, 308] – despite possible side-effects originating from the FE material [312], like e.g., the electrooptic Kerr effect [98, 313] – because the required size of the tuned area can be relatively small. On the other hand, as a SQUID provides a direct quantitative information, it is usually employed for calibration of the MOKE results on, presumably similar, reference samples.

Some of the most remarkable results on magnetic modulation of $STO/La_{0.8}Sr_{0.2}MnO_3/PbZr_{0.2}Ti_{0.8}O_3$ heterostructures were reported by Molegraaf, Vaz and co-workers [247–249], featuring a shift of the FM T_C of 20 K and modulations of the magnetization of ≈20 % with a change of the sign of the modulation at ≈150 K. After correlating the low-T relative change in magnetization and the surface charge density modulation ΔP_r, the pronounced tuning effect was attributed to the formation of an antiferromagnetic (AF) phase which was theoretically predicted by Burton *et al.* [314]. However, those *ab initio* calculations were based on a high doping level of $x = 0.5$ and fully-strained BTO as top-gate FE and did not address the experimentally evident presence of a FM phase showing a pronounced shift in T_C.

Presumably in an attempt to attest this theory, Lu, Burton *et al.* [315] recently investigated FE tuning of BTO-gated LSMO with a relatively high doping level of $x = 0.33$ and thicknesses of 10 to 50 nm in a SQUID magnetometer; the necessary large FE device area was *ex situ* polarized employing a non-contact scanning probe tip, in order to avoid leakage current problems. While a ≈10 % magnetic modulation in h^+ depletion mode was observed at RT, no evidence for the expected AF coupling in accumulation mode was found. The large magnetic tuning effect was explained by a drastically increased screening length caused by a metal-to-insulator transition in the interfacial volume of the LSMO. It should be noted that for this heterostructure no shift in T_C and no crossover in the sign of the effect was found in the investigated T range.

The same LSMO chemical doping level was also studied by Brivio *et al.* [54], employing top- and bottom-gating with STO thin films, where a shift in T_C of 5 K was found in a 3 nm thin LSMO film. In the course of studies an important observation was made that an effective magnetic modulation could only be achieved in top-gating geometry. The absence of the effect for the bottom-gating configuration was ascribed to a magnetically dead layer at the bottom LSMO interface of about 2 nm thickness.

Although the dead layer issue was already dealt with in Section 3.2.1, this topic shall now be revisited for its direct implications on field-effect tuning devices.

X-ray Absorption Spectroscopy (XAS) studies performed by Vaz *et al.* [249] confirmed that for the LSMO/PZT *top*-gate system each FE remanent charge is screened by mobile charges in the LSMO layer. This is another strong evidence for the absence – or at least irrelevance – of a dead layer at the LSMO *top* interface. Fig. 6.1 illustrates the assumed location of the dead layer on a schematic cross-section of a typical arrangement of a LSMO/FE heterostructure.

The existence of magnetically dead layers is a well-known fact for manganite perovskites [172, 174, 237, 238, 316] and their thickness was found to extend up to 2 to 5 nm, depending on the substrate. So far, in all reports on the successful modulation of magnetic or transport properties, the manganite layers have always been thicker than the minimal dead layer thickness. Despite the crucial role of the dead layer in the correct estimation of the total magnetization of the whole LSMO layer – and thus its impact on the *relative* amplitude of the Kerr signal – only few reports on manganite field-effect devices mention or consider the existence of the dead layer [53, 54, 309] and none of the quantitative evaluations of the magnetic modulation account for it.

In the present work an approach to circumvent the uncertainty caused by the dead layer factor is presented by directly correlating the absolute magnetic modulation Δm_{tot} with the *in situ* measured total remanent charge modulation ΔQ on the entire samples. Unlike MOKE, the SQUID magnetometry can directly deliver quantitative magnetization data with unrivaled accuracy and sensitivity. Provided that the space charge region is not disturbed by the dead layer – i.e., the investigated LSMO layer is thicker than the maximum dead layer thickness plus the maximum expected screening length [314]: $5\,\text{nm} + 3\,\text{u.c.} \approx 6.2\,\text{nm} < d_{LSMO}$, and assuming that

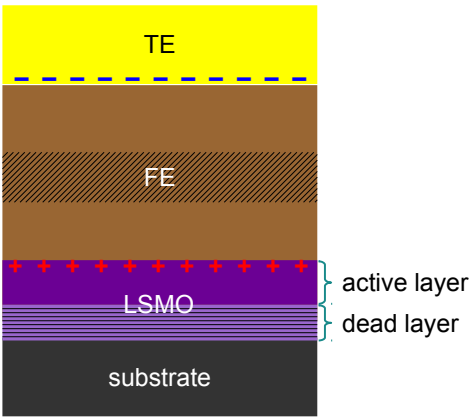

Figure 6.1: Schematic cross-section of an example LSMO-based multiferroic heterostructure, showing the LSMO dead layer formed at the bottom interface. The displayed charges represent the polarization in h^+ accumulation state. The displayed thickness of the FE layer is contracted (hatched area) for clarity.

each FE remanent charge is screened by mobile charges in the LSMO layer [249], the magnetic modulation per charge can be monitored directly.

In situ charging allows for best comparability of the charge states, since *ex situ* charging requires the sample to be removed from and re-installed into the SQUID system [315, 317], which is known to be error prone due to sample handling and mounting variances [231, 232].

A practical challenge for *in situ* charging experiments lies in the requirements for the lateral size of the field-effect device. Since the electrostatic doping is an interface effect, a relatively large device area of several square millimeters is necessary to deliver a significant signal-to-noise (s/n) ratio[2]. This demanding lateral homogeneity of the FE thin films with complete absence of fatal pinholes over a large area has been accomplished by Large-Distance Magnetron Sputtering (LDMS) (see Chapter 5).

In the following it will be shown that the LDMS-grown LSMO/PZT heterostructures possess characteristics, which prove the charge modulation as the sole cause of the ME response, while any contribution from inverse piezoelectric-magnetostrictive coupling can be safely neglected.

The quantitative SQUID tuning data will be compared with the results of Molegraaf, Vaz *et al.* [247–249], including a critical discussion of the impact of a magnetically dead layer on these measurements.

Eventually, the dependence of the ME modulation on T, induced surface charge modulation and the shape of the Field Cooling (FC) curve will be elaborated with a focus on the interplay of AF and FM coupling in this electrostatically controlled interface.

6.2 Experimental details

Although, as presented in Chapter 5, LSMO/PZT heterostructures with suitable FE properties were also grown on MgO substrates, these samples are not suitable for tuning experiments due to the unstrained LSMO's transition into the FM insulating phase at low T (compare Fig. 4.8 on p. 70), which effectively frustrates the FE charging. For this reason (100)-oriented, conductive $SrTiO_3$:Nb (STO:Nb) was chosen as substrate material and $La_{0.87}Sr_{0.13}MnO_3$ and $PbZr_{0.52}Ti_{0.48}O_3$ thin films were Radio Frequency (RF) sputtered on top by means of LDMS, as described in Chapter 4 and Chapter 5 (or [237, 274]).

The thicknesses of the functional oxide layers had to be chosen carefully in order to optimize the properties of the ME devices:

On the one hand a reduction in LSMO film thickness results in reduction of magnetic transition temperatures but on the other hand it increases the relative magnetic modulation by increasing the ratio of tuned to untuned volume.

Furthermore, as stated above, a lower thickness helps reduce (long-range) piezoelectric strain effects on the LSMO film.

Thus, a thickness of 7.2 nm was found to provide a good compromise; the film was also thick enough as not to be affected by the magnetic dead layer. For the PZT layer 90 nm thickness was chosen, being thick enough to be pinhole-free over large areas and thin enough to be – even at low T – fully polarizable in the voltage range of the FE tester (± 10 V). A reduced PZT film thickness also helped reduce the inverse piezoelectric effect by decreasing the – for the 52/48

[2] With a sensitivity of 10^{-8} emu, the SQUID magnetometer can detect $\approx 10^{12}\,\mu_B$; in a classic approximation this is equivalent to $\approx 10^{12}$ electrons.

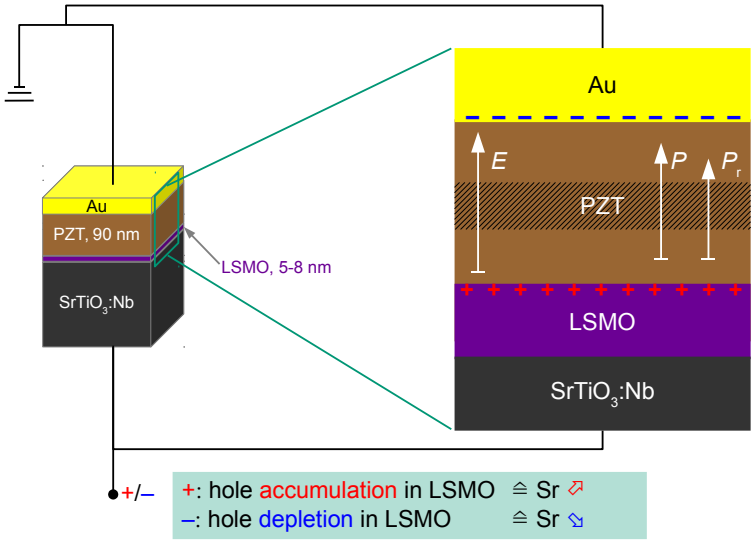

Figure 6.2.: Schematic cross-section of the STO:Nb/LSMO/PZT/Au ME device. The displayed polarity, charges and field vectors represent the h^+ accumulation state.

PZT composition otherwise relatively high – d_{33} piezoelectric coefficient [178, 318] which could induce magnetostrictive coupling in the LSMO layer [305].

An array of 1 mm × 1 mm large Au top electrodes of 25 nm thickness was deposited through a shadow mask by Direct Current (DC) sputtering. Then each of the FE capacitor devices was tested and the device area was measured in an optical microscope.

A schematic cross-section of the layer sequence and the electrical wiring is shown in Fig. 6.2, illustrating the basic idea of this setup. The accumulated charges in the screening region of the LSMO layer modulate the Mn valency in a way which is – in first approximation[3] – equivalent to a reversible modulation of the Sr doping level.

It should be noted that in the present setup – differently from the usual FET nomenclature – the positive electrode was connected to the bottom contact and the negative one to the top-gate contact. This assignment was chosen because the drive electrode of the FE tester is recommended to be placed on the common bottom electrode in order to reduce noise pickup. Besides, this way the sign of the applied voltage corresponds to the induced screening charge in the LSMO layer, which can directly be interpreted as h^+ accumulation and depletion, respectively [4].

Reciprocating Sample Option (RSO) SQUID measurements in an in-plane geometry were carried out in a Quantum Design *MPMS XL5* magnetometer which was accordingly modified to allow for attaching up to four independent electrical connections (see Section 3.8.2). To avoid any spurious signal, solely diamagnetic materials were chosen for contacting the samples.

The sample was bonded to a Cu backing plate which was used as a bottom electrode and the triaged FE devices were bundled into two sets, where each one was addressed with a separate

[3] This naïve picture will be put into perspective later on in the discussion (Section 6.4).

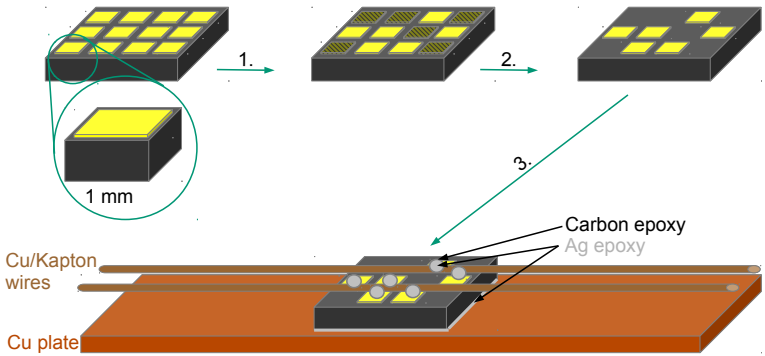

(a) schematic workflow of device preparation

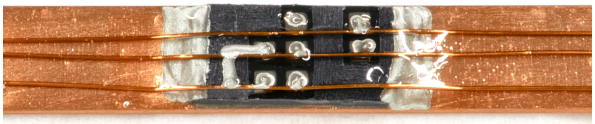

(b) top view of SQUID-ready device

Figure 6.3.: SQUID-compatible contacting and wiring of the ME device. (a): Schematic workflow consisting of triaging of the FE capacitors after deposition of the square Au TEs (1.), (optional) removal of broken FE capacitors – and thus untuned LSMO area – with a diamond (2.) and contacting/wiring of BE and TEs using conductive epoxies and finally securing the whole setup with an insulating epoxy coating (3.). (b): Example of a SQUID-ready device with seven 1 mm^2 capacitors bundled into three sets.

Kapton-coated Cu wire (see Fig. 6.3, depicting an example with three sets). All Cu parts were designed to extend uniformly along the whole sample space (i.e., beyond the RSO scan range). Conductive carbon and silver epoxies, which had been tested for low-T SQUID measurements, were employed for bonding of the top and bottom contacts.

The carbon epoxy was found to be needed as a buffer layer between the Au Top Electrode (TE) and the silver epoxy, in order to prevent the FE devices from premature Time-Dependent Dielectric Breakdown (TDDB), which is supposedly caused by dendritic growth of Ag whiskers driven by the DC E-field [319].

Transparent epoxies were employed to insulate the conductive substrate prior to application of the conductive ones. To protect the sensitive surfaces, a soft nylon filament[4] was used for spreading the epoxies. After each processing step, the respective epoxy was cured for at least 1 h at ≈125 °C on a hot plate. Details of all employed epoxies are specified in Tab. A.3 (p. 141).

The role of the Cu backing plate was twofold: first it served as a bottom electrode, but it also acted as an effective heat sink for possible Ohmic heating, keeping the sample in thermal

[4] A piece of a fishing line, in fact.

equilibrium. In fact, during the successive RSO measurements, no temperature-drift induced signal modulation was detected at any time.

The FE measurements were carried out with a RADIANT TECHNOLOGIES *RT66B* tester. Due to the considerable device area of the combined sets ($2.2\,\mathrm{mm}^2 + 3.9\,\mathrm{mm}^2 = 6.1\,\mathrm{mm}^2$), which means large capacitance (C), and the comparatively high resistance (R) of the STO:Nb substrate, the sample required longer voltage sweeping periods of around 200 to 400 ms to reach polarization saturation. Especially at low T, the parameters needed to be adjusted towards higher voltage and cycle time to compensate for the increased FE coercivity due to the reduced switching speed [56, 218].

For a number of reasons, all magnetic modulation measurements were deliberately performed in FE remanence mode: First of all, the SQUID magnetometry is slow (≈20 s per data point) in comparison to the MOKE one, and a high DC bias voltage applied for longer times would result in degradation, Ohmic heating and ultimately in TDDB of the PZT thin film [223]. Secondly, if due to the degradation processes the overall leakage current rises to about 10 μA, the ensuing current loop can become detectable and distort the actual measurements (see Section 3.8.1). Thirdly, the actually applied charge at the LSMO/PZT interface cannot be reliably determined for statically biased devices, as the real charging current cannot be distinguished from the leakage currents. On top of that, the continuous application of static or periodic bias fields could not only induce thermal effects but also chemically alter the LSMO layer through the migration of oxygen vacancies into the oxide electrode [282, 320]. Using dynamic FE hysteresis measurements for calibration is also not sufficient to adequately determine the saturation polarization due to its inherent vulnerability to frequency-dependent artifacts [213, 220]. In summary, the remanent polarization of a FE is much better defined and can be determined by subtraction of the integrated charge of a non-switching pulse and a switching pulse (Positive-Up Negative-Down (PUND) [220]).

In the present experiment, repetitive RSO measurements were performed in between the triangular PUND test impulses, which were utilized to polarize the PZT and calculate the actual charge accumulated on the whole sample. Analogously, the total magnetic modulation was then calculated as the difference of the magnetizations for opposite FE polarization states.

The benefit from observing only the difference signal is that all unaffected magnetic moments – from untuned LSMO volume and possible spurious contributions from the contacting setup – are automatically canceled out. As this is an absolute measurement, the thickness of the dead layer is also irrelevant as long as the film is thick enough to accommodate the dead layer plus the full screening length. The magnetic modulation measurements were usually performed at relatively low fields of 100 to 200 Oe, below FM saturation, so as to avoid field induced distribution of the magnetic transition temperatures. The other concern was that high magnetic fields could introduce adverse side-effects on the charging behavior of the FE devices due to the modulation of the magnetoresistance of the LSMO bottom electrode [321].

The dependence of the sharpness of the magnetic transition on the external field is demonstrated in the series of FC curves shown in Fig. 6.4. While the Full Width at Half Maximum (FWHM) of the derivative is significantly smaller at lower fields, at high external field even the low-T behavior at around 50 K is affected. It is worth mentioning that these FC curves belong to the same sample whose data will also be presented in Figs. 6.6 to 6.11.

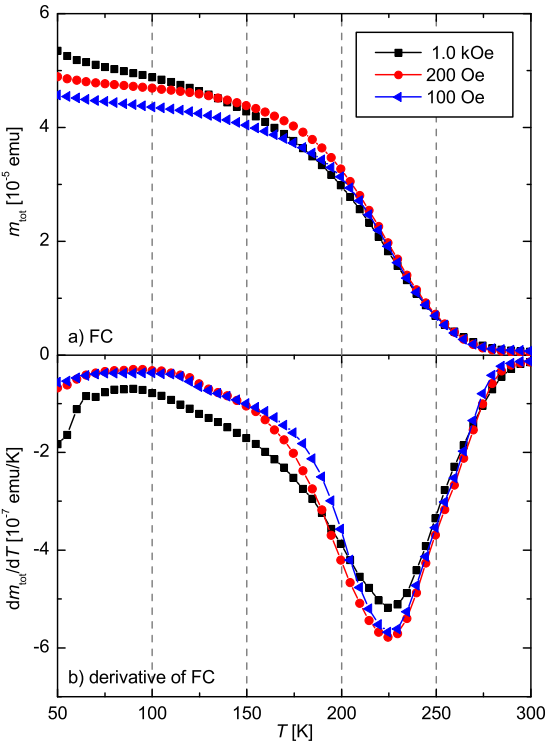

Figure 6.4: Magnetic field dependence of the magnetic transition: FC curves recorded at different external fields (a) and their numerical derivatives (b).

6.3 Results

Although for the main investigations all measurements were carried out exclusively in FE remanence, some preliminary ME tuning results with applied DC E-field will be presented for comparison.

6.3.1 Preliminary studies: DC-biased measurements

More as a proof of principle and for exploring the TDDB limits, some devices were exposed to continuous DC bias voltages instead of merely applying short switching pulses. The side benefit of this method is that even samples with insulating STO substrates could be charged sufficiently, exhibiting similar magnetoeloectric tuning behavior like their simultaneously grown counterparts on conductive STO:Nb. However, due to the large device areas, the leakage current, although unwanted, always plays an important role in these measurements.

An example of the reversible tuning of the magnetic moment by application of a constant E-field modulation at successively reduced T is shown in Fig. 6.5(a). In the corresponding FC measurement in Fig. 6.5(b) the investigated temperatures are highlighted.

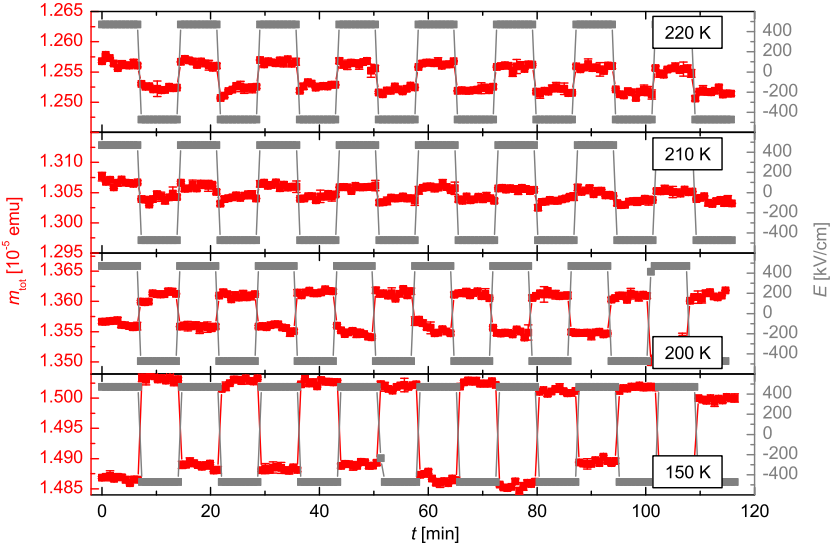

(a) on STO:Nb: magnetic modulation at various temperatures

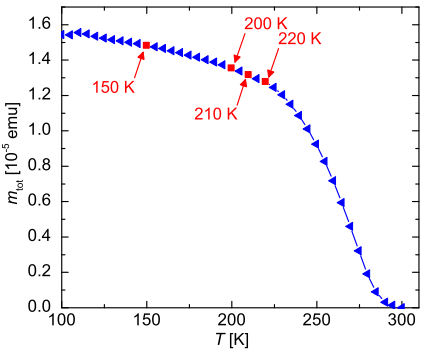

(b) on STO:Nb: FC measurement

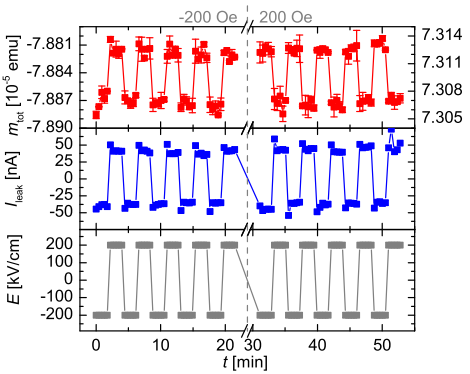

(c) on STO: magnetic modulation at −200 Oe and 200 Oe

Figure 6.5.: Magnetic modulation of a STO:Nb/LSMO(8 nm)/PZT(85 nm) sample with external bias voltage applied, measured at 100 Oe (a). For better comparability of the magnitude of the effects, the axis intervals of the magnetic moments in have identical spans. The temperatures where the magnetic tuning was recorded are highlighted by red square symbols in the FC curve (b). (c): Verification of the tuning effect by reversal of the external field, measured at 100 K on a similar sample with insulating STO substrate.

From these preliminary results it can already be seen that the previously reported crossover of the ME tuning effect (compare Fig. 2.6 on p. 33 or [4, 247]) is indisputable for this device setup: While at 220 K the application of a positive potential to the LSMO layer results in an increased magnetic moment, the effect reduces significantly around 210 K and reverses its sign for lower T. At 150 K the magnitude of the modulation is very pronounced, bringing about a remarkably good s/n ratio, although the FE device area for this sample only measured 1.1 mm^2. However, these in-E-field measurements can only give a qualitative impression of the ME tuning, since the actual FE polarization (P) is not known and, more problematically, the leakage current is always present in the measured signal.

Fig. 6.5(c) illustrates the magnetic tuning for a 2 mm^2 large FE device area of a LSMO/PZT heterostructure grown on insulating STO, consecutively measured at external fields of −200 Oe and 200 Oe[5]. It evidences both the aptitude of the insulating substrate for DC-biased measurements, as well as the negligible impact of artifacts caused by the leakage current (I_{leak}), since the tuning effect changes sign with the external magnetic field. Usually, the leakage-dominated signal is fairly plain to identify as its *sign*, unlike the real tuning, is independent of T and H.

In general, accounting for the leakage is virtually impossible as it depends on T, the polarity and – fatally enough – on the bias-stress and fatigue history of the FE. Usually the lifetime of the samples was not much longer than needed for the measurements shown in Fig. 6.5, as the continuous application of a DC bias eventually resulted in TDDB; the larger the device area, the earlier the breakdown. The post-TDDB leakage current created artificial modulations of the magnetic moment which were of the same magnitude as the actual ME tuning signal.

6.3.2 Measurements in FE remanence

The measurements performed in FE remanence allowed for larger active device areas while still maintaining a very long sample lifetime. Provided that a sensible choice regarding cycling frequency and poling voltage is made, the PZT can be preserved from breakdown, allowing for a large number of measurements on the same device[6]. However, the challenge lies in the necessary adjustment of the parameters affected by the strong T dependence of the FE switching behavior.

The T dependence of the magnetic modulation upon charging and the corresponding FC curve are shown in Fig. 6.6. In order to avoid any assumptions about the dead layer (FC curve, $m_{\square}$) and the screening length (magnetic modulation curve, $\Delta m_{\square}$), both curves are merely normalized on the unit cell area (u.c.^{2}), accounting for the entire LSMO sample area in the first case and for the FE device area in the latter case[7]. For the modulation measurement the FE charge density modulation was kept at $\Delta P_{\text{r}} \approx 20\,\mu\text{C/cm}^2$ ($\approx 0.19\,h^+/\text{u.c.}^2$), which required an adjustment of the FE cycle time to compensate for the temperature drift of the FE switching process. An unchanged magnetic modulation after one day confirmed the previously assessed good FE retention of the PZT thin films (compare Fig. 5.8 on p. 91).

This particular measurement, and the ones shown in Fig. 6.8, were performed on a reduced device area (2.2 mm^2); thus their statistical error is larger. For all other presented measurements

[5] The difference in $|m_{\text{tot}}|$ is caused by the differing magnetic history of both states.

[6] All measurements presented in Fig. 6.4 and Figs. 6.6 to 6.11 (plus Fig. A.8) belong to the very same sample, thus enabling highest comparability.

[7] The screening length itself may even get altered by the FE tuning itself [315].

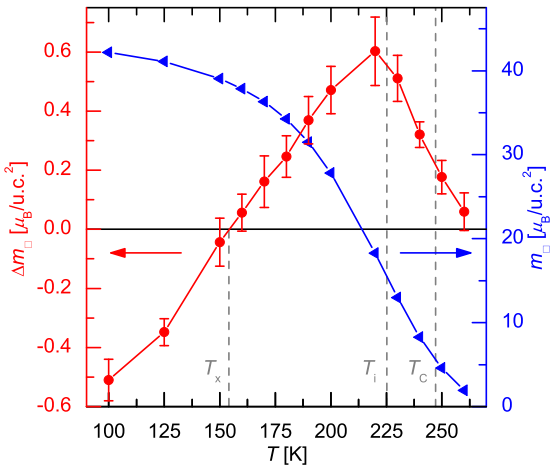

Figure 6.6: Temperature dependence of the magnetic moment per u.c.[2] ($m_\square$) and its modulation ($\Delta m_\square$) for a remanent charge modulation of $\approx 20\,\mu\mathrm{C/cm^2}$ measured at an external field of 200 Oe. T_C, T_i and T_x indicate the Curie temperature (247 K, as determined by Arrott's method [265]), the FC inflection point temperature and the crossover temperature of magnetic modulation, respectively. (*Published in* [297], ©2013, American Physical Society)

in this chapter, where no error bars are shown, the statistical errors are smaller than the symbol sizes.

The magnetic modulation, i.e., the difference of the (unit-cell area normalized) magnetic moments in h^+ accumulation and depletion state, $\Delta m_\square = m_{\square,\mathrm{acc}} - m_{\square,\mathrm{depl}}$, follows the temperature behavior which is expected for low-doped LSMO (compare Fig. 2.6 on p. 33 or [248]). There are three distinctive regimes [247] with a local maximum around the point of inflection T_i of the FC curve, a crossover of the tuning effect at T_x and a reversed sign at lower T (see also Fig. 2.6 on p. 33).

Compared to similar studies with thinner manganite layers [247, 248], the selected LSMO thickness of the LSMO layer of 7.2 nm evidently helped maintain a high Curie temperature of about 247 K even for this low Sr doping level.

In order to verify the genuineness of the magnetic tuning effect, the external magnetic field was also reversed, resulting in an expected reversal of the modulation (see Fig. A.8 on p. 147). Also by varying the number of simultaneously polarized sets of FE devices it could be shown that the magnitude of the modulation scales with the device area.

Fig. 6.7 illustrates the response of the magnetization to the polarization switching of the PZT film and the remanent FE hysteresis for comparison[8]. For the magnetic measurement successively stepped triangular voltage pulses were applied and the magnetic moment of the sample was recorded in the intervals between the pulses. The discrepancy in coercivity and saturation behavior originates from the difference in the time constants of both experiments – for the magnetic modulation curve the E-field for each data point was set by a 200 ms monopolar triangular pulse, while the same pulse duration was used for the full bipolar FE hysteresis.

An essential outcome of this experiment is the fact that both curves are strikingly similar, evidencing a purely electrostatic coupling mechanism with negligible piezoelectric influence. The

[8] For better comparability, both curves are centered with respect to the polarization and magnetization modulation and the latter axis is flipped. Centering of FE hystereses is a common practice, as the net polarization – i.e., the constant of current integration – is not well-defined.

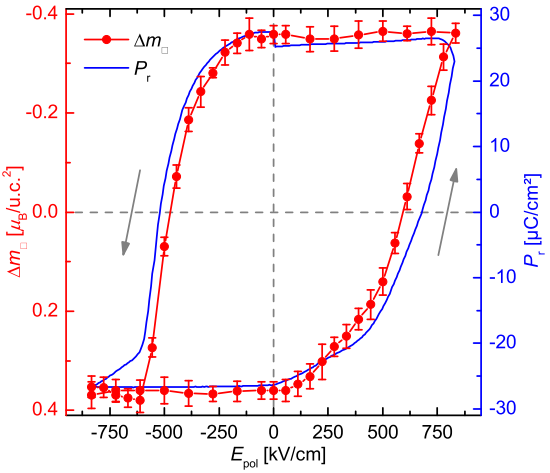

Figure 6.7: Comparison of the FE remanent hysteresis P_r and the response of the magnetic modulation per unit cell area $\Delta m_\square$. Both curves measured consecutively at 50 K and 100 Oe. (*Published in* [297], ©2013, American Physical Society)

lack of the inverse piezoelectric effect is actually expected from the fact that the measurements are carried out only in FE remanence mode, which does not distinguish remanent ferroelastic strain states of the *c*-oriented tetragonal PZT [180]. Furthermore, the apparent absence of any butterfly shaped contribution to the magnetic response loop evidences the insignificance of possible strain-driven contributions caused either by the varying number of 180° FE domain walls for different remanent states of the single-crystalline PZT or by the existence of differently oriented PZT grains in the 5 nm thick relaxation region at the LSMO/PZT interface.

The temperature dependence of the magnetic response to the remanent FE hysteresis is illustrated in Fig. 6.8. The two hystereses represent the switching behavior at the negative and positive regimes of the tuning effect within the temperature range investigated in Fig. 6.6. The difference in coercivities is caused by the temperature dependence of the PZT characteristics and the FE imprint shift induced by the electrode configuration (see Section 5.3.2).

In order to methodically investigate the change in magnetization as a function of the charge modulation ΔQ, the magnetization was recorded for a series of decreasing PUND poling voltages U_{pol} (see Fig. A.3 on p. 142) well below the transition temperature[9]. As Fig. 6.9(a) (and Fig. 6.7) illustrates, the magnetic signal shows very low noise fluctuations and high stability over time. The repetition of the maximum 7.5 V cycle at the end of the sequence confirmed the reproducibility of the charging process. The asymmetry in the decay of the modulation amplitude for positive and negative charging could be ascribed to the previously recorded characteristics of charging currents; the positive half of the FE polarization hysteresis required higher field (or longer time) to reach saturation while the negative side saturated at rather low fields (compare Fig. 6.7 and Section 5.3.2). Unfortunately, charging asymmetry cannot be discerned by the common current integration measurements, because, as already argued, the constant of integration is not known. Although an asymmetric magnetic response of the LSMO to the FE charging cannot be excluded, the relative change of the polarization, however, is well-defined.

[9] A quantitative analysis of the effect around T_C is not meaningful, as the magnitude depends on the sharpness of the magnetic transition.

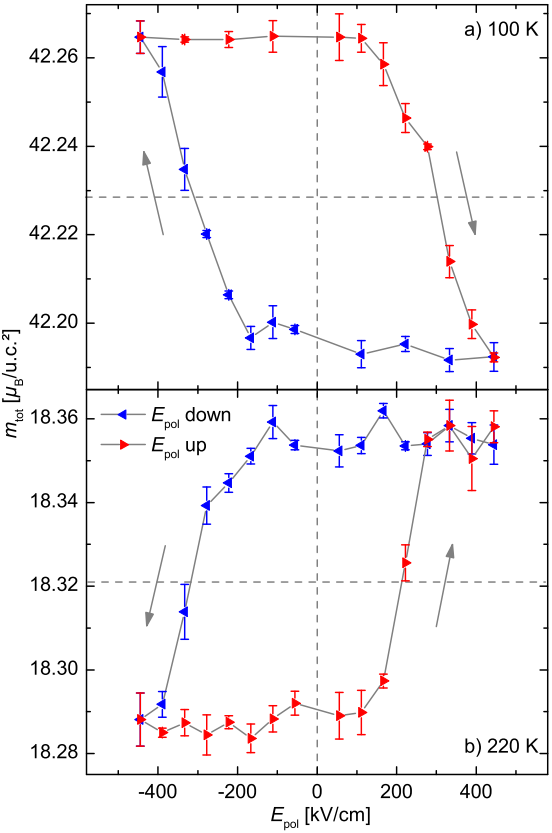

Figure 6.8: Temperature dependence of the magnetic response to the FE remanent hysteresis, measured at an external field of 200 Oe, below (a) and above (b) the crossover temperature T_x. The dashed crosshairs are guides to the eye. (*Published in* [297], ©2013, American Physical Society)

Fig. 6.9(b) shows the absolute magnetic modulation Δm_{tot} as a function of ΔQ as derived from the PUND tests performed in between the magnetic measurements; the 100 Oe curve corresponds to the raw data shown in Fig. 6.9(a). In order to investigate the magnetic field dependence at ±7.5 V, the magnetic modulation was also measured for various fields up to FM saturation. The dashed curve was calculated by scaling the 100 Oe measurement to the value at 2 kOe as a good estimate for the tuning behavior for saturated magnetization.

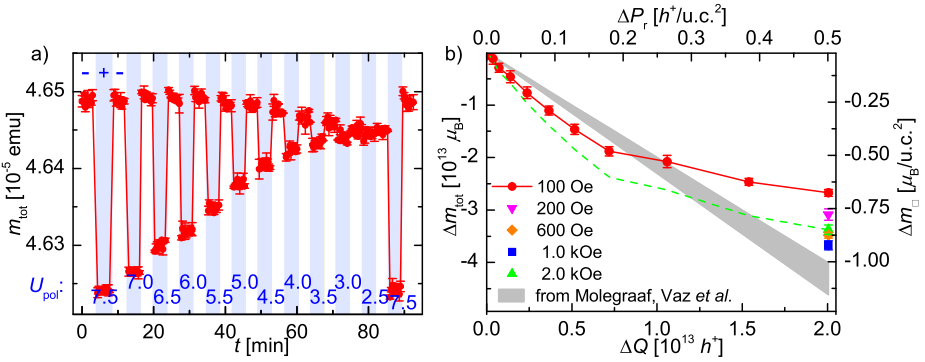

Figure 6.9.: Dependence of the magnetic modulation on the induced charge modulation at 50 K. (a): Raw data illustrating modulation of total magnetic moment at an external field of 100 Oe with the measurements recorded in remanent FE polarization after polarizing as indicated by U_{pol} and the shaded background. (b): Magnetic *versus* charge modulation ΔQ both of the whole sample (Δm_{tot}) and normalized on the LSMO unit cell area ($\Delta m_\square$), respectively. The 100 Oe curve corresponds to the raw data in (a); other fields are shown for comparison; the dashed line visualizes the 100 Oe curve scaled to the saturation moment at 2 kOe. The gray shaded area marks the tuning efficiency as estimated from [247–249]. (*Published in* [297], ©2013, American Physical Society)

6.4 Discussion

The preliminary studies on electrolyte-gated LSMO nanopowder, presented in Chapter 2, revealed a characteristic temperature behavior of the magnetic modulation with a maximum around T_C. Furthermore, a crossover of the effect at lower temperature was evidenced. A side-by-side comparison of the temperature dependence with the present FE thin film gating approach is shown in Fig. 6.10[10].

For best comparability, the results of nanopowder tuning are shown – unlike in Fig. 2.5(b) in Section 2.3 (p. 32) – without normalization to the mass magnetic moment (σ_m). For the thin film system, σ_m and its modulation $\Delta\sigma_m$ are normalized on the LSMO mass with respect to the total sample area (18 mm^2) and the actual FE device area (2.2 mm^2), respectively. Furthermore, the dead layer was not taken into account, since its thickness in the nanopowder is unknown[11].

Although the two presented LSMO-based ME systems have different Sr doping levels (and thus Curie temperatures), morphologies, structural dimensions and gating techniques (and thus ΔQ), the similarity of the T dependence of the magnetic modulations is evident. The more than seven times higher magnitude of the relative effect[12] of the thin film heterostructure results from

[10] Nanopowder sample A1000 was chosen for this comparison, as it provides the best compromise between sharpness of the magnetic transition, effect size and SQUID-accessible temperature range.

[11] The existence of dead layers in nanoparticulate LSMO has been reported e.g., by Curiale *et al.*[322].

[12] Normalization of the effect was performed with respect to the value of σ_m at $T = 50$ K, where the moment has reached a stable level.

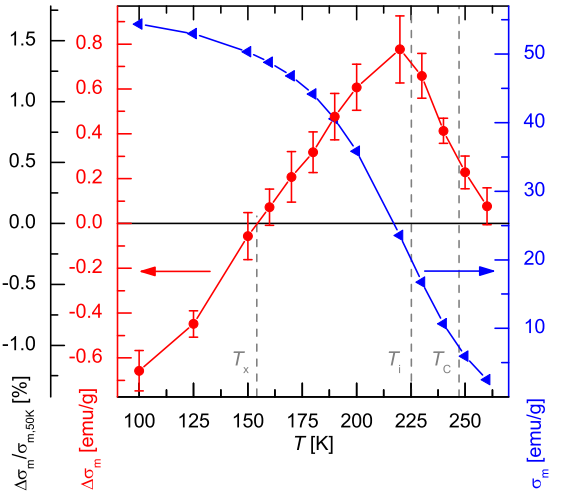

(a) FE-gated $La_{0.87}Sr_{0.13}MnO_3$ thin film

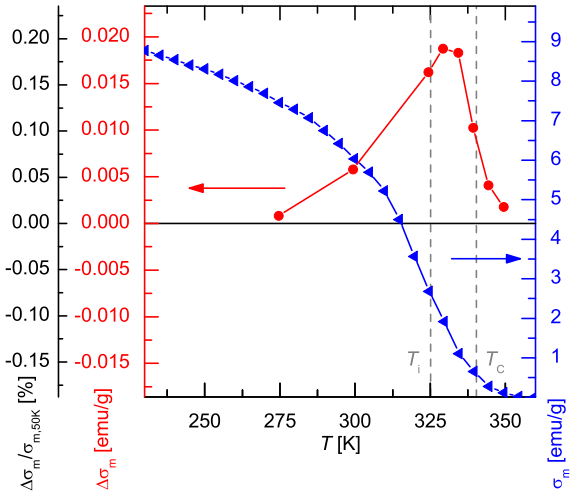

(b) electrolyte-gated $La_{0.75}Sr_{0.25}MnO_3$ nanopowder

Figure 6.10.: Side-by-side comparison of the T dependence of the mass magnetic moment (σ_m) (FC curves, blue) and the field-effect induced modulation thereof (red curves) for ferroelectrically gated LSMO thin film (a) and electrolyte-gated LSMO nanopowder (b). The black axes depict the relative modulation with respect to $\sigma_m(T = 50\,\mathrm{K})$. For measurement details see original data in Fig. 6.6 and Figs. 2.3(c) and 2.5(b), respectively.

the stronger charge modulation of the PZT film, the lower doping level and the better effective surface-to-volume ratio. The latter is unfavorable for the nanopowder due to sintering of the grains, and may even be further reduced due to the electrolyte not being able to access all cavities in between the grains.

With its low-temperature compatibility, the thin film device facilitated the direct proof of the predicted crossover of the tuning effect. Moreover, the accurate area normalization of the applied charge allowed for a quantitative investigation of the field-effect induced magnetic modulation at $T \ll T_C$. As a consequence, the findings in the present study enable a comprehensive discussion of the charge carrier density dependence of magnetic coupling mechanisms in LSMO:

The complexity of a system like LSMO and its response to electrostatic charging require a cautious discussion. So far, the only sources of experimentally established information that are commonly used for discussing electrostatic doping phenomena are the LSMO bulk phase diagrams (see Fig. 1.12 on p. 24, or [104, 111–113]), especially when considering T-dependent relationships [52, 54, 55, 249, 315]. Albeit in many instances this may lead to valid conclusions, the following constraints should always be kept in mind:

- The magnetic properties of the perovskite manganites strongly depend upon the Mn–O–Mn bond angle which may be affected by the chemical inhomogeneity and crystal lattice distortions that are introduced by chemical doping; yet these effects are absent in field-effect devices.

- While the chemically doped compound remains electrically neutral for all Sr compositions, the electrostatically doped interface is subjected to a very strong local electrostatic field.

- The bulk phase diagram may not be applicable when interface or strain effects come into play; magnetically dead layers and strain induced shifts in transition temperatures are some of the striking examples.

The noticeable scatter of characteristics and magnitudes of electrostatic tuning effects in LSMO and related compounds reported in the literature emphasizes potential difficulties in correct interpretation of the underlying physical phenomena. While there have been attempts to theoretically predict the response of a manganite to the FE polarization for certain doping levels [314, 323], there is no generally accepted model available to account for the aforementioned complexities. Of course, eventually, it is also possible that entirely new electronic phases can be formed by field-effect tuning, which are not covered in the bulk phase diagrams at all.

The first essential observation concerns the magnetic modulation versus P_r at low T: a direct coupling of the FE remanent polarization and the magnetic response is apparent (see Fig. 6.7), with the induced change in magnetization closely following the FE polarization. The same applies to the similar measurements performed around T_C [see Fig. 6.8(b)], which qualitatively differ in the sign of the modulation only, as expected [248].

A closer look at the actual charge dependence of the magnetic modulation reveals the non-linearity in the trend above certain FE polarization threshold. When rescaled to the saturated magnetization [Fig. 6.9(b), dashed line], a steeper slope for $\Delta P_r < 0.2\,h^+/\text{u.c.}^2$ can be linearly approximated giving a charge-dependent magnetic tuning coefficient equivalent to the total change of the magnetic moment of one Mn atom: $\alpha_{MQ} \approx -3.6\,\mu_B/h^+$.

It is worth mentioning, as a technical note, that due to the way the charge-dependent magnetic tuning coefficient is calculated, any uncertainty in the determination of the FE device area is entirely irrelevant, as only the total charge modulation on the whole sample is concerned.

At this point it is advisable to put the obtained quantitative results into the context of the reports by Molegraaf *et al.* [247] and the follow-up by Vaz *et al.* [248, 249], where similar LSMO/PZT heterostructures were explored with different experimental tools, namely MOKE magnetometry.

The foremost problem in quantification of MOKE measurements stems from the need for an external calibration, as MOKE can only provide relative values. Thus, for instance, a dead layer at the LSMO bottom interface can drastically change the estimated magnetic moment when averaged over the full film thickness instead of considering only the magnetically active part. The unusually low saturation magnetization of $\approx 0.9\,\mu_B$/Mn reported in [247] is a strong indication for such a dead layer. Interestingly, such a supposition is backed by the measurements reported elsewhere [250, 324]. Consequently, assuming a magnetic moment of 3.3 to $3.6\,\mu_B$/Mn – as the nominal bulk value of $3.8\,\mu_B$/Mn typically is not reached in thin films – the dead layer would come to be about 2.9 to 3.0 nm, a rather credible value. Thus, the tuning coefficient, corrected for the dead layer, $\alpha_{MQ} = \Delta M/\Delta Q$ would be of -2.3 to $-2.1\,\mu_B/h^+$. For better comparison, the corresponding slopes are indicated by the gray shaded area in Fig. 6.9; the actual single data points would be located beyond the axis ranges. It becomes evident from this illustration that, to a great extent, the results obtained by Molegraaf and Vaz *et al.* [247, 250] can be reconciled with the present experimental values just by the sensible assumption of a presence of dead layers in their samples. Of course, at this point, one should bear in mind that the above considerations about the implications of the dead layer presence are hypothetical and must be tested by an independent experiment. Also other factors, such as preparation methods or differences in the doping level, are not accounted for in the above speculations.

In the context of the previous studies, the actual significance of the results presented here rests in their comprehensiveness, i.e., the magnetic modulation upon charging is tracked down continuously from virtually zero to the experimentally attainable maximum charge concentration.

In principle, the charging experiments carried out at low T were meant to extract contributions to the magnetic modulation unaffected by the critical effects at the magnetic transition temperature. A tentative examination of the magnetic response to the surface charge brings attention to two facts: First, for small ΔP_r the dependence is simply linear but right from the start has a high slope (tuning coefficient) of $\alpha_{MQ} \approx -3.6\,\mu_B/h^+$. Second, no evidence for any *abrupt* phase transition upon charging is found.

If the interface magnetism were determined by pure Double-Exchange (DE) mechanism only, one would expect to get a tuning coefficient of $\alpha_{MQ} = -1\,\mu_B/h^+$. This is a consequence of a simple fact that one electrostatically introduced hole is equivalent to the loss of one electron, carrying a magnetic moment of $1\,\mu_B$. The absolute value determined in the present study is much bigger and the actual value of $-3.6\,\mu_B$ suggests that, on average, one electrostatically introduced h^+ annihilates a whole Mn magnetic moment. The most plausible scenario accounting for the apparent disappearance of the entire Mn moment is the presence of AF coupling[13] even for very low electrostatic h^+ doping levels. It looks like the AF phase starts to form right away from the beginning of the charging process and with increasing surface charge density covers more

[13] Only half of the Mn moments align antiparallel, while the other half remains (unchanged) parallel to the external field: $0.5 \cdot 2 \cdot (-3.6\,\mu_B) = -3.6\,\mu_B$.

and more of the LSMO/PZT interface. Moreover, the space expansion of the AF phase over the interface area is a continuous process as can be seen in Fig. 6.9(b). The growth of the AF phase dominates the magnetic modulation for charge densities below $0.2\,h^+/\text{u.c.}^2$. For higher ΔP_r, the ME tuning coefficient α_{MQ} gradually becomes smaller, signaling that induced antiferromagnetism is not the sole contributor to the tuning effect.

The change of tuning slope can be better explained by considering the overall temperature dependence of the tuning effect [Fig. 6.6, or Fig. 6.10(a)]. Phenomenologically, the resultant accumulation and depletion FC curves can be reconstructed from the magnetic modulation by scaling the magnetic moment in the untuned FC curve and then accordingly shifting it back and forth along the T axis (compare Fig. 2.6 on p. 33, or [4, 247]). Taking the untuned FC curve of the entire sample as a starting point, the shifts in T_C for the h^+ accumulation and depletion states can be numerically fitted to the experimentally determined temperature dependence of the magnetic modulation, as shown in Fig. 6.11. With a plausible screening length of 2 u.c. and a dead layer thickness of 2.1 nm, the relative magnetization change between the FE polarization states amounts to about 7 %. The transition temperatures are shifted by $-14\,\text{K}$ and $-24\,\text{K}$ for the accumulation and the depletion state, respectively, resulting in a charge modulated shift of T_C by 10 K. The fact that *both* charged states are shifted to lower T, with respect to the FC curve of the entire sample – representing a superposition of the distribution of the temperature dependence throughout the LSMO thickness – indicates that the Curie temperature of the topmost layers is reduced, compared to the interior of the LSMO film.

While an AF coupling may explain the pronounced (negative) tuning effect at low T, it cannot account for the shift in T_C, which gives rise to the local (positive) maximum of the tuning effect around the FC inflection point temperature (T_i). As has already been pointed out, the magnetic modulation curve, with increasing T, passes a crossover point where the tuning effect changes sign from negative to positive. From the above analysis it is evident that the positive tuning effect around the transition temperature is a straightforward result of the shift in T_C upon charging. Indeed, on the basis of the bulk phase diagram (Fig. 1.12 on p. 24) in the low-doping region, the shift suggests the presence of a ferromagnetically ordered component, which would require

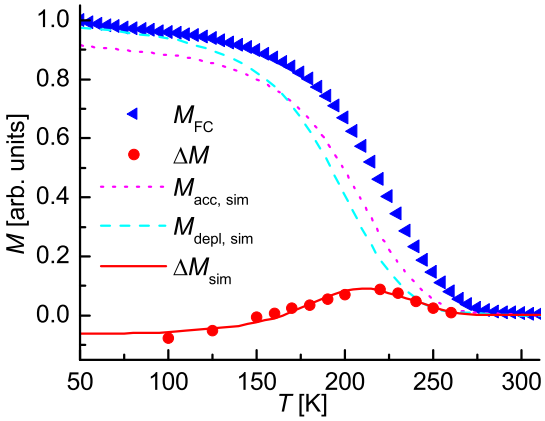

Figure 6.11: Simulation of the temperature dependence of the tuning effect, on the basis of the data shown in Fig. 6.6. (*Published in* [297], ©2013, American Physical Society)

merely a minor charge modulation of less than $0.02\,h^+$/Mn to yield a shift of more than 30 K (compare end of Section 1.6).

The clear indication of the charge-induced AF phase at low T and the FM phase around T_C, together with the continuous temperature dependence of the tuning effect with no sign of any abrupt transitions (Fig. 6.6 [or Fig. 6.10(a)] and [248]) suggest that AF and FM coupling are likely to coexist over the whole temperature range, thus pointing to an electronic phase separation at the LSMO/PZT interface.

For interpretation of the nonlinearity of the charge dependence (Fig. 6.9) in line with the physical picture of the coexisting AF and FM states, the idea of the primary FC curve shifting and rescaling upon charging once more proves to be very useful.

Both the reduction of magnetic moment and the shift towards higher transition temperatures, when switching from the depletion to accumulation state, are a function of the applied ΔP_r. Although, in principle, both the effects happen simultaneously, the change in magnetic moment dominates at low T while the shift in transition temperature is naturally pronounced around T_C. However, at sufficiently high charge density, the charge dependence of the tuning effect at low T gets also influenced by the temperature shift as long as the FC curve is not perfectly leveled off in the respective temperature range. The evident impact of the shape of the FC curve is demonstrated in Fig. 6.12, where the smeared-out transition of a 5 nm LSMO sample causes the magnitude of magnetic modulation at 30 K to level off and then even decrease at higher ΔP_r.

The charge dependence at 110 K, around the point of inflection of the FC curve [Fig. 6.12(b)], gives even more insight into the ME mechanisms.

While showing a nearly linear dependence of the magnetic modulation with respect to the applied ΔP_r, there is a threshold below which no magnetic tuning could be determined with the given experimental accuracy, a behavior which is in strong contrast to the one observed at low T. This can be understood by preferential inducement of the AF coupling for low ΔP_r, presumably within the regions of the nucleating and forming FE domains. In these FE domains the local surface charge density would be high enough to trigger AF interactions, which are difficult to detect around the transition temperature. Only at higher surface charge concentrations does the FM coupling take over the tuning effect.

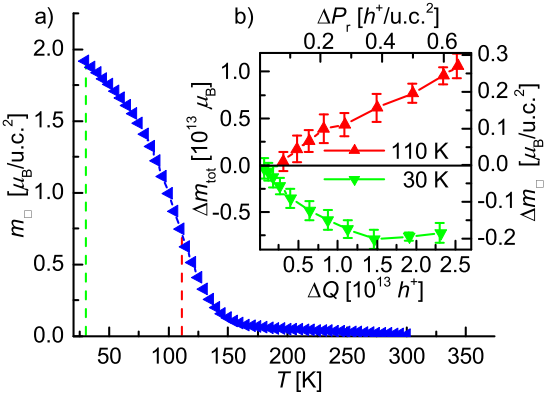

Figure 6.12: Low-T_C sample with 5 nm LSMO layer: FC measurement illustrating the smeared-out transition (a) and its effect on the tuning efficiency below and above T_x at 30 K and 110 K, respectively (b). The measurements were performed at $H = 100$ Oe. (*Published in* [297], ©2013, American Physical Society)

Coming back to the original heterostructure shown in Fig. 6.9, the steep slope – i.e., the high tuning coefficient – at low T and low ΔP_r can be understood as a direct consequence of a pure AF coupling arising from the regions with higher local charge density. Such an inhomogeneous surface charge distribution at the LSMO/PZT interface could be quite naturally imagined during the FE polarization. For instance the regions of enhanced surface charge density would be connected to the process of formation of FE domains. As has already been stated, the increase in T_C has notable impact on the tuning coefficient even at low T because the FC curve does not saturate (i.e., level off). Therefore, upon further charging the reduction of the absolute value of the tuning coefficient is caused by the competition between continuous growth of AF ordered regions and increase of the shift in T_C of the FM phase.

In essence, the explanation of the tuning effects rests in the fundamental fact that the competition of Superexchange (SE), DE, and electron-lattice couplings results in a staggering variety of possible phase states in mixed-valent manganites. Both suppositions, i.e., the appearance of the AF phase and its coexistence with the FM phase upon electrostatic h^+ accumulation, have already found positive support in some theoretical and experimental works. For example in a recent article by Chen *et al.* [325], it is clearly shown from first-principle studies that for the LSMO/PZT, with a nominal Sr doping level of $x = 0.2$, the accumulated holes do change the magnetic interaction of the interfacial manganite from FM to AF. It should be noticed that this theory and the others dealing with the field-effect driven phase transitions in manganites either do not or cannot account for the *insulating* AF phase in the h^+ *depletion* regime which is present in the bulk phase diagram. Indeed, as a matter of fact, the present experimental data also does not show any clear indication of an existence of antiferromagnetism in the h^+ depletion regime.

The proposed scenario of the electrostatically induced coexistence of the AF and FM phases is compellingly backed by the well known phenomenon of spacial electronic phase separation in otherwise chemically homogeneous manganites (see Section 1.6 and [117, 122]). Some experimental evidence of the AF/FM phase separation at a manganite/FE interface one can find, for example, in work by Alberca *et al.* [326]. In this article electronic transport and magnetic properties studies on epitaxial $La_{0.7}Ca_{0.3}MnO_3/BaTiO_3$ films suggest either phase separation between the AF and FM local order, or alternatively a coexistence of in-plane and out-of-plane FM regions. Ultimately, to decide between these scenarios will require a series of *in situ* charging experiments with the sample oriented parallel and perpendicular to the applied magnetic field.

Another aspect that is not directly addressed in these studies, is the dependence of the FE charging effect on the presence of FM domains. For reasons that have been stated in Section 6.2, the present experiments were carried out in a magnetically unsaturated state. However, at least at low T, one should not expect much of a change in the tuning mechanism of the FM phase between magnetically unsaturated and saturated states. In principle, the tuning effect should be the same for all the FM domains so its net value should scale with the total magnetization. Of course, sensitivity of the AF phase formation to the external magnetic field is much more difficult to predict and would require further experimental verification.

6.5 Summary

The highly uniform deposition of multiferroic (MF) $La_{1-x}Sr_xMnO_3$ (LSMO)/$PbZr_yTi_{1-y}O_3$ (PZT) heterostructures provided sufficiently large ferroelectric (FE) device areas of more than 6 mm^2 in size, enabling – for the first time – *in situ* Superconductive Quantum Interference Device (SQUID) magnetization measurements with a simultaneously modulated applied electric

field. Consequently, charge-dependent measurements of the magnetic response were carried out in FE remanence mode and at variable temperatures.

The LSMO layer thickness was chosen as a compromise between two desirable but mutually exclusive goals: a large surface-to-volume ratio on the one hand and a high Curie temperature (T_C) with a sharp magnetic transition on the other. Moreover, the resultant thickness was sufficient to ensure that the magnetically dead layer did not interfere with the screening depth of the electric field applied at the device interface.

Possible artifacts and spurious effects of the magnetic and FE measurements were effectively eliminated by considering only the differential modulations of the total magnetic moment (Δm_{tot}) and the total ferroelectrically induced remanent charge (ΔQ), respectively. A clearly field-effect dominated magnetoelectric (ME) coupling with no inverse piezoelectric effect was evidenced by the system's magnetic response to the FE remanent states. This quantified ME tuning data of the whole sample provides a charge-dependent tuning coefficient $\alpha_{MQ} = \Delta m_{tot}/\Delta Q$. Measured at temperatures well below T_C, the obtained value of $\alpha_{MQ} \approx -3.6\,\mu_B/h^+$ is strikingly large and virtually identical with the magnetic moment per manganese atom.

In temperature-dependent measurements, a reversal of the sign of the ME effect was observed, with a positive extremum for the electron hole (h^+) accumulation mode around T_C. For lower temperatures, the effect gradually decreased to become negative, eventually. On the basis of the phase diagram and the dependence of the magnetic moment on the Sr doping level, the shape of the curve was phenomenologically interpreted by a transformation of the original Field Cooling (FC) curve, including a shift along the temperature axis and a rescaling of the magnetic moment.

An exhaustive analysis of the charge- and temperature-dependent modulation of magnetization, has lead to a physical picture of coexisting ordered ferromagnetic (FM) and antiferromagnetic (AF) phases, where the AF response is stimulated even for very small charge density modulations. In contrast, the competing FM response which is only dominating at temperatures around T_C seems to require a certain threshold to be detectable. Considering typical FE domain structures of unsaturated states, this scenario of spacial electronic phase separation is very plausible as a result of the lateral inhomogeneity of the carrier density.

The obtained tuning coefficient α_{MQ}, which characterizes the magnetic response to the generated screening charge, is independent of the actual value of the FE device area and free of any *a priori* assumptions about the existence of a dead layer or the charge distribution within the screening length. It is thus an excellent starting point for further theoretical considerations and modeling.

7 Conclusions and future work

The high quality of the fabricated $La_{1-x}Sr_xMnO_3$ (LSMO)/$PbZr_yTi_{1-y}O_3$ (PZT) heterostructures, with respect to overall crystallinity, lateral uniformity and smoothness of interfaces, greatly facilitated the fundamental *in situ* studies of the magnetoelectric (ME) coupling in this artificial multiferroic (MF) system. Furthermore, from the technological point of view, this work underlines the usefulness of the comparatively simple Large-Distance Magnetron Sputtering (LDMS) method for deposition of top quality complex oxide structures. In the following potential prospects for both the ME composite system as well as the sputtering technique will be discussed.

With respect to the continuation of the ME effect studies presented in this thesis, it will probably be beneficial to further investigate the magnetic response to the ferroelectrically induced charge modulation with the focus on the specifics of antiferromagnetic (AF) order and formation of AF and ferromagnetic (FM) domains (e.g., by neutron scattering or magnetic dichroism in synchrotron radiation scattering). Furthermore, the influence of the ferroelectric (FE) domain formation and their pattern on the electronic and magnetic phase separation is certainly of interest. For this purpose different kinds of FEs may be employed, in order to explore varying local polarization in the FE domains. Another way to study the effect for lower surface charge modulations would be to use electrolyte or high relative permittivity (κ) dielectrics, which allow for continuous and laterally uniform sweeping of the induced carrier density in the LSMO thin film. In the light of this work, however, in both cases the necessity to perform these measurements in an applied electric field (E) involves the risk of leakage-current induced magnetometry artifacts and the challenge to reliably quantify the actual charge modulation at the interface.

Another somewhat unusual but certainly interesting concept for realizing an induced surface charge would be based on the fact that LSMO is a *p*-type conductor. The combination with a suitable *n*-conductor – such as In_2O_3:Sn (ITO) – should result in a *p-n* junction which in reverse bias would yield an electron hole (h^+)-depletion state in the space charge region of the LSMO.

From electrolyte tuning of noble metal nanopowders (see Section 1.4.1) it is known that the carrier density modulation entails a considerable lattice strain. Although such a strain will mostly be hampered by substrate clamping effects, it may still be interesting to monitor the LSMO lattice parameters in the screening length region during charge cycling (with any field-effect gating method), using depth resolved diffraction of synchrotron radiation.

The dead layer at the LSMO bottom interface may be exploited for growing LSMO/FE Multilayer (ML) structures with asymmetric tuning behavior, as effective field-effect tuning will presumably be limited to the upper interfaces of the LSMO layers. Such ML systems can prove useful in increasing of the ME coupling coefficient (α_{ME}). Of course not only a sensible choice of layer thicknesses would be required for optimization, but more importantly, a FE material which is fully compatible with the growth conditions – especially the substrate temperature – of the LSMO.

To further investigate the nature of ME coupling in LSMO/PZT bilayers, different Sr doping level should be considered. Of course, the optimal doping level of $x \approx 0.3$ is a good candidate. But perhaps even more interesting would be the high-doping region of around 50 %, featuring additional mechanisms provided by the charge ordering phenomenon. These experimental

studies should ideally be accompanied by theoretical modeling, in order to identify the main contributions to the ME tuning at each doping level.

It would definitely be beneficial to investigate similar heterostructures which are based on other manganites like the well-studied $La_{1-x}Ca_xMnO_3$ (LCMO) or maybe $La_{1-x}Ba_xMnO_3$ (LBMO). A low-doped composition of the latter would allow for a direct comparison with the present work, as it can also be stabilized in a metallic phase with elevated Curie temperature (T_C) by means of epitaxial strain (see Section 3.2.1).

Apart form the mixed valent manganites, the closely related Colossal Magnetoresistance (CMR) material $La_{1-x}Sr_xCoO_3$ (LSCO) would be another interesting candidate for FE field-effect tuning. Being based on low-spin configured Co^{3+} cations of the undoped endmember, this material is unlike LSMO not a half metal. As a consequence, the measurement of magnetic tuning will be handicapped, of course, but a tuning effect with respect to (magneto-)transport properties should be measurable.

The outstanding quality of the MF composites grown by the LDMS method gives an idea of the potential that rests in this technique. As a consequence, the logical next step is to test other related materials, i.e., ternary and higher order oxides, to make use of its advantages and further explore its capabilities.

The unique ability of tailoring the concentration of heavy but volatile species by adjusting the pressure – as done for PbO in PZT – may be applicable for other materials containing e.g., Pb, Zn or Bi. A promising candidate is certainly $BiFeO_3$ (BFO). In analogy to the Pb deficiency in PZT, a Bi loss is often observed in Physical Vapor Deposition (PVD)-grown BFO thin films. Judging from the outstanding crystallographic and FE properties of LDMS-grown PZT, with a right set of deposition parameters, similar results should be attainable for BFO thin films.

With the distinct lateral uniformity of the present PZT films, allowing for exceptionally large FE device areas, the deposition process qualifies for other FE perovskites to be tested for their fundamental and practical usefulness. Apart from the mentioned BFO and the well established $BaTiO_3$ (BTO), also the alkaline niobates are promising candidates, in the quest for high-performance lead-free FEs.

As pointed out earlier (Section 5.1), also the choice of the electrode material strongly influences the properties of the FE layer grown on top, be it due to the crystallographic structures or due to the electric and electronic properties of both components. For this reason it would be useful to also concentrate on implementing LDMS deposition technique for conductive oxides, such as e.g., $SrRuO_3$ (SRO), $LaNiO_3$ (LNO) or $YBa_2Cu_3O_{7-x}$ (YBCO).

From a technological point of view, due to the on-axis geometry, the LDMS system is predestined for rapid sequential or even co-deposition of several materials. The latter offers yet another way for controlling the stoichiometry of complex oxides. The former may allow for building artificial superlattices which are known to exhibit very special properties; the famous $LaAlO_3$ (LAO)/$SrTiO_3$ (STO) MLs with their two-dimensional electron gas formed at the interfaces are compelling examples.

Bibliography

[1] J. E. Lilienfeld, *Method and apparatus for controlling electric currents*, 1930, patent:US1745175 (cit. on p. 1).

[2] O. Heil, *Improvements in or relating to electrical amplifiers and other control arrangements and devices*, 1935, patent:GB439457 (cit. on p. 1).

[3] W. Kleemann and P. Borisov, in *Smart Materials for Energy, Communications and Security*, edited by I. Luk'yanchuk and D. Mezzane (Springer Netherlands, 2008), pp. 3–11, 10.1007/978-1-4020-8796-7_1 (cit. on pp. 1, 10, 12).

[4] A. K. Mishra, A. J. Darbandi, P. M. Leufke, R. Kruk, and H. Hahn, *Journal of Applied Physics* **113**, 033913, 10.1063/1.4778918 (2013) (cit. on pp. 2, 27–34, 98, 103, 111).

[5] R. G. Jackson, *Novel Sensors and Sensing (Series in Sensors)* (IOP Publishing, London, 2004), ISBN: 978-0750309899 (cit. on p. 3).

[6] J. Fraden, *Handbook of Modern Sensors*, 3rd ed. (Springer-Verlag, New York, 2004), 10.1007/b97321 (cit. on p. 3).

[7] G. Gliemeroth and K.-H. Mader, *Angewandte Chemie International Edition in English* **9**, 434, 10.1002/anie.197004341 (1970) (cit. on p. 3).

[8] M. Eiswirth and R. J. Schwankner, *Journal of Chemical Education* **62**, 641, 10.1021/ed062p641 (1985) (cit. on p. 3).

[9] M. Wuttig and N. Yamada, *Nature materials* **6**, 824, 10.1038/nmat2009 (2007) (cit. on p. 3).

[10] C. Hall, *International Conference on Storage and Recording Systems* **1994**, 137, 10.1049/cp:19941147 (1994) (cit. on p. 4).

[11] C. H. Ahn, J.-M. Triscone, and J. Mannhart, *Nature* **424**, 1015, 10.1038/nature01878 (2003) (cit. on p. 5).

[12] C. H. Ahn, M. Di Ventra, J. N. Eckstein, C. D. Frisbie, M. E. Gershenson, A. M. Goldman, I. H. Inoue, J. Mannhart, A. J. Millis, A. F. Morpurgo, D. Natelson, and J.-M. Triscone, *Reviews of Modern Physics* **78**, 1185, 10.1103/RevModPhys.78.1185 (2006) (cit. on pp. 5, 10).

[13] S. Dasgupta, G. Stoesser, N. Schweikert, R. Hahn, S. Dehm, R. Kruk, and H. Hahn, *Advanced Functional Materials* **22**, 4909, 10.1002/adfm.201200951 (2012) (cit. on p. 6).

[14] H. Gleiter, J. Weissmüller, O. Wollersheim, and R. Würschum, *Acta Materialia* **49**, 737, 10.1016/S1359-6454(00)00221-4 (2001) (cit. on p. 6).

[15] J. Weissmüller, R. N. Viswanath, D. Kramer, P. Zimmer, R. Würschum, and H. Gleiter, *Science* **300**, 312, 10.1126/science.1081024 (2003) (cit. on p. 6).

[16] D. Kramer, R. N. Viswanath, and J. Weissmüller, *Nano Letters* **4**, 793, 10.1021/nl049927d (2004) (cit. on p. 6).

[17] M. Sagmeister, U. Brossmann, S. Landgraf, and R. Würschum, *Physical Review Letters* **96**, 156601, 10.1103/PhysRevLett.96.156601 (2006) (cit. on p. 6).

[18] A. K. Mishra, C. Bansal, and H. Hahn, *Journal of Applied Physics* **103**, 094308, 10.1063/1.2912982 (2008) (cit. on p. 6).

[19] C. Bansal, S. Sarkar, A. Mishra, T. Abraham, C. Lemier, and H. Hahn, *Scripta Materialia* **56**, 705, 10.1016/j.scriptamat.2006.12.015 (2007) (cit. on p. 6).

[20] S. Dasgupta, R. Kruk, D. Ebke, A. Hütten, C. Bansal, and H. Hahn, *Journal of Applied Physics* **104**, 103707, 10.1063/1.3020526 (2008) (cit. on p. 6).

[21] C. Lemier, S. Ghosh, R. N. Viswanath, G.-T. Fei, and J. Weissmüller, *MRS Proceedings* **876**, R2.6, 10.1557/PROC-876-R2.6 (2011) (cit. on p. 6).

[22] A. K. Mishra, C. Bansal, M. Ghafari, R. Kruk, and H. Hahn, *Physical Review B* **81**, 155452, 10.1103/PhysRevB.81.155452 (2010) (cit. on p. 6).

[23] H. Drings, R. N. Viswanath, D. Kramer, C. Lemier, J. Weissmüller, and R. Würschum, *Applied Physics Letters* **88**, 253103, 10.1063/1.2216897 (2006) (cit. on p. 7).

[24] M. Weisheit, S. Fähler, A. Marty, Y. Souche, C. Poinsignon, and D. Givord, *Science* **315**, 349, 10.1126/science.1136629 (2007) (cit. on p. 7).

[25] K. Shimamura, D. Chiba, S. Ono, S. Fukami, N. Ishiwata, M. Kawaguchi, K. Kobayashi, and T. Ono, *Applied Physics Letters* **100**, 122402, 10.1063/1.3695160 (2012) (cit. on p. 7).

[26] K. Ueno, S. Nakamura, H. Shimotani, A. Ohtomo, N. Kimura, T. Nojima, H. Aoki, Y. Iwasa, and M. Kawasaki, *Nature materials* **7**, 855, 10.1038/nmat2298 (2008) (cit. on p. 7).

[27] A. S. Dhoot, S. C. Wimbush, T. Benseman, J. L. Macmanus-Driscoll, J. R. Cooper, and R. H. Friend, *Advanced materials* **22**, 2529, 10.1002/adma.200904024 (2010) (cit. on p. 7).

[28] A. T. Bollinger, G. Dubuis, J. Yoon, D. Pavuna, J. Misewich, and I. Božović, *Nature* **472**, 458, 10.1038/nature09998 (2011) (cit. on p. 7).

[29] Y. Yamada, K. Ueno, T. Fukumura, H. T. Yuan, H. Shimotani, Y. Iwasa, L. Gu, S. Tsukimoto, Y. Ikuhara, and M. Kawasaki, *Science* **332**, 1065, 10.1126/science.1202152 (2011) (cit. on p. 7).

[30] J. Robertson, *Reports on Progress in Physics* **69**, 327, 10.1088/0034-4885/69/2/R02 (2006) (cit. on p. 8).

[31] G. He and Z. Sun, eds., *High-k Gate Dielectrics for CMOS Technology* (Wiley-VCH Verlag GmbH & Co. KGaA, Weinheim, Germany, Aug. 2012), 10.1002/9783527646340 (cit. on pp. 8, 10).

[32] J. Verweij and J. Klootwijk, *Microelectronics Journal* **27**, 611, 10.1016/0026-2692(95)00104-2 (1996) (cit. on p. 8).

[33] T. Nigam, A. Kerber, and P. Peumans, in 2009 IEEE International Reliability Physics Symposium (Apr. 2009), pp. 523–530, 10.1109/IRPS.2009.5173307 (cit. on p. 8).

[34] H. J. de Wit, *Journal of The Electrochemical Society* **123**, 1479, 10.1149/1.2132623 (1976) (cit. on p. 8).

[35] E. Y. Wu and J. Suñé, *Microelectronics Reliability* **45**, 1809, 10.1016/j.microrel.2005.04.004 (2005) (cit. on p. 8).

[36] G. D. Wilk, R. M. Wallace, and J. M. Anthony, *Journal of Applied Physics* **89**, 5243, 10.1063/1.1361065 (2001) (cit. on p. 8).

[37] M. Leskelä and M. Ritala, *Thin Solid Films* **409**, 138, 10.1016/S0040-6090(02)00117-7 (2002) (cit. on p. 8).

[38] K. Endo, Y. Ishikawa, T. Matsukawa, Y. Liu, S.-i. O'uchi, K. Sakamoto, J. Tsukada, H. Yamauchi, and M. Masahara, *Solid-State Electronics* **74**, 13, 10.1016/j.sse.2012.04.005 (2012) (cit. on p. 8).

[39] A. Walkenhorst, C. Doughty, X. X. Xi, S. N. Mao, Q. Li, T. Venkatesan, and R. Ramesh, *Applied Physics Letters* **60**, 1744, 10.1063/1.107204 (1992) (cit. on p. 8).

[40] J. Mannhart, *Superconductor Science and Technology* **9**, 49, 10.1088/0953-2048/9/2/001 (1996) (cit. on p. 8).

[41] H. Ohno, D. Chiba, F. Matsukura, T. Omiya, E. Abe, T. Dietl, Y. Ohno, and K. Ohtani, *Nature* **408**, 944, 10.1038/35050040 (2000) (cit. on p. 8).

[42] D. Chiba, M. Yamanouchi, F. Matsukura, and H. Ohno, *Science* **301**, 943, 10.1126/science.1086608 (2003) (cit. on p. 8).

[43] D. Chiba, M. Sawicki, Y. Nishitani, Y. Nakatani, F. Matsukura, and H. Ohno, *Nature* **455**, 515, 10.1038/nature07318 (2008) (cit. on p. 8).

[44] D. Chiba, F. Matsukura, and H. Ohno, *Nano letters* **10**, 4505, 10.1021/nl102379h (2010) (cit. on p. 8).

[45] H. Ohno, *Nature materials* **9**, 952, 10.1038/nmat2913 (2010) (cit. on p. 8).

[46] D. Chiba, S. Fukami, K. Shimamura, N. Ishiwata, K. Kobayashi, and T. Ono, *Nature Materials* **10**, 853, 10.1038/nmat3130 (2011) (cit. on p. 9).

[47] D. Chiba, M. Kawaguchi, S. Fukami, N. Ishiwata, K. Shimamura, K. Kobayashi, and T. Ono, *Nature communications* **3**, 888, 10.1038/ncomms1888 (2012) (cit. on p. 9).

[48] A. J. Schellekens, A. van den Brink, J. H. Franken, H. J. M. Swagten, and B. Koopmans, *Nature communications* **3**, 847, 10.1038/ncomms1848 (2012) (cit. on p. 9).

[49] T. Seki, M. Kohda, J. Nitta, and K. Takanashi, *Applied Physics Letters* **98**, 212505, 10.1063/1.3595318 (2011) (cit. on p. 9).

[50] T. Maruyama, Y. Shiota, T. Nozaki, K. Ohta, N. Toda, M. Mizuguchi, A. A. Tulapurkar, T. Shinjo, M. Shiraishi, S. Mizukami, Y. Ando, and Y. Suzuki, *Nature nanotechnology* **4**, 158, 10.1038/nnano.2008.406 (2009) (cit. on p. 9).

[51] S. B. Ogale, V. Talyansky, C. H. Chen, R. Ramesh, R. Greene, and T. Venkatesan, *Physical Review Letters* **77**, 1159, 10.1103/PhysRevLett.77.1159 (1996) (cit. on p. 9).

[52] X. Hong, A. Posadas, A. Lin, and C. Ahn, *Physical Review B* **68**, 134415, 10.1103/PhysRevB.68.134415 (2003) (cit. on pp. 9, 94, 109).

[53] I. Pallecchi, L. Pellegrino, E. Bellingeri, A. Siri, D. Marré, A. Tebano, and G. Balestrino, *Physical Review B* **78**, 024411, 10.1103/PhysRevB.78.024411 (2008) (cit. on pp. 9, 10, 43, 71, 94, 96).

[54] S. Brivio, M. Cantoni, D. Petti, and R. Bertacco, *Journal of Applied Physics* **108**, 113906, 10.1063/1.3516283 (2010) (cit. on pp. 10, 43, 61, 71, 95, 96, 109).

[55] C. Thiele, K. Dörr, W.-M. Lin, K.-H. Müller, and L. Schultz, *Sensors and Actuators A: Physical* **129**, 180, 10.1016/j.sna.2005.11.039 (2006) (cit. on pp. 10, 61, 77, 94, 109).

[56] J. F. Scott, L. Kammerdiner, M. Parris, S. Traynor, V. Ottenbacher, A. Shawabkeh, and W. F. Oliver, *Journal of Applied Physics* **64**, 787, 10.1063/1.341925 (1988) (cit. on pp. 10, 53, 91, 100).

[57] C. H. Ahn, *Science* **284**, 1152, 10.1126/science.284.5417.1152 (1999) (cit. on p. 10).

[58] N. A. Hill, *The Journal of Physical Chemistry B* **104**, 6694, 10.1021/jp000114x (2000) (cit. on pp. 10, 11, 13).

[59] N. A. Spaldin and M. Fiebig, *Science* **309**, 391, 10.1126/science.1113357 (2005) (cit. on pp. 10, 11, 13).

[60] M. Fiebig, *Journal of Physics D: Applied Physics* **38**, R123, 10.1088/0022-3727/38/8/R01 (2005) (cit. on pp. 10, 11).

[61] W. Eerenstein, N. D. Mathur, and J. F. Scott, *Nature* **442**, 759, 10.1038/nature05023 (2006) (cit. on pp. 10–13).

[62] R. Ramesh and N. A. Spaldin, *Nature materials* **6**, 21, 10.1038/nmat1805 (2007) (cit. on pp. 10, 94).

[63] S.-W. Cheong and M. Mostovoy, *Nature materials* **6**, 13, 10.1038/nmat1804 (2007) (cit. on p. 10).

[64] N. Spaldin, *Physics of Ferroelectrics* **218**, 175, 10.1007/978-3-540-34591-6_5 (2007) (cit. on p. 10).

[65] H. Béa, M. Gajek, M. Bibes, and A. Barthélémy, *Journal of Physics: Condensed Matter* **20**, 434221, 10.1088/0953-8984/20/43/434221 (2008) (cit. on pp. 10, 12).

[66] L. W. Martin, S. P. Crane, Y.-H. Chu, M. B. Holcomb, M. Gajek, M. Huijben, C.-H. Yang, N. Balke, and R. Ramesh, *Journal of Physics: Condensed Matter* **20**, 434220, 10.1088/0953-8984/20/43/434220 (2008) (cit. on p. 10).

[67] D. Khomskii, *Physics* **2**, 20, 10.1103/Physics.2.20 (2009) (cit. on pp. 10, 11).

[68] K. Wang, J.-M. Liu, and Z. Ren, *Advances in Physics* **58**, 321, 10.1080/00018730902920554 (2009) (cit. on p. 10).

[69] C. A. F. Vaz, J. Hoffman, C. H. Ahn, and R. Ramesh, *Advanced materials* **22**, 2900, 10.1002/adma.200904326 (2010) (cit. on p. 10).

[70] L. Martin, Y.-H. Chu, and R. Ramesh, *Materials Science and Engineering: R: Reports* **68**, 89, 10.1016/j.mser.2010.03.001 (2010) (cit. on pp. 10, 13, 21, 44, 48, 61).

[71] M. Bichurin, V. Petrov, A. Zakharov, D. Kovalenko, S. C. Yang, D. Maurya, V. Bedekar, and S. Priya, *Materials* **4**, 651, 10.3390/ma4040651 (2011) (cit. on p. 10).

[72] J. Ma, J. Hu, Z. Li, and C.-W. Nan, *Advanced materials* **23**, 1062, 10.1002/adma.201003636 (2011) (cit. on pp. 10, 12).

[73] C. A. F. Vaz, *Journal of physics. Condensed matter : an Institute of Physics journal* **24**, 333201, 10.1088/0953-8984/24/33/333201 (2012) (cit. on p. 10).

[74] C. Ederer and N. A. Spaldin, *Current Opinion in Solid State and Materials Science* **9**, 128, 10.1016/j.cossms.2006.03.001 (2005) (cit. on p. 10).

[75] Y.-H. Chu, L. W. Martin, M. B. Holcomb, and R. Ramesh, *Materials Today* **10**, 16, 10.1016/S1369-7021(07)70241-9 (2007) (cit. on p. 10).

[76] W. Eerenstein, F. D. Morrison, F. Sher, J. L. Prieto, J. P. Attfield, J. F. Scott, and N. D. Mathur, *Philosophical Magazine Letters* **87**, 249, 10.1080/09500830601173053 (2007) (cit. on pp. 10, 14).

[77] M. Blamire, *IEEE Transactions on Magnetics* **44**, 1946, 10.1109/TMAG.2008.924541 (2008) (cit. on pp. 10, 14).

[78] G. Catalan and J. F. Scott, *Advanced Materials* **21**, 2463, 10.1002/adma.200802849 (2009) (cit. on pp. 10, 13).

[79] C. Binek, A. Hochstrat, X. Chen, P. Borisov, W. Kleemann, and B. Doudin, in Journal of Applied Physics, Vol. 97, 10 (2005), p. 10C514, 10.1063/1.1853836 (cit. on pp. 12, 14).

[80] P. Borisov, A. Hochstrat, X. Chen, and W. Kleemann, *Phase Transitions* **79**, 1123, 10.1080/01411590601067318 (2006) (cit. on pp. 12, 14).

[81] P. Borisov, A. Hochstrat, V. V. Shvartsman, and W. Kleemann, *The Review of scientific instruments* **78**, 106105, 10.1063/1.2793500 (2007) (cit. on pp. 12, 14).

[82] T. Kimura, T. Goto, H. Shintani, K. Ishizaka, T. Arima, and Y. Tokura, *Nature* **426**, 55, 10.1038/nature02018 (2003) (cit. on pp. 12, 13).

[83] S. Tiwari and D. Sa, *Journal of physics. Condensed matter* **22**, 225903, 10.1088/0953-8984/22/22/225903 (2010) (cit. on p. 13).

[84] Y. Tokunaga, Y. Taguchi, T.-h. Arima, and Y. Tokura, *Nature Physics* **8**, 838, 10.1038/nphys2405 (2012) (cit. on p. 13).

[85] J. van den Boomgaard, A. M. J. G. van Run, and J. Van Suchtelen, *Ferroelectrics* **14**, 727, 10.1080/00150197608236711 (1976) (cit. on p. 13).

[86] J. van den Boomgaard and A. van Run, *Solid State Communications* **19**, 405, 10.1016/0038-1098(76)91177-7 (1976) (cit. on p. 13).

[87] C. Binek and B. Doudin, *Journal of Physics: Condensed Matter* **17**, L39, 10.1088/0953-8984/17/2/L06 (2005) (cit. on p. 14).

[88] P. Borisov, A. Hochstrat, X. Chen, W. Kleemann, and C. Binek, *Physical Review Letters* **94**, 117203, 10.1103/PhysRevLett.94.117203 (2005) (cit. on p. 14).

[89] X. Chen, A. Hochstrat, P. Borisov, and W. Kleemann, *Applied Physics Letters* **89**, 202508, 10.1063/1.2388149 (2006) (cit. on p. 14).

[90] K. Y. Yun, D. Ricinschi, T. Kanashima, M. Noda, and M. Okuyama, *Japanese Journal of Applied Physics* **43**, L647, 10.1143/JJAP.43.L647 (2004) (cit. on p. 14).

[91] H. Béa, M. Bibes, F. Ott, B. Dupé, X.-H. Zhu, S. Petit, S. Fusil, C. Deranlot, K. Bouzehouane, and A. Barthélémy, *Mechanisms of Exchange Bias with Multiferroic BiFeO_{3} Epitaxial Thin Films*, Jan. 2008, 10.1103/PhysRevLett.100.017204 (cit. on p. 14).

[92] Y.-H. Chu, L. W. Martin, M. B. Holcomb, M. Gajek, S.-J. Han, Q. He, N. Balke, C.-H. Yang, D. Lee, W. Hu, Q. Zhan, P.-L. Yang, A. Fraile-Rodríguez, A. Scholl, S. X. Wang, and R. Ramesh, *Nature materials* **7**, 478, 10.1038/nmat2184 (2008) (cit. on p. 14).

[93] T. H. E. Lahtinen, J. O. Tuomi, and S. van Dijken, *Advanced materials* **23**, 3187, 10.1002/adma.201100426 (2011) (cit. on p. 14).

[94] J. Dho and M. G. Blamire, *Applied Physics Letters* **87**, 252504, 10.1063/1.2147717 (2005) (cit. on p. 14).

[95] V. Laukhin, V. Skumryev, X. Martí, D. Hrabovsky, F. Sánchez, M. García-Cuenca, C. Ferrater, M. Varela, U. Lüders, J. Bobo, and J. Fontcuberta, *Physical Review Letters* **97**, 227201, 10.1103/PhysRevLett.97.227201 (2006) (cit. on p. 14).

[96] H. Zheng, J. Wang, S. E. Lofland, Z. Ma, L. Mohaddes-Ardabili, T. Zhao, L. Salamanca-Riba, S. R. Shinde, S. B. Ogale, F. Bai, D. Viehland, Y. Jia, D. G. Schlom, M. Wuttig, A. Roytburd, and R. Ramesh, *Science* **303**, 661, 10.1126/science.1094207 (2004) (cit. on p. 15).

[97] S. Sahoo, S. Polisetty, C.-G. Duan, S. Jaswal, E. Tsymbal, and C. Binek, *Physical Review B* **76**, 092108, 10.1103/PhysRevB.76.092108 (2007) (cit. on p. 15).

[98] S. Brivio, D. Petti, R. Bertacco, and J. C. Cezar, *Applied Physics Letters* **98**, 092505, 10.1063/1.3554432 (2011) (cit. on pp. 16, 95).

[99] Y. Zhang, J. Liu, X. H. Xiao, T. C. Peng, C. Z. Jiang, Y. H. Lin, and C. W. Nan, *Journal of Physics D: Applied Physics* **43**, 082002, 10.1088/0022-3727/43/8/082002 (2010) (cit. on p. 16).

[100] Z. Li, J. Hu, L. Shu, Y. Zhang, Y. Gao, Y. Shen, Y. Lin, and C. W. Nan, *Journal of Applied Physics* **110**, 096106, 10.1063/1.3660694 (2011) (cit. on p. 16).

[101] A. Mardana, S. Ducharme, and S. Adenwalla, *Nano letters* **11**, 3862, 10.1021/nl201965r (2011) (cit. on p. 16).

[102] G. Jonker and J. Van Santen, *Physica* **16**, 337, 10.1016/0031-8914(50)90033-4 (1950) (cit. on p. 17).

[103] R. von Helmolt, J. Wecker, B. Holzapfel, L. Schultz, and K. Samwer, *Physical Review Letters* **71**, 2331, 10.1103/PhysRevLett.71.2331 (1993) (cit. on pp. 17, 18).

[104] B. Dabrowski, X. Xiong, Z. Bukowski, R. Dybzinski, P. Klamut, J. Siewenie, O. Chmaissem, J. Shaffer, C. Kimball, J. Jorgensen, and S. Short, *Physical Review B* **60**, 7006, 10.1103/PhysRevB.60.7006 (1999) (cit. on pp. 17, 18, 22, 24, 33, 38, 62, 71, 72, 76, 109).

[105] J. Van Santen and G. Jonker, *Physica* **16**, 599, 10.1016/0031-8914(50)90104-2 (1950) (cit. on p. 17).

[106] G. Jonker, *Physica* **22**, 707, 10.1016/S0031-8914(56)90023-4 (1956) (cit. on p. 17).

[107] C. Zener, *Physical Review* **81**, 440, 10.1103/PhysRev.81.440 (1951) (cit. on pp. 17, 21).

[108] C. Zener, *Physical Review* **82**, 403, 10.1103/PhysRev.82.403 (1951) (cit. on pp. 17, 21).

[109] J. Volger, *Physica* **20**, 49, 10.1016/S0031-8914(54)80015-2 (1954) (cit. on p. 18).

[110] S. Jin, T. H. Tiefel, M. McCormack, R. A. Fastnacht, R. Ramesh, and L. H. Chen, *Science (New York, N.Y.)* **264**, 413, 10.1126/science.264.5157.413 (1994) (cit. on p. 18).

[111] A. Urushibara, T. Arima, A. Asamitsu, G. Kido, and Y. Tokura, *Physical Review B* **51**, 14103, 10.1103/PhysRevB.51.14103 (1995) (cit. on pp. 18, 24, 33, 42, 59, 62, 109).

[112] Y. Tokura and Y. Tomioka, *Journal of Magnetism and Magnetic Materials* **200**, 1, 10.1016/S0304-8853(99)00352-2 (1999) (cit. on pp. 18, 20, 21, 23, 24, 33, 59, 109).

[113] O. Chmaissem, B. Dabrowski, S. Kolesnik, J. Mais, J. Jorgensen, and S. Short, *Physical Review B* **67**, 094431, 10.1103/PhysRevB.67.094431 (2003) (cit. on pp. 18, 22, 24, 33, 109).

[114] J.-H. Park, E. Vescovo, H. Kim, and C. Kwon, *Nature* **392**, 794, 10.1038/33883 (1998) (cit. on pp. 18, 22).

[115] A. P. Ramirez, *Journal of Physics: Condensed Matter* **9**, 8171, 10.1088/0953-8984/9/39/005 (1997) (cit. on pp. 18, 23, 28).

[116] J. M. D. Coey, M. Viret, and S. von Molnár, *Advances in Physics* **48**, 167, 10.1080/000187399243455 (1999) (cit. on pp. 18–20, 24, 25, 43, 61).

[117] E. Dagotto, T. Hotta, and A. Moreo, *Physics Reports* **344**, 1, 10.1016/S0370-1573(00)00121-6 (2001) (cit. on pp. 18–20, 23, 26, 113).

[118] W. Prellier, P. Lecoeur, and B. Mercey, *Journal of Physics: Condensed Matter* **13**, R915, 10.1088/0953-8984/13/48/201 (2001) (cit. on pp. 18, 41–43).

[119] K. Dörr, "Ferromagnetic manganites: spin-polarized conduction and competing interactions", Habilitation (Technische Universität Dresden, 2006), urn:nbn:de:swb:14-1193676987929-14995 (cit. on p. 18).

[120] J. Goodenough, ed., *Localized to itinerant electronic transition in perovskite oxides* (Springer, Berlin, 2001), ISBN: 3540675221 (cit. on p. 18).

[121] T. Kaplan, *Physics of manganites*, edited by T. Kaplan and S. Mahanti (Kluwer Academic, New York, 2002), ISBN: 0-306-47091-8 (cit. on p. 18).

[122] E. Dagotto, *Nanoscale phase separation and colossal magnetoresistance: the physics of manganites and related compounds*, edited by E. Dagotto (Springer, Berlin, 2003), ISBN: 3-540-43245-0 (cit. on pp. 18, 23, 113).

[123] S. Wolff, D. Grimwood, J. McKinnon, M. Turner, D. Jayatilaka, and M. Spackman, *CrystalExplorer*, 2012, http://ra.bcs.uwa.edu.au/CrystalExplorer/ (cit. on pp. 19, 39, 40, 45).

[124] L. Pinsard, J. Rodríguez-Carvajal, and A. Revcolevschi, *Journal of Alloys and Compounds* **262-263**, 152, 10.1016/S0925-8388(97)00371-X (1997) (cit. on pp. 19, 38).

[125] J. Kanamori, *Journal of Physics and Chemistry of Solids* **10**, 87, 10.1016/0022-3697(59)90061-7 (1959) (cit. on pp. 20, 25).

[126] P. Anderson, *Physical Review* **79**, 350, 10.1103/PhysRev.79.350 (1950) (cit. on p. 21).

[127] J. B. Goodenough, *Physical Review* **100**, 564, 10.1103/PhysRev.100.564 (1955) (cit. on pp. 22, 25).

[128] X. Xiong, B. Dabrowski, O. Chmaissem, Z. Bukowski, S. Kolesnik, R. Dybzinski, C. Kimball, and J. Jorgensen, *Physical Review B* **60**, 10186, 10.1103/PhysRevB.60.10186 (1999) (cit. on p. 22).

[129] S. Satpathy, Z. Popović, and F. Vukajlović, *Physical Review Letters* **76**, 960, 10.1103/PhysRevLett.76.960 (1996) (cit. on p. 23).

[130] J.-H. Park, C. Chen, S. Cheong, W. Bao, G. Meigs, V. Chakarian, and Y. Idzerda, *Physical Review Letters* **76**, 4215, 10.1103/PhysRevLett.76.4215 (1996) (cit. on p. 23).

[131] H. Hwang, S. Cheong, N. Ong, and B. Batlogg, *Physical Review Letters* **77**, 2041, 10.1103/PhysRevLett.77.2041 (1996) (cit. on p. 23).

[132] L. Rodriguez-Martinez and J. Attfield, *Physical Review B* **54**, R15622, 10.1103/PhysRevB.54.R15622 (1996) (cit. on p. 24).

[133] J. Hemberger, A. Krimmel, T. Kurz, H.-A. Krug von Nidda, V. Ivanov, A. Mukhin, A. Balbashov, and A. Loidl, *Physical Review B* **66**, 094410, 10.1103/PhysRevB.66.094410 (2002) (cit. on p. 24).

[134] E. O. Wollan and W. C. Koehler, *Physical Review* **100**, 545, 10.1103/PhysRev.100.545 (1955) (cit. on p. 24).

[135] B. T. Venkatesan and M. Rajeswari, *Philosophical Transactions of the Royal Society A: Mathematical, Physical and Engineering Sciences* **356**, 1661, 10.1098/rsta.1998.0240 (1998) (cit. on p. 26).

[136] J. B. Mooney and S. B. Radding, *Annual Review of Materials Science* **12**, 81, 10.1146/annurev.ms.12.080182.000501 (1982) (cit. on p. 28).

[137] A. J. Darbandi, T. Enz, and H. Hahn, *Solid State Ionics* **180**, 424, 10.1016/j.ssi.2009.01.004 (2009) (cit. on p. 28).

[138] H. P. Klug and L. E. Alexander, *X-Ray Diffraction Procedures for Polycrystalline and Amorphous Materials* (John Wiley & Sons, Inc., New York, 1974), ISBN: 978-0471493693 (cit. on p. 28).

[139] B. D. Cullity, *Elements of X-ray Diffraction* (Addison Wesley, Reading, Massachusetts, 1956), ISBN: 978-0201610918, http://archive.org/details/elementsofxraydi030864mbp (cit. on p. 28).

[140] S. Kolesnik, B. Dabrowski, J. Mais, M. Majjiga, O. Chmaissem, A. Baszczuk, and J. Jorgensen, *Physical Review B* **73**, 214440, 10.1103/PhysRevB.73.214440 (2006) (cit. on p. 31).

[141] R. Ranjan, S. K. Mishra, and D. Pandey, *Journal of Applied Physics* **92**, 3266, 10.1063/1.1483921 (2002) (cit. on pp. 38, 45, 86).

[142] Y. A. Abramov, V. G. Tsirelson, V. E. Zavodnik, and S. A. Ivanov, *Acta Crystallographica Section B Structural Science* **51**, 942, 10.1107/S0108768195003752 (1995) (cit. on pp. 38, 39).

[143] M. Steins, J. Doerschel, and P. Reiche, *Zeitschrift für Kristallographie - New Crystal Structures* **212**, 77, http://www.oldenbourg.de/verlag/zkristallogr/mn-ncsc9702.htm (1997) (cit. on pp. 38, 39).

[144] J. Zhao, N. L. Ross, and R. J. Angel, *Journal of Physics: Condensed Matter* **16**, 8763, 10.1088/0953-8984/16/47/026 (2004) (cit. on pp. 38, 40).

[145] V. G. Tsirelson, A. S. Avilov, Y. A. Abramov, E. L. Belokoneva, R. Kitaneh, and D. Feil, *Acta Crystallographica Section B Structural Science* **54**, 8, 10.1107/S0108768197008963 (1998) (cit. on pp. 38, 40).

[146] M. Khalid, A. Setzer, M. Ziese, P. Esquinazi, D. Spemann, A. Pöppl, and E. Goering, *Physical Review B* **81**, 214414, 10.1103/PhysRevB.81.214414 (2010) (cit. on p. 37).

[147] D. G. Schlom, L.-Q. Chen, C.-B. Eom, K. M. Rabe, S. K. Streiffer, and J.-M. Triscone, *Annual Review of Materials Research* **37**, 589, 10.1146/annurev.matsci.37.061206.113016 (2007) (cit. on p. 37).

[148] M. Kawasaki, K. Takahashi, T. Maeda, R. Tsuchiya, M. Shinohara, O. Ishiyama, T. Yonezawa, M. Yoshimoto, and H. Koinuma, *Science* **266**, 1540, 10.1126/science.266.5190.1540 (1994) (cit. on p. 37).

[149] G. Koster, B. L. Kropman, G. J. H. M. Rijnders, D. H. A. Blank, and H. Rogalla, *Applied Physics Letters* **73**, 2920, 10.1063/1.122630 (1998) (cit. on p. 37).

[150] B. C. Chakoumakos, D. G. Schlom, M. Urbanik, and J. Luine, *Journal of Applied Physics* **83**, 1979, 10.1063/1.366925 (1998) (cit. on p. 39).

[151] T. Łukasiewicz, M. Świrkowicz, H. Sakowska, A. Turos, M. Leszczyński, and R. Ratajczak, *Journal of Crystal Growth* **237-239**, 1118, 10.1016/S0022-0248(01)02066-8 (2002) (cit. on p. 39).

[152] S. Tidrow, A. Tauber, W. Wilber, R. Lareau, C. Brandle, G. Berkstresser, A. Ven Graitis, D. Potrepka, J. Budnick, and J. Wu, *IEEE Transactions on Applied Superconductivity* **7**, 1766, 10.1109/77.620924 (1997) (cit. on p. 39).

[153] S. Bueble, K. Knorr, E. Brecht, and W. W. Schmahl, *Surface Science* **400**, 345, 10.1016/S0039-6028(97)00891-1 (1998) (cit. on p. 39).

[154] A. B. Posadas, M. Lippmaa, F. Walker, M. Dawber, C. Ahn, and J. M. Triscone, *Physics of Ferroelectrics* **304**, 219, 10.1007/978-3-540-34591-6_6 (2007) (cit. on pp. 40, 47, 48, 61).

[155] F. Tsui, M. C. Smoak, T. K. Nath, and C. B. Eom, *Applied Physics Letters* **76**, 2421, 10.1063/1.126363 (2000) (cit. on pp. 41, 42, 47, 62, 63).

[156] A. J. Millis, T. Darling, and A. Migliori, *Journal of Applied Physics* **83**, 1588, 10.1063/1.367310 (1998) (cit. on p. 41).

[157] M. Sirena, L. Steren, and J. Guimpel, *Thin Solid Films* **373**, 102, 10.1016/S0040-6090(00)01113-5 (2000) (cit. on p. 41).

[158] L. B. Steren, M. Sirena, and J. Guimpel, *Journal of Applied Physics* **87**, 6755, 10.1063/1.372831 (2000) (cit. on p. 41).

[159] J. Zhang, H. Tanaka, T. Kanki, J.-H. Choi, and T. Kawai, *Physical Review B* **64**, 184404, 10.1103/PhysRevB.64.184404 (2001) (cit. on pp. 42, 71).

[160] T. Kanki, H. Tanaka, and T. Kawai, *Solid State Communications* **114**, 267, 10.1016/S0038-1098(00)00038-7 (2000) (cit. on pp. 42, 71).

[161] F. S. Razavi, G. Gross, H.-U. Habermeier, O. Lebedev, S. Amelinckx, G. Van Tendeloo, and A. Vigliante, *Applied Physics Letters* **76**, 155, 10.1063/1.125687 (2000) (cit. on pp. 42, 71).

[162] A. Vigliante, U. Gebhardt, A. Rühm, P. Wochner, F. S. Razavi, and H. U. Habermeier, *Europhysics Letters* **54**, 619, 10.1209/epl/i2001-00337-8 (2001) (cit. on pp. 42, 71).

[163] C. Kwon, M. Robson, K.-C. Kim, J. Gu, S. Lofland, S. Bhagat, Z. Trajanovic, M. Rajeswari, T. Venkatesan, A. Kratz, R. Gomez, and R. Ramesh, *Journal of Magnetism and Magnetic Materials* **172**, 229, 10.1016/S0304-8853(97)00058-9 (1997) (cit. on p. 42).

[164] Y. Suzuki, C. Tsai, H. Y. Hwang, S.-W. Cheong, and R. B. Van Dover, *MRS Proceedings* **474**, 205, 10.1557/PROC-474-205 (2011) (cit. on p. 42).

[165] Y. Konishi, Z. Fang, M. Izumi, T. Manako, M. Kasai, H. Kuwahara, M. Kawasaki, K. Terakura, and Y. Tokura, *Journal of the Physics Society Japan* **68**, 3790, 10.1143/JPSJ.68.3790 (1999) (cit. on pp. 42, 70).

[166] A. Tebano, C. Aruta, P. Medaglia, F. Tozzi, G. Balestrino, A. Sidorenko, G. Allodi, R. De Renzi, G. Ghiringhelli, C. Dallera, L. Braicovich, and N. Brookes, *Physical Review B* **74**, 245116, 10.1103/PhysRevB.74.245116 (2006) (cit. on pp. 42, 47, 70).

[167] C. Ma, Z. Yang, and S. Picozzi, *Journal of physics. Condensed matter* **18**, 7717, 10.1088/0953-8984/18/32/019 (2006) (cit. on pp. 42, 62, 68).

[168] R. A. Rao, D. Lavric, T. K. Nath, C. B. Eom, L. Wu, and F. Tsui, *Applied Physics Letters* **73**, 3294, 10.1063/1.122749 (1998) (cit. on p. 42).

[169] Y. Suzuki, Y. Wu, J. Yu, U. Ruediger, A. D. Kent, T. K. Nath, and C. B. Eom, *Journal of Applied Physics* **87**, 6746, 10.1063/1.372828 (2000) (cit. on p. 43).

[170] A. Barman and G. Koren, *Applied Physics Letters* **77**, 1674, 10.1063/1.1309028 (2000) (cit. on p. 43).

[171] L. Ranno, A. Llobet, R. Tiron, and E. Favre-Nicolin, *Applied Surface Science* **188**, 170, 10.1016/S0169-4332(01)00730-9 (2002) (cit. on p. 43).

[172] J. Z. Sun, D. W. Abraham, R. A. Rao, and C. B. Eom, *Applied Physics Letters* **74**, 3017, 10.1063/1.124050 (1999) (cit. on pp. 43, 59, 96).

[173] R. P. Borges, W. Guichard, J. G. Lunney, J. M. D. Coey, and F. Ott, *Journal of Applied Physics* **89**, 3868, 10.1063/1.1331658 (2001) (cit. on p. 43).

[174] M. Huijben, L. W. Martin, Y.-H. Chu, M. B. Holcomb, P. Yu, G. Rijnders, D. H. A. Blank, and R. Ramesh, *Physical Review B* **78**, 094413, 10.1103/PhysRevB.78.094413 (2008) (cit. on pp. 43, 61, 73, 96).

[175] S. B. Ogale, Y. H. Li, M. Rajeswari, L. S. Riba, R. Ramesh, T. Venkatesan, A. J. Millis, R. Kumar, G. K. Mehta, R. Bathe, and S. I. Patil, *Journal of Applied Physics* **87**, 4210, 10.1063/1.373054 (2000) (cit. on p. 43).

[176] R. Herger, P. Willmott, C. Schlepütz, M. Björck, S. Pauli, D. Martoccia, B. Patterson, D. Kumah, R. Clarke, Y. Yacoby, and M. Döbeli, *Physical Review B* **77**, 085401, 10.1103/PhysRevB.77.085401 (2008) (cit. on pp. 43, 59).

[177] S. Ganesan and M. Pecht, eds., *Lead-free Electronics* (John Wiley & Sons, Inc., Hoboken, New Jersey, 2006), ISBN: 978-0471-78617-7 (cit. on p. 43).

[178] N. Izyumskaya, Y.-I. Alivov, S.-J. Cho, H. Morkoç, H. Lee, and Y.-S. Kang, *Critical Reviews in Solid State and Materials Sciences* **32**, 111, 10.1080/10408430701707347 (2007) (cit. on pp. 43, 44, 46, 47, 56, 82, 91, 98).

[179] Y. H. Chu, L. W. Martin, Q. Zhan, P. L. Yang, M. P. Cruz, K. Lee, M. Barry, S. Y. Yang, and R. Ramesh, *Ferroelectrics* **354**, 167, 10.1080/00150190701454867 (2007) (cit. on p. 44).

[180] D. Damjanovic, *Reports on Progress in Physics* **61**, 1267, 10.1088/0034-4885/61/9/002 (1998) (cit. on pp. 44, 53, 105).

[181] S. Yang, H. Bao, C. Zhou, Y. Wang, X. Ren, Y. Matsushita, Y. Katsuya, M. Tanaka, K. Kobayashi, X. Song, and J. Gao, *Physical Review Letters* **104**, 197201, 10.1103/PhysRevLett.104.197201 (2010) (cit. on p. 44).

[182] V. C. Lo, *Journal of Applied Physics* **92**, 6778, 10.1063/1.1520718 (2002) (cit. on pp. 45, 90).

[183] Y. S. Hwang and S. H. Paek, *Journal of Materials Science Letters* **14**, 322, 10.1007/BF00592138 (1995) (cit. on p. 46).

[184] P. Muralt, *Journal of Micromechanics and Microengineering* **10**, 136, 10.1088/0960-1317/10/2/307 (2000) (cit. on pp. 46, 53).

[185] R. Reshmi, V. Natarajan, and M. K. Jayaraj, *Integrated Ferroelectrics* **117**, 104, 10.1080/10584587.2010.489432 (2010) (cit. on p. 46).

[186] C. Paz de Araujo, J. F. Scott, and G. W. Taylor, eds., *Ferroelectric Thin Films: Synthesis and basic Properties* (Gordon and Breach Publishers, Amsterdam, 1996), ISBN: 2884491899 (cit. on pp. 47, 53).

[187] K. Wasa and M. Kitabatake, *Thin film materials technology: sputtering of compound materials* (William Andrew Publishing/Noyes, 2004), ISBN: 0815514832 (cit. on p. 47).

[188] T. Yasumoto, N. Yanase, K. Abe, and T. Kawakubo, *Japanese Journal of Applied Physics* **39**, 5369, 10.1143/JJAP.39.5369 (2000) (cit. on p. 47).

[189] Y. Liu, Y. Du, M. Zhang, H. Yan, and Y. Wang, *Vacuum* **81**, 826, 10.1016/j.vacuum.2006.09.016 (2007) (cit. on pp. 47, 63).

[190] Z. Konstantinović, J. Santiso, D. Colson, A. Forget, L. Balcells, and B. Martínez, *Journal of Applied Physics* **105**, 063919, 10.1063/1.3093862 (2009) (cit. on p. 47).

[191] O. I. Lebedev, G. V. Tendeloo, S. Amelinckx, H. L. Ju, and K. M. Krishnan, *Philosophical Magazine A* **80**, 673, 10.1080/01418610008212075 (2000) (cit. on p. 47).

[192] M.-J. Casanove, P. Baulès, C. Roucau, D. Magnoux, J.-F. Bobo, M. Bibes, L. Balcells, and J. Fontcuberta, *MRS Proceedings* **696**, N9.8, 10.1557/PROC-696-N9.8 (2011) (cit. on p. 47).

[193] S. Ramanathan, *Thin Film Metal-Oxides: Fundamentals and Applications in Electronics and Energy* (Springer, Berlin, 2009), ISBN: 978-1-4419-0664-9 (cit. on pp. 47, 61).

[194] H. Chou, S. G. Hsu, C. B. Lin, and C. B. Wu, *Applied Physics Letters* **90**, 062501, 10.1063/1.2437706 (2007) (cit. on p. 47).

[195] P. Dey, T. K. Nath, and A. Taraphder, *Applied Physics Letters* **91**, 012511, 10.1063/1.2750399 (2007) (cit. on pp. 47, 62).

[196] S.-M. Nam and T. Tsurumi, *Japanese Journal of Applied Physics* **43**, 2672, 10.1143/JJAP.43.2672 (2004) (cit. on p. 47).

[197] T. Motohiro and Y. Taga, *Thin Solid Films* **112**, 161, 10.1016/0040-6090(84)90493-0 (1984) (cit. on p. 47).

[198] R. E. Somekh, *Journal of Vacuum Science & Technology A: Vacuum, Surfaces, and Films* **2**, 1285, 10.1116/1.572396 (1984) (cit. on p. 47).

[199] K. Sreenivas and M. Sayer, *Journal of Applied Physics* **64**, 1484, 10.1063/1.341822 (1988) (cit. on pp. 47, 82).

[200] E. Cattan, *Journal of Vacuum Science & Technology A: Vacuum, Surfaces, and Films* **11**, 2808, 10.1116/1.578645 (1993) (cit. on p. 47).

[201] D. Depla and W. Leroy, *Thin Solid Films* **520**, 6337, 10.1016/j.tsf.2012.06.032 (2012) (cit. on pp. 47, 48, 67, 82).

[202] N. Motegi, *Journal of Vacuum Science & Technology B: Microelectronics and Nanometer Structures* **13**, 1906, 10.1116/1.587833 (1995) (cit. on p. 48).

[203] A. A. Mayo, *Journal of Vacuum Science & Technology B: Microelectronics and Nanometer Structures* **15**, 1788, 10.1116/1.589526 (1997) (cit. on p. 48).

[204] S. Mahieu, G. Buyle, D. Depla, S. Heirwegh, P. Ghekiere, and R. De Gryse, *Nuclear Instruments and Methods in Physics Research Section B: Beam Interactions with Materials and Atoms* **243**, 313, 10.1016/j.nimb.2005.09.018 (2006) (cit. on pp. 49, 50).

[205] P. Kelly and R. Arnell, *Vacuum* **56**, 159, 10.1016/S0042-207X(99)00189-X (2000) (cit. on p. 50).

[206] M. Birkholz, *Thin Film Analysis by X-Ray Scattering* (Wiley-VCH Verlag GmbH & Co. KGaA, Weinheim, FRG, Oct. 2005), 10.1002/3527607595 (cit. on p. 51).

[207] D. Bowen, *High resolution X-ray diffractometry and topography* (Taylor & Francis, London, 1998), ISBN: 0850667585 (cit. on pp. 51, 85).

[208] H. Lüth, *Solid Surfaces, Interfaces and Thin Films*, Graduate Texts in Physics (Springer, Berlin, 2010), 10.1007/978-3-642-13592-7 (cit. on p. 51).

[209] T. L. Alford, L. C. Feldman, and J. W. Mayer, *Fundamentals of nanoscale film analysis* (Springer Science+Business Media, New York, 2007), ISBN: 978-0-387-29260-1 (cit. on p. 52).

[210] M. A. Nicolet, J. W. Mayer, and I. V. Mitchell, *Science* **177**, 841, 10.1126/science.177.4052.841 (1972) (cit. on p. 52).

[211] M. Mayer, in AIP Conference Proceedings (1999), pp. 541–544, 10.1063/1.59188 (cit. on p. 52).

[212] K. Rabe, C. Ahn, and J.-M. Triscone, eds., *Physics of Ferroelectrics: A Modern Perspective* (Springer, Heidelberg, 2007) (cit. on pp. 53, 82).

[213] M. Dawber and J. F. Scott, *Reviews of Modern Physics* **77**, 1083, 10.1103/RevModPhys.77.1083 (2005) (cit. on pp. 53, 56, 100).

[214] D. Damjanovic, in *The science of hysteresis*, Vol. 3 (Academic Press, Oxford, 2006) Chap. 4, pp. 337–465, 10.1016/B978-012480874-4/50022-1 (cit. on p. 53).

[215] J. F. Scott, *Journal of Physics: Condensed Matter* **20**, 021001, 10.1088/0953-8984/20/02/021001 (2008) (cit. on p. 53).

[216] S. Aggarwal, S. Madhukar, B. Nagaraj, I. G. Jenkins, R. Ramesh, L. Boyer, and J. T. Evans, *Applied Physics Letters* **75**, 716, 10.1063/1.124492 (1999) (cit. on pp. 53, 91).

[217] E. J. Guo, K. Dörr, and A. Herklotz, *Applied Physics Letters* **101**, 242908, 10.1063/1.4772006 (2012) (cit. on p. 53).

[218] P. K. Larsen, G. L. M. Kampschöer, M. J. E. Ulenaers, G. A. C. M. Spierings, and R. Cuppens, *Applied Physics Letters* **59**, 611, 10.1063/1.105402 (1991) (cit. on pp. 54, 100).

[219] V. Bornand, S. Trolier-McKinstry, K. Takemura, and C. A. Randall, *Journal of Applied Physics* **87**, 3965, 10.1063/1.372442 (2000) (cit. on p. 54).

[220] K. M. Rabe, M. Dawber, C. Lichtensteiger, C. Ahn, and J. Triscone, *Physics of Ferroelectrics* **30**, 1, 10.1007/978-3-540-34591-6_1 (2007) (cit. on pp. 54, 100).

[221] L. L. Boyer, N. Velasquez, and J. T. Evans, *Japanese Journal of Applied Physics* **36**, 5799, 10.1143/JJAP.36.5799 (1997) (cit. on p. 54).

[222] O. Auciello, ed., *Science and technology of electroceramic thin films* (Kluwer Academic, Dordrecht, The Netherlands, 1995), ISBN: 0-7923-3332-2 (cit. on pp. 55, 81, 91).

[223] J.-l. Chen, H.-m. Chen, and J. Y.-m. Lee, *Applied Physics Letters* **69**, 4011, 10.1063/1.117854 (1996) (cit. on pp. 55, 100).

[224] P. Juan, H. Chou, and J. Lee, *Microelectronics Reliability* **45**, 1003, 10.1016/j.microrel.2004.11.004 (2005) (cit. on pp. 56, 83).

[225] C. A. Schneider, W. S. Rasband, and K. W. Eliceiri, *Nature Methods* **9**, 671, 10.1038/nmeth.2089 (2012) (cit. on p. 56).

[226] P. Klapetek, D. Nečas, and C. Anderson, *Gwyddion user guide*, http://gwyddion.net (cit. on p. 56).

[227] B. Josephson, *Physics Letters* **1**, 251, 10.1016/0031-9163(62)91369-0 (1962) (cit. on p. 56).

[228] J. Clarke and A. I. Braginski, eds., *The SQUID Handbook. Vol. I Fundamentals and Technology of SQUIDs and SQUID Systems*, Vol. 21, 5 (Wiley-VCH, Weinheim, Aug. 2004), pp. 583–583, ISBN: 3-527-40229-2 (cit. on p. 56).

[229] J. Clarke and A. I. Braginski, eds., *The SQUID Handbook. Vol. II, Applications of SQUIDs and SQUID Systems* (Wiley-VCH, Weinheim, 2006), ISBN: 978-3-527-40408-7 (cit. on p. 56).

[230] QuantumDesign, *Magnetic Property Measurement System – MPMS-XL*, 2005, http://www.lot-qd.de/files/downloads/qd/en/mpms%5C_broschure%5C_en.pdf (cit. on pp. 56, 57, 59).

[231] A. Ney, T. Kammermeier, V. Ney, K. Ollefs, and S. Ye, *Journal of Magnetism and Magnetic Materials* **320**, 3341, 10.1016/j.jmmm.2008.07.008 (2008) (cit. on pp. 57, 97).

[232] M. Sawicki, W. Stefanowicz, and A. Ney, *Semiconductor Science and Technology* **26**, 064006, 10.1088/0268-1242/26/6/064006 (2011) (cit. on pp. 57, 97).

[233] Y. Wu, Y. Suzuki, U. Rüdiger, J. Yu, A. D. Kent, T. K. Nath, and C. B. Eom, *Applied Physics Letters* **75**, 2295, 10.1063/1.124995 (1999) (cit. on p. 59).

[234] S. Yang, W. Kuang, C. Ho, W. Tse, M. Lin, S. Lee, Y. Liou, and Y. Yao, *Journal of Magnetism and Magnetic Materials* **226-230**, 690, 10.1016/S0304-8853(01)00102-0 (2001) (cit. on p. 59).

[235] X. Chen, H.-U. Habermeier, H. Zhang, G. Gu, M. Varela, J. Santamaria, and C. Almasan, *Physical Review B* **72**, 104403, 10.1103/PhysRevB.72.104403 (2005) (cit. on p. 59).

[236] L. V. D. Pauw, *Philips Technical Review* **20**, 220 (1958) (cit. on p. 59).

[237] P. M. Leufke, A. K. Mishra, A. Beck, D. Wang, C. Kübel, R. Kruk, and H. Hahn, *Thin Solid Films* **520**, 5521, 10.1016/j.tsf.2012.04.064 (2012) (cit. on pp. 61, 63, 65–67, 69, 70, 76, 77, 96, 97).

[238] B. Kim, D. Kwon, J. H. Song, Y. Hikita, B. G. Kim, and H. Y. Hwang, *Solid State Communications* **150**, 598, 10.1016/j.ssc.2009.12.041 (2010) (cit. on pp. 61, 96).

[239] A. Tebano, A. Orsini, P. G. Medaglia, and G. Balestrino, *Applied Physics Letters* **94**, 242503, 10.1063/1.3155136 (2009) (cit. on p. 61).

[240] S. Valencia, Z. Konstantinovic, A. Gaupp, D. Schmitz, L. Balcells, and B. Martínez, *Journal of Applied Physics* **109**, 07D718, 10.1063/1.3545814 (2011) (cit. on p. 61).

[241] C.-L. Wu, P.-W. Lee, Y.-C. Chen, L.-Y. Chang, C.-H. Chen, C.-W. Liang, P. Yu, Q. He, R. Ramesh, and Y.-H. Chu, *Physical Review B* **83**, 020103, 10.1103/PhysRevB.83.020103 (2011) (cit. on p. 61).

[242] R. Martínez, A. Kumar, R. Palai, R. S. Katiyar, and J. F. Scott, *Journal of Applied Physics* **107**, 114107, 10.1063/1.3437627 (2010) (cit. on p. 61).

[243] Z. Yang, C. Ke, L. Sun, W. Zhu, L. Wang, X. Chen, and O. Tan, *Solid State Communications* **150**, 1432, 10.1016/j.ssc.2010.05.022 (2010) (cit. on p. 61).

[244] M. Ziese, I. Vrejoiu, and D. Hesse, *Applied Physics Letters* **97**, 052504, 10.1063/1.3470101 (2010) (cit. on p. 61).

[245] W. Eerenstein, M. Wiora, J. L. Prieto, J. F. Scott, and N. D. Mathur, *Nature materials* **6**, 348, 10.1038/nmat1886 (2007) (cit. on pp. 61, 93).

[246] H. Béa, M. Bibes, M. Sirena, G. Herranz, K. Bouzehouane, E. Jacquet, S. Fusil, P. Paruch, M. Dawber, J.-P. Contour, and A. Barthélémy, *Applied Physics Letters* **88**, 62502, 10.1063/1.2170432 (2006) (cit. on p. 61).

[247] H. J. A. Molegraaf, J. Hoffman, C. A. F. Vaz, S. Gariglio, D. van der Marel, C. H. Ahn, and J.-M. Triscone, *Advanced Materials* **21**, 3470, 10.1002/adma.200900278 (2009) (cit. on pp. 61, 95, 97, 103, 104, 107, 110, 111).

[248] C. A. F. Vaz, Y. Segal, J. Hoffman, R. D. Grober, F. J. Walker, and C. H. Ahn, *Applied Physics Letters* **97**, 042506, 10.1063/1.3472259 (2010) (cit. on pp. 61, 95, 97, 104, 107, 109, 110, 112).

[249] C. A. F. Vaz, J. Hoffman, Y. Segal, J. W. Reiner, R. D. Grober, Z. Zhang, C. H. Ahn, and F. J. Walker, *Physical Review Letters* **104**, 127202, 10.1103/PhysRevLett.104.127202 (2010) (cit. on pp. 61, 95–97, 107, 109, 110).

[250] C. A. F. Vaz, Y. Segal, J. Hoffman, F. J. Walker, and C. H. Ahn, *Journal of Vacuum Science & Technology B: Microelectronics and Nanometer Structures* **28**, C5A6, 10.1116/1.3427140 (2010) (cit. on pp. 61, 77, 83, 85, 86, 89, 110).

[251] S. K. Singh, S. B. Palmer, D. McK. Paul, and M. R. Lees, *Applied Physics Letters* **69**, 263, 10.1063/1.117944 (1996) (cit. on p. 61).

[252] E. Vlakhov, K. Nenkov, T. Donchev, and A. Spasov, *Vacuum* **69**, 255, 10.1016/S0042-207X(02)00341-X (2002) (cit. on pp. 62, 63).

[253] W. Prellier, M. Rajeswari, T. Venkatesan, and R. L. Greene, *Applied Physics Letters* **75**, 1446, 10.1063/1.124720 (1999) (cit. on pp. 62, 63, 75, 76).

[254] J. F. Bobo, D. Magnoux, R. Porres, B. Raquet, J. C. Ousset, A. R. Fert, C. Roucau, P. Baulès, M. J. Casanove, and E. Snoeck, *Journal of Applied Physics* **87**, 6773, 10.1063/1.372837 (2000) (cit. on pp. 63, 77).

[255] T. Petrisor, M. S. Gabor, A. Boulle, C. Bellouard, C. Tiusan, and O. Pana, *Journal of Applied Physics* **109**, 123913, 10.1063/1.3596807 (2011) (cit. on pp. 63, 75, 76).

[256] P. Orgiani, A. Y. Petrov, R. Ciancio, A. Galdi, L. Maritato, and B. A. Davidson, *Applied Physics Letters* **100**, 042404, 10.1063/1.3676268 (2012) (cit. on pp. 63, 75, 76).

[257] G. Velu, D. Remiens, and B. Thierry, *Journal of the European Ceramic Society* **17**, 1749, 10.1016/S0955-2219(97)00031-9 (1997) (cit. on pp. 67, 82).

[258] A. Stierle and E. Vlieg, in *Modern Diffraction Methods* (Wiley-VCH Verlag GmbH & Co. KGaA, 2012), pp. 221–257, 10.1002/9783527649884.ch8 (cit. on p. 68).

[259] C. Aruta, G. Balestrino, A. Tebano, G. Ghiringhelli, and N. B. Brookes, *Europhysics Letters* **80**, 37003, 10.1209/0295-5075/80/37003 (2007) (cit. on p. 68).

[260] T. Santos, S. May, J. Robertson, and A. Bhattacharya, *Physical Review B* **80**, 155114, 10.1103/PhysRevB.80.155114 (2009) (cit. on p. 68).

[261] M. Belmeguenai, S. Mercone, C. Adamo, T. Chauveau, L. Méchin, P. Monod, P. Moch, and D. G. Schlom, *Journal of Nanoparticle Research* **13**, 5669, 10.1007/s11051-011-0334-y (2011) (cit. on p. 68).

[262] V. Vlasko-Vlasov, Y. Lin, D. Miller, U. Welp, G. Crabtree, and V. Nikitenko, *Physical Review Letters* **84**, 2239, 10.1103/PhysRevLett.84.2239 (2000) (cit. on p. 71).

[263] M. Ziese, I. Vrejoiu, A. Setzer, A. Lotnyk, and D. Hesse, *New Journal of Physics* **10**, 063024, 10.1088/1367-2630/10/6/063024 (2008) (cit. on p. 71).

[264] M. Egilmez, M. Saber, I. Fan, K. Chow, and J. Jung, *Physical Review B* **78**, 172405, 10.1103/PhysRevB.78.172405 (2008) (cit. on p. 71).

[265] A. Arrott, *Physical Review* **108**, 1394, 10.1103/PhysRev.108.1394 (1957) (cit. on pp. 72, 104).

[266] H. E. Stanley, *Introduction to phase transitions and critical phenomena* (Oxford University Press, Oxford, 1971), ISBN: 0-19-505316-8 (cit. on p. 72).

[267] A. Tozri, E. Dhahri, E. Hlil, and M. Valente, *Solid State Communications* **151**, 315, 10.1016/j.ssc.2010.11.036 (2011) (cit. on p. 72).

[268] J. Geck, P. Wochner, D. Bruns, B. Büchner, U. Gebhardt, S. Kiele, P. Reutler, and A. Revcolevschi, *Physical Review B* **69**, 104413, 10.1103/PhysRevB.69.104413 (2004) (cit. on p. 72).

[269] T. F. Zhou, G. Li, X. G. Li, S. W. Jin, and W. B. Wu, *Applied Physics Letters* **90**, 042512, 10.1063/1.2432292 (2007) (cit. on p. 75).

[270] U. Gebhardt, N. Kasper, A. Vigliante, P. Wochner, H. Dosch, F. Razavi, and H.-U. Habermeier, *Physical Review Letters* **98**, 096101, 10.1103/PhysRevLett.98.096101 (2007) (cit. on p. 75).

[271] G. Turner, A. Sikorski, D. McKenzie, G. Smith, K. Ng, and D. Cockayne, *Physica C: Superconductivity* **170**, 473, 10.1016/0921-4534(90)90018-A (1990) (cit. on p. 76).

[272] M.-J. Casanove, C. Roucau, P. Baulès, J. Majimel, J.-C. Ousset, D. Magnoux, and J. Bobo, *Applied Surface Science* **188**, 19, 10.1016/S0169-4332(01)00709-7 (2002) (cit. on p. 77).

[273] A. M. Haghiri-Gosnet, J. Wolfman, B. Mercey, C. Simon, P. Lecoeur, M. Korzenski, M. Hervieu, R. Desfeux, and G. Baldinozzi, *Journal of Applied Physics* **88**, 4257, 10.1063/1.1309040 (2000) (cit. on p. 77).

[274] P. M. Leufke, R. Kruk, D. Wang, C. Kübel, and H. Hahn, *AIP Advances* **2**, 032184, 10.1063/1.4756997 (2012) (cit. on pp. 81, 84, 86, 87, 89, 91, 97).

[275] T. Nakamura, Y. Nakao, A. Kamisawa, and H. Takasu, *Applied Physics Letters* **65**, 1522, 10.1063/1.112031 (1994) (cit. on p. 81).

[276] H. N. Al-Shareef, O. Auciello, and A. I. Kingon, *Journal of Applied Physics* **77**, 2146, 10.1063/1.359572 (1995) (cit. on p. 81).

[277] X. Wang, Y. Wang, J. Yin, and Z. Liu, *Scripta Materialia* **46**, 783, 10.1016/S1359-6462(02)00076-3 (2002) (cit. on p. 81).

[278] R. Ramesh, W. K. Chan, B. Wilkens, H. Gilchrist, T. Sands, J. M. Tarascon, V. G. Keramidas, D. K. Fork, J. Lee, and A. Safari, *Applied Physics Letters* **61**, 1537, 10.1063/1.107488 (1992) (cit. on p. 81).

[279] M.-S. Chen, T.-B. Wu, and J.-M. Wu, *Applied Physics Letters* **68**, 1430, 10.1063/1.116103 (1996) (cit. on p. 81).

[280] C. B. Eom, R. B. Van Dover, J. M. Phillips, D. J. Werder, J. H. Marshall, C. H. Chen, R. J. Cava, R. M. Fleming, and D. K. Fork, *Applied Physics Letters* **63**, 2570, 10.1063/1.110436 (1993) (cit. on p. 81).

[281] R. Ramesh, H. Gilchrist, T. Sands, V. G. Keramidas, R. Haakenaasen, and D. K. Fork, *Applied Physics Letters* **63**, 3592, 10.1063/1.110106 (1993) (cit. on p. 81).

[282] F. Chen, Q. Z. Liu, H. F. Wang, F. H. Zhang, and W. Wu, *Applied Physics Letters* **90**, 192907, 10.1063/1.2737912 (2007) (cit. on pp. 81, 82, 85, 86, 90, 91, 100).

[283] W. Wu, K. H. Wong, C. L. Choy, and Y. H. Zhang, *Applied Physics Letters* **77**, 3441, 10.1063/1.1327279 (2000) (cit. on pp. 81, 82, 86, 90, 91).

[284] W. Wu, Y. Wang, G. K. H. Pang, K. H. Wong, and C. L. Choy, *Applied Physics Letters* **85**, 1583, 10.1063/1.1786662 (2004) (cit. on pp. 81, 90).

[285] S. Kalpat and K. Uchino, *Journal of Applied Physics* **90**, 2703, 10.1063/1.1385580 (2001) (cit. on p. 82).

[286] F. Mitsugi, Y. Yamagata, T. Ikegami, K. Ebihara, J. Narayan, and A. M. Grishin, *Japanese Journal of Applied Physics* **39**, 5418, 10.1143/JJAP.39.5418 (2000) (cit. on p. 86).

[287] J. J. Lee and S. B. Desu, *Ferroelectrics Letters Section* **20**, 27, 10.1080/07315179508204723 (1995) (cit. on p. 90).

[288] W. Wu, K. H. Wong, and C. L. Choy, *Applied Physics Letters* **85**, 5013, 10.1063/1.1827929 (2004) (cit. on p. 90).

[289] S. Aggarwal, A. M. Dhote, R. Ramesh, W. L. Warren, G. E. Pike, D. Dimos, M. V. Raymond, B. A. Tuttle, and J. T. Evans, *Applied Physics Letters* **69**, 2540, 10.1063/1.117732 (1996) (cit. on p. 90).

[290] G. E. Pike, W. L. Warren, D. Dimos, B. A. Tuttle, R. Ramesh, J. Lee, V. G. Keramidas, and J. T. Evans, *Applied Physics Letters* **66**, 484, 10.1063/1.114064 (1995) (cit. on p. 90).

[291] T. Friessnegg, S. Aggarwal, R. Ramesh, B. Nielsen, E. H. Poindexter, and D. J. Keeble, *Applied Physics Letters* **77**, 127, 10.1063/1.126898 (2000) (cit. on p. 90).

[292] J. Lee, R. Ramesh, V. G. Keramidas, W. L. Warren, G. E. Pike, and J. T. Evans, *Applied Physics Letters* **66**, 1337, 10.1063/1.113234 (1995) (cit. on p. 90).

[293] J. F. Scott, C. A. Araujo, B. M. Melnick, L. D. McMillan, and R. Zuleeg, *Journal of Applied Physics* **70**, 382, 10.1063/1.350286 (1991) (cit. on p. 90).

[294] S. Dussan, A. Kumar, J. F. Scott, and R. S. Katiyar, *Applied Physics Letters* **96**, 072904, 10.1063/1.3327889 (2010) (cit. on pp. 90, 91).

[295] J. F. M. Cillessen, M. W. J. Prins, and R. M. Wolf, *Journal of Applied Physics* **81**, 2777, 10.1063/1.363961 (1997) (cit. on p. 91).

[296] S. Ray, M. Algueró, J. Ricote, M. Calzada, C. Prieto, A. de Andrés, and M. Garcia-Hernández, *Materials Letters* **60**, 1714, 10.1016/j.matlet.2005.12.007 (2006) (cit. on p. 91).

[297] P. M. Leufke, R. Kruk, R. A. Brand, and H. Hahn, *Physical Review B* **87**, 094416, 10.1103/PhysRevB.87.094416 (2013) (cit. on pp. 93, 104–107, 111, 112).

[298] M. K. Lee, T. K. Nath, C. B. Eom, M. C. Smoak, and F. Tsui, *Applied Physics Letters* **77**, 3547, 10.1063/1.1328762 (2000) (cit. on p. 93).

[299] K. Dörr, O. Bilani-Zeneli, A. Herklotz, A. D. Rata, K. Boldyreva, J.-W. Kim, M. C. Dekker, K. Nenkov, L. Schultz, and M. Reibold, *The European Physical Journal B* **71**, 361, 10.1140/epjb/e2009-00296-x (2009) (cit. on p. 94).

[300] R. K. Zheng, Y. Wang, H. L. W. Chan, C. L. Choy, and H. S. Luo, *Applied Physics Letters* **90**, 152904, 10.1063/1.2721399 (2007) (cit. on p. 94).

[301] R. K. Zheng, Y. Jiang, Y. Wang, H. L. W. Chan, C. L. Choy, and H. S. Luo, *Applied Physics Letters* **93**, 102904, 10.1063/1.2979688 (2008) (cit. on p. 94).

[302] Q. X. Zhu, W. Wang, X. Q. Zhao, X. M. Li, Y. Wang, H. S. Luo, H. L. W. Chan, and R. K. Zheng, *Journal of Applied Physics* **111**, 103702, 10.1063/1.4716188 (2012) (cit. on p. 94).

[303] C. Thiele, K. Dörr, O. Bilani, J. Rödel, and L. Schultz, *Physical Review B* **75**, 054408, 10.1103/PhysRevB.75.054408 (2007) (cit. on p. 94).

[304] C. Thiele, K. Dörr, L. Schultz, E. Beyreuther, and W.-M. Lin, *Applied Physics Letters* **87**, 162512, 10.1063/1.2108129 (2005) (cit. on p. 94).

[305] K. Dörr and C. Thiele, *physica status solidi (b)* **243**, 21, 10.1002/pssb.200562441 (2006) (cit. on pp. 94, 98).

[306] S. Mathews, *Science* **276**, 238, 10.1126/science.276.5310.238 (1997) (cit. on p. 94).

[307] T. Kanki, Y.-G. Park, H. Tanaka, and T. Kawai, *Applied Physics Letters* **83**, 4860, 10.1063/1.1632028 (2003) (cit. on pp. 94, 95).

[308] T. Kanki, H. Tanaka, and T. Kawai, *Applied Physics Letters* **89**, 242506, 10.1063/1.2405861 (2006) (cit. on pp. 94, 95).

[309] X. Hong, A. Posadas, and C. H. Ahn, *Applied Physics Letters* **86**, 142501, 10.1063/1.1897076 (2005) (cit. on pp. 94–96).

[310] J. Hoffman, X. Hong, and C. H. Ahn, *Nanotechnology* **22**, 254014, 10.1088/0957-4484/22/25/254014 (2011) (cit. on pp. 94, 95).

[311] Y. W. Yin, M. Raju, W. J. Hu, X. J. Weng, X. G. Li, and Q. Li, *Journal of Applied Physics* **109**, 07D915, 10.1063/1.3564970 (2011) (cit. on p. 94).

[312] I. E. Chupis, *Low Temperature Physics* **23**, 213, 10.1063/1.593479 (1997) (cit. on p. 95).

[313] H. Wieder and D. Collins, *Physical Review* **120**, 725, 10.1103/PhysRev.120.725 (1960) (cit. on p. 95).

[314] J. Burton and E. Tsymbal, *Physical Review B* **80**, 174406, 10.1103/PhysRevB.80.174406 (2009) (cit. on pp. 95, 96, 109).

[315] H. Lu, T. A. George, Y. Wang, I. Ketsman, J. D. Burton, C.-W. Bark, S. Ryu, D. J. Kim, J. Wang, C. Binek, P. A. Dowben, A. Sokolov, C.-B. Eom, E. Y. Tsymbal, and A. Gruverman, *Applied Physics Letters* **100**, 232904, 10.1063/1.4726427 (2012) (cit. on pp. 95, 97, 103, 109).

[316] K.-H. Müller, K. Dörr, T. Walter, M. Sahana, K. Brand, and L. Schultz, *Journal of Magnetism and Magnetic Materials* **242-245**, 447, 10.1016/S0304-8853(01)01337-3 (2002) (cit. on p. 96).

[317] D. Preziosi, D. Hesse, M. Alexe, M. Wahler, and G. Schmidt, in DPG-Verhandlungen (2013), MA, http://www.dpg-verhandlungen.de/year/2013/conference/regensburg/static/ma2.pdf (cit. on p. 97).

[318] M. Nguyen, "Ferroelectric and piezoelectric properties of epitaxial PZT films and devices on silicon", PhD thesis (Universiteit Twente, 2010), ISBN: 978-90-365-3047-7, http://doc.utwente.nl/71949/ (cit. on p. 98).

[319] S. Krumbein, *IEEE Transactions on Components, Hybrids, and Manufacturing Technology* **11**, 5, 10.1109/33.2957 (1988) (cit. on p. 99).

[320] J. J. Lee, C. L. Thio, and S. B. Desu, *Journal of Applied Physics* **78**, 5073, 10.1063/1.359737 (1995) (cit. on p. 100).

[321] S. Dussan, A. Kumar, R. S. Katiyar, S. Priya, and J. F. Scott, *Journal of physics. Condensed matter* **23**, 202203, 10.1088/0953-8984/23/20/202203 (2011) (cit. on p. 100).

[322] J. Curiale, M. Granada, H. E. Troiani, R. D. Sánchez, A. G. Leyva, P. Levy, and K. Samwer, *Applied Physics Letters* **95**, 043106, 10.1063/1.3187538 (2009) (cit. on p. 107).

[323] S. Dong, X. Zhang, R. Yu, J.-M. Liu, and E. Dagotto, *Physical Review B* **84**, 155117, 10.1103/PhysRevB.84.155117 (2011) (cit. on p. 109).

[324] H. Molegraaf, J. Hoffman, J. Stahn, and S. Gariglio, in THIOX Thin Films For Novel Oxide Devices Final Meeting (2008), o62, http://www.thiox2008.lamia.infm.it/orals/o62.htm (cit. on p. 110).

[325] H. Chen and S. Ismail-Beigi, *Physical Review B* **86**, 024433, 10.1103/PhysRevB.86.024433 (2012) (cit. on p. 113).

[326] A. Alberca, C. Munuera, J. Tornos, F. J. Mompean, N. Biskup, A. Ruiz, N. M. Nemes, A. de Andres, C. León, J. Santamaría, and M. García-Hernández, *Physical Review B* **86**, 144416, 10.1103/PhysRevB.86.144416 (2012) (cit. on p. 113).

Appendices

A Supplementary material

A.1 Materials and methods

A.1.1 Calibration of the sputtering system

As mentioned in Section 3.3.2, the LDMS chamber was brand new and put into use at the beginning of the present studies. For this reason a comprehensive test of the system was performed prior to the main project.

It is established knowledge that the substrate temperature has great influence on microstructure, morphology and even stoichiometry of (oxide) thin films. Although the thermocouple at the heating head of the manipulator of the sputtering system is of avail for controlled temperature ramps, it is too distant to give accurate temperature readings of the sample holder or the substrate itself. Thus, the sample temperature was calibrated with a type-K thermocouple directly mounted in the center of a sample holder. To get reasonable thermal contact and at the same time electrical insulation, the sensor was tightly clamped between two quartz sheets.

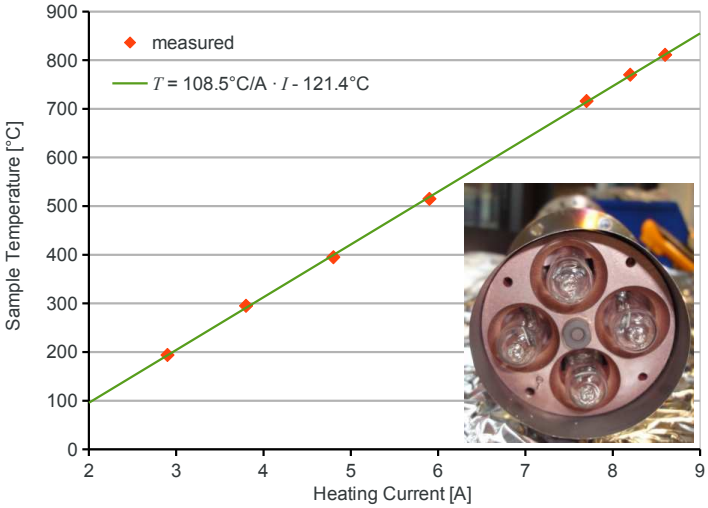

Figure A.1.: Dependence of sample temperature and heating current of the heated manipulator of the sputtering chamber. The inset shows a photograph of the heating head and the halogen lamps. The type-K thermocouple is located between the left and bottom lamp.

Heating voltage and current were monitored and correlated with the sample temperature. It was found that there is a linear relationship between the heating current and the temperature (see Fig. A.1). In subsequent measurements, after occasional lamp exchange, this calibration relation was again confirmed. Due to the very low resistance of the halogen bulbs[1], changes in the contact resistance during oxidation of the lamp sockets and wiring clamps have considerable impact on the required voltages and thus the total heating power. However, as only the power drain in close vicinity of the sample is of importance for the sample temperature, only the resistance of the halogen bulbs is relevant. As a consequence, the heating current is the most reliable measure for the sample temperature.

Another important helpful information for operating a sputtering system is the accessible pressure window for a certain gas flow. Pressure regulation with the throttle valve in front of the Turbo Molecular Pump (TMP) (compare Fig. 3.9(c) on p. 49), which is operated by the *Baratron* gauge controller via a stepping motor, works best when the desired working pressure (p_{work}) is not too close to boundaries of the regulation range (darker solid lines in Fig. A.2).

As illustrated in Fig. A.2, the fully closed position of the throttle valve still allows for considerable gas flow through the TMP. Thus, if higher p_{work} is required, the process gas flow (Ar and/or O_2) needs to be increased. However, at a gas flow of more than ≈160 sccm, the load on the TMP exceeds its capability. As a workaround, the speed of the TMP can intentionally be decreased in advance. The regulation window for the TMP speed reduced to 200 Hz is depicted by the blue area in the diagram in Fig. A.2. Compared to the full-speed regulation window (orange area), the throttled window is much smaller and not linear. Thus, the accurate choice of the process gas flow is more important in this setting.

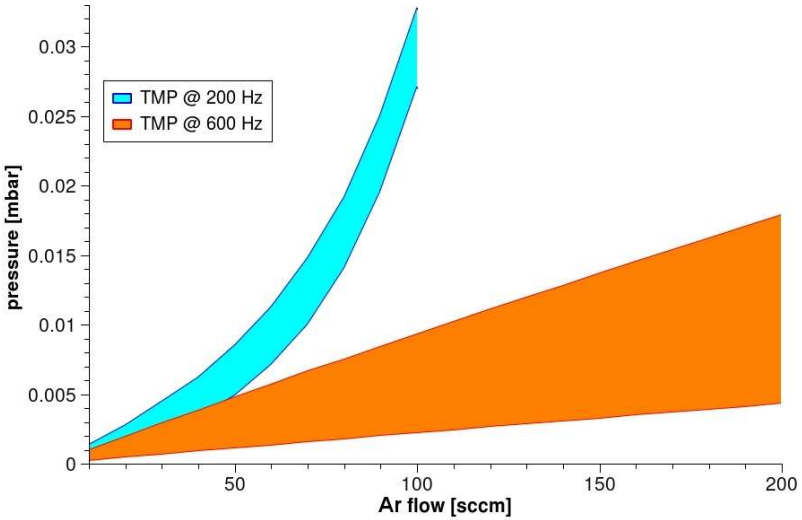

Figure A.2.: Accessible pressure window of the sputtering system as a function of the Ar flow, for the TMP set to full speed (600 Hz) and throttled to 33 % (200 Hz), respectively.

[1] The resistance of a single bulb ranges from $< 1\,\Omega$ at RT to $2.3\,\Omega$ at maximum power of 250 W.

A.1.2 Sputter targets

The functional thin film materials employed in this work, i.e., LSMO and PZT (see Section 3.2), were deposited from commercially available – though custom made – sputtering targets; Tab. A.1 gives an overview of the compositions, bonding types and supplier data.

To facilitate a good thermal contact between the targets' copper backing plates and the water-cooled magnetrons, an indium or a graphite foil was placed at the interface, when mounting the targets.

Table A.1.: List of sputter targets employed for the present studies. All targets have a diameter of 76.2 mm (3 "), thickness of ≈3 mm and are bonded to a 2 to 3 mm thick copper backing plate.

material	composition	bonding type	supplier	part/lot number
LSMO	$La_{0.75}Sr_{0.25}MnO_3$	elastomer	KURT J. LESKER	part-#: EJTLASRMNSPL04 lot-#: PRD033053/06-09-09
	$La_{0.65}Sr_{0.35}MnO_3$			part-#: EJTLASRMNSPL09 lot-#: PRD058633/12-08-10
PZT	$PbZr_{0.52}Ti_{0.48}O_3$	indium-tin sapphire + resin	SURFACENET	lot-#: 2360140710 lot-#: 3468190412

A.1.3 Single crystal substrates

Five kinds of (nominally) single crystal oxide substrates were used (see Section 3.1); a listing of supplier and batch information can be found in Tab. A.2. Apart from the annealing in Ultra-High Vacuum (UHV) prior to film deposition (see Section 4.2), no other substrate treatment was performed.

The substrates were sorted out by means of High-Resolution X-ray Diffraction (HRXRD) Rocking Curves (RCs) on their (001) or (002) reflections regarding their single-crystallinity. In cases where mosaicity was observed, the substrates were replaced by the supplier or were at least not used for studies, where the mosaicity poses a problem, e.g., for the Reciprocal Space Map (RSM) measurements.

Table A.2.: List of substrate batches employed for the present studies. All substrates are (100)-oriented – in (pseudo-)cubic coordinates – and epi-polished.

material	composition	dimensions [mm^3]	supplier	lot number
LAO	$LaAlO_3$	$10 \times 10 \times 0.5$	SurfaceNet	2290160210
LSAT	$(La_{0.3}Sr_{0.7})(Al_{0.65}Ta_{0.35})O_3$	$10 \times 10 \times 0.5$	SurfaceNet	2469270510
MgO	MgO	$10 \times 10 \times 0.5$	SurfaceNet	2289160210
		$10 \times 5 \times 0.5$		2571190710
STO	STO	$10 \times 10 \times 0.5$	Crystal GmbH	d 793
		$10 \times 5 \times 0.5$	SurfaceNet	2570190710
		$10 \times 5 \times 0.5$	SurfaceNet	2780101210
		$10 \times 5 \times 1$	SurfaceNet	24212
STO:Nb	$SrTiO_3$:Nb(0.5 wt.%)	$10 \times 3 \times 0.5$	SurfaceNet	2288220310
		$10 \times 5 \times 0.5$		3070080711

A.1.4 Epoxies

In Section 6.2, the workflow for the Superconductive Quantum Interference Device (SQUID)-compatible ME device preparation was explained in detail (see also Fig. 6.3). The various conductive and insulating epoxies used in this procedure are listed in Tab. A.3.

The low-viscosity *HT 2* epoxy was found to work best as a protective coating of the sample surface. The curing process had to take place at Room Temperature (RT), as otherwise at elevated temperatures, the initially spread resin would immediately flow together into droplets. The fast-curing high-viscosity epoxy was mainly employed for fixing of the wires and other mechanical stabilization of the like.

Table A.3.: List of two-component epoxies that were used for SQUID-compatible contacting and fixation of the ME devices for *in situ* tuning experiments.

product	supplier	description
H20E	EPO-TEK Epoxy Technology, Inc.	silver-based conductive epoxy
EC 261 C	Polytec PT GmbH	carbon-based conductive epoxy
10 Min. Epoxy	R&G Faserverbundwerkstoffe GmbH	high-viscosity, fast-curing, transparent glue
HT 2	R&G Faserverbundwerkstoffe GmbH	low-viscosity, slow-curing, transparent laminating resin

A.1.5 *In situ* polarization cycling in SQUID

The *in situ* tuning experiments in the SQUID magnetometer (Chapter 6) were carried out in FE remanence (see Section 6.2 for details). In order to quantify the modulation of remanent FE polarization (P_r), and to enable a time-resolved analysis of the charging process, a triangular Positive-Up Negative-Down (PUND) pulse sequence was employed, where the Reciprocating Sample Option (RSO) measurements were performed in between, as depicted in the pulse train sketch in Fig. A.3.

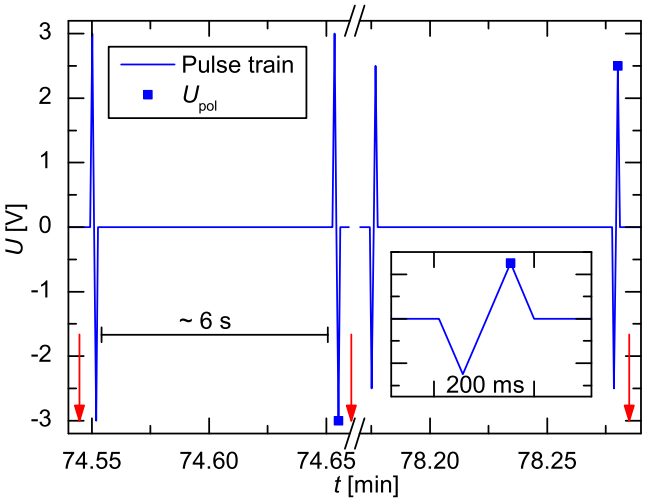

Figure A.3.: Extract of the triangular PUND pulse train employed for charging the device with different voltages U_{pol} and the calculation of the modulation of the remanent polarization ΔP_r. The RSO SQUID measurements were performed at the times indicated by the red arrows. The inset shows a single triangular bipolar waveform.

A.2 Results

A.2.1 Influence of the sputtering conditions on the LSMO microstructure

The discussion of the influence of the O_2 partial pressure (p_{O2}) and the sputtering method on the microstructure of the LSMO thin films in Chapter 4 (Section 4.3.1, pp. 63) is mostly focusing on the STO substrates, which play the major role in the subsequent chapters. However, the microstructure of the other investigated substrates – $(La_{0.3}Sr_{0.7})(Al_{0.65}Ta_{0.35})O_3$ (LSAT), LAO and MgO – was also characterized by means of RSMs, revealing some remarkable differences[2].

Like in the case of the STO substrate, high-p_{O2} RF sputtering of LSMO on LSAT (100) results in a commensurate growth [see Fig. A.4(a)] which in turn leads to a periodic twinning. The latter is also nicely visible in the RSM on the symmetric (002)-reflection, where two satellite peaks appear along the rocking curve direction of the scan, i.e., along the h component. The satellites along the vertical direction are identical with the finite thickness oscillations (Laue fringes) that were already resolved in the θ-2θ diffraction pattern in Fig. 4.5(b).

Regarding the growth on LAO (100) substrates, the high compressive in-plane strain induced by the substrate can only be maintained in the oxygen-deficient conditions [Fig. A.5(a)], whereas a higher p_{O2} causes strain relaxation regardless of the sputtering mode (A.5(b)&(c) which is accompanied by a reduction of the c lattice parameter. However, the in-plane lattice parameter is still smaller and the out-of-plane parameter larger than the bulk lattice constants, indicating

[2] The RSMs shown in this section are plotted in reciprocal space units (r.s.u.) of the respective substrate.

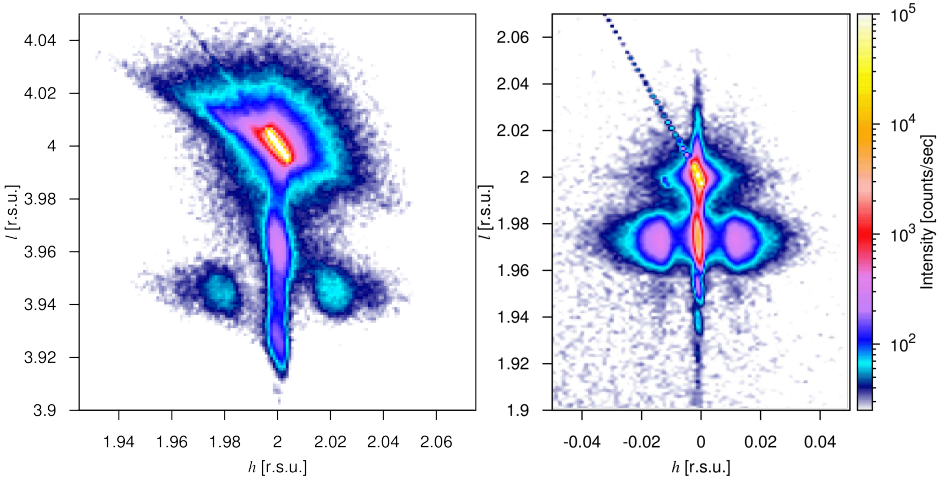

(a) (204)-reflection **(b)** (002)-reflection

Figure A.4.: RSMs on the asymmetric (204)- and the symmetric (002)-reflection of 28 nm LSMO on LSAT (100), deposited in RF mode at $p_{O2} = 0.72$ Pa.

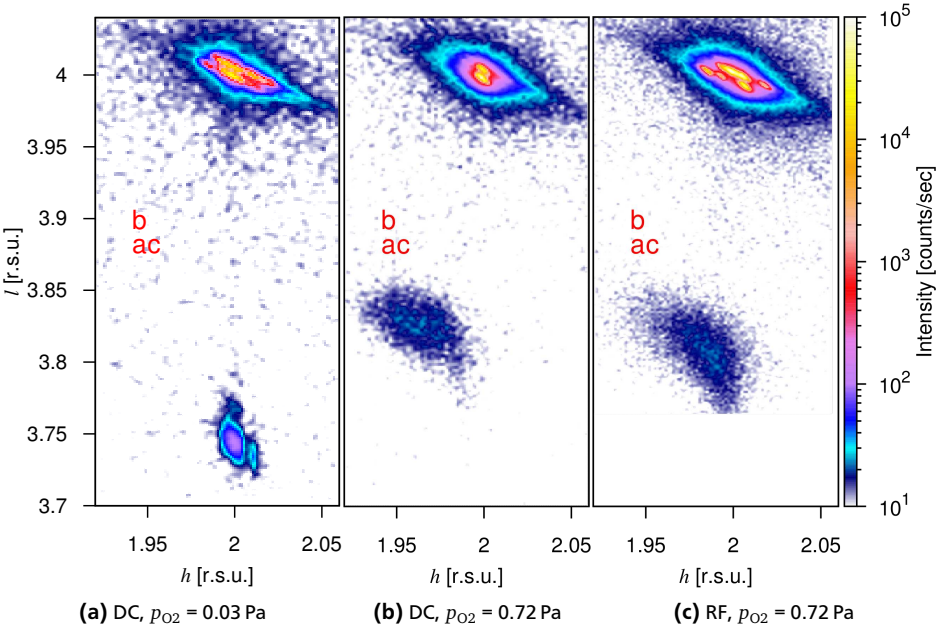

Figure A.5.: RSMs on the (204)-reflection of 20 to 30 nm LSMO on LAO (100), deposited in DC and RF mode at low and high O_2 partial pressures, as indicated. The letters a, b and c indicate the theoretically expected location of the LSMO reflection for fully relaxed growth along the correspondent crystal direction.

a residual lattice strain presence. From these RSMs the common problem of twin formation in LAO single crystals can also be seen: none of the investigated substrates showed a single-peak reflection.

The θ-2θ diffractogram [Fig. 4.5(d) on p. 67] already suggested and the Scanning Transmission Electron Microscopy (STEM) studies finally confirmed (Fig. 4.7 on p. 69) a fully relaxed growth mode, caused by the high lattice mismatch of LSMO on MgO. The corresponding RSMs for the two most distinct deposition parameter sets are shown in Fig. A.6 for completeness. As visualized in the statistical evaluation (Fig. 4.12), the RSMs confirm that on MgO the LSMO lattice parameters are only marginally affected by the sputtering mode and p_{O2}. However, it should be mentioned that this structural indifference does not apply to the magnetic properties which are still strongly compromised by a low O_2 partial pressure and the Direct Current (DC) sputtering mode.

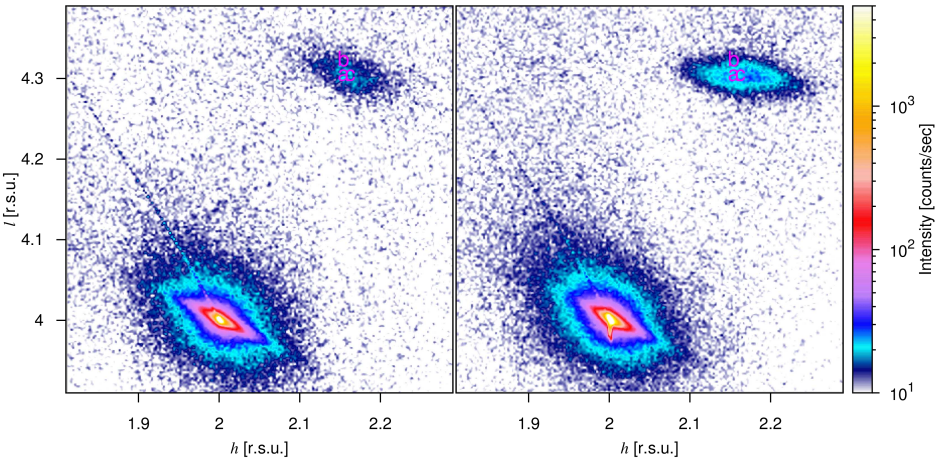

(a) DC-sputtered, p_{O2} = 0.03 Pa, d_{LSMO} = 18 nm **(b)** RF-sputtered, p_{O2} = 0.72 Pa, d_{LSMO} = 29 nm

Figure A.6.: RSMs on the (204)-reflection of LSMO on MgO (100), deposited in DC mode at low O_2 partial pressure (p_{O2}) and in RF mode at high p_{O2}, respectively. The letters a, b and c indicate the theoretically expected location of the LSMO reflection for unstrained growth along the correspondent crystal direction.

A.2.2 Microstructure of the LSMO-PZT interface

In Section 5.3.1 the microstructure of the LSMO-PZT system was analyzed and discussed. In addition to the STEM results already presented (Fig. 5.4 and Fig. 5.5), the two micrographs shown in Fig. A.7 focus on the strain relaxation mechanisms at the LSMO-PZT interface. Fig. A.7(a) features an example of a typical extended misfit dislocation around a grain of different orientation. In this example the number of unit cells gets reduced from eight to seven between the two continuous rows of atoms. While the relaxation via dislocations seems to be the preferred mechanism, in a few cases the formation of an amorphous interfacial phase is locally observable [see Fig. A.7(b)]. This phase extends to a thickness of less than 5 nm and is also laterally very confined. For this reason, epitaxial *c*-oriented growth of the PZT layer starts behind this relaxation region, which is most likely induced by the adjacent well-ordered volume, where the relaxation region is crystalline.

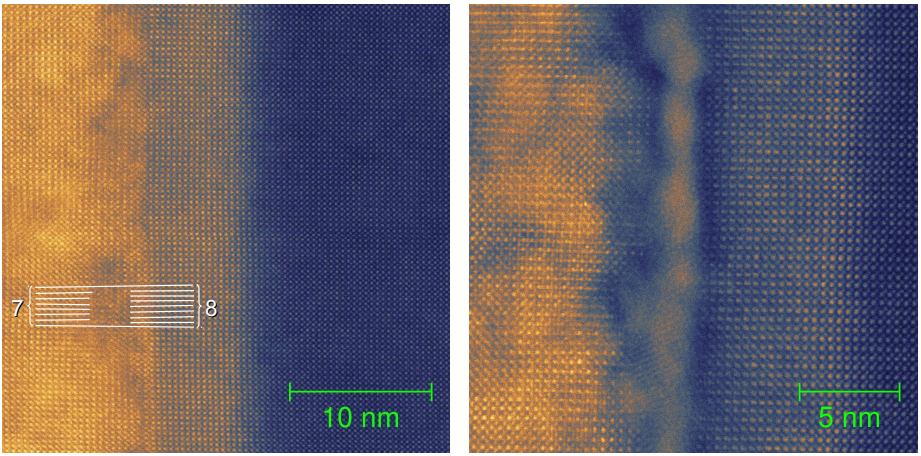

(a) extended dislocation **(b)** amorphous grains

Figure A.7.: STEM micrographs of the LSMO-PZT interface illustrating the strain relaxation mechanisms: (a): extended dislocation around a grain of different orientation, (b): formation of an amorphous phase at the interface. The layer sequence from right to left is STO:Nb/LSMO/PZT for both images.

A.2.3 Field dependence of magnetoelectric tuning

The ME tuning experiments presented in Chapter 6 were all performed at positive external magnetic fields. The reversal of the external field is an important test in order to discover possible artifacts, e.g., originating from leakage currents, and to validate the tuning effect. Ideally the reversal of the magnetic field should only result in a change of sign in the magnetic signal with preserved magnitude of the magnetic modulation.

Fig. A.8 illustrates the magnetic response to the remanent FE hysteresis at external fields of 200 Oe and −200 Oe, respectively. The difference in the absolute magnetic moments ($\approx 42\,\mu_B$/u.c.^{2} *versus* $\approx 52\,\mu_B$/u.c.^{2}) originates from the different magnetic histories: the measurement at 200 Oe was performed after Field Cooling (FC) in the same field, while the −200 Oe one was taken after saturating the sample in a negative field. However, apart from this difference, the tuning response is perfectly mirrored, as it is expected for an artifact-free measurement.

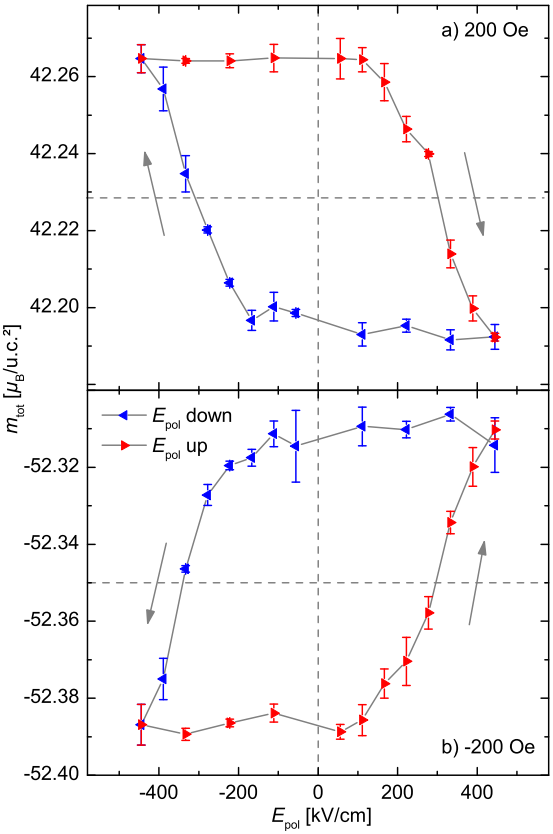

Figure A.8: Verification of the magnetic response to the FE remanent hysteresis at 100 K: Comparison of the low temperature response at a positive magnetic field (a) with the modulations measured at opposite magnetic field (b). For better comparability of the magnitude of the effects, the axis intervals of the magnetic moments have identical spans; the dashed crosshairs are guides to the eye.

B Personal data

B.1 Curriculum vitae (Lebenslauf)

Persönliche Daten

Name:	Philipp Moritz Leufke
Geburtsdatum:	28.02.1981
Geburtsort:	Titisee-Neustadt

Schulbildung

20. Juni 2000	Erwerb der allgemeinen Hochschulreife am Kreisgymnasium Titisee-Neustadt

Studium

Oktober 2001 – Juni 2007	Studium der Physik an der Universität Konstanz
Juli 2006 – Juni 2007	Diplomarbeit in der Emmy-Noether-Nachwuchsgruppe von Dr. M. Albrecht, Arbeitsgruppe Prof. G. Schatz, Titel: „Direkte Laserinterferenz-Strukturierung von Co/Pd- Multischichtsystemen mit senkrechter Anisotropie“
19. Juni 2007	Abschluss als Diplomphysiker

Berufstätigkeit

August 2007 – Januar 2009	Wissenschaftlicher Mitarbeiter am Karlsruher Institut für Technologie (KIT), Institut für Nanotechnologie (INT): Planung, Aufbau und Betreuung eines Ultrahochvakuum (UHV)-Labors
Februar 2009 – März 2012	Doktorarbeit am KIT/INT zum Thema der vorliegenden Dissertation
seit April 2012	Wissenschaftlicher Mitarbeiter am KIT/INT: Planung, Beschaffung und Inbetriebnahme von Dünnschichtabscheideanlagen (ALD, PLD) im Rahmen des Karlsruhe Nano Micro Facility (KNMF) und Betreuung eines UHV Labors

B.2 Publications

B.2.1 Conference contributions

In situ SQUID studies of magnetoelectric coupling in LSMO/PZT heterostructures

P. M. Leufke, A. K. Mishra, R. Kruk, Di Wang and H. Hahn,
Fifth Seeheim Conference on Magnetism (SCM2013), September 29th – October 3rd, 2013, *Frankfurt*

In situ SQUID studies of magnetoelectric LSMO/PZT heterostructures

P. M. Leufke, A. K. Mishra, Di Wang, R. Kruk and H. Hahn,
European Congress and Exhibition on Advanced Materials and Processes (EUROMAT), September 8–13, 2013, *Sevilla*

Electrostatic tuning of large-distance sputtered LSMO/PZT heterostructures

P. M. Leufke, A. K. Mishra, D. Wang, R. Kruk, and H. Hahn, Frühjahrstagung DPG, Sektion Kondensierte Materie, Fachverband Dielektrische Festkörper, March 10–15, 2013, *Regensburg*.

Studies on interface structures in multiferroic materials

D. Wang, P. M. Leufke, A. K. Mishra, E. Troester, T. Scherer, C. Kübel, R. Kruk, and H. Hahn, 15th European Microscopy Congress (EMC), September 16–21, 2012, *Manchester*.

Nonlinear optics on the silicon platform

W. Freude, L. Alloatti, A. Melikyan, R. Palmer, D. Korn, N. Lindenmann, T. Vallaitis, D. Hillerkuss, J. Li, A. Barklund, R. Dinu, J. Wieland, M. Fournier, J. Fedeli, S. Walheim, P. M. Leufke, S. Ulrich, P. Vincze, H. Hahn, H. Yu, W. Bogaerts, P. Dumont, R. Baets, B. Breiten, F. Diederich, M. T. Beels, I. Biaggio, Th. Schimmel, C. Koos, and J. Leuthold, Optical Fiber Communication Conf. (OFC), March 4–8, 2012, *Los Angeles*.

Sputtering deposition and characterization of epitaxial LSMO thin films

P. M. Leufke, A. K. Mishra, R. Kruk, and H. Hahn, Frühjahrstagung der Deutschen Physikalischen Gesellschaft, Fachverband Magnetismus, March 13–18, 2011, *Dresden*.

TEM investigation on the structures of $La_{0.75}Sr_{0.25}MnO_3$ thin films

D. Wang, A. K. Mishra, P. M. Leufke, T. Scherer, and C. Kübel, 2nd ANKA/KNMF Joint Users Meeting, October 7–8, 2010, *Karlsruhe*.

Two different coercivity lattices in Co/Pd MLs generated by single-pulse laser interference lithography

P. M. Leufke, S. Riedel, P. Leiderer, J. Boneberg, G. Schatz, M. Albrecht, H. Rohrmann, M.-S. Lee, J. Li, and T. Eimüller, 4th Seeheim Conference on Magnetism, March 28th – April 1st, 2010, *Frankfurt*.

Magnesium secondary batteries based on V_2O_5 cathodes

W. Lohstroh, P. M. Leufke, and H. Hahn, Frühjahrstagung der Deutschen Physikalischen Gesellschaft, Fachverband Metall- und Materialphysik, March 21–26, 2010 *Regensburg*.

Atomic layer deposition and characterization of bismuth oxide thin films

P. M. Leufke, N. Donia, S. Mathur, and H. Hahn, Frühjahrstagung der Deutschen Physikalischen Gesellschaft, Fachverband Dielektrische Festkörper, March 22–27, 2009 *Dresden*.

Atomic layer deposition and characterization of $BiFeO_3$ thin films

P. M. Leufke, J. Ellrich, and H. Hahn, 72. Jahrestagung der Deutschen Physikalischen Gesellschaft und DPG Frühjahrstagung des Arbeitskreises Festkörperphysik, Fachverband Magnetismus, February 25–29, 2008, *Berlin*.

Magnetization reversal in laser-interference patterned Co/Pd MLs studied by full-field Kerr microscopy

M.-S. Lee, J. Li, B. Redeker, P. M. Leufke, S. Riedel, P. Leiderer, J. Boneberg, M. Albrecht, and T. Eimüller, 72. Jahrestagung der Deutschen Physikalischen Gesellschaft und DPG Frühjahrstagung des Arbeitskreises Festkörperphysik, Fachverband Dünne Schichten, February 25–29, 2008, *Berlin*.

Direct laser interference patterning of magnetic thin films

S. Fischer, P. Leufke, S. Riedel, M. Albrecht, P. Leiderer, and J. Boneberg, 72. Jahrestagung der Deutschen Physikalischen Gesellschaft und DPG Frühjahrstagung des Arbeitskreises Festkörperphysik, Fachverband Magnetismus, February 25–29, 2008, *Berlin*.

Direct laser-interference patterning of Co/Pd ML systems with perpendicular anisotropy

P. M. Leufke, S. Riedel, P. Leiderer, J. Boneberg, G. Schatz, and M. Albrecht, 3rd Seeheim Conference on Magnetism, August 2007, *Frankfurt*.

Direct laser interference patterning of perpendicular Co/Pd ML films

P. M. Leufke, S. Riedel, P. Leiderer, J. Boneberg, and M. Albrecht, Frühjahrstagung der Deutschen Physikalischen Gesellschaft, Fachverband Magnetismus, March 26–30, 2007, *Regensburg*.

B.2.2 Journal articles

In situ magnetometry studies of magnetoelectric LSMO/PZT heterostructures

P. M. Leufke, R. Kruk, R. A. Brand, and H. Hahn, *Physical Review B* **87**, 094416, 10.1103/PhysRevB.87.094416 (2013).

Room temperature reversible tuning of magnetism of electrolyte-gated $La_{0.75}Sr_{0.25}MnO_3$ nanoparticles

A. K. Mishra, A. J. Darbandi, P. M. Leufke, R. Kruk, and H. Hahn, *Journal of Applied Physics* **113**, 033913, 10.1063/1.4778918 (2013).

Ferroelectric *vs.* structural properties of large-distance sputtered epitaxial LSMO/PZT heterostructures

P. M. Leufke, R. Kruk, D. Wang, C. Kübel, and H. Hahn, *AIP Advances* **2**, 032184, 10.1063/1.4756997 (2012).

Large-distance rf- and dc-sputtering of epitaxial $La_{1-x}Sr_xMnO_3$ thin films

P. M. Leufke, A. K. Mishra, A. Beck, D. Wang, C. Kübel, R. Kruk, and H. Hahn, *Thin Solid Films* **520**, 5521, 10.1016/j.tsf.2012.04.064 (2012).

Surface plasmon polariton absorption modulator

A. Melikyan, N. Lindenmann, S. Walheim, P. M. Leufke, S. Ulrich, J. Ye, P. Vincze, H. Hahn, Th. Schimmel, C. Koos, W. Freude, and J. Leuthold, *Optics Express* **19**, 8855, 10.1364/OE.19.008855 (2011).

External electric field driven 3D ordering architecture of silver (I) oxide meso-superstructures

J. Fanga, P. M. Leufke, R. Kruk, D. Wang, T. Scherer, and H. Hahn, *Nano Today* **5**, 175, 10.1016/j.nantod.2010.05.002 (2010).

Two different coercivity lattices in Co/Pd MLs generated by single-pulse laser interference lithography

P. M. Leufke, S. Riedel, M.-S. Lee, J. Li, H. Rohrmann, T. Eimüller, P. Leiderer, J. Boneberg, G. Schatz, and M. Albrecht, *Journal of Applied Physics* **105**, 113915, 10.1063/1.3126714 (2009).